



UNIVERSITAT POLITÈCNICA  
DE CATALUNYA  
BARCELONATECH

## *Nonlinear modeling and characterization of SAW devices for communications systems*

**Marta González Rodríguez**

**ADVERTIMENT** La consulta d'aquesta tesi queda condicionada a l'acceptació de les següents condicions d'ús: La difusió d'aquesta tesi per mitjà del repositori institucional UPCommons (<http://upcommons.upc.edu/tesis>) i el repositori cooperatiu TDX (<http://www.tdx.cat/>) ha estat autoritzada pels titulars dels drets de propietat intel·lectual **únicament per a usos privats** emmarcats en activitats d'investigació i docència. No s'autoritza la seva reproducció amb finalitats de lucre ni la seva difusió i posada a disposició des d'un lloc aliè al servei UPCommons o TDX. No s'autoritza la presentació del seu contingut en una finestra o marc aliè a UPCommons (*framing*). Aquesta reserva de drets afecta tant al resum de presentació de la tesi com als seus continguts. En la utilització o cita de parts de la tesi és obligat indicar el nom de la persona autora.

**ADVERTENCIA** La consulta de esta tesis queda condicionada a la aceptación de las siguientes condiciones de uso: La difusión de esta tesis por medio del repositorio institucional UPCommons (<http://upcommons.upc.edu/tesis>) y el repositorio cooperativo TDR (<http://www.tdx.cat/?locale-attribute=es>) ha sido autorizada por los titulares de los derechos de propiedad intelectual **únicamente para usos privados enmarcados** en actividades de investigación y docencia. No se autoriza su reproducción con finalidades de lucro ni su difusión y puesta a disposición desde un sitio ajeno al servicio UPCommons No se autoriza la presentación de su contenido en una ventana o marco ajeno a UPCommons (*framing*). Esta reserva de derechos afecta tanto al resumen de presentación de la tesis como a sus contenidos. En la utilización o cita de partes de la tesis es obligado indicar el nombre de la persona autora.

**WARNING** On having consulted this thesis you're accepting the following use conditions: Spreading this thesis by the institutional repository UPCommons (<http://upcommons.upc.edu/tesis>) and the cooperative repository TDX (<http://www.tdx.cat/?locale-attribute=en>) has been authorized by the titular of the intellectual property rights **only for private uses** placed in investigation and teaching activities. Reproduction with lucrative aims is not authorized neither its spreading nor availability from a site foreign to the UPCommons service. Introducing its content in a window or frame foreign to the UPCommons service is not authorized (*framing*). These rights affect to the presentation summary of the thesis as well as to its contents. In the using or citation of parts of the thesis it's obliged to indicate the name of the author.



UNIVERSITAT POLITÈCNICA DE CATALUNYA  
BARCELONATECH

Departament de Teoria del Senyal  
i Comunicacions

---

Ph.D. Thesis

# Nonlinear modeling and characterization of SAW devices for communications systems

---

Author: Marta González Rodríguez

Advisors: Juan Carlos Collado Gómez, Ph.D.  
Full Professor  
Universitat Politècnica de Catalunya (UPC)

José María González Arbesú, Ph.D.  
Associate Professor  
Universitat Politècnica de Catalunya (UPC)

Components and Systems for Communications Research Group  
Department of Signal Theory and Communications  
Universitat Politècnica de Catalunya

December 19, 2022



*“Perseverance in the face of challenges  
can lead to great rewards.”*

---



# Abstract

Nowadays, worldwide exploding growth in mobile devices puts a lot of pressure on the mobile communications technologies since an enormous amount of requirements, mainly focused on delivering enhanced mobile broadband services to consumers, are needed. The ever-increasing data rate requirements and the support for wireless technologies, like 5th Generation (5G), set a lot of pressure to manufacturers in finding new solutions to face the coexistence and integration of several radio systems operating in the Radio-Frequency (RF) modules.

This scenario introduces a variety of challenges that have to be faced when using multi-band operation. One of them is to fight against the desensitization in the RF front-end due to the generation of spurious signals by the nonlinearity of passive components inside the handset. Passive InterModulation (PIM) is becoming a major concern in the design of RF transceivers where the transmitter and receiver share the antenna, since it can cause receiver blocking. PIM might arise from different components such as antennas, mixers, filters, etc. Among the components into the RF chain, the filtering stage is one of the critical components since apart from high selectivity and miniaturization, they also have to meet low PIM specifications and thus, becoming a challenging task for RF designers.

For tackling these technological constraints, acoustic wave filters have been giving response to this need because of their outstanding performance, and have become a suitable solution for the emerging communications standards. Bulk Acoustic Wave (BAW) and Surface Acoustic Wave (SAW) are nowadays the main technologies, offering filtering structures with very low insertion losses and good out-of-band rejection that are in compliance with current system specifications. Despite it seems clear that the acoustic technology shows major advantages, there are some drawbacks too. One of them is that both BAW and SAW resonators exhibit a nonlinear behavior giving place to Intermodulation (IMD) and Harmonic distortion (H). Accordingly, RF front-end high linearization demands may become an issue to be solved in the definition of new advanced services in future standards.

There has been an upsurge in interest recently in the modeling and simulation of the nonlinearities of SAW devices during the last two decades. Despite different approaches, for example based on Finite Element Model (FEM), Coupling of Modes (COM) or P-Matrix, has been widely used, there is a lack of consensus about the

nonlinear generation driven by the difficulty to identify geometry-independent material parameters that could predict the nonlinear behavior of any resonator before manufacturing.

In particular, to this end, the thesis will be focused on the accurate nonlinear characterization of SAW devices. The modeling and simulation of nonlinearities on SAW resonators will be one of the most important milestones of the thesis. Specifically, the development of fundamental circuit models to account for the nonlinear mechanism occurring in SAW resonators and, the implementation of mathematical techniques to synthesize circuit networks based on these models, to reduce the computational time and to further improve the simulation and modeling of these resonators.

The novelty of this thesis lies in the development of a characterization process for SAW resonators allowing to predict the behavior of new devices with other geometries. To be successful in this process, an equivalent nonlinear circuit model is proposed. The developed model is distributed and directly related to the local constitutive equations of the piezoelectricity. Special efforts are expended towards developing a new method of analysis for the simulation of both H and IMD generation in SAW resonators and filters. Several experimental verifications have shown that despite of its simplicity, the proposed model is extremely consistent and fast to simulate the linear and nonlinear response of different devices using only a geometry-independent nonlinear parameter.

# Acknowledgements

It is always hard to know where to start since many people have contributed to this work and for this day to be possible with their support, collaboration, love and guidance.

I am deeply indebted to my thesis advisors Carlos and Chema, words cannot describe my gratitude to them. Thanks a lot for allow me to work with you and give me the opportunity to start my research career. You encouraged me to pursue the Ph.D and it is the best decision I could make. I have no regrets because I couldn't have been happier and more fortunate.

Both of you have been my inspiration every day, the light and the compass that have guided me. You always shared your immense knowledge and kept me motivated all this years, specially during tough times. I am extremely grateful for your untiring dedication and patience during all this years, for always have the door open whenever I needed from you. I could not have undertaken this journey without both of you and you are very responsible for making me what I am today. Thanks for being my mentors, the best ones. Thank you very much for all the good and funny moments shared together, I will never forget.

Also, I would like to thank to all my research group mates David, Rafa and Carlitos for the fantastic work environment and the funny moments lived together. I would be remiss in not mentioning Marc and Antoni for their friendship and all the coffee times shared together all this years. Many thanks to all the great people at EETAC community, from professors to laboratory technicians and all the people I have had the pleasure of collaborating with all these years.

Special thanks should also go to my dearests friends from Madrid, to worry, to love me and to be there whenever I need them even with the distance. I am extremely grateful to have them in my life since they are the best family, or as we say, the self-chosen family. I have had the pleasure of sharing the best moments of my life with you guys and you are a very important part of the fact that I have been able to get here.

I want to express my gratitude to all the people from SAW R&D at Qorvo Inc for their feedback and fruitful discussions. I would like to extend my sincere thanks to Dr. Robert Aigner and Dr. Sebastian Huebner for all this years of support and for giving me the opportunity of joining the SAW R&D Munich team. I couldn't



feel more grateful to be able to grow professionally and personally surrounded by my team mates and all the excellent people at the Munich office. I am eager to see what future holds for me.

Last but not the least, I would like to acknowledge all my family, my grandparents and my uncles and aunts for their affection and support during all this years. Needless to say that my parents have made possible everything I am now. Special thanks to my mum and sister for providing me with unfailing support and continuous encouragement throughout all my life even in the hardest moments. To my father, because he has made it possible, I hope you feel proud of me and you can see me succeed.

To Carles, for your unconditional love, for always been there when needed as well as much-needed support at difficult times. You had give me the strength and encourage me to follow my dreams no matter what. Thanks for putting up with me all these years and, for still holding.

It has been a long journey, almost ten years at Barcelona and they have been the best and happiest of my life. This accomplishment would not have been possible without all of you and I am grateful from the bottom of my heart. The best is yet to come!

Marta

# Contents

<b>Acronyms</b>	<b>xiii</b>
<b>1 Introduction</b>	<b>1</b>
1.1 Understanding acoustic technology . . . . .	1
1.2 State of the art, SAW challenges . . . . .	4
1.3 Motivation and objectives . . . . .	8
1.4 Thesis outline . . . . .	10
<b>2 Fundamental theory of the electrical characterization of acoustic devices</b>	<b>13</b>
2.1 Introduction . . . . .	13
2.2 Mechanics in solids . . . . .	13
2.2.1 Strain . . . . .	14
2.2.2 Stress . . . . .	15
2.2.3 Hooke's law . . . . .	16
2.3 One-dimensional mechanical equation of motion . . . . .	17
2.4 Piezoelectricity . . . . .	20
2.5 Constitutive equations . . . . .	22
2.6 Nonlinear constitutive equations . . . . .	23
2.7 Nonlinear distortion . . . . .	24
2.7.1 Time-domain nonlinear equations . . . . .	24
2.7.2 Passive intermodulation and harmonic generation . . . . .	27
<b>3 Modeling of Surface Acoustic Wave resonators</b>	<b>31</b>
3.1 Introduction . . . . .	31
3.1.1 SAW parameters . . . . .	32
3.1.2 Review of SAW device modeling and applications . . . . .	34
3.1.3 Nonlinear modeling approaches . . . . .	42
3.2 Mason-based linear models . . . . .	46
3.2.1 Mason linear model . . . . .	46
3.2.2 Equivalent circuits for SAW based on Mason model . . . . .	50
3.2.3 Distributed model of the whole transducer . . . . .	58

3.2.4	Discretized model of the MR and NMR sections . . . . .	61
3.2.5	Linear measurements . . . . .	62
3.3	Nonlinear discretized model . . . . .	70
3.3.1	Derivation of the crossed-field nonlinear discretized Model . . . . .	71
<b>4</b>	<b>Input-Output Equivalent Sources (IOES) method</b>	<b>77</b>
4.1	Introduction . . . . .	77
4.2	Y-matrix analysis . . . . .	79
4.2.1	Admittance matrix formulation . . . . .	80
4.2.2	Y-matrix block: node connection between different sections in Matlab <sup>®</sup> . . . . .	81
4.2.3	Y-block matrix algorithm . . . . .	84
4.3	Matlab <sup>®</sup> linear model . . . . .	87
4.4	Input-Output Equivalent Sources (IOES) . . . . .	88
4.4.1	Introduction . . . . .	88
4.4.2	IOES method step-by-step . . . . .	89
4.4.3	Matlab <sup>®</sup> nonlinear model . . . . .	101
4.4.4	Full simulation process . . . . .	102
4.4.5	IOES method validation . . . . .	103
<b>5</b>	<b>Nonlinear characterization</b>	<b>109</b>
5.1	Introduction . . . . .	109
5.2	LSAW resonators measurements . . . . .	110
5.2.1	Description of resonators . . . . .	110
5.2.2	IMD3 and H3 measurement system . . . . .	111
5.2.3	IMD3 measurements . . . . .	113
5.2.4	H3 measurements . . . . .	114
5.2.5	H2 measurement system . . . . .	116
5.2.6	H2 and H3 measurements . . . . .	117
5.3	TC-SAW resonator measurements . . . . .	121
5.3.1	Description of resonators . . . . .	121
5.3.2	IMD3, H3 and H2 measurement system . . . . .	122
5.3.3	IMD3 measurements . . . . .	124
5.3.4	H3 measurements . . . . .	126
5.3.5	H2 measurements . . . . .	127
5.4	LSAW resonators response analysis . . . . .	128
5.4.1	Broadband linear response measurements versus simulations . . . . .	129
5.4.2	IMD3 nonlinear characterization . . . . .	130
5.4.3	IMD3 characterization process validation . . . . .	133
5.4.4	H3 characterization . . . . .	135
5.4.5	H3 characterization process validation . . . . .	136
5.4.6	Non-uniform electric field: edge-E linear model . . . . .	138

5.4.7	Out-of-band IMD3 characterization . . . . .	147
5.4.8	H2 nonlinear fitting and characterization . . . . .	156
5.5	TC-SAW resonators response analysis . . . . .	165
5.5.1	Broadband linear response measurement versus simulations .	165
5.5.2	IMD3 and H3 nonlinear characterization of TC-SAW resonators	167
5.5.3	IMD3 and H3 nonlinear fitting of TC-SAW resonators . . . .	169
5.6	Summary measurements results . . . . .	178
5.6.1	LT-SAW . . . . .	178
5.6.2	TC-SAW . . . . .	179
<b>6</b>	<b>Application of the IOES to SAW filters</b>	<b>181</b>
6.1	Introduction . . . . .	181
6.2	Ladder filters . . . . .	182
6.2.1	Linear measurements . . . . .	183
6.2.2	Matlab <sup>®</sup> linear simulations of ladder filters . . . . .	185
6.2.3	Nonlinear measurements of ladder filters . . . . .	187
6.2.4	Nonlinear simulations of ladder filters . . . . .	196
6.2.5	Analysis of the nonlinear response of ladder filters . . . . .	201
6.2.6	Conclusions . . . . .	205
6.3	CRF filters . . . . .	206
6.3.1	Linear measurements . . . . .	206
6.3.2	Matlab <sup>®</sup> linear simulations of CRF filters . . . . .	208
6.3.3	Nonlinear measurements of CRF filters . . . . .	210
6.3.4	Nonlinear simulations of CRF filters . . . . .	212
6.3.5	Analysis of the nonlinear response of CRF filters . . . . .	215
6.3.6	Conclusions . . . . .	218
6.4	Nonlinear lumped model . . . . .	219
6.5	Nonlinear simulations with lumped model . . . . .	223
<b>7</b>	<b>High-power characterization and other set-ups</b>	<b>233</b>
7.1	Feed-forward cancellation . . . . .	233
7.1.1	Introduction . . . . .	233
7.1.2	Proposed method description . . . . .	234
7.1.3	High-power measurements and results . . . . .	236
7.1.4	Performance evaluation . . . . .	242
7.2	Tone-injection modulated signals . . . . .	244
7.2.1	IMD3 cancellation expressions . . . . .	245
7.2.2	Measurement system . . . . .	246
7.2.3	Experimental results . . . . .	248
<b>8</b>	<b>Conclusions and future research lines</b>	<b>253</b>
8.1	Conclusions . . . . .	253

8.2	Future research lines . . . . .	256
<b>Appendices</b>		<b>261</b>
<b>A</b>	<b>Admittance matrix formulation</b>	<b>261</b>
A.0.1	Admittance matrix concatenation process in Matlab . . . . .	261
<b>B</b>	<b>Frequency domain nonlinear equations</b>	<b>263</b>
<b>C</b>	<b>Standing wave patterns at targeted frequency for remix purposes (metallized region)</b>	<b>265</b>
<b>D</b>	<b>Simulation parameters</b>	<b>267</b>
D.1	L-SAW resonators . . . . .	267
D.1.1	Uniform electric field . . . . .	267
D.1.2	Edge-E electric field . . . . .	269
D.1.3	IMD3 out-of-band . . . . .	271
D.1.4	H2 response . . . . .	272
D.2	TC-SAW . . . . .	273
D.2.1	Uniform electric field . . . . .	273
D.2.2	Edge-E electric field . . . . .	275
<b>E</b>	<b>List of author's contributions</b>	<b>279</b>
E.1	Research Contributions . . . . .	279
E.2	Academic Contributions . . . . .	281
<b>Bibliography</b>		<b>283</b>

# Acronyms

<b>2D</b>	Two Dimensional
<b>3D</b>	Three Dimensional
<b>3G</b>	Third-Generation
<b>4G</b>	Fourth-Generation
<b>5G</b>	Fifth-Generation
<b>6G</b>	Sixth-Generation
<b>ADS</b>	Advanced Design System
<b>AlN</b>	Aluminum Nitride
<b>AM</b>	Amplitude Modulation
<b>ARB</b>	ARbitrary Waveform
<b>ATL</b>	Acoustic Transmission Line
<b>AW</b>	Acoustic Wave
<b>BAW</b>	Bulk Acoustic Wave
<b>BEM</b>	Boundary-Element Method
<b>BVD</b>	Butterworth-Van Dyke
<b>CA</b>	Carrier Aggregation
<b>CDMA</b>	Code Division Multiple Access
<b>COM</b>	Coupling Of Modes
<b>CRF</b>	Coupled Resonator Filters
<b>CW</b>	Continuous Wave
<b>DAC</b>	Digital to Analog Converter
<b>DMS</b>	Double-Mode Structure
<b>DUT</b>	Device Under Test
<b>EB</b>	Electron Beam
<b>ECM</b>	Equivalent Circuit Model
<b>EM</b>	Electromagnetic

<b>EVM</b>	Error Vector Magnitude
<b>FBAR</b>	Film Bulk Acoustic Resonator
<b>FEM</b>	Finite Element Method
$f_p$	Parallel Resonant Frequency
$f_s$	Series Resonant Frequency
<b>FS</b>	Frequency Synthesizer
<b>GSM</b>	Global System for Mobile Communications
<b>GUI</b>	Graphical User Interface
<b>H</b>	Harmonic distortion
<b>H2</b>	Second Harmonic
<b>H3</b>	Third Harmonic
<b>HB</b>	Harmonic Balance
<b>HP</b>	High -Power
<b>HPA</b>	High-Power Amplifier
<b>HPF</b>	High Pass Filter
<b>HPH</b>	High-Power Heating
<b>I</b>	In-phase
<b>IC</b>	Integrated Circuit
<b>IDT</b>	InterDigital Transducer
<b>IEEE</b>	Institute of Electrical and Electronics Engineers
<b>IES</b>	Interdigital Electrode System
<b>IF</b>	Intermediate Filter
<b>IHP</b>	Incredible High Performance
<b>IM</b>	InterModulation
<b>IMD</b>	InterModulation Distortion
<b>IMD2</b>	second-order InterModulation Distortion
<b>IMD3</b>	third-order InterModulation Distortion
<b>IOES</b>	Input-Output Equivalent Sources
<b>LiNbO<sub>3</sub></b>	Lithium Niobate
<b>LiTaO<sub>3</sub></b>	Lithium Tantalate
<b>LPF</b>	Low Pass Filter
<b>LSAW</b>	Leaky-SAW
<b>LTE-A</b>	Long Term Evolution - Advanced
<b>LT-SAW</b>	Lithium Tantalate-Surface Acoustic Wave

<b>MIMO</b>	Multiple-Input, Multiple-Output
<b>Mo</b>	Molybdenum
<b>MR</b>	Metallized Region
<b>NMR</b>	Non-Metallized Region
<b>PA</b>	Power Amplifier
<b>PBC</b>	Periodic Boundary Conditions
<b>PIM</b>	Passive InterModulation
<b>PML</b>	Perfectly Matched Layer
<b>PMM</b>	P-Matrix Model
<b>Q</b>	Quadrature
<b>Q-factor</b>	Quality factor
<b>RF</b>	Radio Frequency
<b>Rx</b>	Receive
<b>SA</b>	Spectrum Analyzer
<b>SAW</b>	Surface Acoustic Wave
<b>SBUE</b>	Stop-Band Upper Edge
<b>SF</b>	Scaling Factor
<b>SG</b>	Signal Generator
<b>SiO<sub>2</sub></b>	Silicon Dioxide
<b>SMR</b>	Solidly Mounted Resonator
<b>SPUDT</b>	Single Phase UniDirectional Transducer
<b>TC-SAW</b>	Temperature Compensated Surface Acoustic Wave
<b>TF-SAW</b>	Thin Film Surface Acoustic Wave
<b>TL</b>	Transmission Line
<b>Tx</b>	Transmit
<b>UPC</b>	Universitat Politècnica de Catalunya
<b>V<sub>i</sub></b>	In-phase Voltage
<b>VM</b>	Vector Modulator
<b>V<sub>q</sub></b>	Quadrature Voltage
<b>VNA</b>	Vector Network Analyzer
<b>VSG</b>	Vector Signal Generator
<b>VSWR</b>	Voltage Standing Wave Ratio
<b>XBAR</b>	laterally eXcited Bulk Acoustic Resonators
<b>W</b>	Tungsten





# Chapter 1

## Introduction

### 1.1 Understanding acoustic technology

Connectivity has become unequivocally a prevalent necessity of today's society. Smartphones, tablets, wearable devices among others, have changed the society life-style and they have become essential in the daily basis of many people. Finding new solutions to face the coexistence of several radio systems at the same time, and including them in a single portable device is the future of wireless market innovation.

During the last years, it has been an explosive growth of the smartphone market especially in supporting fourth Generation (4G) Long Term Evolution - Advanced (LTE-A) with bands ranging from 0.7 to beyond 2.6 GHz. The introduction of the carrier Aggregation (CA) and Multiple-Input, Multiple-Output (MIMO) techniques to enhance data rates in the limited and narrowly packed spectrum, puts further stress on the utilization of multiple bands in a limited bandwidth. Nowadays, the smart-phone market is changing at an incredible pace and the continuous need for high data rate and more users is driving the adoption of fifth generation (5G) LTE and WiFi 6. As technology evolves, the increase in data rates, transfer velocity and latency reduction or the power and linearity requirements among others, are service advances that are inherently connected to the performance specifications. Consequently, the number of frequency bands supported by the average smart-phone keeps increasing, requiring additional RF-filters to support the crowded spectrum.

The requirements for the use of CA introduces new challenges since many of these bands are very close together and, therefore, require highly selective filters with good isolation and out-of-band rejection. Moreover, it is essential that they can operate without detrimental mutual interference leading to the development of multiplexer filter solutions. Existing difficulty when using multi-band operation is to maintain linearity in order to avoid nonlinear mixing products falling into one of the receiving bands of the device.

At the same time as a matter of complexity, there is also an issue of volume. Miniaturization is mandatory in order to fit such a large number of RF filters into the limited space assigned to the RF section of a portable device. This demands for continuous research on filters for a performance improvement and a size reduction.

Acoustic wave technology has been giving response to this need, and has become the best solution up-to-date capable of fulfilling performance and size specifications. With the use of acoustic resonators, the electromagnetic (EM) wave to be filtered is transformed into a mechanical wave propagating through a material. The propagation velocity of the acoustic wave in the material is much lower than the EM propagation velocity in vacuum and, since the frequency is unaltered, the resulting acoustic wave has a micron-order wavelength. An EM wave transforms itself to an acoustic wave because of the piezoelectric effect that produces a deformation of the material when a voltage is applied on it. The application of such voltage to the piezoelectric slab will determine how the acoustic wave is induced and guided (propagating mode) through the structure. There are several ways to do that, but most of them can be classified into two cases, BAW and SAW resonators.

In the case of a BAW resonator, the piezoelectric plate is sandwiched between metallic electrodes. The most used piezoelectric material for BAW devices is aluminum nitride (AlN). When a voltage difference is applied to the electrodes, the piezoelectric effect generates an acoustic wave propagating vertically in the bulk structure, that is, in the direction of the electric field. The fundamental resonance frequency, one-half of the acoustic wavelength, is determined by the thickness and material properties of the piezoelectric and the electrodes. There are several ways to confine the acoustic wave which results in two different types of BAW resonators as depicted in Fig. 1.1: Film Bulk Acoustic Resonators (FBAR) and Solidly Mounted Resonators (SMR)

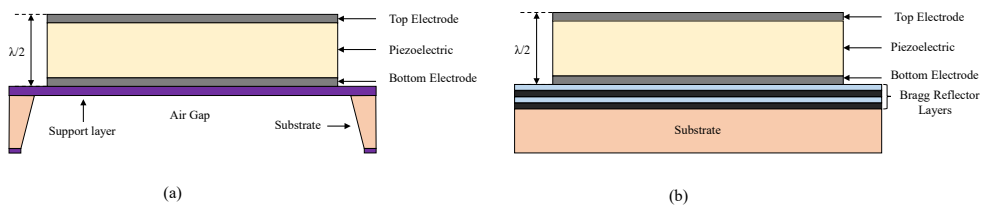


**Figure 1.1:** BAW resonators technologies (a) Cross-section of a FBAR resonator (b) Cross-section of an SMR.

In the FBAR case, the idea is to confine the acoustic wave creating an air-gap cavity below the bottom electrode, as depicted in Fig. 1.1 (a). Using an electrical analogy, the air cavity acts as a short-circuit, forcing the acoustic wave to reflect between the top and bottom electrodes and, therefore, generating the resonant mode. In the SMR configuration, a Bragg reflector is placed below the bottom electrode, as shown in Fig. 1.1 (b). Specifically, it consists of alternating multiple low and high acoustic impedance layers, i.e., metal and oxide layers, confining the acoustic wave to certain conditions of reflection.

Meanwhile, in a SAW resonator the wave propagates along the surface of the piezoelectric plate. SAW devices are generally manufactured on a Lithium Tantalate ( $\text{LiTaO}_3$ ) or Lithium Niobate ( $\text{LiNbO}_3$ ) crystal substrates. Induction of such a wave is possible by means of metallic interdigital transducers (IDT) and reflective gratings patterned on the piezoelectric material. Basically, an electrical signal (microwave signal) applied at the IDT stimulates a micro-acoustic wave that propagates along the surface thanks to the piezoelectric effect. Applying a voltage to such crystal will provoke a mechanical deformation, converting electrical energy into mechanical energy. The length and the separation between the electrodes in the propagation direction will define the working frequency of the transducer, being  $\lambda/4$  the separation between consecutive digits. Since the order of magnitude of the phase velocity is small, this fact allows many wavelengths to be adapted across the IDTs in a very small device, improving this way the effectiveness of the piezoelectric transduction.

Fig.1.2 shows a basic 1-port SAW resonator with reflectors at both sides. As shown, each period of the IDT consists of three metallic strips at the surface of the substrate. The strips are aligned and connected alternatively by the two bus bars. By applying a RF voltage between the bus bars, the electric field generates a periodic strain on the surface and excites a SAW propagating along the surface of the substrate. On this structure, the resonance condition happens when periodicity of the structure equals the acoustic wave wavelength ( $\lambda = 2d$ ).

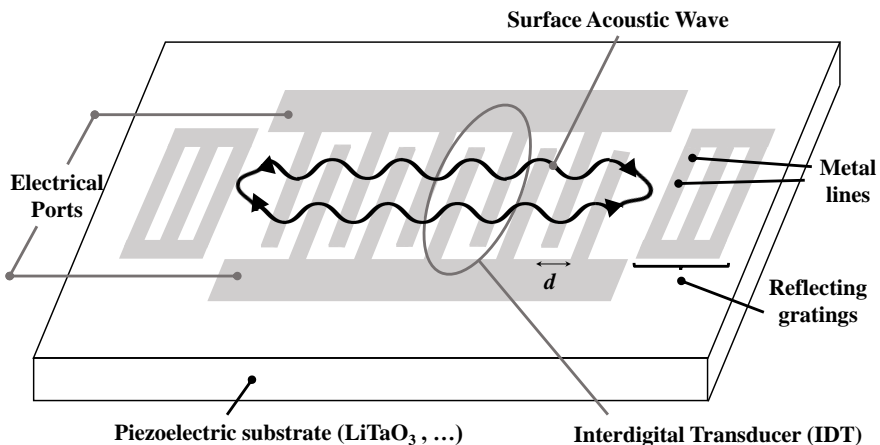


**Figure 1.2:** Schematic picture of a 1-port SAW resonator.

Furthermore, as we can see in Fig. 1.2, a resonator cavity is formed between the two side reflectors. Inside the cavity, all the energy is controlled -delivered and extracted- through the acoustic resonator by the SAW transducer. Reflectors are used to trap effectively the acoustic energy, creating reflection back to the transducer. If the structure is electrically excited, it is possible to create an electrical res-

onant structure with a resonance ( $f_s$ ) and anti-resonance ( $f_p$ ) frequency response. Both  $f_s$  and  $f_p$  can be tuned by controlling the period of the fingers and the metal thickness on the substrate. Note that the thickness of the substrate is much larger than the distance between electrodes to ensure that only SAW modes propagate. Controlling which modes propagate through the structure is important to avoid parasitic resonances.

## 1.2 State of the art, SAW challenges

Despite the existence of SAW was first discovered in 1885 by Lord Rayleigh, it did not receive engineering attention until many years after. Acoustic waves have been used in electronics for many years, mainly using quartz resonators, because it provides high quality factor (Q-factor) values due to the low acoustic losses. In 1965, the first SAW devices were made, introducing exceptional versatility because of the use of the IDTs transducers

First applications of SAW devices were in military systems, using delay lines for pulse expansion and compression. Basically, this applications used the effect that the velocity of the SAW on a typical crystal is five orders of magnitude lower than that of the electric signal. After that, the high-volume fabrication of TV intermediate frequency (IF) filters started around 1975, replacing the previous LC filters [2].

It is widely known that SAW technology has been ubiquitous applied to communications systems contributing to the development of different devices such as high frequency oscillators, convolvers, correlators, switching devices for optical applications, and so on. In mobile communications systems, SAW devices have been also applied and contributed to the development of portable devices, being the band-pass filtering the most notable application. The next evolution came with the beginning of Global System for Mobile Communications (GSM) which required narrowband IF filters for the selection of the channels usually using Double-Mode Structure (DMS) filters, which are composed by an inline arrangement of input and output transducers backed by reflectors at the outer sides of the acoustic track and also using Single-Phase Unidirectional Transducer (SPUDT) filters.

Then, in early 2000 with the development of GSM standard, the number of SAW IF filters decreased dramatically since mainly inter-stage filters were used in GSM-based cellular phones [3]. By this time, SAW filter technology was based on two techniques. One is the DMS-filter, and the second one is the ladder-type, where acoustic resonators are connected alternatively in series and shunt, shaping the frequency response.

With the advent of third-Generation (3G), the number of required filters increased significantly since duplexers were needed. The majority of these filters were implemented in SAW and BAW technology. A key advantage of acoustic devices is that waves are confined inside of the devices creating standing waves with high-Q factors on the order of some thousand. These high-Q resonances are the basis of the frequency selectivity and low-loss that acoustic filters achieve [4]. Specifically,

SAW technology found a good niche to meet the technical requirements of filters applications up to 1.9 GHz in multiple-access technologies such as code Division Multiple Access (CDMA) used in 2G and GSM in 3G, where the insertion loss and rejection specifications are less rigorous than 4G or 5G bands. In addition, various IEEE 802.11 standards, including 802.11ac/af/ad/ah, are also adopting under-1-GHz frequencies, leading to a broader use of SAW devices.

Moreover, the frequency of operation of SAW resonators has traditionally been limited by integrated circuit (IC) manufacturing capabilities as the frequency is defined by the tiny IDT electrodes. Currently, the common commercial upper frequency limit for SAW is located around 2.5 GHz, as for higher frequencies it would require a very small lithography resolution. Also, for high frequencies, the filter insertion loss is limited by resistivity of the electrodes and as stated in [5], at frequencies above 2 GHz the comb-fingers will be very small and it can suffer of power handling problems. Instead, BAW is a complementary technology to SAW, allowing narrowband filters with excellent rejection at frequencies above 1.5 GHz and up to 6 GHz.

An overview of the main differences between SAW and BAW technologies can be summarized on Table. 1.1. The most common SAW manufacturing processes can be divided in three groups: the standard SAW, the so-called Temperature Compensated (TC-SAW) and the Thin-Film (TF)-SAW. The main differences between them basically lies in how the structure is made along with the substrate used in each case.

With regard the main BAW technologies we can found, the SMR and FBAR technologies which has been previously introduced, and the newly laterally eXcited BAW Resonators (XBAR). The former is based on an Interdigital Electrode System (IES) looking like the IDT but is mainly used to create horizontal electric field which in turn generates shear deformation - standing wave thickness resonance between the electrodes.

**Table 1.1:** Acoustic filter technology overview [1].

SAW	TC-SAW	TF-SAW	BAW-SMR	BAW-FBAR	BAW-XBAR
<b>Lateral Propagation</b>			<b>Vertical Propagation</b>		
<b>Application</b>					
4G	4G	4G/5G	4G/5G	4G/5G	4G/5G
<b>Cost (+ High Cost, - Low Cost)</b>					
---	--	-	-	+	(Est.) --
<b>Process Steps (+ Complex, - Simple)</b>					
-	+	++	+++	++	+++
<b>Structure</b>					
Air Cavity	Oxide	Air Cavity	Air Cavity	Air Cavity	Air Cavity
Single Crystal Piezo	Single Crystal Piezo	Single Crystal Piezo	Polycrystal Piezo	Polycrystal Piezo	Polycrystal Piezo
		Backside Parasitic	Backside Parasitic	Air Cavity	Air Cavity
<b>Substrate</b>					
Single Crystal Piezo	Single Crystal Piezo	Piezo on Insulator	Silicon	Silicon	Piezo on Insulator

One of the merits of SAW is that manufacturing process is simpler and, therefore are more cost-effective in comparison with BAW. However, SAW filters that are used in RF front-ends have to meet certain power durability requirements and exhibit a minimum frequency stability. It is known that SAW filters are also very temperature sensitive, being the low-power durability one of the major concerns. The stiffness of the substrate material tends to decrease at higher temperatures and acoustic velocity diminishes. A SAW filter's response may fluctuate by as much as 4 MHz into the operating temperature range. This limitation has become more significant as guard bands become narrower and consumer devices are specified to operate across a wide temperature range (typically,  $-20^{\circ}\text{C}$  to  $85^{\circ}\text{C}$ ). Fulfilling these requirements in addition to the high-Q factors was achieved with the development of TC-SAW resonators. For TC-SAW technology, an additional layer of Silicon Dioxide ( $\text{SiO}_2$ ) on the top of the IDT is added, to reduce the frequency shift due to temperature variations. Moreover, in terms of performance and market uptake TC-SAW is the dominant technology. Lately, TF-SAW technology is disrupting the market since shows results comparable with BAW filters at a lower cost and directly competes with them in performance.

As stated previously, the performance requirements of new wireless standards and their narrowly spaced channels has produced some difficulties to enhance the performance of high-Q filters because of the rigorous requirements. Existing bands will continue to be supported or may be re-farmed for more advanced communications standards, usually requiring even more state-of-the-art filters. Although

advances in SAW and BAW filters may fulfill current demands for performance and physical size, future wireless standards could require greater tunability and smaller package sizes [6].

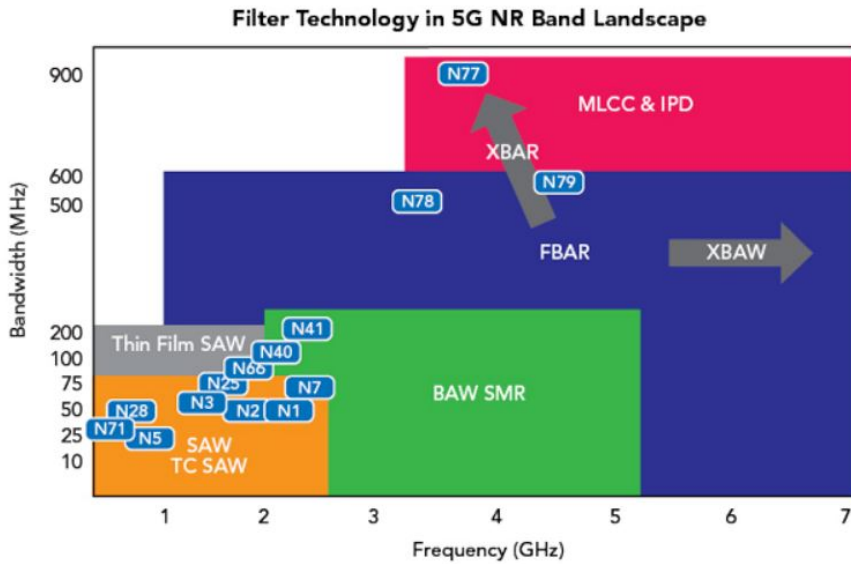


Figure 1.3: SAW and BAW filters technologies applications [1].

As Fig.1.3 depicts, with the rise of 5G not only the legacy SAW and TC-SAW filters will be used on the low frequency range. The so-called Thin-Film(TF)-SAW filter technology definitely appears into the market and, performance-wise directly competes with a BAW filter in some frequency bands. Lately, [7],[8] an Incredible High Performance (IHP) SAW structure was released by Murata Co., Ltd, which is composed by a combination of thin piezoelectric material with a Bragg reflector stack. Such structure can concentrate the energy of leaky SAW, and achieve a higher quality factor and coupling factor of SAW resonators. In this technology, the thermal compensation mechanism comes directly from the substrate.

Accompanying the extension of the future frequency range of the systems, SAW devices must overcome the high-frequency challenge and move to these frequencies too. Some researchers [9] have developed some ultra-fine fabrication techniques based on Electron Beam (EB) lithography for low-loss wide-band SAW filters beyond 5 GHz and up to 10 GHz reaching a level at which practical applications should be considered in the future.



## 1.3 Motivation and objectives

Although SAW filters are passive devices, they suffer from both a nonlinear response due to its inherent nonlinear behavior and a relatively unstable temperature performance, since the material properties of the resonant structures change significantly with temperature.

The analysis of nonlinearities occurring in passive devices, although being weak, are becoming a challenging requirement and taking a growing attention, due to their effects in the high demanded performance of nowadays receivers. PIM that can produce receiver blocking, might be caused by components placed close to the antenna if this is shared by the transmitters and the receivers. PIM might arise by different causes [10], such as degradation of materials, bad RF connections, thermal effects or intrinsic nonlinearities arising inside of the components: antennas, isolators, connectors, filters, etc. All of them must meet low PIM specifications becoming a challenging task for the RF designers of such devices.

Proper nonlinear models and simulation techniques help to reduce the time-to-market if those models can predict, before manufacturing, the PIM performance of these devices, which, in a general sense, are size comparable to the wavelength. A proven good approach is to work with distributed nonlinear models in which the nonlinear effect is locally described, allowing to find shape and size-independent nonlinear material parameters that can be later used for the design of any device. The main drawback of this approach is that the device must be discretized in many unit-cells describing the nonlinearities locally, and it leads to a high computation time, especially if the device has a lot of potential distributed nonlinear components, such as multiplexers, which include many resonators.

In comparison with highly nonlinear components, such as diodes or transistors, passive components are weakly nonlinear. For weak nonlinearities we understand that the generated H and IMD are significant, but there is not significant saturation or detuning at the fundamental signals. Under these premises, nonlinear analyses can be simplified if we do not constrain the analysis to the strict accomplishment of power conservation [11],[12].

Among the existing major nonlinear distortions in the frond-end, desensitization is a common one. In particular, the generation of third-order InterModulation Distortion (IMD3) in frequency selective devices is becoming a major concern in the design of RF transceivers, where the transmitter and receiver share the antenna, because it can cause interfering signals at a given receiver band affecting its sensitivity. In a duplexer structure, the Transmit (Tx) and Receive (Rx) signals continuously work at the same time but with different frequency bands. Both Tx and Rx filtered signals share the same antenna pin and in some cases, it may occur a degradation of receiver sensitivity due to the presence of a Tx leakage signal due to the limited isolation between Tx and Rx, creating RF frequency components falling into the receiver band. Moreover, spurious emissions of IMD products might be an issue. This IMD products are created inside the duplexers and could be harmful if they drop in the Rx band since the signal to noise ratio of the receiver will be affected.

These IMD products are due to the intermodulation between the Tx signal and external interfering signals.

It is known that SAW duplexers offer a second-order nonlinearity suppression that is roughly a few tens of dB better than that offered by RF BAW duplexers. Due to the presence of two electrodes with alternated polarity per acoustic wavelength, SAW resonators offer inherently better 2nd order nonlinearity than BAW devices. However, they are worst in terms of 3rd order nonlinearity. Because second-order nonlinearity requirements for SAW duplexers are usually not an issue, modeling effort of the thesis will be focused in third-order nonlinearity: harmonic (H3) and IMD3 dependency.

Although electro-acoustic filters offer a complex nonlinear behavior, these problems indeed open a path for properly address the origin of those nonlinear sources. Modeling of SAW devices has given attention of research academia over the last years, specially for the nonlinear behavior, since there is a lack of generalized consensus about its origin. The main objective of the thesis is to significantly contribute to this topic, providing innovative solutions to evaluate this concern and developing SAW circuitual models accounting for the nonlinear manifestations.

The challenge in the nonlinear modeling lies in finding innovative ways to effectively simulate nonlinearities occurring in SAW devices. To be successful with this objectives, there is a five-fold purpose that which can be summarized as follows:

- Special efforts are expended towards the creation of new distributed linear and nonlinear circuitual models. In these respects, the new models are related to the local constitutive equations and they must depend exclusively on the physical parameters of the materials and their dimensions. They should reproduce the standing wave pattern of the field along the structure at a given frequency.
- Design of a new method for the simulation of both H and IMD generation in SAW devices. A mathematical technique will be developed to simulate the previous circuitual models in order to reduce the computational time.
- Implementation of innovative measurement systems schemes involving multi-tone signals are also disclosed. Based on a better understanding of the sources contributing to the nonlinear response, several measurement campaigns of different devices under diverse scenarios have been performed. Experimental verification of these measurements have indicated very encouraging results with regard the IMD3 and H3 response including both resonators and filters.
- Development of a characterization process for SAW devices. The idea is to use both, the developed models and the measurement systems for the characterization of the material physical properties. This characterization process allows to find the geometry-independent nonlinear parameters, which only depend on the physical properties of the materials, contributing to the generation of a given spurious signal. With this, it is expected a full understanding of all the sources contributing to the nonlinear paradigm.

- The final part of the thesis is focused on applying the developed nonlinear models to analyze the nonlinear response of more complex structures such as ladder-type and Coupled Resonators Filters (CRF) structures.

Consequently, achieving these objectives, it is expected to be able to contribute significantly in the aforementioned issues, in order to help in the design of a new generation of SAW electro-acoustic filters capable of addressing some of the forthcoming technological challenges of the coming years.

## 1.4 Thesis outline

After this introducing chapter, Chapter 2 is dedicated to introduce the fundamental theory of piezoelectricity and acoustic propagation followed by the piezoelectric constitutive equations. Finally, the potential nonlinear distortion effects and the spurious signals generation mechanism are introduced.

Chapter 3 includes the modeling of SAW resonators. A review of the most popular modeling techniques is introduced. Some comparisons between the existing different nonlinear models are presented, and the main advantages and drawbacks of each one are remarked. Furthermore, it presents the developed crossed-field-based linear distributed circuitual model, which depends only on the physical parameters of the SAW resonator. The model is first validated with comparison of measured versus simulated linear response of several resonators with different geometries. Finally, the nonlinear extension of the distributed circuitual model is derived to properly account for the nonlinear effects. The nonlinear circuitual modeling of a  $\lambda$ -section and a whole transducer is outlined.

Chapter 4 introduces the mathematical technique used to evaluate the nonlinear origin in SAW resonators, called Input-Output Equivalent Sources (IOES) method. This is a numerical tool providing an innovative solution to analyze the previous circuitual models at the same time as reducing the computational time. To analyze the entire transducer structure, we present an admittance matrix description of each of the different regions composing the whole resonator. After that, the procedure of the mathematical method is presented, starting with the linear evaluation at the fundamental frequencies and followed with the distributed nonlinear sources calculations. The basic linear and nonlinear simulation flow-chart of the mathematical tool is presented as well as how the acoustical and electrical connections are done for the different regions. The IOES method is validated with comparison with commercial software simulations. Moreover, allows to evaluate the simulated nonlinear response of provided SAW resonators in comparison with measured results.

Chapter 5 is focused on the nonlinear characterization of SAW resonators. At first, the different measurement systems used to perform the nonlinear evaluation of given resonators are presented as well as its corresponding measurements. Following this, the nonlinear response analysis is performed, from the broadband linear analysis towards the nonlinear fitting of the IMD3, H3 and second-harmonic (H2)

nonlinear response. The main goal at this point is to find geometry-independent material parameters that could predict the nonlinear behavior and, therefore, a unique identification of the parameters will be performed evaluating different geometry, shape and stack configuration resonators.

Chapter 6 is devoted to analyze the linear and nonlinear response of more complex structures such as ladder filters and coupled resonators filters using the IOES method. After that, the chapter presents the nonlinear lumped model as an alternative method to evaluate nonlinearities. This new method is validated with nonlinear simulations considering a ladder-type filter.

Chapter 7 outlines other complementary characterization set-ups used during the thesis to complement the characterization process of SAW and BAW resonators.

Finally, Chapter 8 summarizes the conclusions as well as the future research lines of the thesis.



## Chapter 2

# Fundamental theory of the electrical characterization of acoustic devices

### 2.1 Introduction

The aim of this chapter is to introduce some concepts of piezoelectricity and its application to the propagation of an acoustic wave. The derivation of the related equations comes from the works in [13], [14]. The physics related to the behavior of the acoustic waves on solid materials used in electromechanical transducers will be introduced following [15–18], with the purpose to provide the reader the needed framework to understand the physical effects that are matter in this thesis.

The equations involving the propagation of an acoustic wave through a crystal slab are outlined to introduce later the linear piezoelectric constitutive equations relating the electromagnetic and acoustic field magnitudes present in the piezoelectric material. The linear constitutive equations are further extended to its nonlinear domain and, finally, the basics of nonlinear distortion and generation mechanism are described.

### 2.2 Mechanics in solids

Newton's mechanics, assumes that a solid body becomes deformed when subjected to external forces. The effect of these forces provokes, at the same time, the creation of internal forces called stresses, and also deformations called strains. The concepts of strain and stress will be introduced in next subsections. Moreover, a brief introduction of mechanics is given in order to help the reader to understand some

physical mechanics concepts that will be further used in the next sections.

### 2.2.1 Strain

Because of the elasticity of a body, when it is subjected to external forces it experiments deformations. Those deformations can be represented by a dimensionless strain tensor  $S$  if its particles are displaced relative to each other. We can consider the strain expressed as the motion of a particle which represents an elementary region of the material. Suppose that, in the equilibrium state, a particle of the material is located at the point  $x = (x_1, x_2, x_3)$ . When the material is not in equilibrium state, this particle is displaced by an amount of  $\vec{u} = (u_1, u_2, u_3)$  where the components  $u_1, u_2$  and  $u_3$  are in general functions of the coordinates  $x_1, x_2, x_3$ . Therefore, a particle with equilibrium position  $x$  has been displaced to a new position  $x + \vec{u}$  as depicted in Fig. 2.1.

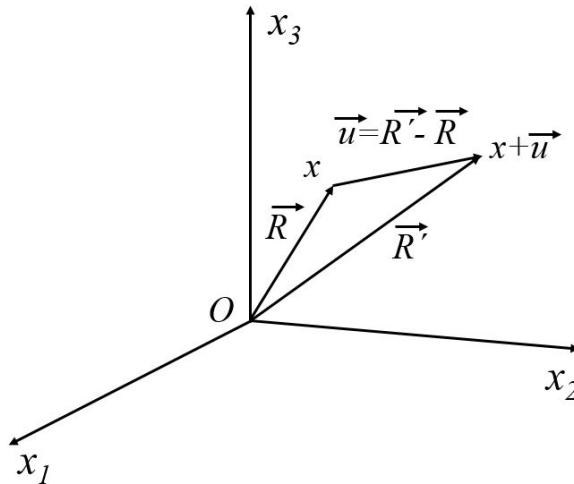


**Figure 2.1:** General definition of 3D strain.

Since deformations do not only occur in one direction, a tensor of rank two is needed. Therefore, following [17] the strain tensor can be defined by

$$S_{ij} = \frac{1}{2} \left( \frac{\partial u_i}{\partial x_j} + \frac{\partial u_j}{\partial x_i} \right) \quad i, j = 1, 2, 3, \quad (2.1)$$

where  $u_i$  and  $u_j$  is the particle displacement vector,  $x_i$  and  $x_j$  are coordinates, and the two indices  $i$  and  $j$  can range over the three coordinates 1, 2, 3 in a three dimensional space. With this definition, any displacement or rotation of the material (there is no deformation) cause no strain, and therefore, the strain is related to the internal forces. Moreover, the strain is a second-rank tensor and it is clearly symmetrical, so that follows  $S_{ij} = S_{ji}$ .

In addition, for the case  $i = j$  the strain ends up with the form

$$S_{ii} = \frac{\partial u_i}{\partial x_i} \quad i, j = 1, 2, 3, \quad (2.2)$$

equation 2.2 is called the normal strain, and represents a dilation or contraction of the body in the direction defined by the index  $i$ . However, the term  $S_{ij}$  evaluated for the case  $i \neq j$  is called shear strain and represents the deformation in a plane. Depending whether it involves deformations in one or both directions of the plane in an equal way, it is called a simple shear strain, or a pure shear strain, respectively.

## 2.2.2 Stress

The effect of external forces if a solid is subjected to a deformation, produces some other internal forces between the particles. These forces are called stresses and can be defined by the Cauchy stress tensor [19]. The Cauchy stress tensor accounts for the tensor transformation law under a change in the system of coordinates. Moreover, it can be represented graphically if we suppose a cube as the one represented in Fig. 2.2 with its edges along the Cartesian axes. When a force  $F_i$  is exerted normal to one of its faces, the stresses tensor  $T_{ij}$  expressed in  $[N/m^2]$  are the forces per unit of area that can be resolved into three components along the three axes following:

$$F_i = \left( \frac{\partial T_{i1}}{\partial x_1} + \frac{\partial T_{i2}}{\partial x_2} + \frac{\partial T_{i3}}{\partial x_3} \right) dx_1 dx_2 dx_3 = \sum_j \frac{\partial T_{ij}}{\partial x_j} dx_1 dx_2 dx_3 \quad i, j = 1, 2, 3 \quad (2.3)$$

the  $i$ th index specifies the direction in which the force component acts, while the  $j$ th index identifies the direction of the normal vector of the surface upon which is acting, as depicted in Fig. 2.2.

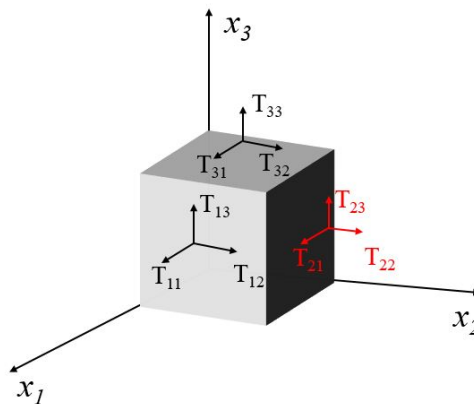


**Figure 2.2:** Representation of the Cauchy stress tensor on a cube.



In [18] it is demonstrated that  $T_{ij} = T_{ji}$  and therefore Voigt notation can be applied to define the stress. In the same way as stated for the strains, the stresses tensor includes the normal stresses for  $i = j$  which act perpendicular to the sectional areas of an isolated stress cube. They are related to active tensile or compressive forces. In each case, the two shear forces of each sectional area lie in a given plane and act perpendicular to the normal stress. There are also a total of six different shear stresses if  $i \neq j$ . The first index position in the shear stress vector indicates to which stress normal the shear stress belongs, while the second index position indicates the direction of the shear stress vector.

### 2.2.3 Hooke's law

Hooke's law states that for small stresses applied to a one-dimensional system, the stress is proportional to the strain by means of the stiffness constant  $c$ . If we assume there is a linear relation between the internal stresses (force applied to an object) and the deformations (strains), we can write

$$T = cS \quad (2.4)$$

where  $c$  is called the stiffness constant of the material and has units of stress (since strain is dimensionless). The parameters  $T$  and  $c$  would be tensors in the general system, but can be represented by one component for one-dimensional longitudinal or shear wave propagation.

If we consider to express this relation in tensor form, using the Voigt notation [18] of stress and strain, we can obtain a stress tensor of rank two relating both magnitudes as follows

$$T_i = c_{ij}S_j \quad i, j = 1, 2, \dots, 6 \quad (2.5)$$

where the equation 2.5 is known as the Hooke's law for continuous media. Moreover, since  $c_{ij}$  is the stiffness tensor and, assuming the mechanical internal energy  $U$  is twice continuously differentiable [17], the symmetry of the stiffness tensor can be demonstrated by

$$c_{ij} = \frac{\partial^2 U}{\partial S_i \partial S_j} = \frac{\partial^2 U}{\partial S_j \partial S_i} = c_{ji} \quad (2.6)$$

this further reduces the number of material constants to 21, being the most general anisotropic linear elastic material defined by 21 material constants.

## 2.3 One-dimensional mechanical equation of motion

For simplicity, we shall assume that the waves of interest in acoustic wave propagation are divided into two basic types. The first one is a longitudinal wave, in which the motion of a particle in the acoustic medium is only in the direction of propagation. The second type is the shear wave, in which the motion of a particle in the medium is transverse to the direction of propagation. Moreover, all the physical quantities involved, this is the particle displacements, particle velocity, stress, strain, elasticity and the piezoelectric coupling constant (that will be later defined), can be expressed in terms of one direction of propagation.

As stated previously, the force per unit area applied to a solid is called the stress  $T$ . In the one-dimensional case, the force stretches or compresses the body. The stress is related to the deformation in the internal structure of the body. The nature of the deformation depends on the orientation of the area. The area is considered a vector with a direction normal to the surface as depicted in Fig. 2.3.

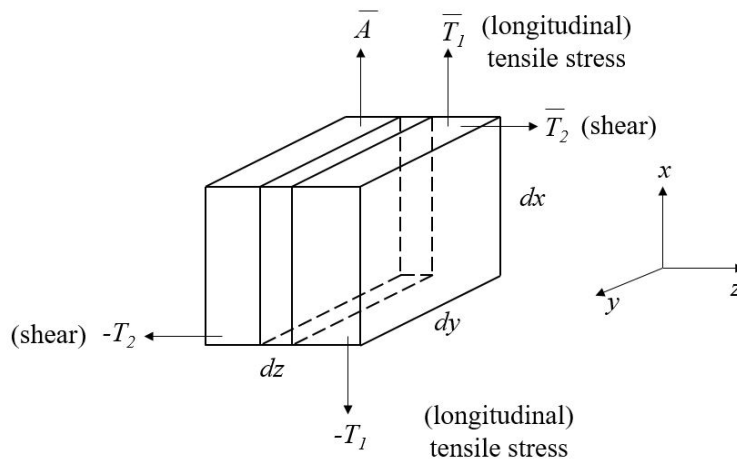


**Figure 2.3:** Traction forces relative to the area of an isotropic medium.

The orientation of the area  $A$  determines whether the stress is considered longitudinal ( $T_1$  and  $-T_1$ ), and the components are parallel to the area vector  $\vec{A}$ , or shear ( $T_2$  and  $-T_2$ ), when the components are transversal to  $\vec{A}$ . A further distinction between stress and force comes from the fact that stresses always occur in opposite (but not always equal) pairs, as it can be seen in Fig. 2.3. These stress components are individually referred to as traction forces, and, like stress, they are denoted by the letter  $T$ . When the force is in a direction opposite to the area the stress is called compressive stress and when the force is in the same direction is called tensile stress.

If we consider, in the one-dimensional case, that the plane  $z$  in the body is displaced in the  $z$ -direction by a longitudinal stress, it causes a mechanical displacement of the material called  $u$ . We can use a Taylor expansion to show that, to first order, the change in  $u$  in a length  $dz$  is  $du$ , where

$$du = \frac{\partial u}{\partial z} dz = S dz \quad (2.7)$$

and therefore the fractional extension of the material, the strain  $S$ , is defined as

$$S = \frac{\partial u}{\partial z} \quad (2.8)$$

Moreover, the relation between the force and the stress components can be expressed as

$$dF = \frac{\partial T}{\partial z} \Delta z A \quad (2.9)$$

being the cross-sectional area defined as  $A = dx dy$ . Consider now the equation of motion of a point in the material when a small, time-variable stress is applied to it. Based on the previous definition 2.9, Newton's second law can be rewritten as

$$dF = \frac{\partial T}{\partial z} \Delta z A = \rho A \Delta z \frac{\partial^2 u}{\partial t^2} \Rightarrow \frac{\partial T}{\partial z} = \rho \frac{\partial^2 u}{\partial t^2} \quad (2.10)$$

where the left-hand of equation 2.10 is the applied force equals to the product of the mass density  $\rho$  in [ $Kg/m^3$ ] by the differential volume by the acceleration. The right-hand of equation 2.10 represents the equation of motion.

Furthermore, the particle velocity of the material is given by the time derivative of the particle displacement:

$$v = \frac{\partial u}{\partial t} \quad (2.11)$$

Additionally, we may now use again equation 2.4 referring to Hooke's law together with equations 2.8-2.11 to define and obtain the one-dimensional mechanical wave equation. The first step is to apply the partial time derivative to equation 2.4 and 2.8 obtaining the following expressions

$$\frac{\partial T}{\partial t} = c \frac{\partial S}{\partial t} \quad (2.12)$$

$$\frac{\partial S}{\partial t} = \frac{\partial^2 u}{\partial z \partial t} \quad (2.13)$$

Moreover, equation 2.12 and 2.13 can be redefined in terms of the particle velocity (2.11) following

$$\frac{\partial T}{\partial t} = c \frac{\partial v}{\partial z} \Rightarrow \frac{\partial v}{\partial z} = \frac{1}{c} \frac{\partial T}{\partial t} \quad (2.14)$$

$$\frac{\partial S}{\partial t} = \frac{\partial v}{\partial z} \quad (2.15)$$

Next step is to differentiate equation 2.10 with respect  $z$  and equation 2.14 with respect time obtaining respectively

$$\frac{1}{\rho} \frac{\partial^2 T}{\partial z^2} = \frac{\partial^2 v}{\partial t \partial z} \quad (2.16)$$

$$\frac{\partial^2 v}{\partial z \partial t} = \frac{1}{c} \frac{\partial^2 T}{\partial t^2} \quad (2.17)$$

Finally, equating the cross derivatives of equation 2.16 and 2.17, the one-dimensional mechanical wave equation can be obtained

$$\frac{1}{\rho} \frac{\partial^2 T}{\partial z^2} = \frac{1}{c} \frac{\partial^2 T}{\partial t^2} \quad (2.18)$$

Also, if we consider the steady-state, equation 2.18 becomes

$$\frac{\partial^2 T(z)}{\partial z^2} = -\frac{\rho}{c} \omega^2 T(z) \quad (2.19)$$

where the phase velocity of the mechanical wave,  $v_a$  can be obtained as

$$v_a = \sqrt{\frac{c}{\rho}} \quad (2.20)$$

Furthermore, assuming sinusoidal steady-state for a continuous wave of frequency  $\omega$ , the solution of 2.19 is

$$T(z) = T_0^+ e^{-j\beta_a z} + T_0^- e^{j\beta_a z} \quad (2.21)$$

with  $T_0^+$  and  $T_0^-$  being the stress at the origin of coordinates of the wave propagating in the the  $z$ -direction and opposite to that respectively, and  $\beta_a$  being a parameter called the phase constant, corresponding to

$$\beta_a = \omega \sqrt{\frac{c}{\rho}} = \frac{\omega}{v_a} \quad (2.22)$$

## 2.4 Piezoelectricity

In order to analyze the propagation of the acoustic wave through a piezoelectric slab we briefly review the concept of piezoelectricity. As commented previously, EM waves undergo a transduction process to acoustic waves mandated by the piezoelectric effect. The piezoelectric effect refers to an electro-mechanical interaction that refers to the capability of a material of transforming an applied mechanic stress or pressure to an electric field.

When a solid material is placed in an externally applied electric field the solid body adapts to this perturbation and undergoes a deformation, or strain  $S$ . If it returns to its original form when the forces are removed, it is said to be elastic. The piezoelectric generation of elastic waves along the surface or in the bulk are the main core of electro-acoustics theory. Piezoelectric is the class of dielectric material that can be polarized apart from the electric field by application of a mechanical stress  $T$ . These mechanical forces or stress arise because the material tends to return to the state before deformation occurs, ensuring mechanical equilibrium. When an electric field is applied to such material, it changes its mechanical dimensions. Conversely, an electric field is generated in a piezoelectric material that is strained.

Piezoelectricity involves the coupling between mechanical and electrical properties of a crystal material. Taking that into account and assuming the one-dimensional case, the constitutive equation involving the calculation of the electrical displacement  $D$  due to an electric field  $E$  [17] can be written as

$$D = \varepsilon E + eS \quad (2.23)$$

Furthermore, if equation 2.23 is generalized to three dimensions and we express the displacement vector in Einstein's summation convention (double sum notation) we obtain [20]

$$D_i = \varepsilon_{ij} E_j + e_{ijk} S_{jk} \quad i, j, k = 1, 2, 3 \quad (2.24)$$

if the medium is isotropic  $\varepsilon_{ij} = \varepsilon_r \varepsilon_0$  being  $\varepsilon_r$  the relative dielectric constant.

Moreover, the piezoelectric constants  $e_{ijk}$  expressed in units  $[C/m^2]$  relate changes of displacement  $D_i$  to strain  $S_{jk}$  in the solid having the electric field constant, so that

$$e_{ijk} = \left( \frac{\partial D_i}{\partial S_{jk}} \right)_E \quad (2.25)$$

here the subscript  $E$  refers to held the electric field constant. Moreover, the previous piezoelectric constants can be expressed as a tensor of rank two with  $i$  rows and  $\alpha$  columns, being  $\alpha = (j, k) = 1, 2, \dots, 6$  and thus

$$e_{i\alpha} = \begin{vmatrix} e_{11} & e_{12} & e_{13} & e_{14} & e_{15} & e_{16} \\ e_{21} & e_{22} & e_{23} & e_{24} & e_{25} & e_{26} \\ e_{31} & e_{32} & e_{33} & e_{34} & e_{35} & e_{36} \end{vmatrix} \quad (2.26)$$

Considering the strain tensor symmetric and using Voigt notation, equation 2.24 can be written as

$$D_i = \varepsilon_{ij}E_j + e_{i\alpha}S_\alpha \quad i, j = 1, 2, 3 \quad \alpha = 1, 2, \dots, 6 \quad (2.27)$$

In a similar way, when the electric field is applied to the piezoelectric crystal, the field will drive ions to displace in opposite directions resulting in a deformation. Thus, we shall now determine the stress  $T$  in a piezoelectric medium due to an electric field  $E$ . This is known as the Lippmann effect or the inverse piezoelectric effect. Assuming the one-dimensional case, the application of Hooke's law leads to the result

$$T = cS - eE \quad (2.28)$$

where  $e$  is the piezoelectric constant and  $c$  is the stiffness constant. Likewise, the inverse piezoelectric coefficient, generalising equation 2.28 considering the three dimensions, to relate the stress  $T_{jk}$  to the electric field  $E_i$  is obtained from the constants  $e_{ijk}$ . This relations show that, if a strain produces an electric displacement for a constant electric field given by equation 2.25, then an applied electric field will produce a stress at constant strain given by

$$\left( \frac{\partial T_{jk}}{\partial E_i} \right)_S = -e_{ijk} \quad (2.29)$$

Considering this, and if the solid is also subject to a strain  $S_{lm}$  then

$$T_{jk} = c_{jklm}S_{lm} - e_{ijk}E_i \quad i, j, k = 1, 2, 3 \quad (2.30)$$

Which, if the stress tensor is considered symmetric and using Voigt notation, can be redefined as

$$T_\alpha = c_{\alpha\beta}S_\beta - e_{i\alpha}E_i \quad i = 1, 2, 3 \quad \alpha, \beta = 1, 2, \dots, 6 \quad (2.31)$$

being  $\alpha$  and  $\beta$ , with values 1 to 6, correspond to a 6 x 6 square array and  $\alpha$  is related to  $(jk)$  and  $\beta$  to  $(lm)$ .

Finally, looking at equations 2.27 and 2.31 the terms  $c_{\alpha\beta}$  and  $\varepsilon_{ij}$  can be redefined as partial derivatives in the form

$$c_{\alpha\beta}^E = \left( \frac{\partial T_\alpha}{\partial S_\beta} \right)_E \quad (2.32)$$

$$\varepsilon_{ij}^S = \left( \frac{\partial D_i}{\partial E_j} \right)_S \quad (2.33)$$

where the previous equations have the superscripts  $E$  and  $S$  respectively which indicates that the electric constitutive relation and the Hooke's law can only be applied when the field  $S$  and  $E$  are held constant.

## 2.5 Constitutive equations

Summarizing, the direct and inverse piezoelectric effect can be expressed by means of the well-known linear piezoelectric constitutive equations following

$$T_\alpha = c_{\alpha\beta}^E S_\beta - e_{i\alpha} E_i \quad i = 1, 2, 3 \quad \alpha, \beta = 1, 2, \dots, 6 \quad (2.34)$$

$$D_i = \varepsilon_{ij}^S E_j + e_{i\alpha} S_\alpha \quad i, j = 1, 2, 3 \quad \alpha = 1, 2, \dots, 6 \quad (2.35)$$

Furthermore, when the material is not piezoelectric since there is no effect of the electric field, the constitutive relations can be written as

$$T_\alpha = c_{\alpha\beta} S_\beta \quad \alpha, \beta = 1, 2, \dots, 6 \quad (2.36)$$

$$D_i = \varepsilon_{ij}^S E_j \quad i, j = 1, 2, 3 \quad (2.37)$$

The piezoelectric effect can be described by the the well-known linear piezoelectric constitutive equations 2.34 and 2.35, where  $T$  is the stress expressed in  $[N/m^2]$ ,  $S$  is the strain and is dimensionless,  $c^E$  is the stiffness constant in  $[N/m^2]$ ,  $e$  is the piezoelectric coefficient in  $[C/m^2]$ ,  $\varepsilon^S$  is the material permittivity in  $[F/m]$ ,  $E$  is the electric field in  $[V/m]$  and  $D$  is the displacement current vector in  $[A]$ . For simplicity, these equations are usually written as:

$$T = c^E S - eE \quad (2.38)$$

$$D = \varepsilon^S E + eS \quad (2.39)$$

Note that the superscripts in the variables denotes they are evaluated under specific conditions, namely constant electric field or constant stress. The first equation is a modification of the traditional Hooke's Law to account for the effect on

stress of an external electric field. The second equation describes how stress has an effect on the electrical displacement. Therefore, the above equations describe how the mechanical and electrical properties of the material couple together.

## 2.6 Nonlinear constitutive equations

In the last two decades, a lot of progress has been made to model and simulate the nonlinear behavior of the electroacoustic devices [21–23]. The most complete description of a nonlinear model of BAW resonators is found in [23]. The models used in the aforementioned publications are based on the nonlinear constitutive equations of the piezoelectricity, which are time-domain locally defined and then applied at any point of the circuit. This model has been extensively used for finding the derivative material constants of the piezoelectric material appearing in those equations.

Concretely, this nonlinear distributed model extended the previous one-dimensional mechanical equations up to its nonlinear domain by adding the terms  $\Delta T$  and  $\Delta D$  ([24]) to the constitutive equations of (2.38),(2.39) and obtaining

$$T = c^E S - eE + \Delta T \quad (2.40)$$

$$D = eS + \varepsilon^S E + \Delta D \quad (2.41)$$

where, following the nomenclature of [24], these nonlinear terms  $\Delta T$  and  $\Delta D$ , truncated to a third-order polynomial, are defined as

$$\begin{aligned} \Delta T &= c_2^E \frac{S^2}{2} + c_3^E \frac{S^3}{6} - \varphi_3 \frac{E^2}{2} + \varphi_5 SE - \chi_9 \frac{S^2 E}{2} + \chi_7 \frac{E^2 S}{2} - e_3^E \frac{E^3}{6} \\ \Delta D &= \varepsilon_2^S \frac{E^2}{2} + \varepsilon_3^S \frac{E^3}{6} - \varphi_5 \frac{S^2}{2} + \varphi_3 SE + \chi_9 \frac{S^3}{6} - \chi_7 \frac{S^2 E}{2} + e_3^E \frac{SE^2}{2} \end{aligned} \quad (2.42)$$

being those nonlinear terms defined by several second-order ( $c_2^E$ ,  $\varphi_3$ ,  $\varphi_5$ ,  $\varepsilon_2^S$ ) and third-order ( $c_3^E$ ,  $\varepsilon_3^S$ ,  $\chi_9$ ,  $\chi_7$ ,  $e_3^E$ ) coefficients.

Moreover, using this set of equations is possible to obtain the nonlinear sources that are applied to the equivalent circuit models. Further details about the nonlinear model and the nonlinear sources calculations will be given in Chapter 3 and Chapter 4 respectively.



## 2.7 Nonlinear distortion

Linearity requirements and nonlinear distortion impact on the current RF handset have been discussed in [25], [26], [27]. In summary, among the major effects of nonlinear distortion we can find:

- The new spectrum generation by means of spurious signals, for example harmonics or IM products produced at any RF frequencies other than the operation frequency, due to the nonlinearity of the devices. This can cause desensitization, which is defined as the degradation of receiver sensitivity due to the presence of the Tx signal [28]
- Saturation or detuning effects. The first one, saturation or gain compression occurs when the device output power has been overpassed and consequently the device starts to saturate. The second one represents the shift of the frequency response due for example, thermal effects or changes of bias point provoked by appearing DC components due to the nonlinearity [29].
- The signal quality degradation of complex modulated signals characterized by the Error Vector Magnitude (EVM), which is a measure of how far the constellation points of the real signal are off from their ideal location.

Overall, duplexers inside RF-handsets play a very important role in both the harmonics and intermodulation performances of the frond-end system. Here is where acoustic technology in the form of RF filters gets the focus, since, despite its superior performances, acoustic filters also exhibit inherent nonlinear behavior. Therefore, the thesis will focus on harmonic and intermodulation measurements and models of both SAW resonators and filters for mobile communications systems.

The objective of this section is to briefly present the main time-domain and frequency-domain equations describing the nonlinear manifestations generated in an example of Device Under Test (DUT). The purpose is to understand the nonlinear distortion phenomena introduced in [29], [30] but considering its most general terms and from a system perspective.

### 2.7.1 Time-domain nonlinear equations

At first, we will consider a linear system with a DUT whose input is a single-tone sinusoidal stimulus signal  $v_{in,L}(t)$  which takes the form of

$$v_{in,L}(t) = A \cos(\omega_1 t + \phi_1) \quad (2.43)$$

At its output, the DUT will generate another signal in which the nonlinear behavior response of the DUT is considered. Consequently, the nonlinear output

signal of the DUT (if a Taylor series is considered and truncated up to a third-order) will take the form

$$\begin{aligned}
 v_{out,NL}(t) &= a_1 v_{in,L}(t) + a_2 v_{in,L}^2(t) + a_3 v_{in,L}^3(t) = \\
 &= a_1 A \cos(\omega_1 t + \phi_1) + \frac{1}{2} a_2 A^2 + \frac{1}{2} a_2 A^2 \cos(2\omega_1 t + 2\phi_1) \\
 &\quad + \frac{3}{4} a_3 A^3 \cos(\omega_1 t + \phi_1) + \frac{1}{4} a_3 A^3 \cos(3\omega_1 t + 3\phi_1) \quad (2.44)
 \end{aligned}$$

The nonlinear response of the DUT includes some additional terms indicating that some spurious signals appearing at frequencies different than the one of the input signal are generated. This is usually named as spectral regrowth. These new spurious signals appear at frequencies multiple of the fundamental frequency  $m\omega_1$  or the so-called H's frequencies, degrading the whole performance of the system. In addition, note that the coefficient of the fundamental signal becomes  $(a_1 + \frac{3}{4}a_3A^3)$ , which manifests saturation effects ( $a_3 < 0$ ), which will be significant if  $a_1 < a_3A^2$ . In our case we will not be interested in such effects because the input power will not be high enough.

Now, if we consider that the DUT is fed by a different excitation signal which now consists of a temporal signal formed by the combination of two sinusoids,  $v_{1,L}(t)$  and  $v_{2,L}(t)$  :

$$v_{in,L}(t) = v_{1,L}(t) + v_{2,L}(t) = A_1 \cos(\omega_1 t + \phi_1) + A_2 \cos(\omega_2 t + \phi_2) \quad (2.45)$$

The nonlinear signal generated at the device output will be more complex. This nonlinear signal, up to a third-degree polynomial, is formed by the following frequency components

$$\begin{aligned}
v_{out,NL}(t) &= a_1 v_{in,L}(t) + a_2 v_{in,L}^2(t) + a_3 v_{in,L}^3(t) = \\
&= \frac{1}{2} a_2 A_1^2 + \frac{1}{2} a_2 A_2^2 + \\
&\quad + a_1 A_1 \cos(\omega_1 t + \phi_1) + \frac{3}{4} a_3 A_1^3 \cos(\omega_1 t + \phi_1) + \frac{3}{2} a_3 A_1 A_2^2 \cos(\omega_1 t + \phi_1) + \\
&\quad + a_1 A_2 \cos(\omega_2 t + \phi_2) + \frac{3}{4} a_3 A_2^3 \cos(\omega_2 t + \phi_2) + \frac{3}{2} a_3 A_1^2 A_2 \cos(\omega_2 t + \phi_2) + \\
&\quad + \frac{1}{2} a_2 A_1^2 \cos(2\omega_1 t + 2\phi_1) + \frac{1}{2} a_2 A_2^2 \cos(2\omega_2 t + 2\phi_2) + \\
&\quad + \frac{1}{4} a_3 A_1^3 \cos(3\omega_1 t + 3\phi_1) + \frac{1}{4} a_3 A_2^3 \cos(3\omega_2 t + 3\phi_2) + \\
&\quad + a_2 A_1 A_2 \cos((\omega_1 + \omega_2)t + \phi_1 + \phi_2) + a_2 A_1 A_2 \cos((\omega_2 - \omega_1)t - \phi_1 + \phi_2) + \\
&\quad + \frac{3}{4} a_3 A_1^2 A_2 \cos((2\omega_1 - \omega_2)t + 2\phi_1 - \phi_2) + \\
&\quad + \frac{3}{4} a_3 A_1 A_2^2 \cos((2\omega_2 - \omega_1)t - \phi_1 + 2\phi_2) + \\
&\quad + \frac{3}{4} a_3 A_1 A_2^2 \cos((2\omega_2 + \omega_1)t + \phi_1 + 2\phi_2) + \\
&\quad + \frac{3}{4} a_3 A_1^2 A_2 \cos((2\omega_1 + \omega_2)t + 2\phi_1 + \phi_2). \tag{2.46}
\end{aligned}$$

A closer examination of the previous equations gives us information about the new generated frequencies. All the new output frequency components occur at a linear combination of the excitation frequencies  $\omega_1$  and  $\omega_2$  or

$$\omega_{m,n} = |m\omega_1 \pm n\omega_2| \tag{2.47}$$

being  $\omega_{m,n}$  called the mixing frequency and  $m, n = 0, \pm 1, \pm 2, \pm 3, \dots$

The sum of the absolute values on  $m$  and  $n$  is called the order of the mixing product, which is defined as  $|m| + |n|$ , whereas the order of a given H is defined as  $|m|$  for  $\omega_1$  and  $|n|$  for  $\omega_2$ . The former nonlinear components generated by the DUT might cause degradation in the communication system if falling in a receiver band. Those new frequency components are distributed in the frequency spectrum as is depicted in Fig. 2.4. Note that the linear components of the fundamental frequencies  $\omega_1$  and  $\omega_2$  are shown in solid lines whereas the 2nd and 3rd order nonlinear components are represented in dotted and dashed lines respectively.

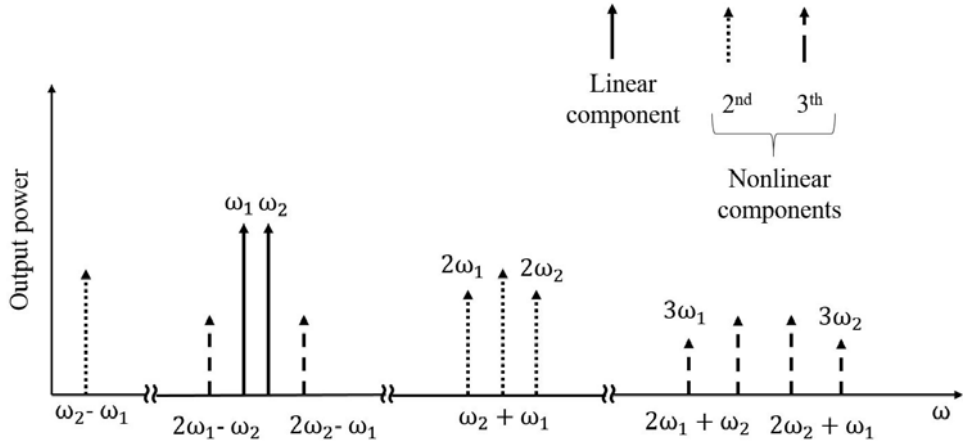


**Figure 2.4:** Frequency spectrum of second and third order nonlinear components at the output of a given nonlinear DUT.

## 2.7.2 Passive intermodulation and harmonic generation

Commonly, nonlinear distortion is associated to active devices. But nothing further from the truth, nonlinearity might be present in all metal or semiconductor junctions and therefore these nonlinearities appear even in RF connectors, antennas, isolators, filters etc. This effect is known as PIM and, in some cases, their effects are quite relevant due to, for example, the high-demanded performance of nowadays receivers. PIM can produce receiver blocking caused by the components placed close to the antenna if this is shared by the Tx and the Rx. Furthermore, PIM might arise from different causes such as bad or undesired contacts, temperature variations, or by intrinsic nonlinear characteristics of a given physical phenomenon.

From the previous equation 2.46 is possible to consider only the harmonics and intermodulations and thus look at the nonlinear frequency components which are associated to the PIM generation. Moreover, the related equations can also be represented in the frequency domain. Frequency-domain equations in the steady-state are mathematical expressions that provide closed-form expressions of a given H or IMD for weak nonlinearities. These closed-form expressions are based in the Volterra series analysis, which is an analytical procedure capable of describing the response of a certain class of nonlinear systems [29]. For weak nonlinearities we understand that the generated H and IMD in a nonlinear circuit are significant, but there is not significant saturation or detuning at the fundamental signals.

Considering the previous equation (2.46) in the frequency domain, we can obtain closed-form expressions for the harmonic distortion of the second order and third order spurious signals

$$V_{out,NL}(2\omega_1) = \frac{1}{2}a_2 |A_1|^2 e^{j2\phi_1} = \frac{1}{2}a_2 A_1^2, \quad (2.48)$$

$$V_{out,NL}(2\omega_2) = \frac{1}{2}a_2 |A_2|^2 e^{j2\phi_2} = \frac{1}{2}a_2 A_2^2, \quad (2.49)$$

$$V_{out,NL}(3\omega_1) = \frac{1}{4}a_3 |A_1|^3 e^{j3\phi_1} = \frac{1}{4}a_3 A_1^3, \quad (2.50)$$

$$V_{out,NL}(3\omega_2) = \frac{1}{4}a_3 |A_2|^3 e^{j3\phi_2} = \frac{1}{4}a_3 A_2^3. \quad (2.51)$$

Similarly, the corresponding equations defined in the frequency domain for the IMD products of second and third order respectively will take the form

$$V_{out,NL}(\omega_2 - \omega_1) = a_2 |A_1| |A_2| e^{j(\phi_2 - \phi_1)} = a_2 A_1^* A_2, \quad (2.52)$$

$$V_{out,NL}(\omega_2 + \omega_1) = a_2 |A_1| |A_2| e^{j(\phi_1 + \phi_2)} = a_2 A_1 A_2, \quad (2.53)$$

$$V_{out,NL}(2\omega_1 - \omega_2) = \frac{3}{4}a_3 |A_1|^2 |A_2| e^{j(2\phi_1 - \phi_2)} = \frac{3}{4}a_3 A_1^2 A_2^* \quad (2.54)$$

$$V_{out,NL}(2\omega_2 - \omega_1) = \frac{3}{4}a_3 |A_1| |A_2|^2 e^{j(2\phi_2 - \phi_1)} = \frac{3}{4}a_3 A_1^* A_2^2. \quad (2.55)$$

Moreover, the generation of the H's or the IM products might be caused by direct generation involving the fundamental frequencies as in equation 2.46, or by the so-called remix effects meaning that, for example, a generated IMD2 can be remixed with a fundamental signal to create an IMD3. Fig. 2.5 depicts the possible combinations for the generation of H3 and IMD3 due to remix-effects.

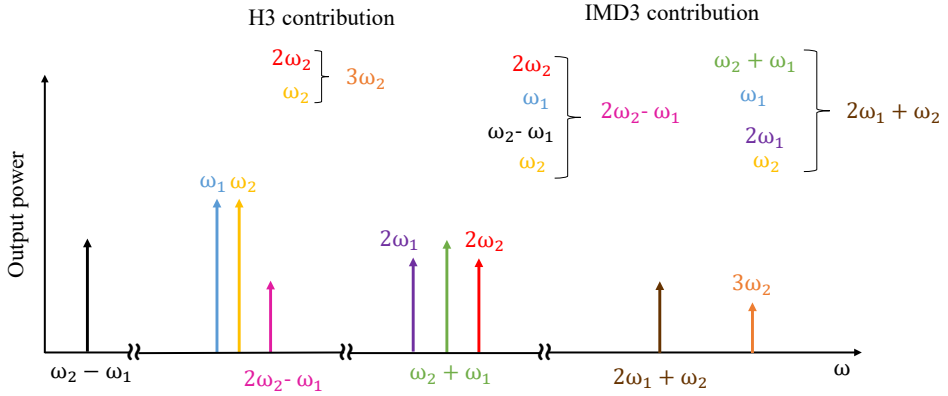


**Figure 2.5:** Example of representation of remixing frequencies.

This chapter has introduced the physics related to the behavior of the acoustic waves of solids materials used in electromechanical transducers. Moreover, the analysis and the solution to the wave equation of the mechanical wave in one dimension has been carried out. After that, the piezoelectric effect is taken into account as a coupling between mechanical and electrical properties of a crystal material. The basic equations involving the acoustic wave propagation and electroacoustic conversion in a piezoelectric medium has been presented in the form of the linear and nonlinear constitutive equations. Finally, the major sources of nonlinear distortion as well as the main time-domain and frequency-domain equations describing the nonlinear manifestations generated in a simple example has been presented.



## Chapter 3

# Modeling of Surface Acoustic Wave resonators

### 3.1 Introduction

The need of designing high-performance SAW devices requires the development of efficient and accurate simulation tools. In this chapter, an overview of some of the most common modeling methods is presented. Current Section 3.1 presents the most important parameters for a SAW device design and outlines a brief survey of the different models and nonlinear approaches. Section 3.2 presents the Mason-based linear models and the linear distributed model developed during the thesis and its particularities. By **distributed** we mean a model in which the acoustic propagation is described by an acoustic transmission line with circuit parameters forming a T-network. Note that as will be explained later, to find the solution of the linear distributed model it is not necessary to discretize the circuit into many unitary cells.

In this section, the method for calculating the main SAW parameters, is given. Specifically, the main parameters used in order to create the linear model are presented as well as the linear measurements. Moreover, the solution of the one-dimensional mechanical wave in both a non-piezoelectric and piezoelectric slab is outlined. Note that in a one-dimensional model, it is assumed that the wave propagation phenomena is evaluated along one dimension. After that, the linear and nonlinear distributed circuital model for the SAW transducer is analyzed.

Finally, Section 3.3 describes the nonlinear **discretized** model established during this PhD thesis. As a discretized model, it is considered that the entire SAW transducer can be differentiated into two regions: metallized and not metallized. At the same time, the discretized model consists of discretizing into unit-cells each section of the different regions by cascading many unit-cells of a given circuit, each one modeling a thin slab  $\Delta z$  of the Transmission Line (TL).



### 3.1.1 SAW parameters

In this subsection, the most relevant SAW parameters used for the modeling will be outlined. The most important parameter for SAW device design is its center frequency, which is determined by the period of the IDT fingers and the acoustic velocity. If it is considered a surface acoustic wave in a periodic grating and we assume the perturbation to be weak, the resonance frequency of a SAW device is determined by the equation

$$f_0 = \frac{v_{phase}}{\lambda} \quad (3.1)$$

where  $f_0$  is the resonance frequency,  $v_{phase}$  is the phase velocity and  $\lambda$  is the acoustic wavelength, which in turn is defined by the electrode pitch (as shown in Fig. 3.1 in the IDT by the governing equation

$$\lambda = 2 \cdot p \quad (3.2)$$

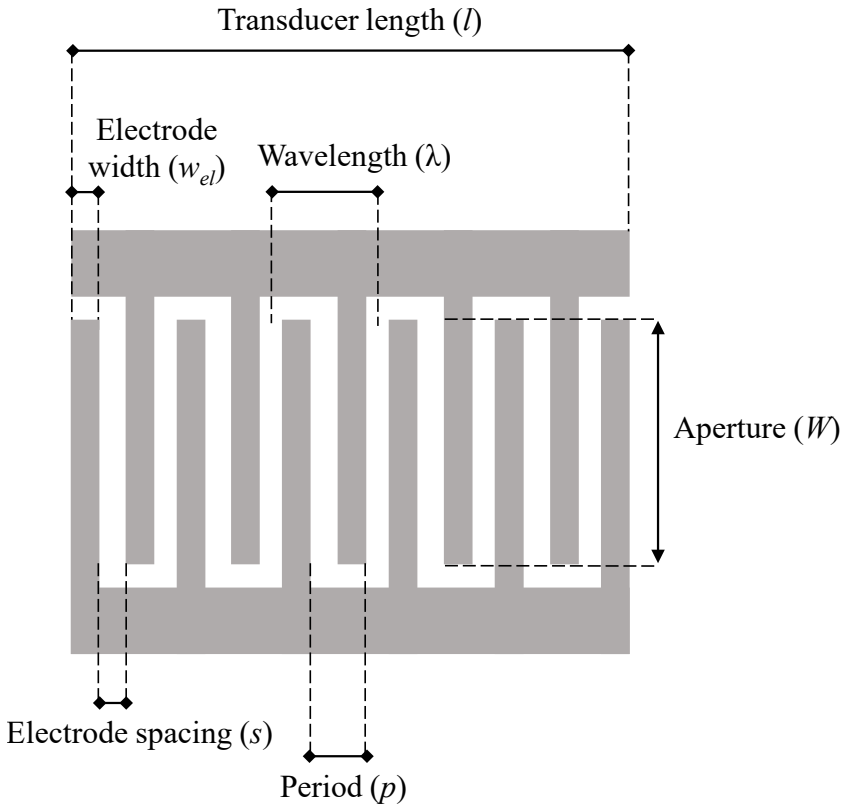


**Figure 3.1:** Example representation of linear IDT parameters.

Since the acoustic wavelength is defined as two-times the electrode pitch or period  $p$ , from now on we will use the term  $\lambda$ -section referring to a circuit that represents a wavelength of the transducer.

The previous equation 3.1 is true if weak periodic perturbation is considered and thus, strong coupling occurs if the wave-number  $\beta$  is close to a multiple of half the structure wave-number  $\pi/p$  so that,

$$\beta \approx n \frac{\pi}{p}, \quad n \in Z \quad (3.3)$$

such that

$$\beta_{-n} = \beta - n \frac{2\pi}{p} \approx -\beta \quad (3.4)$$

the Bragg condition is fulfilled [38]. This Bragg condition can be defined as the reflections of the wave components which at the same time will lead to the resonance and the formation of the stop-band phenomena [38].

As explained in [38] the study of the eigenmodes of the periodic system will lead to a dispersion relation whose solution defines the stop-band. One of the solution of this dispersion relation can be defined as the stop-band upper edge frequency (SBUE) and is related to the Bragg reflections commented above.

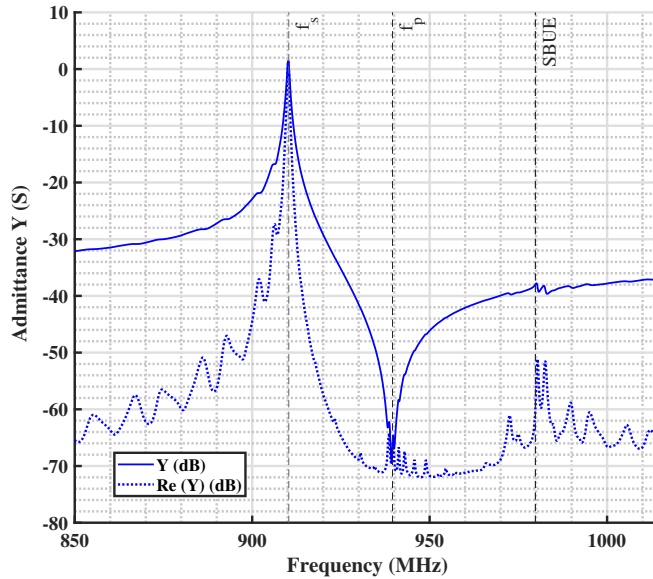


**Figure 3.2:** Example representation of linear response of a resonator. Dashed vertical lines define the resonance frequency, the antiresonance frequency and the SBUE respectively.

Figure 3.2 shows an example of the linear response of a resonator. Solid blue traces represent the admittance and dashed traces the conductance respectively. As you can see, the SBUE is marked in the response with a horizontal dashed line.

Moreover, another important parameter is the so-called duty factor or metallization ratio  $\eta$  which is defined as the ratio between the electrode width  $w_{el}$  over the period  $p$ . In other words, is a parameter that indicates the metal proportion of the electrodes over a period

$$\eta = \frac{w_{el}}{p} \quad (3.5)$$

As Fig. 3.1 depicts, the width of the transducer in the transversal direction of the propagation, namely the aperture, is defined as  $W$ . The aperture is defined in terms of  $\lambda$ . The aperture length is used to avoid the SAW diffraction problem which can be decreased by employing wider acoustic apertures with typical values ranging from  $10\lambda$  to  $100\lambda$  [31]. In addition, the transducer length  $l$  is also defined in terms of the wavelength  $\lambda$ , and defines the total number of electrodes.

### 3.1.2 Review of SAW device modeling and applications

As stated in [32] the most frequently used models for SAW resonators are nowadays the Coupling-of-Modes (COM) model, the P-matrix model (PMM) and the equivalent circuit models (ECM). The basic assumption of all these models is that the acoustic forces and displacements, as well as the dynamic electric potential in an anisotropic substrate, can be summarized in one single scalar quantity - the wave amplitude normalized to the power flow.

In addition, there are other methods of analysis for example, numerical simulators based on finite element method (FEM). A brief survey of these different models and method will be given.

#### Coupling of Modes

The Coupling of Modes theory is an elegant method for modeling systems with spatially varying periodic properties. After the introduction of the COM formalism by Pierce [33] in 1954, COM was successfully applied in optics and microwaves. In 1976 and 1977 Suzuki et al. ([34] and [35][36]) introduced the COM theory in the SAW field. In 1989 Wright [37] formulated the COM equations for the general case with spatially varying transduction, reflection and SAW velocity. Also propagation loss and the electrode resistivity was taken into account.

One of the main features of the COM theory lies in its intuitive approach, without the need for formal derivation. COM model is the most used since excitation, propagation and scattering of SAW can be considered in a very compact model, and it allows to model all kinds of low-loss filters very accurately [38]. The accuracy of the results basically depends on the precision of the parameters used in the modeling.

The COM formalism can be applied to a unit section like the one shown in Fig. 3.3 formed by a set of electrodes deposited on the surface of a piezoelectric crystal. Let us consider an external voltage  $V$  connected to the bus bars and therefore, exciting waves. The former excited waves propagate under the electrodes, generating a current flow  $I$ . As depicted in Fig. 3.3, the COM approximation considers two wave quantities or "modes" propagating forward  $\varphi_+(x)$  and backward  $\varphi_-(x)$  along the  $x$ -axis.

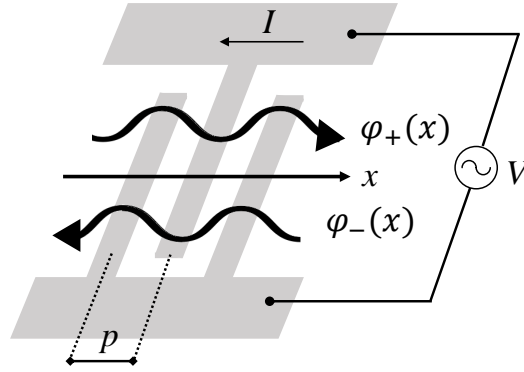


**Figure 3.3:** Schematic of a unit section and a half of a SAW resonator applying COM method.

Moreover, if it is assumed a constant mechanical periodicity in the structure, pitch  $p$ , and introducing the slowly varying fields  $R(x)$  and  $S(x)$  [38], these two waves can be defined as

$$\begin{cases} \varphi_+(x) = R(x)e^{-i\pi x/p} \\ \varphi_-(x) = S(x)e^{+i\pi x/p} \end{cases} \quad (3.6)$$

where  $R(x)$  and  $S(x)$  are the wave amplitudes. Introducing the detuning parameter  $\delta$  [38] as

$$\delta = \frac{\omega}{v} - \frac{\pi}{p} - i\gamma = \frac{2\pi(f - f_0)}{v} - i\gamma, \quad (3.7)$$

the final COM equations [38] can be expressed as

$$\begin{cases} \frac{dR(x)}{dx} = -i\delta R(x) + i\kappa S(x) + i\alpha V \\ \frac{dS(x)}{dx} = -i\kappa^* R(x) + i\delta S(x) - i\alpha^* V \\ \frac{dI(x)}{dx} = -2i\alpha^* R(x) - 2i\alpha S(x) + i\omega CV \end{cases} \quad (3.8)$$

where  $v$  represents the velocity,  $\gamma$  the attenuation,  $\kappa$  the reflectivity or coupling parameter,  $\alpha$  the transduction coefficient and  $C$  is the static capacitance. The previous COM parameters represent the independent parameters to be determined. More detailed explanations and the formulation for each of the previous COM parameters can be found in [38].

In the general case, the COM differential equations have no closed-form solution, so that they have to be solved numerically. The most common approach, however, is an extraction of COM parameters from measured data [39],[40]. Since the COM model allows the calculation of the admittance, it is possible to determine those quantities based on fitting the computed admittance of the COM with performed measurements and then, extracting the COM parameters from the admittance.

### **P-matrix model**

The P-matrix model has been invented by Tobolka in 1979 [41] and is now widely used [42, 43]. It is not a model by itself, but a mathematical representation of any model with two acoustic ports and one electrical port. A detailed introduction of the P-matrix theory can be found in Chapter 2 of [44]. It is a mixed matrix representation of an IDT with three ports (Fig. 3.4). The two acoustic ports are described by an scattering matrix, and the electric port is described by an admittance. On the other hand, consider the bulk wave second order effects in SAW devices are also important. For modeling the bulk wave conversion generally more than two acoustic ports have to be used in the P-matrix. However, a simple method is to implement the bulk wave conversion as losses at the finger edges since at surface discontinuities (electrode finger edges) surface waves are reflected and bulk waves are excited [45]. Moreover, the direct excitation of bulk waves and their effect on the surface wave frequency response can be included in a post-processing step [46].

The P-matrix model can be combined in a modular way with programs making it a very powerful tool for calculating very different types of SAW devices. Consequently, the whole SAW IDT section can be simulated by cascading multiple elementary cells by their acoustic ports. Each elementary cell is represented by a three-port network with two acoustic ports and one electrical port.

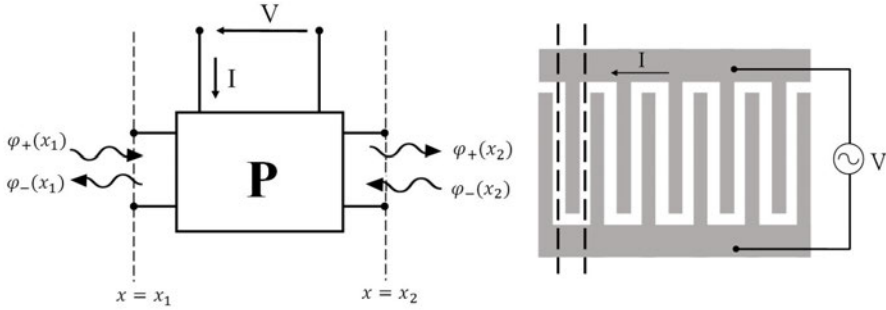


**Figure 3.4:** Symbolic description of an elementary cell of the P-matrix model.

In Fig. 3.4,  $V$  and  $I$  are the electrical voltage and current excited on the electrode;  $\varphi_+(x_1)$  and  $\varphi_-(x_1)$  correspond to the incident and reflected waves at the left side of the elementary cell and  $\varphi_+(x_2)$  and  $\varphi_-(x_2)$  are their equivalent on the right side of the cell. Besides, the elementary cell establishes the cell boundaries for the calculation of the P-matrix, which relates amplitudes of outgoing waves and current intensity  $I$  in terms of incoming wave amplitudes and voltage  $V$ .

Furthermore, the P-matrix representation is commonly used with the COM model. Since the previous COM equations (3.8) are linear, the response is linearly related to the boundary conditions. Consequently, the elementary cell may be described by a 3-by-3 so-called *P – matrix* [41] following

$$\begin{bmatrix} \varphi_-(x_1) \\ \varphi_+(x_2) \\ I \end{bmatrix} = \begin{bmatrix} P_{11}(f) & P_{12}(f) & P_{13}(f) \\ P_{21}(f) & P_{22}(f) & P_{23}(f) \\ P_{31}(f) & P_{32}(f) & P_{33}(f) \end{bmatrix} \begin{bmatrix} \varphi_+(x_1) \\ \varphi_-(x_2) \\ V \end{bmatrix} \quad (3.9)$$

where the upper left 2-by-2 submatrix describes the scattering of waves entering into the structure. Moreover,  $P_{11}$  and  $P_{22}$  are the acoustic or reflection coefficients;  $P_{12} = P_{21}$  corresponds to the acoustic transmission coefficient;  $P_{13}$  and  $P_{23}$  are called excitation efficiency, which are related to the piezoelectricity; the components  $P_{31}$  and  $P_{32}$  measure the current generated in the IDT by the arriving waves. Finally,  $P_{33}$  represent the admittance, describing the acoustic and electrostatic currents due to the drive of the voltage  $V$ .

Later, in 2001 [47] published a comprehensive method to describe the pseudo-SAW response of an individual electrode. The whole SAW IDT section can be simulated by cascading multiple individual elementary cells by their two acoustic ports 1 and 2. Then the SAW resonator's electrical admittance is obtained by cascading the scattering parameter of the gratings on each end of the P-matrix of the transducer [28].

### **FEM models**

Purely numerical simulators have been also developed by many authors [48–50] where typically the wave motion of both electrodes and piezoelectric substrate is described. Field theory is the most appropriate theory for the design of SAW devices as it involves the resolution of all the partial differential equations for a given excitation. Finite Element Method (FEM) or Green’s function techniques using the boundary-element method (BEM) are some examples of numerical representations of field theory that provide two dimensional (2D) and three dimensional (3D) simulations of SAW devices. Moreover, with the use of simulation tools such as COMSOL<sup>®</sup> or ANSYS<sup>®</sup> is possible to take into account most of the physical effects of SAW devices such as transverse effects like radiation in bus bars.

One of the key advantages of using FEM models is that they are potentially more accurate than phenomenological models but at the same time, they require high computation times. Moreover FEM requires a minimum mesh to ensure proper convergence and it depends on the frequency of operation. The substrate depth needs to consider certain number of wavelengths hence a 3D FEM representation of an entire SAW structure would require of thousands of elements and nodes.

Fortunately, because SAW devices consists of periodic sections in most of the cases, it suffices to consider a period of the total array consisting of a pair of electrodes with a defined Periodic Boundary Conditions (PBC) and a Perfectly Matched Layer (PML) leading to a drastic decrease of the required computational time.

### **Equivalent circuit models (ECM)**

As seen previously, it has been briefly outlined different methods to analyze high-performance SAW devices. In all the models the parameters are extracted phenomenologically. Consequently, accurate determination of these parameters is a common problem. In all the exposed cases, the parameters depend on the geometry and the physical properties of the electrodes and the substrate.

In the design procedure of SAW devices, the use of ECM provides a general view of the device response over a short calculation time using conventional circuit simulators. They are a good approach for getting the frequency response, impedance parameters or even to determine the major dimensions and parameters in number of fingers, finger width or aperture. However, they are subject to some simplifications and restrictions.

One of the main equivalent circuit model used for simulations is the well-known Butterworth-Van Dyke (BVD) model [51]. Specifically, the BVD model is an equivalent electrical circuit made up of lumped components which reproduces the main resonances of acoustic wave resonators and models the narrow-band response. This model is the most used by the acoustic filter designer because of its simplicity.

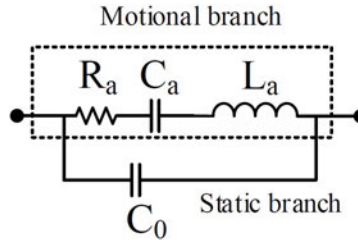


**Figure 3.5:** Schematic of the 2-Port BVD equivalent circuit model.

The BVD model of Fig. 3.5 is formed by two different branches. The upper branch, named motional or acoustic branch, is formed by the series resistor  $R_a$  representing the mechanical losses [52]; the motional inductance  $L_a$ , and the motional capacitance  $C_a$ . The lower branch, called static or electric branch, is composed by a so-called static capacitance  $C_0$ . The BVD model can accurately represent the resonator input impedance following

$$Z(\omega) = \frac{\omega^2 C_a L_a - 1 - j\omega(C_a L_a)}{\omega^2 R_a C_a C_0 + j\omega\{\omega^2 C_0 C_a L_a - (C_a + C_0)\}} \quad (3.10)$$

The value of the lumped elements in the BVD model is dependent on the geometry parameters of the transducers as well as the substrate parameters and dimensions. Overall, the BVD lumped element equivalent circuit model gives an accurate representation of the resonator frequency behavior and has the flexibility of and easy implementation in commercial circuit analysis simulators. However, the model itself is not capable of analyzing the surface acoustic wave generation and propagation.

The other popular model is a more physical model called Mason equivalent circuit model [15], [16]. In this equivalent circuit, the SAW propagation is modeled as a wave propagating in a transmission line, being the free surface and the metallized area described as well by different characteristic impedances of the transmission line. As will be further explained in this chapter, the Mason circuit is formed by three ports as depicted in Fig. 3.6. Ports 1 and 2 are acoustic ports where  $F_1$  and  $F_2$  represent the mechanical forces and  $v_1$  and  $v_2$  the mechanical velocities at the left and right edges respectively. Port 3 is the electrical port with an excitation voltage  $U_3$  and current  $I_3$ .



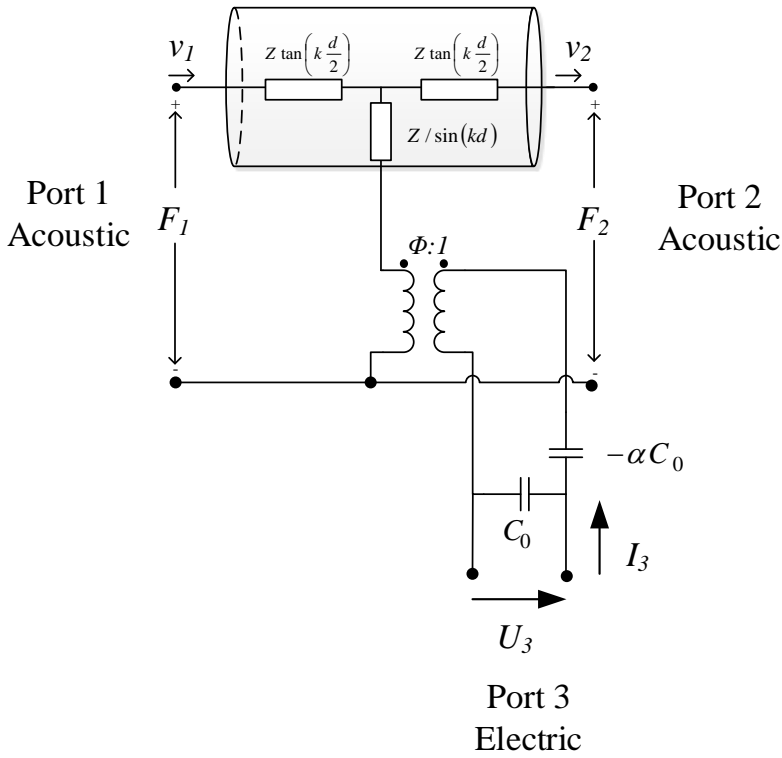


**Figure 3.6:** Mason equivalent circuit model. Top ports are mechanical ports whereas bottom node is electrical port.

Many authors successfully used ECM in the past [53–56]. The main advantage of the ECM is that it can be easily implemented in circuit simulation tools. A further advantage is that it permits an efficient modeling of the electric and mechanical interaction of piezoelectric transducer elements based on the piezoelectric constitutive equations.

With regard to this PhD thesis, the equivalent circuit models used are based on the Mason circuit [15] of Fig. 3.6. Specifically, depending on whether the dominant electric field is considered to be parallel to the propagation or normal to the acoustic propagation vector, the Mason model is called In-line or crossed-field model respectively. The diagram of Fig. 3.6 corresponds to the In-line model when  $\alpha = 1$  and to crossed-field model for  $\alpha = \infty$ .

In relation to the In-line model, when analyzing the current  $I$  through a piezoelectric medium is given by the contribution of two different terms, the first one is due to the displacement current through a capacitance  $C_0$ , and the second term is due to the conversion between mechanical and electrical energy (i.e. due to the

piezoelectric effect). As a result, the turn ratio of the transformer  $\Phi$  will be directly proportional to  $C_0$ . Moreover, due to the definition of  $V$  and  $I$  at the electrical side of the transformer, we can state that  $I$  is directed away from the node to the transformer and consequently the voltage drop in the capacitor must be negative, resulting in a series negative capacitor on the electrical side of the transformer (see Fig. 3.6). This capacitor behaves like a capacitor (i.e. its reactance varies inversely as the frequency), but the value of its reactance is positive (like an inductor).

Nevertheless, along this thesis the crossed-field Mason circuit has been used. The difference between these two equivalent circuits lies in the fact that in the case of the crossed-field model the negative capacitor is short-circuited ( $\alpha = \infty$ ). The introduction of a Mason equivalent circuit for one periodic section of an IDT by means of a three-port network, was introduced by Smith [53] in 1969. There, the two acoustic ports and the electric port of an IDT are described by an admittance matrix  $Y$ . Many refinements have been made since then and the corresponding literature is enormous.

Furthermore, some publications as [55] used a modified approach that is extended to include internal finger reflections based on the crossed-field equivalent circuit. Specifically, the method divides the IDT into half wavelength sections. These sections are further divided into zones. Being two of the zones un-metallized areas around one zone that is comprised of a metal finger. Each zone is modelled by a transmission line matrix equivalent circuit (Fig. 3.7). Two identical circuits model the un-metallized areas, while the middle circuit models the area under the metal finger.

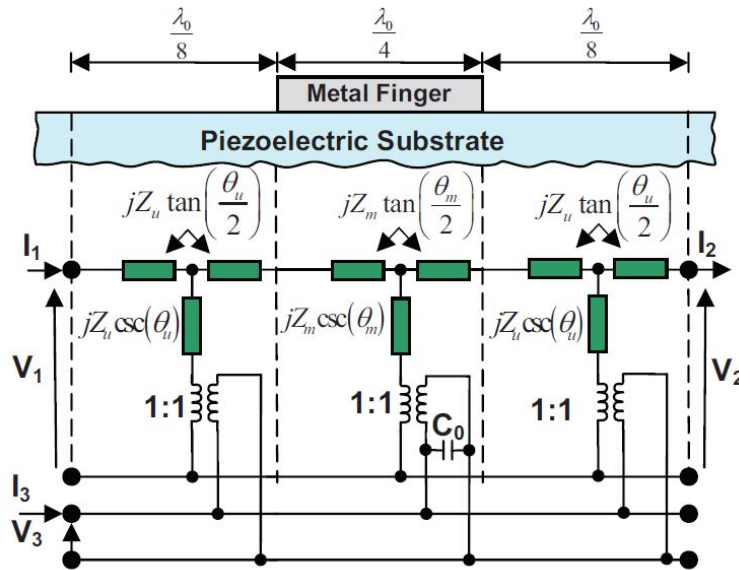


Figure 3.7: Metallized and un-metallized areas circuitual models [55].

For the development of this PhD, the same idea used in [55] of separating the electrodes in metallized and non-metallized zones will be used to create a linear circuitual model that takes into account the separation between zones. To better model the nonlinear performance of the structure, a similar approach is used with the difference that now a discretized equivalent circuit is developed and extended to its nonlinear form.

Moreover, a full resonator simulation can be done by cascading  $M$  (number of electrodes) unit Mason crossed-field circuits (of one electrode each section) at their ports 1 and ports 2 and connecting properly their electrical port 3 in parallel. More details about the Mason crossed-field model is presented in the next section 3.2.

### 3.1.3 Nonlinear modeling approaches

In the last two decades, a lot of progress has been made to model and simulate the nonlinear behavior of BAW electroacoustic devices [21–23]. Due to the complexity of SAW and their longer propagation distance, SAW nonlinearity modeling is inherently more difficult and there is less published literature on this topic. This concern led to also extend the research on modeling and simulation of nonlinearities on SAW devices [43, 56–65]. These references used different approaches, for example, based on FEM [57], ECM [58], [56], based on COM theory [59–63] or P-Matrix [43, 64, 65]. Despite of the different published approaches, there is still a lack of generalized consensus about the origin of the nonlinear behavior. References [59, 66, 67] state that the nonlinearities are given by nonlinear elasticity, dielectric constant and electromechanical coupling. Moreover, [68] studies the nonlinearities arisen from the electrode crystallinity, and [69–71] aim to the bulk modes. The lack of consensus is driven by the difficulty to identify geometry-independent material parameters that could predict the nonlinear behavior of any resonator before manufacturing. One reason might be the distributed nature of the nonlinearities in acoustic devices.

Regarding the nonlinear models, in 2009, [72] studied the IMD products of SAW resonators and discussed the difference in nonlinear performance between SAW and BAW resonators. Later, [58] stated that SAW resonators offer inherently better 2nd-order nonlinearity but worst 3rd-order nonlinearity in comparison with BAW devices. Here a nonlinear BVD model was used to model the effects like harmonics or IMD3.

The nonlinear simulation of a SAW resonator was done by assuming a quadratic dependence of the motional inductance  $L_a$  on the value of the current  $I$  and thus creating a 3rd order coefficient of the inductor  $L_{a3}$ . The nonlinear coefficient  $L_{a3}$  was determined by fitting Harmonic Balance (HB) simulations results to the measurements. Moreover, [58] claimed that the reason of only choosing current-dependent inductance is that non-linearity was assumed to be mostly related to the propagation of the acoustic wave and wave velocity. The resulting BVD nonlinear model is shown in Fig. 3.8.

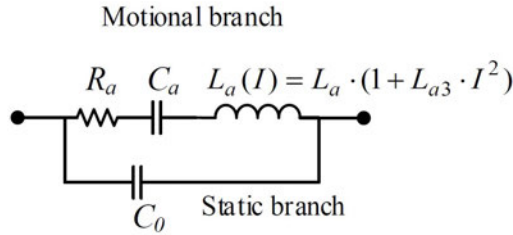


**Figure 3.8:** The nonlinear BVD equivalent circuit model [58].

Afterwards, [73] explained the four possible causes of nonlinearities in SAW resonators: (1) nonlinearity of electromechanical conversion (nonlinearity of piezoelectric constant: electric to mechanical), (2) nonlinearity of electromechanical conversion (nonlinearity of piezoelectric constant: mechanical to electrical) piezoelectric constant, (3) nonlinearity of SAW elasticity (nonlinearity of elastic constant), and (4) nonlinearity of IDT capacitance (nonlinearity of dielectric constant). In [73] only (3) was considered, as the nonlinearity of the elastic constant indicates the nonlinear elasticity of SAW. In this approach, a one-dimensional phenomenological model based in COM was used to establish a nonlinear relation between stress and strain.

Moreover, [56] presented a novel nonlinear Mason equivalent circuit model including a 3rd order nonlinear coefficient in the wave propagation. It was assumed that the nonlinearity of SAW resonators came from the nonlinear elasticity of the piezoelectric substrate, they developed a nonlinear model extending the constitutive equations to higher orders. The constitutive equations were presented previously in Chapter 2. Specifically, the nonlinear term was implemented into the Mason circuit as a nonlinear capacitor in the mechanical part of the circuit as shown in Fig. 3.9. As it can be seen, the equivalent transmission line of one electrode was separated into  $N$  sub-sections and an individual nonlinear capacitor was added to cross each sub-section of the transmission line. These nonlinear capacitors  $C_{NL}$  account for the overall nonlinear capacitance for each transmission line section and were used to account for the third order nonlinearities in the form of a voltage dependent capacitor.

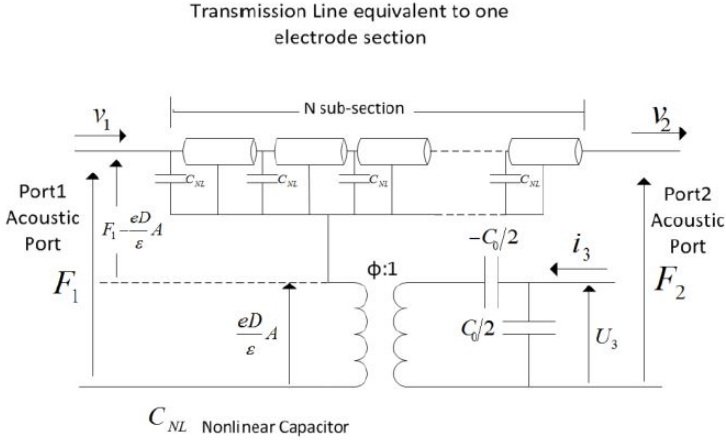


**Figure 3.9:** The nonlinear Mason model for one electrode section of a SAW transducer. The transmission line is splitted into  $N$  sections [56].

Nonlinearities in TC-SAW devices were discussed in [74] and stated that for SAW devices, the interaction between the metal (Al) and piezoelectric substrate (LiTaO<sub>3</sub>) at high power, involves geometrical and material nonlinearities. The term geometrical nonlinearity in [74] is used to refer the 2nd order terms, whereas material nonlinearities pertains to nonlinear terms associated with higher order. They conclude that the metal is the dominant source of third order nonlinearity in SAW devices. To understand such undesired effects, FEM simulations combined with a nonlinear P-matrix representation was applied to find out the role of different materials.

In addition, in 2012 Solal et al [65] published a nonlinear P-matrix based on the COM model. Specifically, the nonlinear P-matrix is recognized as a nonlinear wave model which is built by assuming that the propagation of the SAW on a substrate can be described as

$$\frac{\delta^2 s}{\delta t^2} = v^2 \frac{\delta}{\delta x^2} (s + \beta s^2 + \gamma s^3) \quad (3.11)$$

where the acoustic wave can be represented as a scalar  $s$  being the mechanical strain,  $v$  the wave velocity, and finally  $\beta$  and  $\gamma$  are, respectively, the 2nd order and 3rd order nonlinear coefficients whose origins are in the nonlinear part of the elastic coefficients.

In this case, they concluded that 3rd harmonics are obtained predominantly from the mixing of 2nd harmonics and fundamental tones. Moreover, their analysis method started with the linear P-matrix analysis at the fundamental tones, then source terms depending on the wave amplitudes at the fundamentals were added to represent the generation of mixing products along the propagation path. The full details of the nonlinear P-matrix model derivation can be found in [65].

After that, several publications have used the nonlinear P-matrix model [64], [42] to describe the IMD3 or even combining the COM equations to find an extended nonlinear P-matrix formalism [63].

Besides, in the case of nonlinearities of SAW resonators which is of the most interest of this PhD thesis, the use of distributed equivalent circuit models is particularly useful. Distributed models are required to reproduce the standing wave pattern of the fields along the structure at a given frequency. This is because nonlinear effects, governed by the piezoelectric constitutive equations, arise locally at each position of the structure depending of those field magnitudes, and they manifest at the output port, which at the end is the point where measurements are taken. Sweeping the frequency of the excitation, each potential contributor (source of nonlinearity) causes a characteristic frequency pattern, which enables to discern between them. This characterization process allows to find the geometry-independent nonlinear coefficients, which only depend on the physical properties of the materials, contributing to the generation of a given spurious signal.

During the PhD thesis we have further developed previous Mason-based ECM models to make them discretized. Among the common drawbacks of using these circuitual models, are their lack to reproduce other effects such as bulk-wave scattering, transversal acoustic radiation, etc. Often these simplifications are reasonable, but in some cases the ignored-effects results in an unexpected device behavior. Nevertheless, even though the nonlinear Mason model is a one-dimensional equivalent circuit with some assumptions on acoustic wave propagation, still is an efficient physical model governed by piezoelectric constitutive wave equations over which is possible to obtain geometry-independent nonlinear parameters and its usefulness and accuracy is justified by the good agreement between simulations and measurements of SAW resonators that will be further discussed in Chapter 5.

When simulating a single resonator, the simulations are time consuming, but the problem small enough to keep the simulation time into a few seconds (of course depending on the number of frequency points to be analyzed). Although convergence problems may appear depending on the input power and the separation between fundamental frequencies in a two-tone experiment, HB analysis has proven its efficiency and usefulness. Nevertheless, when simulating more complex devices, such as filters or duplexers, the problem size is too big to keep the computation time into reasonable values. Several alternatives have been developed during the last years to reduce the computation time significantly. Under certain assumptions the number of nonlinear sources of a distributed model can be reduced going to the most simplified model consisting on having only two nonlinear sources in an equivalent nonlinear BVD model [75]. These models are much faster than those distributed, and they have been satisfactorily used in the design of filtering devices to evaluate or minimize the nonlinear performance in the early stages of the design process. Even so, those lumped models are accurate only in a limited bandwidth or for certain nonlinear scenarios that are usually required by the customers, they do not have the capability of predicting unexpected nonlinear effects in a broadband scenario due to the lack of the distributed nature of the problem.

Basically, the model employed in this thesis is based on a physical nonlinear model derived from the physics of the acoustic wave propagation and using an equivalent circuit approach to account for the nonlinear effects. Then, since the model is based on an equivalent circuit approach, is possible to perform a mathematical technique to analyze the previous circuitual networks. With this mathematical expressions is possible to account for the nonlinear distributed effects and design a new method to simulate H and IMD products, requiring much less time and effort compared to the simulation using other nonlinear physical models.

## 3.2 Mason-based linear models

In this section, the solutions of the one-dimensional mechanical wave in both a non-piezoelectric and a piezoelectric slab are outlined. After that, equivalent circuit model based on Mason model and the linear distributed circuitual model for the SAW propagation is described. Moreover, the linear measurements are outlined to validate the model and finally, derivation of the nonlinear discretized model is presented.

### 3.2.1 Mason linear model

Our main objective in this section is to relate the generation of acoustic waves in SAW resonators and their propagation with a one-dimensional equivalent circuit. This equivalent circuit describes the electrical characteristics of an acoustic structure. Specifically, the propagation of the acoustic wave can be modeled as a Transmission Line (TL) and to obtain the corresponding equations an analogy between force and voltage, and particle velocity and current will be assumed. Note that here it is assumed that only one mode is propagating. The pure acoustic model is extended in the Mason model to account for the electro-acoustic conversion.

#### Acoustic propagation in a non-piezoelectric media considering a discretized circuit

The next subsection is devoted to obtain the equations relating the acoustic propagation in a non-piezoelectric media considering a distributed LC-circuit model. The aforementioned non-piezoelectric slab, with cross-section area  $A$ , is based on the application of the Hooke's law to the constitutive relations of equation 2.36 of Chapter 2 following

$$T = c^E S \quad (3.12)$$

Combining the previous equation with the relation  $F = -TA$  we obtain

$$F = -c^E SA \quad (3.13)$$

which by considering equation 2.8 can also be expressed as

$$F = -c^E \frac{\partial u}{\partial z} A \quad (3.14)$$

Now taking the partial derivative of the force  $F$  respect to the time and bringing in the particle velocity  $v = j\omega u$  (harmonic regime) we obtain

$$j\omega F = -c^E \frac{\partial v}{\partial z} A \quad (3.15)$$

and isolating the velocity from the previous equation, we finally obtain

$$\frac{\partial v}{\partial z} = \frac{-j\omega F}{c^E A} \quad (3.16)$$

On the other hand, starting with Newton's 2nd law we recall equation 2.10

$$\frac{\partial F}{\partial z} = -j\omega A \rho v \quad (3.17)$$

If 3.16 and 3.17 are considered, we have the following set of equations

$$\begin{cases} \frac{\partial v}{\partial z} = \frac{-j\omega F}{c^E A} \\ \frac{\partial F}{\partial z} = -j\omega A \rho v \end{cases} \quad (3.18)$$

if we perform an analogy with the Telegrapher's Equations but using 3.18, we can obtain a circuit as the one in the Fig. 3.10 for a thin slab of thickness  $\Delta z$ .

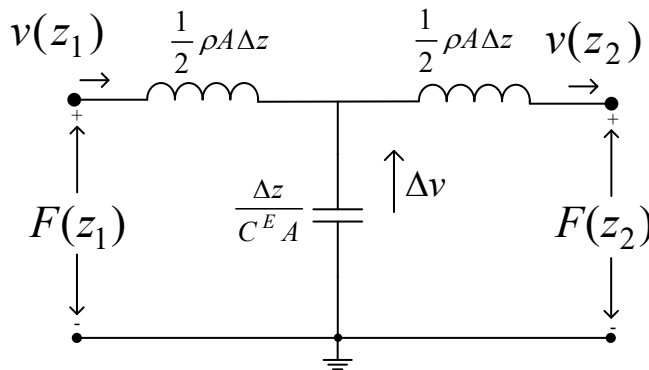


**Figure 3.10:** Equivalent circuit of the analogy of Telegrapher's Equations with mechanical equations for a non-piezoelectric media.



where the first row of 3.18 represents the increase of current (velocities)

$$\Delta v = v(z_2) - v(z_1) = -\frac{j\omega F \Delta z}{c^E A} \quad (3.19)$$

and the second row the sum of voltages(forces)

$$\Delta F = F(z_2) - F(z_1) = -\rho A \Delta z j\omega v \quad (3.20)$$

Equation (3.18) leads to the wave equations for the force, already written in 2.19, and for the velocity. Those equations are

$$\frac{\partial^2 F(z)}{\partial z^2} = -\frac{\rho}{c} \omega^2 F(z) \quad (3.21)$$

$$\frac{\partial^2 V(z)}{\partial z^2} = -\frac{\rho}{c} \omega^2 V(z) \quad (3.22)$$

### Equivalent T-network of an acoustic transmission line

This subsection is devoted to analyze the mechanical wave when it is propagating in a non-piezoelectric material according to the wave equation obtained in (2.18). Moreover, considering a lossless non-piezoelectric slab, the scenario to be analyzed is a non-piezoelectric slab of finite thickness  $d = z_2 - z_1$  and cross-section  $A$ , bounded by planes  $z = z_1$  and  $z = z_2$ .

The solution of equation 3.22 for the particle velocity  $v$  is

$$v = V_0^+ e^{-jkz} + V_0^- e^{jkz} \quad (3.23)$$

and for the force  $F$

$$F = Z(V_0^+ e^{-jkz} - V_0^- e^{jkz}) \quad (3.24)$$

where we can define the mechanical or acoustic impedance  $Z$  as

$$Z = \rho v A \quad (3.25)$$

According to equations 3.23 and 3.24 the corresponding forces and particle velocities at  $z_1$  and  $z_2$  are

$$F_1 = Z(V_0^+ e^{-jkz_1} - V_0^- e^{jkz_1}) \quad (3.26)$$

$$F_2 = Z(V_0^+ e^{-jkz_2} - V_0^- e^{jkz_2})$$

$$v_1 = V_0^+ e^{-jkz_1} + V_0^- e^{jkz_1}$$

$$v_2 = V_0^+ e^{-jkz_2} + V_0^- e^{jkz_2}$$

and isolating  $V_0^+$  and  $V_0^-$  we obtain respectively

$$V_0^+ = \frac{v_1 e^{jkz_2} - v_2 e^{jkz_1}}{2j \sin(kd)} ; V_0^- = \frac{v_2 e^{-jkz_1} - v_1 e^{-jkz_2}}{2j \sin(kd)} \quad (3.27)$$

and then substituting 3.27 into 3.26 respectively, we can also find the forces  $F_1$  and  $F_2$  at the left and right boundaries respectively but without considering the electric field

$$F_1 = -j \frac{Z}{\sin(kd)} (v_1 - v_2) + jZ \tan\left(\frac{kd}{2}\right) v_1 \quad (3.28)$$

$$F_2 = -j \frac{Z}{\sin(kd)} (v_1 - v_2) - jZ \tan\left(\frac{kd}{2}\right) v_2 \quad (3.29)$$

The previous set of equations represent the solution of the mechanical wave in a non-piezoelectric slab as a function of the applied force  $F$ , the particle velocity  $v$  and the acoustical impedance  $Z$ . Moreover, the previous relations stands for a circuit representation if Kirchhoff's voltage equations are considered. The corresponding equivalent circuit model for a non-piezoelectric material is the one depicted in Fig. 3.11, which is the classic distributed T-impedance equivalent network for a transmission line where the current  $I$  is represented by the particle velocity  $v$  and the voltage  $V$  by the force  $F$ .

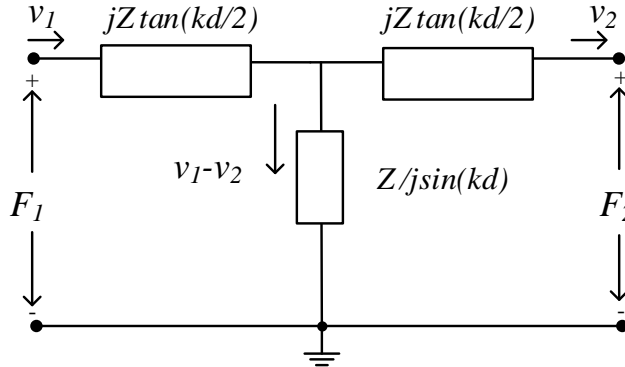


**Figure 3.11:** Equivalent circuit model consisting in a T-network representing a non-piezoelectric slab of thickness  $d$  and cross-section  $A$ .

### 3.2.2 Equivalent circuits for SAW based on Mason model

Based on the theory about the piezoelectric medium presented by Berlincourt et al [76] and based on the equivalent circuit of an electromechanical transducer presented by Mason [15], Smith et al [53] developed the equivalent circuit for IDT composed of  $M$  periodic  $\lambda$ -sections of the form shown in Fig. 3.12. Following this method, we assume that a pair of bulk wave transducers are arranged acoustically in cascade and electrically in parallel.

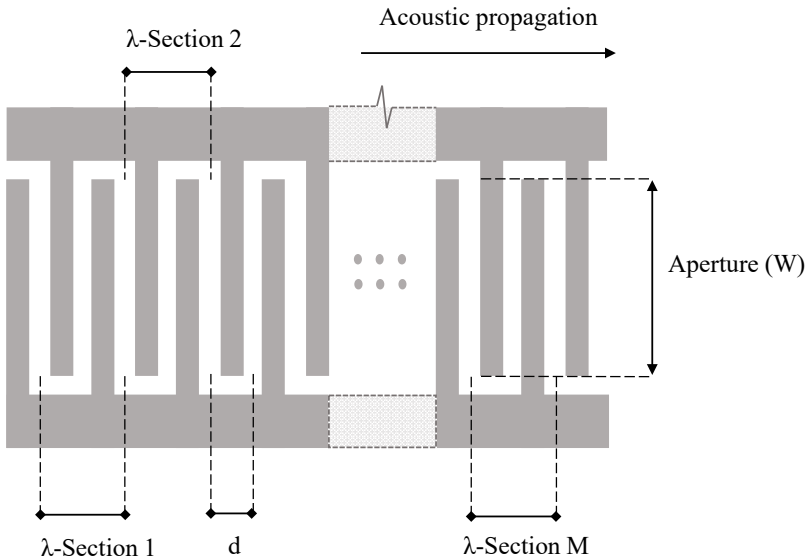


**Figure 3.12:** Example IDT description composed by  $M$  periodic sections.

A unit section of length  $d$  of an IDT can be represented by a Mason equivalent circuit. The length  $d$  is normally designed to be  $\lambda/2$  of the wave propagating on the substrate at its operation frequency. Therefore, each periodic  $\lambda$ -section is considered to be of length  $2d$  with one pair of electrodes and their corresponding gaps as shown in Fig. 3.13 (a). As seen, within one periodic  $\lambda$ -section the electric field polarities change between adjacent electrodes. Moreover, the electric field of such structure can be approximated into two main components: one parallel to the wave propagation (at  $z$ -direction, as shown in Fig. 3.13 (b)) and the other one normal to the wave propagation (at  $x$ -direction, as shown in Fig. 3.13 (c)).

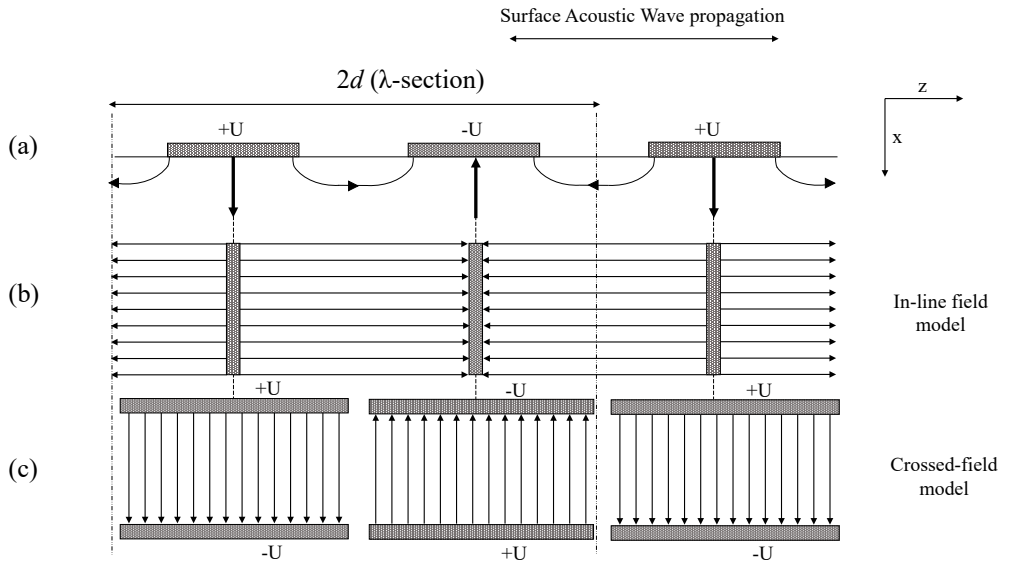


**Figure 3.13:** Simplified electric field patterns and analogy with bulk acoustic wave resonators. (a) Simplified actual field. (b) Approximated E-field pattern for In-line field model. (c) Approximated E-field pattern for crossed-field model.

Since the Mason model is only a one-dimensional equivalent circuit approach, the assumption is made considering that one of the two existing electric field components plays a dominant role. If it is assumed that the parallel electric field is dominant, the model is called In-line. Contrary to that, if it is assumed that the normal component plays a dominant role, represent the so-called crossed-field model. For the purpose of this thesis, it is assumed that the normal component is the one playing the dominant role therefore, the crossed-field model is the one used. The important advantage is that each periodic  $\lambda$ -section can be represented by the desired Mason's equivalent circuit.

### One-dimensional mechanical wave in a piezoelectric slab: Mason crossed-field model

As discussed before in section 3.2.1, it is possible to find an analogy between mechanical quantities force  $F$  and particle velocity  $v$  to their electrical counterparts voltage  $V$  and current intensity  $I$  respectively. The previous analogy can be illustrated by an equivalent electromechanical circuit which describes the electrical characteristics of an acoustic structure as we have seen in the previous subsection. Consequently, the analysis of the propagation of the acoustic wave through the piezoelectric slab will follow the same equations.

The equations considering a piezoelectric slab and using the Mason model can be broadly found in [13, 15, 44]. Basically, the equations will be similar to those of equation 3.28 and 3.29 by adding a new term due to the piezoelectric effect. Specifically, since the piezoelectric is a dielectric material, the presence of an external electric field  $E$  with a displacement current through a capacitance and the conversion between the mechanical and electrical energy due to the piezoelectric effect must be considered.

Taking this into account, the desired equivalent circuit model must consider a configuration of the piezoelectric plate as the one following Fig. 3.14 where the acoustic propagation is in the  $z$ -direction (perpendicular to the electric field). An electric field can excite an acoustic wave normal to its polarization because the piezoelectric matrix couples electrical and mechanical fields of varying orientations.

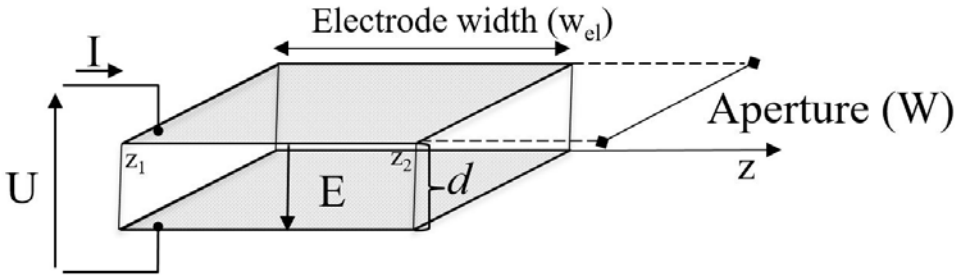


**Figure 3.14:** Crossed-field model exemplification. The resonator is considered to have lateral field excitation and the electric field is in the plane perpendicular to the surface acoustic wave propagation.

Here we just recall equations 2.38 and 2.39

$$T = c^E S - eE \quad (3.30)$$

$$D = \varepsilon^S E + eS \quad (3.31)$$

### Distributed Mason crossed-field model

The equations described here for the Mason crossed-field model are following the guidelines of [15] and [17]. In this case, the acoustic propagation is considered as a T-network circuit formed by a transmission line and where the piezoelectric contribution is given by the second term of equation 3.30. Furthermore, the cross-sectional area is defined as  $A = Ww_{el}$  and the lateral area as  $A_L = Wd$  and those definitions will be used frequently in the following sections.

Let us start writing the current definition in terms of the electrical displacement

$$I = -j\omega DA \quad (3.32)$$

and assuming  $I$  is uniform across width and using equation 3.31

$$I = -j\omega (\varepsilon^S E + eS) A \quad (3.33)$$

and then using the strain definition we get

$$I = -j\omega \varepsilon^S EA - j\omega eW (u_2 - u_1) \quad (3.34)$$

where the electric field  $E$  is assumed to be uniform along the parallel plates and, the electric potential at the electrodes is given by

$$U = -Ed \quad (3.35)$$

The previous equation 3.34 is formed by two terms: the contribution of the external  $E$  field, and the acoustically-generated component.

Considering the definition of static capacitance as

$$C_0 = \frac{\varepsilon^S W w_{el}}{d} \quad (3.36)$$

the equation 3.34 becomes

$$I = j\omega C_0 U - eW (v_2 - v_1) \quad (3.37)$$

Following the procedure described in [17], we recall again equations 3.28 and 3.29 to obtain the corresponding equations that include the added force due to the piezoelectric effect

$$F_1 = -j \frac{Z}{\sin(kd)} (v_1 - v_2) + jZ \tan\left(\frac{kd}{2}\right) v_1 + A_L eE \quad (3.38)$$

$$F_2 = -j \frac{Z}{\sin(kd)} (v_1 - v_2) - jZ \tan\left(\frac{kd}{2}\right) v_2 + A_L e E \quad (3.39)$$

Finally, the previous equations can be represented in the well-known crossed-field Mason equivalent circuit for a piezoelectric plate as depicted in Fig. 3.15.

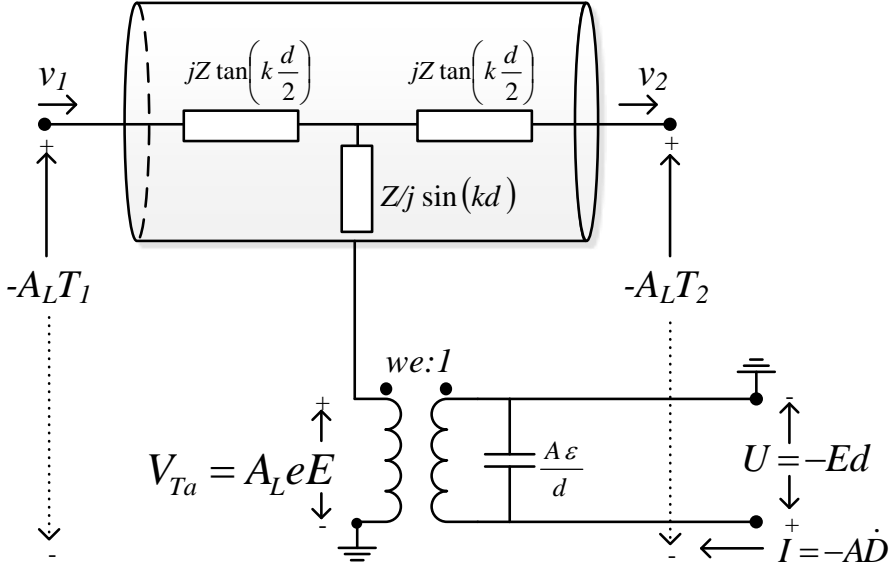


**Figure 3.15:** Equivalent crossed-field electro-mechanical Mason circuit for a piezoelectric material of thickness  $d$ . The electric field is normal to the direction of propagation of waves.

On another note, in practical implementations since the goal is to reproduce some device behavior it is mandatory to include the losses in the equivalent circuit models. This can be done if we change the previous propagation  $k$  by a new propagation constant  $\gamma$  defined by

$$\gamma = \alpha + j\beta = \alpha + j \frac{\omega}{v_{phase}} \quad (3.40)$$

being  $v_{phase}$  the phase velocity and  $\alpha$  the attenuation constant which can be defined as [18]

$$\alpha = \frac{1}{2} \eta \omega^2 \frac{\sqrt{\rho c}}{c^2} \quad (3.41)$$

with  $\eta$  being the viscosity,  $\rho$  the mass density and  $c$  the stiffness constant. Note that also the impedances  $\frac{1}{j\sin(kd)}$  and  $j\tan\left(\frac{kd}{2}\right)$  must be replaced by  $\frac{1}{\sinh(\gamma d)}$  and  $\tanh\left(\frac{\gamma d}{2}\right)$  respectively.

The previous relations involve an electromechanical impedance matrix formed by a three-port circuit as the one in Fig. 3.16

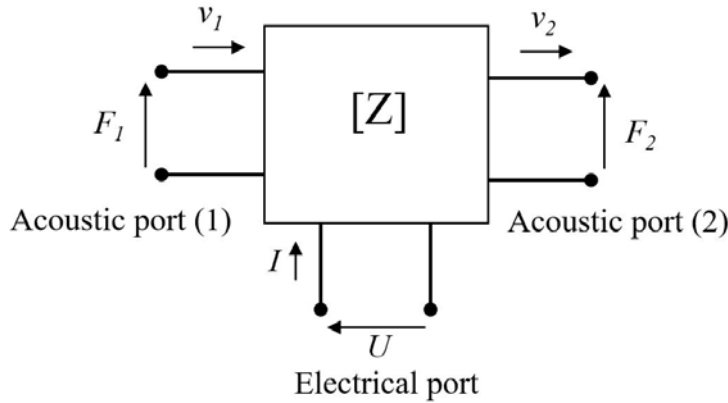


**Figure 3.16:** Equivalent impedance matrix representing a piezoelectric solid.

Being the top acoustical ports related to the forces applied at the boundaries with its corresponding particle displacement, and the bottom electrical port related to the intensity current generated due to the piezoelectric effect.

### Unit-cell of a discretized Mason crossed-field model

As stated previously, the main goal of the circuitual model is to properly know the intensity of the field magnitudes at different positions along the SAW structure. Because of that, the Mason-based crossed-field model must be a distributed model in such a way that a given section of the IDT, either the electrode or the separation between them, is discretized in many elemental cells. Specifically, the previous equivalent circuit of Fig. 3.15 can be modeled discretizing the desired section into many unit-cells which represent a slab of thickness  $\Delta z$ .

To obtain the equations for the crossed-field Mason model it is necessary to consider the previous constitutive equations (3.30) and (3.31) presented in Chapter 2. At the acoustic domain, by use of the voltage-force equivalence of (2.9) and scaling 3.30 by the lateral area  $-A_L$  we obtain

$$-A_L T = -A_L c^E S + A_L e E \quad (3.42)$$



and this equation is fulfilled in the Mason model of Fig. 3.17. Note that equation 3.42 considers a loss-less case with  $G = 0$ . Moreover, on the left-hand side of the equation 3.42 we have the voltage-force equivalence and on the right-hand side, the first term corresponds to the voltage drop on a distributed capacitor  $C_d$ . Note that  $\Delta v = j\omega(u_2 - u_1) = j\omega S\Delta z$  is defined as the difference between the particle velocities  $v_1$  and  $v_2$  which is equivalent to the current flowing through the T-network. So, if the equivalence capacitor  $C_{eq}$  is defined as

$$C_{eq} = C_d\Delta z = \frac{1}{c^E A_L} \Delta z \quad (3.43)$$

and its corresponding voltage drop is calculated by means of the current  $\Delta v$  and the impedance of  $C_{eq}$ , resulting in  $-A_L c^E S$  which corresponds with the first term and satisfies equation 3.30. Moreover, the second term of 3.42 corresponds to the voltage drop on the acoustic side of the transformer denoted as  $V_{Ta}$ . This voltage drop is  $V_{Ta} = \Phi V_{in}$ . Besides, the turn ratio is defined as  $\Phi = eW$  and  $V_{in} = -Ed$  is the voltage drop at two parallel plates separated by a distance  $d$  and with an electric field  $E$  hence,  $V_{Ta} = eW(-Ed) = -A_L eE$  which satisfies the other term of equation 3.30.

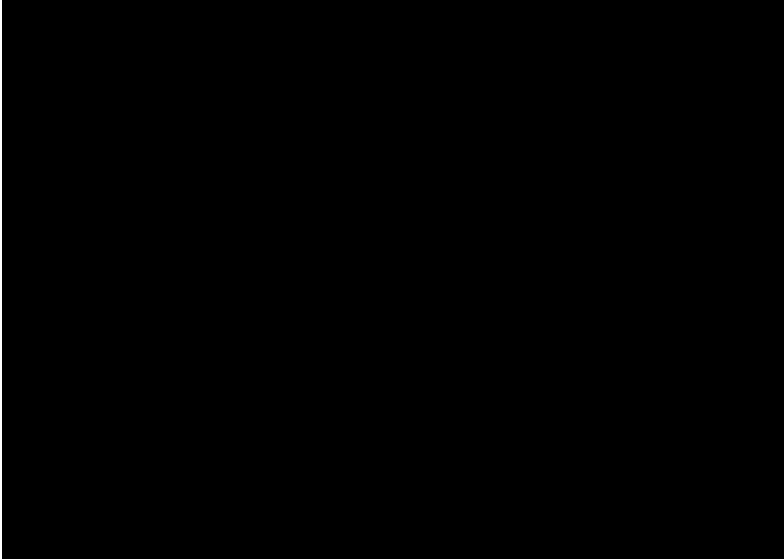


**Figure 3.17:** Unit-cell of the crossed-field distributed electro-mechanical Mason circuit for an electrode section of length  $\Delta z$ .

At the electrical side of the circuit, scaling (3.31) by the area of the electrode  $A$  and taking its time derivative in phasor form we can write:

$$-j\omega DA = -j\omega eSA - j\omega \varepsilon^S EA \quad (3.44)$$

where the left-hand side of the above equation represents the total current  $I_{IN}$  through an area  $A = W\Delta z$ . On the right-hand side, the first term corresponds to the current flowing to the electrical side of the transformer  $I_{Te}$ , and is defined by  $I_{Te} = \Phi I_{Ta}$  and therefore, substituting  $A$  and the previous  $\Delta v$ , the current is defined as  $I_{Te} = -j\omega\epsilon SA$ . The second term of 3.44 is the current  $I_{C'0}$  on the electrostatic capacitance  $C'_0$  defined as  $I_{C'0} = j\omega C'_0 V_{in} = -j\omega C'_0 Ed$  and considering the definition of  $C'_0$ , the current is defined as  $I_{C'0} = -j\omega\epsilon^S EA$ .

Moreover, Fig. 3.17 shows the unit-cell of an electrode section, accounting for the electro-acoustic interactions and wave propagation in the SAW propagation direction which, at the same time, is modeled as an acoustic transmission as the one of Fig. 3.10 with distributed parameters  $C_d$  and  $L_d$  and including the material losses with a conductance  $G_d$  following

$$C_d = \frac{1}{A_L c^E} \quad (3.45)$$

$$L_d = \rho A \quad (3.46)$$

$$G_d = \frac{1}{A_L \eta} \quad (3.47)$$

where  $A_L$ ,  $\rho$  and  $\eta$  are the lateral area, mass density and viscosity respectively. Furthermore, Fig. 3.17 represents a unit-cell modeling a thin  $\Delta z$  slab and the whole section of the electrode of length  $w_{el}$ . In addition, the whole section is modeled cascading a finite number  $N$  of unit-cells, whose length is  $\Delta z = w_{el}/N$  as depicted in Fig. 3.18

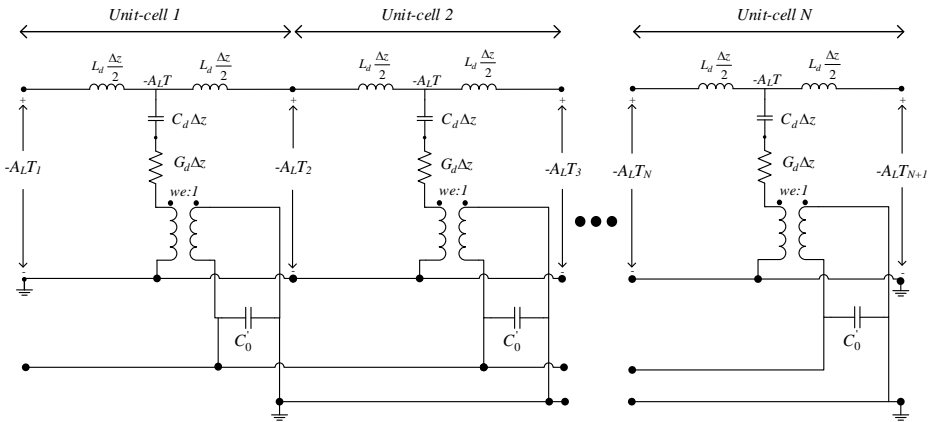


**Figure 3.18:** Distributed cross-field electro-mechanical Mason circuit for an electrode section of length  $w_{el}$  formed by  $N$  unit-cells.

Analogously, if the section to evaluate is the separation between electrodes, the corresponding distributed Mason model is the one of Fig. 3.19, where only acoustic propagation is considered. Note that the previous equivalent circuit is very similar to with the one shown in Fig. 3.10 since the separation between the electrodes section is considered as an acoustic transmission line.

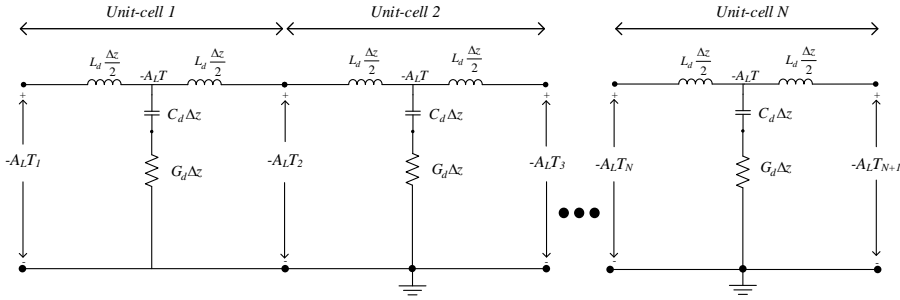


**Figure 3.19:** Unit-cell of the crossed-field distributed mechanical Mason circuit for an electrode separation section of length  $s$  formed by  $N$  unit-cells.

### 3.2.3 Distributed model of the whole transducer

Prior to perform the nonlinear characterization, a linear model of the whole transducer must be used, whose accuracy to emulate the linear measurements entails a proper modeling of the nonlinearities.

In contrast to the BVD model which is an equivalent circuit of the resonator, the Mason model represents the acoustic propagation and the transduction for all the electrodes of a device making possible to simulate the nonlinearities of the full-structure. From a modeling point of view, the use of distributed models is required to reproduce the standing wave pattern of the fields along the structure at a given frequency. This is because nonlinear effects, governed by the piezoelectric constitutive equations, arise locally at each position of the structure depending of those field magnitudes and they manifest at the output port, which at the end is the point where measurements are taken. Sweeping the frequency of the excitation, each potential contributor (source of nonlinearity) causes a characteristic frequency pattern, which enables to discern between them. This characterization process allows to find the geometry-independent nonlinear coefficients, which only depend on the physical properties of the materials, contributing to the generation of a given spurious signal. Specially, the use of distributed models allows to have full information about the intensity of a given field magnitude at any desired position of your structure under evaluation.

As explained in the previous subsection, for this thesis it is assumed that the main driver of the surface acoustic wave generation is the transverse electric field beneath the electrodes. Following that, and as it was done in [77], we use the crossed-field Mason circuit approach [53]. In this model, the electric field distribution under

the electrodes is approximated as being normal to the acoustic propagation direction [53], and it is assumed that the normal component is constant and it mainly generates Rayleigh waves in a direction perpendicular to the excitation field [44].

In order to simulate a full resonator structure is mandatory to create a block diagram as shown in Fig. 3.20

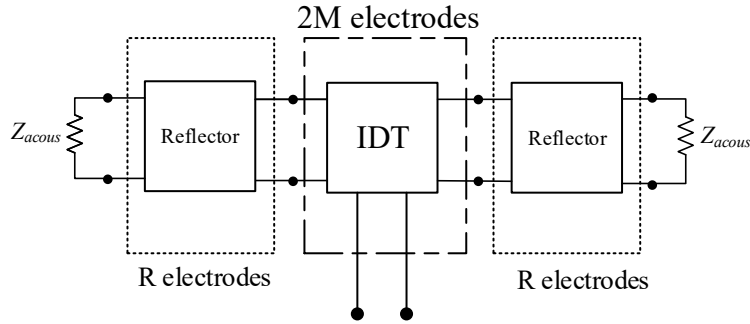


**Figure 3.20:** Simulation block diagram of a SAW resonator.

Moreover, for both IDT and reflector sections the distributed model is made up by cascading many periodic  $M$   $\lambda$ -sections and  $R$   $\lambda/2$ -sections respectively. Specifically, the IDT is made by cascading multiple  $M$  sections by their top acoustical ports and connecting their bottom electrical ports in parallel as shown in Fig. 3.21 (a). For the reflector, the  $R$  sections are cascaded considering the electrical port shorted (see Fig. 3.21 (b)). That means, the transducer is formed in total by  $2M + 2R$  electrodes.

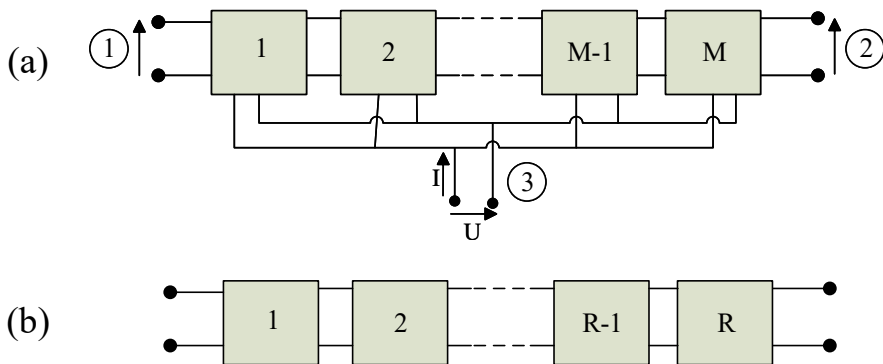


**Figure 3.21:** (a) Simulation block diagram of  $M$   $\lambda$ -sections of the IDT. (c) Simulation block diagram of  $N_{ref}$   $\lambda/2$ -sections of the reflector.

On top of that, the conventional crossed-field model is not discretized and there is a Mason equivalent circuit for each period of the structure that is, for each pair of digits of the IDT [44],[28]. We have modified this model separating the metallized regions (MR) and the non-metallized regions (NMR) of the  $\lambda/2$ -section as seen into the dashed box of the IDT in Fig. 3.22. Note that  $\lambda/2$ -section represents a half period of the corresponding IDT or reflector. Doing so, a  $\lambda/2$ -section of the IDT is made up by three sub-circuits: a crossed-field Mason-based circuit for the MR section representing the area beneath the electrodes that is ended on each acoustic side by a NMR section (T-circuit) where only acoustic propagation is considered.

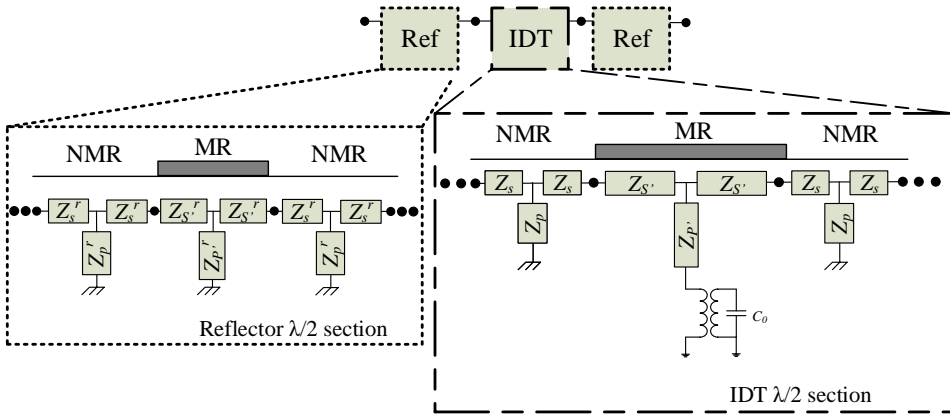


**Figure 3.22:** Analysis model using the crossed-field approximation [26], [29].

For the reflectors, only acoustic propagation is considered along the electrode section and thus, each  $\lambda/2$ -section is composed by three cascaded T-networks with differentiation between NMR and MR regions as depicted in Fig. 3.22. By doing so, we have developed a Mason-based model that is a general model and operates with a parameter set which not only depends on the piezoelectric substrate but on the specific geometry of the transducers such as the aperture, pitch or duty factor.

Consequently, each MR or NMR section, whether of the IDT or acoustic reflector, has its own acoustic impedance and phase velocity. The circuit parameters of the T-circuits are described by series ( $Z_s$ ) and shunt impedances ( $Z_p$ ):

$$Z_s = Z_{0,m} \tanh(\gamma_m \frac{L_m}{2}) \quad (3.48)$$

$$Z_p = Z_{0,m} / \sinh(\gamma_m L_m) \quad (3.49)$$

where the subscript  $m$  indicates the region MR or NMR,  $L_m$  is the width of the section,  $\gamma_m = \alpha_m + j \frac{\omega}{v_m}$  is the propagation constant and  $Z_{0,m} = \rho_m A_L v_m$  is

the characteristic impedance, being  $\rho_m$  and  $A_L$  the mass density and lateral area defined previously. Although there are different phase velocities  $v_m$  for the MR and NMR of the IDT and reflector, only very small relative variations are needed. Such differentiation between IDT and reflector circuit parameters is required to model most of the features of the linear response. It will be further discussed in Chapter 5. The transformer ratio  $\Phi$  and capacitance  $C_0$  of the cross-field model of Fig. 3.22 are given by  $\Phi = eW$  and  $C_0 = \epsilon_{r,eff} \cdot \epsilon_0 \frac{A}{d}$  respectively. The values of the relative dielectric constant  $\epsilon_{r,eff}$  must be considered as effective values because it must be fine-tuned to adjust the linear simulations of this simplified model to the measurements as it will be discussed in the next sections. Therefore, and besides the geometrical parameters, aperture ( $w$ ), pitch ( $d$ ) and duty factor ( $\eta$ ), the lineal model is fully described by means of the mass density ( $\rho$ ), effective dielectric constant ( $\epsilon_{r,eff}$ ), piezoelectric constant ( $e$ ), and acoustic wave velocities ( $v_m$ ) of the MR and NMR regions.

### 3.2.4 Discretized model of the MR and NMR sections

The distributed model can be discretized into many unit-cells as depicted in Fig. 3.22. The MR will be modeled cascading many unit-cells of the crossed-field Mason circuit, each one modeling a thin slab of width  $\Delta z$ , where the wave propagates along the z-direction beneath the electrodes, until reaching the NMR, which is modeled cascading unit-cells of short acoustic transmission lines (ATL) of length  $\Delta z$ .

Obviously, the discretized model must provide identical linear response as the non-discretized one. However, as it will be shown in Section 3.3 it allows to apply locally the nonlinear constitutive equations of the piezoelectricity with parameters that are independent of the in-plane geometry (shape) of the IDT's and reflectors.

Considering this, the previous distributed equivalent circuit models of Fig. 3.17 and Fig. 3.19 representing an unitary-cell of the NMR and MR regions respectively, can be analogously described in terms of a short transmission line using the T-circuit parameters of equations 3.48 and 3.49 as shown in Fig. 3.23.

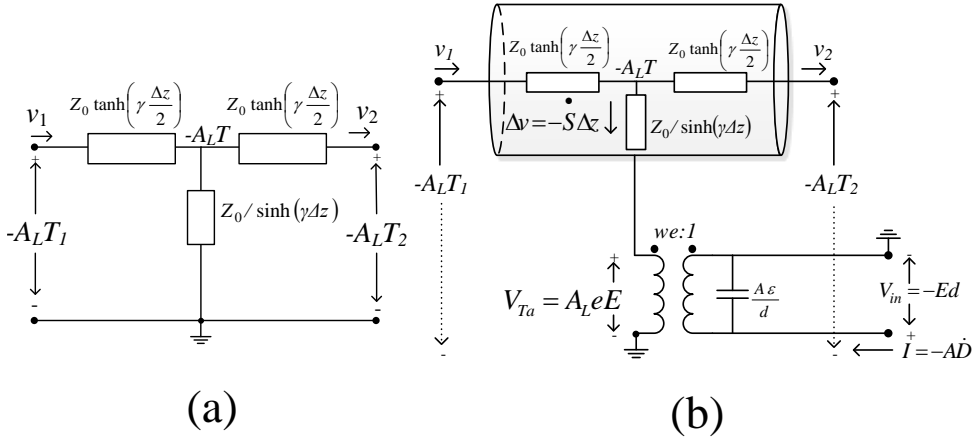


**Figure 3.23:** (a) Distributed linear equivalent circuit model for a NMR. (b) Distributed linear equivalent circuit model for a MR.

Furthermore, the unit-cell of a MR corresponding to Fig. 3.23(b) can be described in terms of the linear piezoelectric constitutive equations 2.38 and 2.39 of Chapter 2, which represents the relationship among the field magnitudes stress  $T$ , strain  $S$ , electric field  $E$  and electric flux density  $D$ .

Those equations are implemented in the equivalent circuit of the Mason model of Fig. 3.23(b), where the voltage represents the force  $F$ , and the current represents the particle velocity  $\Delta v$ , which are related with the variables of (2.38)-(2.39) following:

$$F = -T A_L \quad (3.50)$$

$$\Delta v = j\omega S \Delta z \quad (3.51)$$

where  $A_L$  is the electrode's lateral area defined previously. The acoustic wave propagates in the longitudinal direction, modeled as a simple acoustic transmission line. Finally, the terminal voltage and current on a piezoelectric plate of area  $A$  are found by equations 3.32 and 3.35.

### 3.2.5 Linear measurements

Prior to proceed with the nonlinear characterization of the devices, the linear model described in previous section must be able to reproduce the linear response of the resonators with different geometries or stack configuration. This is required to further reproduce the standing wave pattern of the fields along the structure at a given frequency, which will be used into the nonlinear model. Because of that, the linear distributed model uses a set of variables which not only depend on the piezoelec-

tric substrate (i.e the effective dielectric constant and piezoelectric constant) but also on the specific geometry of the transducers such as the aperture, the resonator pitch or the duty factor. Undoubtedly, since we are using a Mason-based equivalent circuit model, among the used variables in the model we can also find the acoustic impedance and phase velocities described in previous subsections and their corresponding associated variables.

Several one-port Leaky-SAW (LSAW) resonators for the Long Term Evolution (LTE) B66 band were measured. Those resonators cover a frequency range from 1.8 to 2.3 GHz and use the same LiTaO<sub>3</sub> substrate. From now on, we will refer to these resonators as Lithium-Tantalate (LT)-SAW. All the devices are composed by 100 electrode pairs ( $M = 100$ ) in the IDT region and 20 electrode pairs ( $R = 20$ ) in each reflector. The aperture is  $20\lambda$  with a variable pitch from 850 to 1100 nm and different duty factors. The tested devices are classified into 2 sets. The first set (Set 1) corresponds to six resonators with the same pitch (950 nm) and different duty factor from 40%, 45%, 50%, 55%, 60% and 65%. The second set (Set 2) is composed by four resonators with different pitch from 850 to 1100 nm and a duty factor of 50%. Note that all the details about the linear parameters used for the linear simulations can be found in Appendix D section D.1.1.

Table 3.1 shows the main linear parameters used, corresponding to the phase velocities for each region  $V_{MR}$  and  $V_{NMR}$ , the equivalent for the reflectors  $V_{MRr}$  and  $V_{NMRr}$ , the effective dielectric constant  $\epsilon_{r,eff}$  and the piezoelectric constant  $e$ . The last four rows correspond to the Set 2 resonators where P refers to the pitch and M to the duty factor in the used naming convention. With regard to Set 1, all the six resonators are simulated with the same parameters but the effective dielectric constant  $\epsilon_{r,eff}$ . The total capacitance of the IDT  $C_T$  is very roughly calculated using the simple expression

$$C_T = 2M \cdot \epsilon_{r,eff} \epsilon_0 \cdot \frac{A}{d} \quad (3.52)$$

where  $A$  and  $d$  correspond to the in-plane area of an electrode and the pitch, respectively. As discussed in previous sections, the relative dielectric constant must be considered as an effective parameter that is fine tuned for each resonator. Despite of this simple approach of the total IDT capacitance, this parameter is within the range between 47 and 50 for all the resonators with different duty factor (Set 1) while it scales very well with the pitch since  $\epsilon_{r,eff} = 48$  is used for all the Set 2 resonators.



**Table 3.1:** SAW resonators linear parameters.

Resonator	$V_{MR}$ [m/s]	$V_{NMR}$ [m/s]	$V_{MR_r}/$ $V_{MR}$ [m/s]	$V_{NMR_r}/$ $V_{NMR}$ [m/s]	$\epsilon_{r,eff}$	$e$
All Set 1	3904	4318	1.035	0.954	47-50	1.95
P850M50	3875	4318	1.035	0.954	48	1.95
P900M50	3888	4318	1.035	0.953	48	1.95
P1000M50	3916	4318	1.035	0.954	48	1.95
P1100M50	3939	4318	1.035	0.953	48	1.95

Note that all the parameters of Set 2 are the same than those of Set 1 but small differences (within  $\pm 0.9\%$ ) in the velocities of the MR sections. We consider than these small variations are reasonable due to the simplicity of the model that assumes uniform electric field beneath the electrodes.

The values of the velocities into the reflector regions are slightly tuned to reproduce the small spurious resonances appearing in the right side of the input admittance which corresponds with the SBUE. Note that these velocities have almost the same ratio respect to their counterparts of the active area. This slight difference could be explained by small influences of the electric field into the wave velocities in the MR and NMR.

Any parameter of a given resonator could be additionally fine-tuned to better reproduce the measurements. However, we decided to preserve the same parameters, but the ones mentioned above, to keep the simplicity of the model and demonstrate that despite of being a very simplified equivalent circuit, the model is consistent enough to reproduce the narrowband response of the resonators.

Note that bulk-wave radiation [78] is not considered into this model. As stated in [78], this effect has a significant impact on the admittance of 42-LT SAW resonators, and it has less impact as the number of IDT finger pairs increases. Although the resonators we have measured have many electrode pairs (100), that is the reason that might explain the disagreement at frequencies above the antiresonance, between the measurements and the simulations. However, as it will be discussed into the following Chapters, it does not have a significant impact into the in-band IMD3.

### *Narrowband measurements versus simulations*

Considering the previous set of linear parameters, the next step is to test if the linear model is able to reproduce both the narrowband and broadband linear response of the resonators. Figure 3.24 and Fig. 3.25 depicts the agreement of the measured (blue trace) input admittance and simulations (red trace) of the resonators corresponding to Set 1. Moreover, Fig. 3.25 shows also the agreement between the measured (blue trace) and simulated (red trace) phase response.

Note that in both Fig. 3.24 and Fig. 3.25 an artificial offset (a factor 1/10 per resonator and -10 degrees per resonator respectively) was added for easy viewing of the traces.

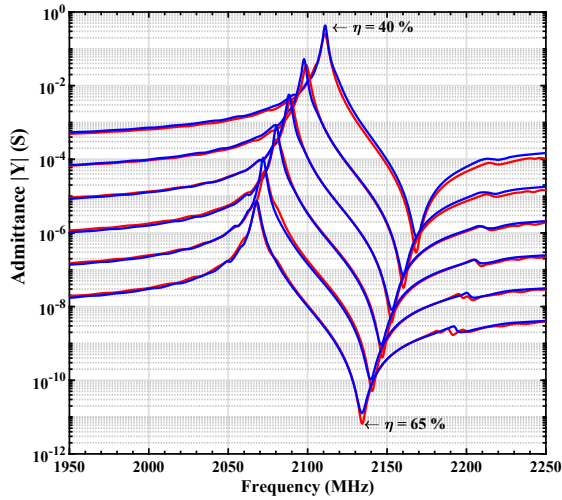


**Figure 3.24:** Measured (blue trace) and simulated (red trace) narrowband input admittance magnitude response of Set 1 resonators having same pitch and different duty factor.

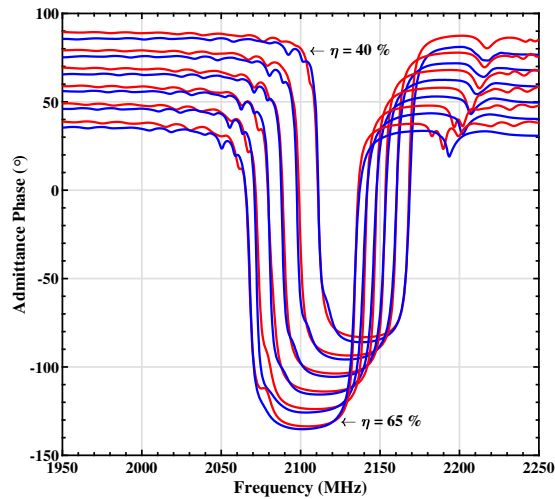


**Figure 3.25:** Measured (blue trace) and simulated (red trace) narrowband admittance phase response of Set 1 resonators having same pitch and different duty factor.

Furthermore, Fig. 3.26 and Fig. 3.27 depicts the agreement of measurements and simulations of resonators corresponding to Set 2. Again those figures are using the same artificial offset factor.

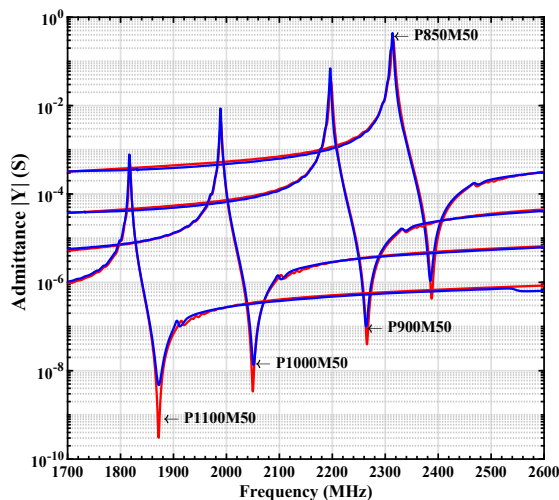


**Figure 3.26:** Measured (blue trace) and simulated (red trace) narrowband input admittance magnitude response of Set 2 resonators having fixed duty factor and variable pitch.

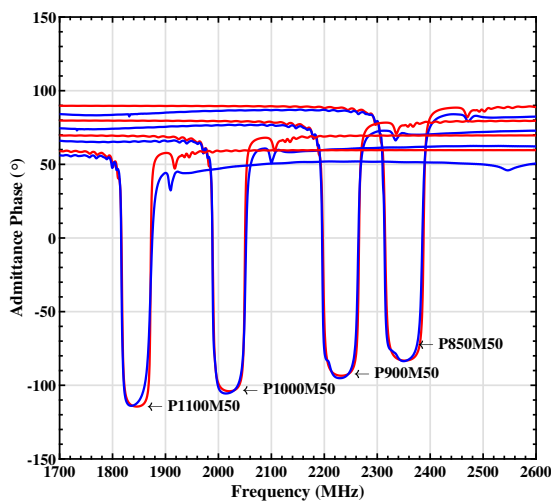


**Figure 3.27:** Measured (blue trace) and simulated (red trace) narrowband admittance phase response of Set 2 resonators having fixed duty factor and variable pitch.

For the completeness of the thesis we have also measured resonators with a different stack configuration. Moreover, this new set of resonators has a very important characteristic since they are temperature compensated TC-SAW resonators. Our main goal with this new measurements is to demonstrate that although a very simplified model is being used, the model is consistent enough even to reproduce the response of resonators with different stack configuration. Note that all the details about the linear parameters used for the linear simulations of TC-SAW resonators can be found in Appendix D section D.2.

Specifically, the simulations versus the measurements of three sets of TC-SAW resonators are shown below. In all cases, these are groups of resonators in which the pitch is variable and the duty factor is fixed. Fig. 3.28 and Fig. 3.29 show a group on resonators with variable pitches from [redacted] and a fixed [redacted]

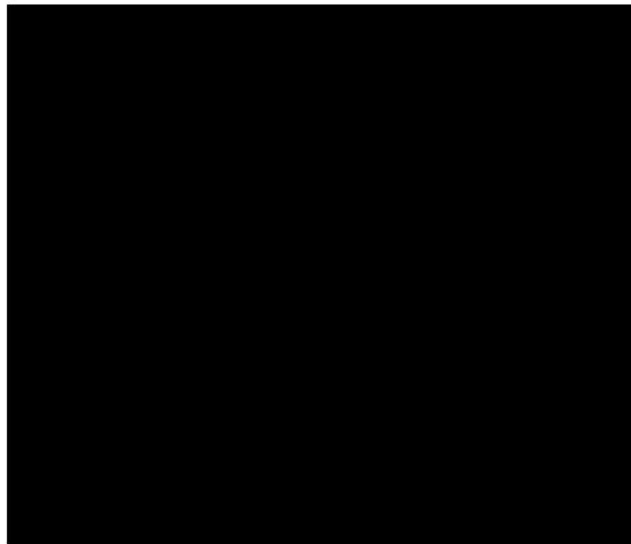


**Figure 3.28:** Measured (blue trace) and simulated (red trace) narrowband input admittance magnitude response of TC-SAW resonators having fixed duty factor of [redacted] and variable pitch.

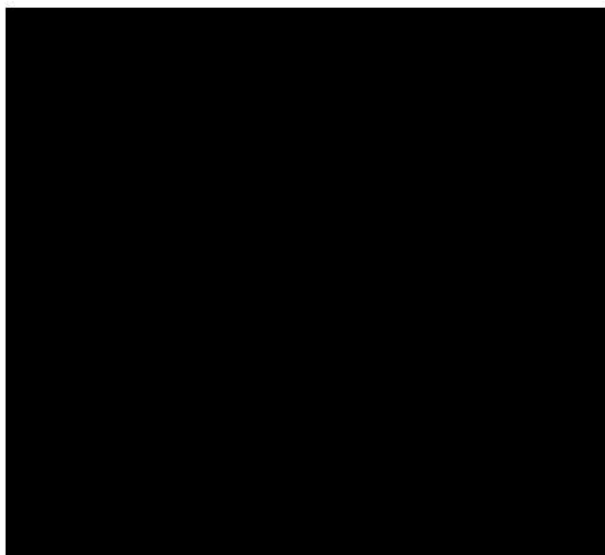


Figure 3.29: Measured (blue trace) and simulated (red trace) narrowband admittance phase response of TC-SAW resonators having fixed duty factor of [REDACTED] and variable pitch.

The following figures from Fig. 3.30 to Fig. 3.33 are identical but in those cases, using a duty factor of [REDACTED] respectively.

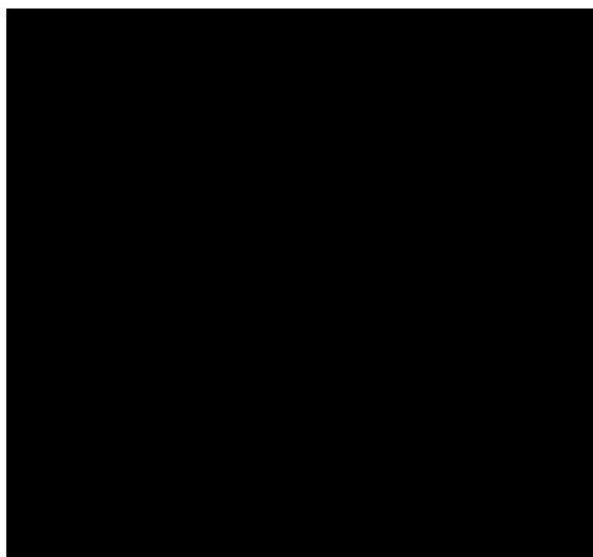
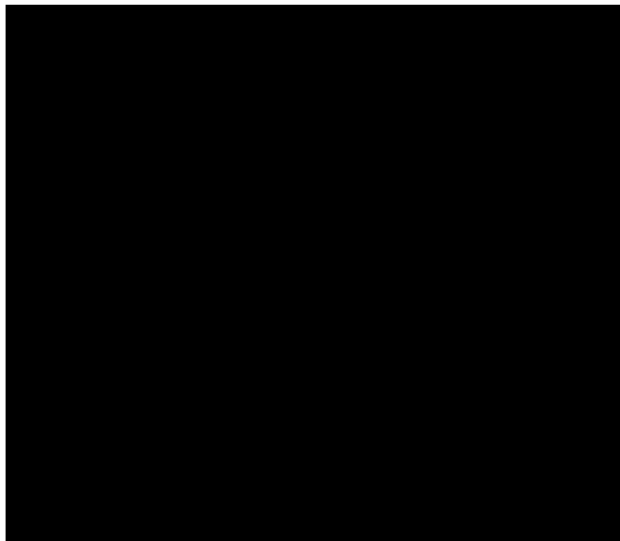


Figure 3.30: Measured (blue trace) and simulated (red trace) narrowband input admittance magnitude response of TC-SAW resonators having fixed duty factor of [REDACTED] and variable pitch.



**Figure 3.31:** Measured (blue trace) and simulated (red trace) narrowband admittance phase response of TC-SAW resonators having fixed duty factor of  $\frac{1}{2}$  and variable pitch.



**Figure 3.32:** Measured (blue trace) and simulated (red trace) narrowband input admittance magnitude response of TC-SAW resonators having fixed duty factor of  $\frac{1}{2}$  and variable pitch.

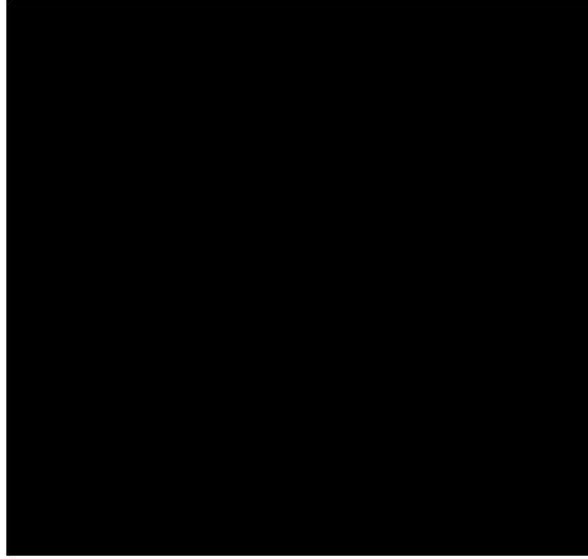


**Figure 3.33:** Measured (blue trace) and simulated (red trace) narrowband admittance phase response of TC-SAW resonators having fixed duty factor of  $\blacksquare$  and variable pitch.

As it can be seen in all the figures, there are a good agreement between simulations (red trace) and measurements (blue trace). With this last measurements we can conclude that the linear model is consistent and has no limitations on the narrowband modeling of resonators with different stack configuration.

### 3.3 Nonlinear discretized model

Further investigation of the nonlinear properties of SAW devices is needed to account for a full device modeling where the linear and nonlinear response is evaluated. Specifically, the previous linear distributed model will be extended to include the nonlinear behavior. The source of electro-acoustic nonlinearities has been widely studied in the past using equivalent circuit models. Although the generation of those nonlinear effects can be diverse, it can be explained using well-known piezoelectric constitutive nonlinear equations (Section 2.6). In our analysis, the crossed-field Mason circuit approach will be used. As explained in previous subsections, in this model the electric field distribution under the electrodes is approximated as being normal to the piezoelectric surface and it generates Rayleigh waves in a direction perpendicular to the excitation field.

The nonlinear circuit model is based on the one used in BAW [23, 24, 79]. Those references were based in the so-called in-line Mason model, in which the acoustic wave propagates in the same direction than the electric field. This significant difference, in comparison with the crossed-field model, leads to a different nonlinear model that was briefly introduced in [77] and is further discussed in this subsection.

### 3.3.1 Derivation of the crossed-field nonlinear discretized Model

Although the in-line model used in BAW resonators [23] and the crossed-field model for SAW devices are based on the same set of constitutive equations of Section 2.6, using as independent variables the electric field  $E$  and the strain  $S$ , the nonlinear source  $T_{NL}$  (see Fig. 3.34) of the crossed-field model does not depend on the nonlinear electrical displacement  $\Delta D$  defined in [23]. Moreover, the nonlinear source placed in the electrical part of the Mason model of Fig. 3.34 is a nonlinear current source  $I_{NL}$  instead of a voltage source (see dashed box of Fig. 3.34). The reason is that the in-line model of BAW devices uses  $D$  and  $S$  as independent variables and therefore it does not have a straightforward implementation from the constitutive equation as the cross-field model has. Note that since the distributed circuit model is based on the Mason model, the following equations are implemented considering that the voltage represents the force and the current the particle velocity, respectively.

#### Nonlinear discretized model of the MR section

Analogously as in the previous subsection, the nonlinear model is also discretized into many nonlinear unit-cells. Each nonlinear unit-cell of both NMR and MR section can be described using the previous piezoelectric constitutive equations (2.38), (2.39) if those become nonlinear by adding the terms  $\Delta T$  and  $\Delta D$  according to 2.40 and 2.41

$$T = c^E S - eE + \Delta T \quad (3.53)$$

$$D = eS + \varepsilon^S E + \Delta D \quad (3.54)$$

where, following the nomenclature of [24], these nonlinear terms  $\Delta T$  and  $\Delta D$ , truncated to a third-order polynomial, were already shown in equation 2.44 and we recall here to easy the readiness

$$\begin{aligned} \Delta T &= c_{2,MR}^E \frac{S^2}{2} + c_{3,MR}^E \frac{S^3}{6} - \phi_{3,MR} \frac{E^2}{2} + \phi_{5,MR} S E \\ &\quad - \chi_{9,MR} \frac{S^2 E}{2} + \chi_{7,MR} \frac{E^2 S}{2} + e_{3,MR}^E \frac{E^3}{6} \\ \Delta D &= \varepsilon_{2,MR}^S \frac{E^2}{2} + \varepsilon_{3,MR}^S \frac{E^3}{6} - \phi_{5,MR} \frac{S^2}{2} + \phi_{3,MR} S E \\ &\quad + \chi_{9,MR} \frac{S^3}{6} - \chi_{7,MR} \frac{S^2 E}{2} + e_{3,MR}^E \frac{S E^2}{2} \end{aligned} \quad (3.55)$$

being those nonlinear terms defined by several second-order ( $c_{2,MR}^E$ ,  $\phi_{3,MR}$ ,  $\phi_{5,MR}$ ,  $\varepsilon_{2,MR}^S$ ) and third-order ( $c_{3,MR}^E$ ,  $\varepsilon_{3,MR}^S$ ,  $\chi_{9,MR}$ ,  $\chi_{7,MR}$ ,  $e_{3,MR}^E$ ) coefficients.



To consider the previous nonlinear terms, it is necessary to extend the crossed-field Mason model as indicated in Fig. 3.34. This is the same circuit as described in previous section 3.2.2 with the linear model but adding the nonlinear sources. At the acoustic domain, we scale (3.53) by  $-A_L$  to obtain

$$-A_L T = -A_L c^E S + A_L e E - \Delta T A_L \quad (3.56)$$

and this equation is fulfilled in the Mason model of Fig. 3.34. The first two terms of left-hand side of the previous equation are the same as explained in the linear discretized model. The last term includes the nonlinear source, which corresponds to a nonlinear voltage source as is defined by

$$T_{NL} = \Delta T A_L \quad (3.57)$$

Note that (3.56) considers propagation without losses for simplicity. Losses, which are not included in Fig. 3.34, can be easily included considering a complex elastic constant in (3.56) as described in [18].



**Figure 3.34:** Nonlinear unit-cell of the MR section of an electrode.

In addition, scaling (3.54) by  $A$  the area of the electrode and taking its time derivative in phasor form we can write:

$$-j\omega DA = -j\omega eSA - j\omega \varepsilon^S EA - j\omega \Delta DA \quad (3.58)$$

The first terms of equation 3.58 are the same as for the linear discretized mode. Finally, the last term corresponds to the nonlinear source on the electrical domain. Besides, equation (3.58) indicates that an additional current source  $I_{NL}$  in parallel with the electrostatics capacitance must be included in the Mason model as depicted in Fig. 3.35 as is defined as

$$I_{NL} = -j\omega A \Delta D \quad (3.59)$$

Note that Fig. 3.35 represents the nonlinear unit-cell of the MR section of an electrode considering the previously defined nonlinear sources  $T_{NL}$  and  $I_{NL}$  and for the acoustic side, the T-network is considered analogously as a short transmission line with series and shunt impedance  $Z_s$  and  $Z_p$  respectively. Moreover, the T-network is equivalent to the LC T-network of Fig. 3.34 when the transmission line is electrically very short. However, due to the distributed character of the nonlinearity, the circuit of Fig. 3.35 must be only used for short transmission lines. The advantage of using Fig. 3.35 instead of Fig. 3.34 is that the transmission line cannot be discretized when the circuit is linearly solved, which makes easier the implementation of the code to solve the circuit as it will be seen in Chapter 4.

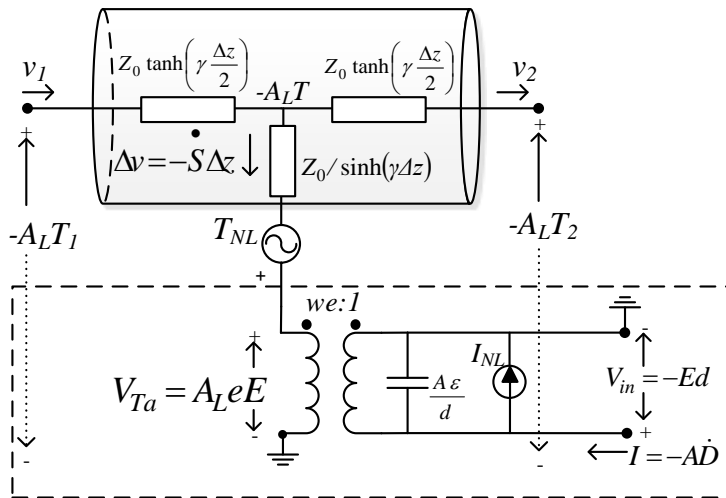


**Figure 3.35:** Nonlinear unit-cell of the MR section of an electrode with ATL.

Finally, the set of equations formed by equation 3.57 and equation 3.59 represent the nonlinear distributed sources of a MR section. In contrast with the in-line distributed model, the nonlinear source  $T_{NL}$  (see Fig. 3.34 and Fig. 3.35) of the crossed-field model, does not depend on the nonlinear electrical displacement  $\Delta D$  defined in [23] but only on the nonlinear stress  $\Delta T$ .

### Nonlinear discretized model of the NMR section

Furthermore, the equations and model of the NMR sections, whose unit-cell is depicted in Fig. 3.36 also considering a T-network, are much simpler as only acoustic wave propagation is considered. The nonlinear Hooke's law up to a third order expansion is:

$$T = cS + T_{NL} \quad (3.60)$$

$$T_{NL} = \frac{1}{2}c_{2,NMR}S^2 + \frac{1}{6}c_{3,NMR}S^3$$

where  $c$ ,  $c_{2,NMR}$  and  $c_{3,NMR}$  corresponds to the elastic constants of a given material and its corresponding nonlinear derivatives.

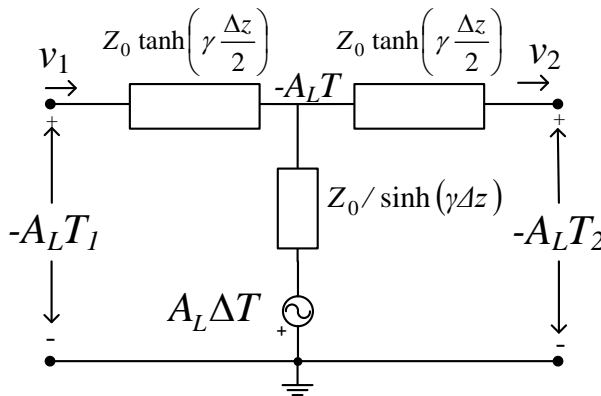


**Figure 3.36:** Nonlinear unit-cell of the NMR section.

### Modelling of a $\lambda$ -section

The active resonator's area can be represented using an equivalent circuit for an IDT composed of  $M$   $\lambda$ -sections as depicted in Fig. 3.37 (a). Moreover, Fig. 3.37 (b) shows a  $\lambda$ -section formed by two MR sections (two digits) and tree NMR sections

for the acoustic propagation. Note that the far right and left side boxes are denoted as NMR/2 just to illustrate that the length of those sections is half the separation between fingers since we are cascading identical  $\lambda$ -sections to form the IDT. MR and NMR sections are connected in cascade for the acoustic propagation and the two digits of a period are connected changing the polarity as depicted in Fig. 3.37 (b). Note that Fig. 3.37 depicts the specific case of a one-port resonator with one of the electrical ports connected to ground.

Finally, Figure 3.37 (c) shows how the MR and NMR are discretized into many unit-cells ( $N$ ) to account for the distributed nonlinear sources, which depend on the local field magnitudes.

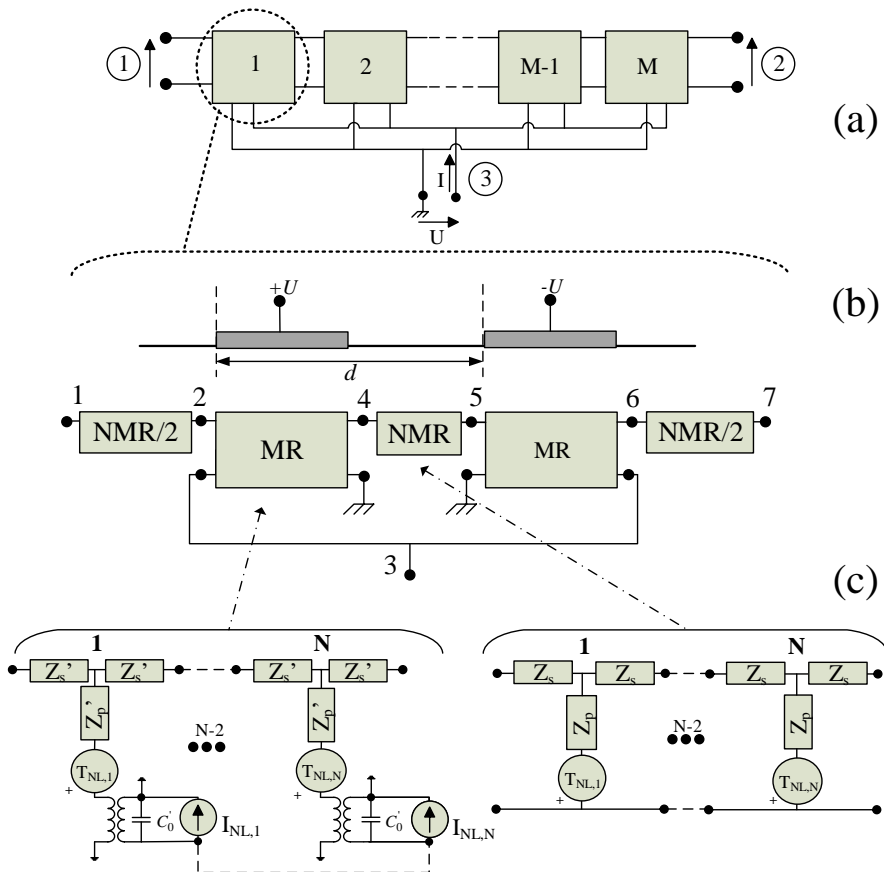


**Figure 3.37:** (a) Schematic of the reference SAW resonator for  $M$   $\lambda$ -sections connected acoustically in cascade and electrically in parallel. (b) Example of the equivalent circuit for a  $\lambda$ -section with two electrodes. (c) Both MR and NMR are composed of  $N$  nonlinear unit-cells.

### *Modelling of $M$ $\lambda$ -sections and reflectors*

The whole transducer is made up of  $M$   $\lambda$ -sections sections as Fig. 3.37 (a) depicts. The reflector can be also configured using the same scheme of Fig. 3.37 (a) and Fig. 3.37 (b) but keeping the electrical ports shorted. Then those subcircuits both  $M$   $\lambda$ -sections and  $R$  reflectors (see Fig. 3.20) will be cascaded by their top acoustical ports represented by port 1 and port 2 of Fig. 3.37 (a).

Therefore, if a resonator is comprised by, for example, one hundred  $\lambda$ -sections and let us assume that each  $\lambda$ -section requires at least 40 unit-cells (as it will be discussed in Chapter 4), the simulation of the discretized model (4.000 nonlinear unit-cells) using commercial software becomes unfeasible. In this context, it is worth to analyze the circuit using the IOES method we describe in the next chapter.

## Chapter 4

# Input-Output Equivalent Sources (IOES) method

### 4.1 Introduction

During the last years, it has been demonstrated that discretized circuit models are particularly useful to find the nonlinear material parameters that characterize the nonlinearities of BAW resonators [23, 24, 79, 80] according with well-known piezoelectric constitutive equations. The models are based on the nonlinear constitutive equations of the piezoelectricity, which are time-domain locally defined and then applied at any point of the circuit. As commented previously in Chapter 3, the use of discretized models are required to reproduce the standing wave pattern of the fields along the structure at a given frequency, since nonlinear effects, arise locally at each position of the structure depending of those field magnitudes. Sweeping the frequency of the excitation, each potential contributor (source of nonlinearity) causes a characteristic frequency pattern, which enables to discern between them [79]. This characterization process allows to find the geometry-independent nonlinear parameters, which only depend on the physical properties of the materials, contributing to the generation of a given spurious signal.

Unfortunately, the main drawback of the discretized approaches is that the number of nonlinear unit-cells to analyze can be considerable large increasing dramatically the computing time. While a solidly mounted resonator (SMR)-type BAW resonator is formed by 100 to 400 unit-cells [81], [82] -at least ten unit-cells per wavelength along the whole stack of materials- and distributed models can be analyzed by conventional HB simulations, the nonlinear analysis of a "discretized" SAW resonator is not a trivial task. A SAW resonator might be comprised by two hundred of digits, and therefore the total electrical length into the propagating direction could be one hundred wavelengths. Simulating several thousands of nonlinear unit-cells using commercial simulators is a very time-consuming task and might be

even unfeasible depending on the transducer length to be analyzed or when more complex structures are considered.

The main goal of this thesis is to define and use a characterization process in SAW resonators to find the nonlinear material parameters, which allows to predict the behavior of new devices with other geometries. To be successful in this process there are three key aspects that must be tackled:

1. The model must be distributed and directly related to local nonlinear constitutive equations commonly accepted by the scientific community.
2. The solution (nonlinear parameters) must be unique and able to explain the nonlinearities of resonators with different shape.
3. The method used to solve the problem must be rigorous, fast and applicable to solve more complicated circuits like filters or duplexers.
4. Then, this parameter (or parameters) can be used for predicting the nonlinear behavior of new resonators and filters using the same materials before manufacturing.

The model we will use is a discretized implementation of the well-known cross-field Mason model, which is directly related to the local constitutive equations of the piezoelectricity. Despite of its simplicity, it will be demonstrated that it is extremely consistent to simulate the in-band third order intermodulation of different resonators using only a few geometry-independent nonlinear parameters. Beyond the equivalent circuit, the main contribution of this work is the method we have developed to solve the circuit.

According to the Thevenin and Norton theorems, any n-port circuit with many internal linear voltages or current source has an equivalent circuit with only n-sources. This chapter describes the development of this new method for the simulation of both H and IMD generation in passive distributed circuits. The method is called the Input-Output Equivalent Sources (IOES) method and it allows to perform extremely fast and robust simulations of large distributed weak nonlinear circuits.

The method we describe in this chapter allows to find these equivalent current sources that, once placed at the boundary nodes of a given network with many internal sources will provide the same results. But the simplification of weak nonlinearities, this method is mathematically rigorous, it is not restricted to narrowband scenarios, and remix effects are also considered. Although the application of the IOES method was initially introduced to analyze BAW resonators [83], this chapter describes the application of this method particularly to SAW resonators and filters.

In this chapter, we include all the specific details of the IOES method to be applied to SAW resonators. Moreover, details of all the frequency-domain equations involved to evaluate the distributed model at each frequency of interest, including indirect effects (remix effects) are included. The nonlinear analysis of all the resonator structure including the reflectors is also considered.

To the best of our knowledge, this method is the only feasible method for the analysis of weak nonlinearities in SAW resonators without losing the full distributed nature of the problem with several distributed nonlinear sources per wavelength. Besides, validation of the characterization process considering simulations and measurements of many resonators with different stack configurations and different duty factors and pitches will be further discussed in Chapter 5.

## 4.2 Y-matrix analysis

This section explains the methodology carried out in the Matlab<sup>®</sup> implementation of the IOES method to simulate weak nonlinearities avoiding the HB algorithm. Basically, the IOES analysis is based in the admittance matrix description of the whole circuit. First, the admittance matrix for the different MR and NMR must be calculated. After that, details about the node connection between different sections that form a period is presented and, finally, the total Y-matrix of many periods is assembled.

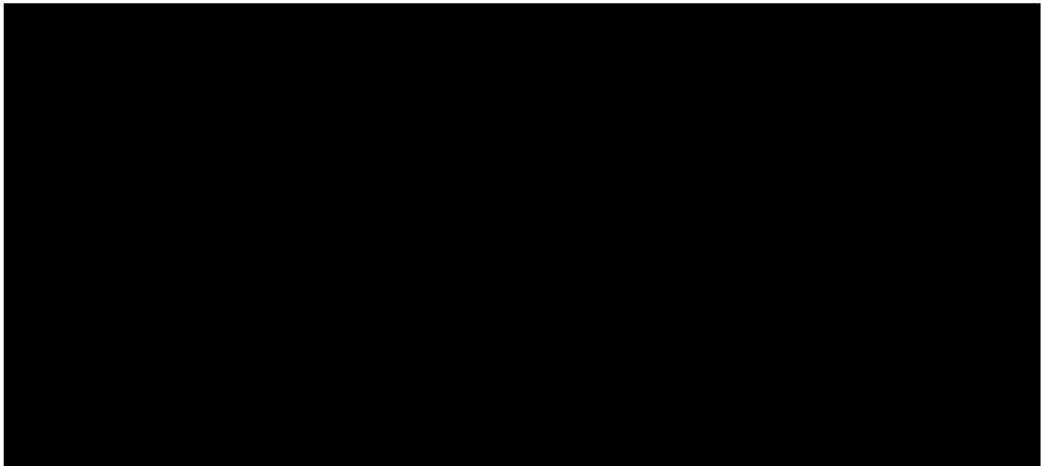
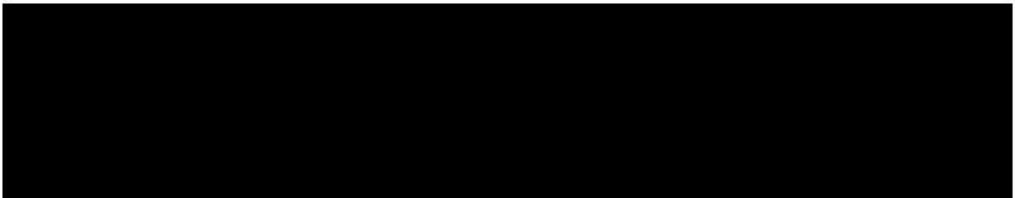


Figure 4.1: Example of a simplified block diagram of the Y-matrix blocks on an example IDT structure.



Moreover, although the IOES method could be applied to other nonlinear models previously described, we have developed it to simulate the reference distributed model described in Chapter 3, which basically consists on a Mason-based crossed-field model for the MR section and a nonlinear T-network for the NMR. The entire structure, both the IDT and the reflectors, is considered nonlinear.

### 4.2.1 Admittance matrix formulation

This subsection is devoted to present the admittance matrix formulation of the different MR and NMR.

#### NMR cell

The non-metallized cell is considered as an acoustic transmission line and modeled as a 2-port conventional T-network circuit following Fig. 4.2, whose admittance matrix is defined by the equation 4.1.

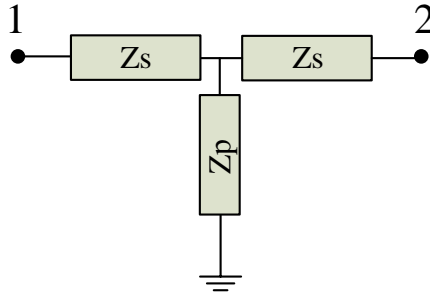


**Figure 4.2:** Schematic section of a NMR T-network.

$$Y_{NMR} = \frac{1}{z_s(2z_p + z_s)} \begin{bmatrix} z_p + z_s & -z_p \\ -z_p & z_p + z_s \end{bmatrix} \quad (4.1)$$

where  $z_s$  and  $z_p$  correspond to the series and shunt acoustic impedances and are defined in equation 3.48.

MR cell

In the case of the metallized cell, the 4-port crossed-field Mason model is considered having mechanical ports 1 and 2 and electrical ports 3 and 4 as depicted in Fig. 4.3, whose admittance matrix is given by equation 4.2.

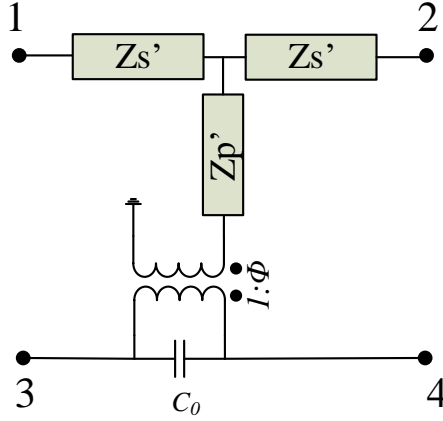


Figure 4.3: 4-Port MR crossed-field network.

$$Y_{MR} = \begin{bmatrix} \left(1 + \frac{z_{p'}}{z_{s'}}\right) \frac{1}{D} & \left(\frac{-z_{p'}}{z_{s'}}\right) \frac{1}{D} & \frac{\Phi}{D} & -\frac{\Phi}{D} \\ \left(\frac{-z_{p'}}{z_{s'}}\right) \frac{1}{D} & \left(1 + \frac{z_{p'}}{z_{s'}}\right) \frac{1}{D} & \frac{\Phi}{D} & -\frac{\Phi}{D} \\ \frac{\Phi}{D} & \frac{\Phi}{D} & \frac{2\Phi^2 + j\omega C_0(2z_{p'} + z_{s'})}{D} & -\frac{2\Phi^2 + j\omega C_0(2z_{p'} + z_{s'})}{D} \\ -\frac{\Phi}{D} & -\frac{\Phi}{D} & -\frac{2\Phi^2 + j\omega C_0(2z_{p'} + z_{s'})}{D} & \frac{2\Phi^2 + j\omega C_0(2z_{p'} + z_{s'})}{D} \end{bmatrix} \quad (4.2)$$

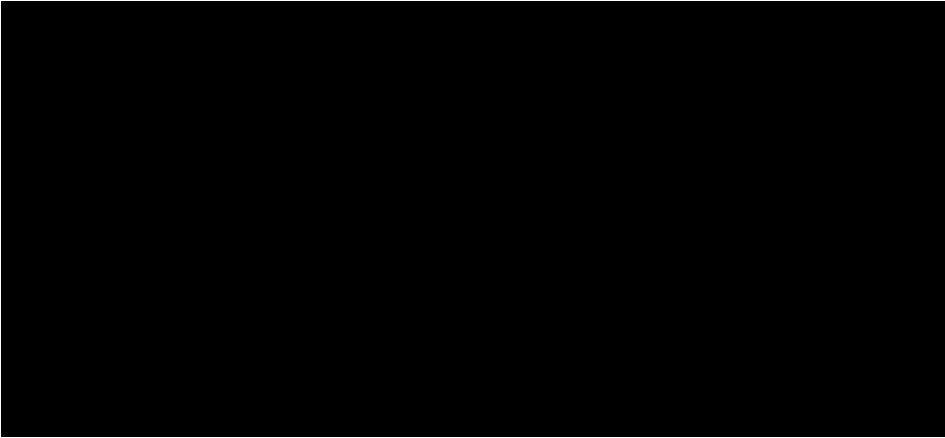
with  $D = (2z_{p'} + z_{s'})$  and where  $\Phi$  corresponds to the turn ratio of the transformer of Fig. 4.3 (see section 3.3.1) and  $C_0$  to the static capacitance defined in equation 3.52.

#### 4.2.2 Y-matrix block: node connection between different sections in Matlab<sup>®</sup>

The following subsection explains the different types of Y-matrix blocks that we have both in the reflector and in the IDT regions. The node numbering definition is described and examples of the connection between all the matrices are given.

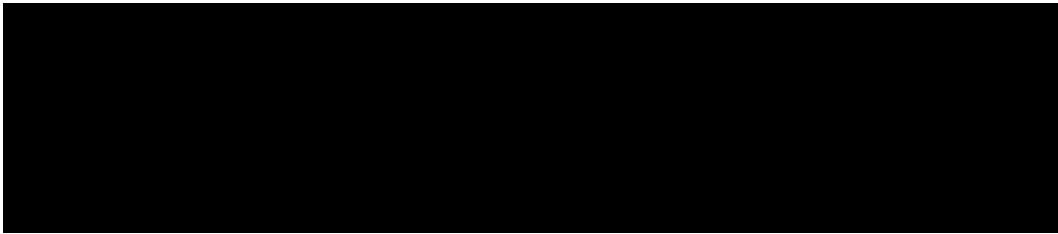
Reflector Y-matrix block

Fig. 4.4 shows the Y-matrix block of the reflector which [redacted]  
[redacted]  
[redacted] in Fig. 4.4 that basically is the matrix that will be further reproduced R-times.



**Figure 4.4:** Y-matrix block of reflector electrode that will be used R-times.

Fig. 4.5 shows an example if we consider a reflector section formed by two electrodes and the corresponding node numbering. [redacted]  
[redacted]



**Figure 4.5:** Y-matrix block of two reflector electrodes connection.

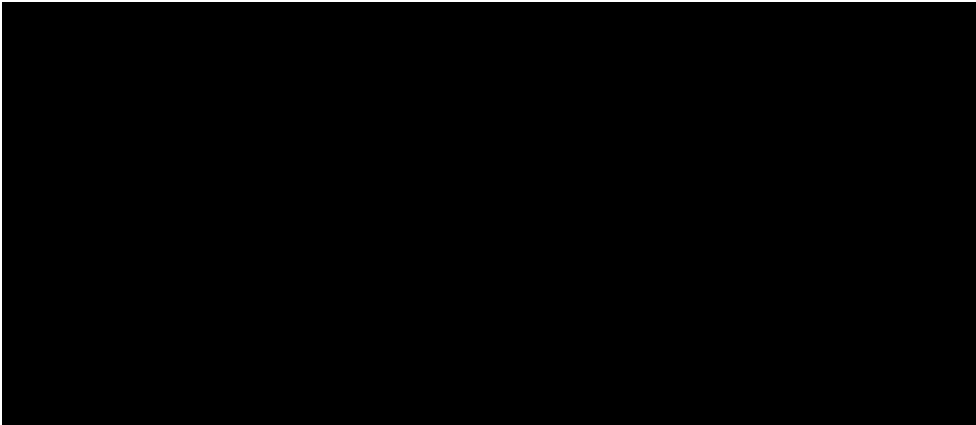
IDT Y-matrix block

Fig. 4.6 depicts the Y-matrix block of a  $\lambda$ -section of the IDT [redacted]. Basically, this matrix is made up by assembling the admittance matrix of each MR and NMR corresponding to Fig. 4.2 and Fig. 4.3 respectively. [redacted]



[redacted]. These five sections compose the IDT

$\lambda$ -section and stand for the "mY\_IDT matrix" that will be reproduced M-times.



**Figure 4.6:** Y-matrix block of IDT  $\lambda$ -sections that will be used M-times.

As this structure will be repeated



Moreover, Fig. 4.7 depicts an example considering an IDT formed by two  $\lambda$ -sections.

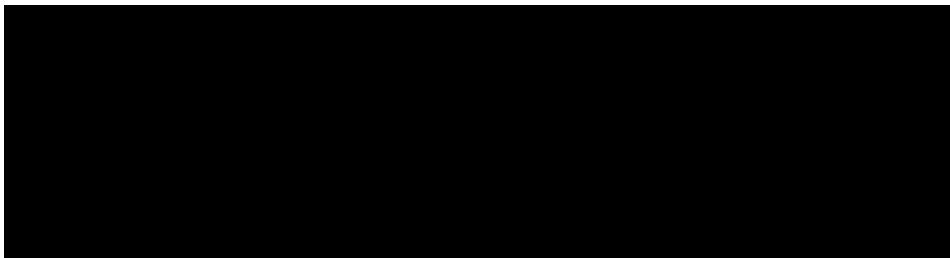


**Figure 4.7:** Example Y-matrix block of two IDT  $\lambda$ -sections connection.

Finally, Fig. 4.8 represent an entire one-port resonator formed by two  $\lambda/2$ -sections reflectors (like Fig. 4.5) on each side and a two  $\lambda$ -sections IDT (like Fig. 4.7) in the middle. Node numbering corresponds of the resulting nodes of the hole Y-matrix. Acoustic impedance is set at both ends to finish the structure whose value is set as the same as the acoustic impedance of a NMR of the reflector.

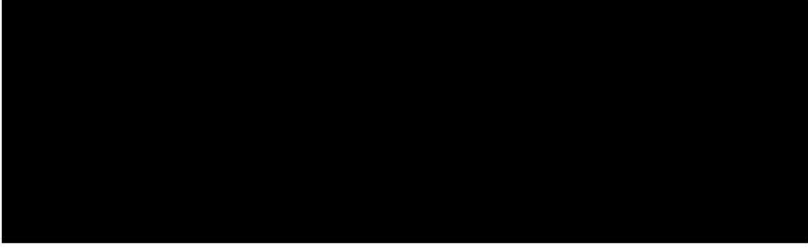


Figure 4.8: Example Y-matrix block of entire resonator structure, reflectors and IDT.

### 4.2.3 Y-block matrix algorithm

In order to connect the different types of matrices explained in the previous subsection two algorithms in Matlab<sup>®</sup> have been developed: one devoted to the creation of the Y-block matrix of the reflector and another one for the IDT section. Both of them have a set of conditions depending on the number of electrodes in the reflector and IDT region. Below it is summarized the flow diagrams for both reflector and IDT.

#### Reflector Y-matrix algorithm

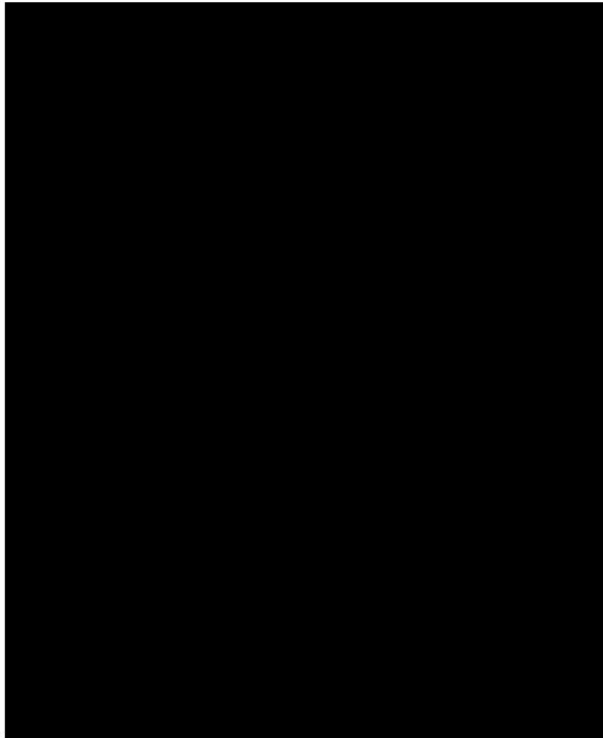
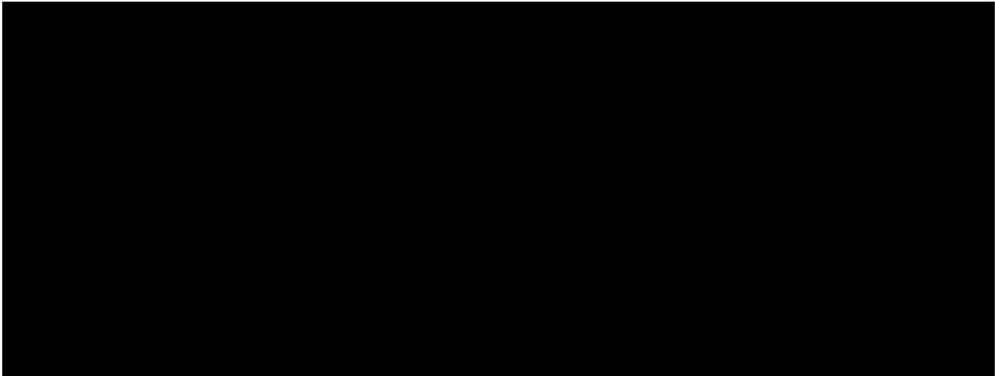


Figure 4.9: Reflector flowchart Y-matrix block algorithm.



#### IDT Y-matrix algorithm

At this point,  $mY\_total$  contains the left-hand side reflector. Therefore, the algorithm needs to add all the IDT structure to the  $mY\_total$  matrix.

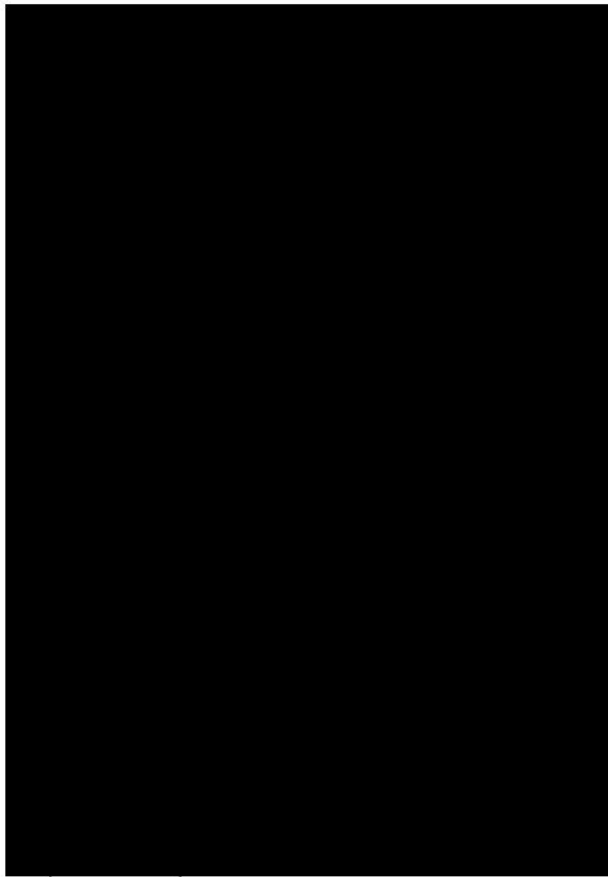


Figure 4.10: IDT flowchart Y-matrix block algorithm.

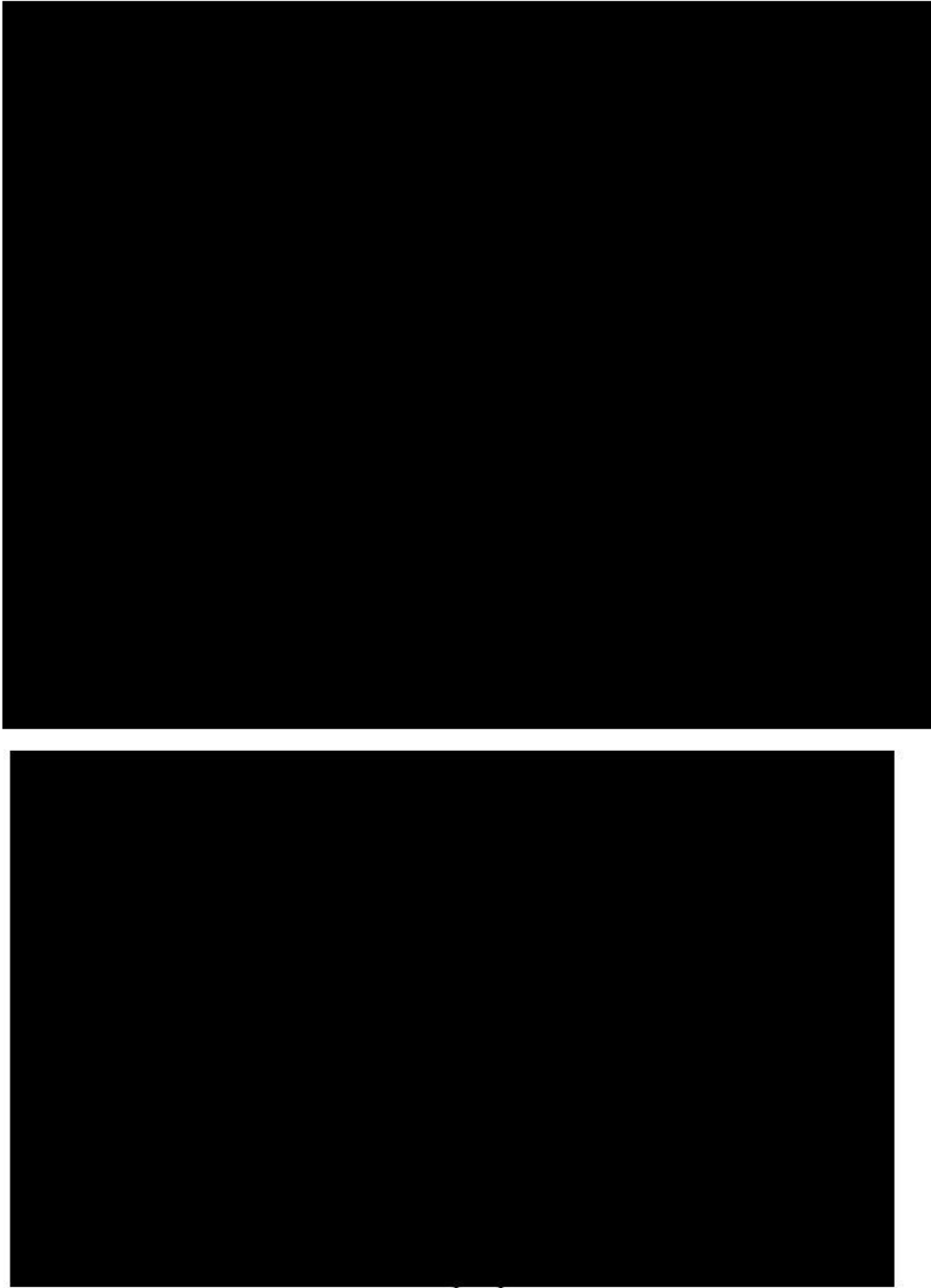


Figure 4.11: *Y*-matrix block of entire resonator structure including the measurement set-up.

Moreover, apart from the measurement system file we are also adding an ideal transmission line to account for the delay caused by the probe itself, which is not included into the calibration planes of the measurement system. To correct the small errors on the phase caused by the probe, it is necessary to add some electrical length in form of an ideal transmission line. If you want to perform one-tone measurements for example to get only the harmonics products, the procedure is the same but just using a 3-port Touchstone-type file and one fundamental tone.

### 4.3 Matlab<sup>®</sup> linear model

Below is the detailed step-by-step procedure of how the linear solution is done in the Matlab<sup>®</sup> IOES tool. Please note that details about the specific Matlab<sup>®</sup> functions are not disclosed due to confidential reasons. So the main steps for the linear algorithm will be the following:

```
[REDACTED]
```



It is important to outline that when the circuit is linearly solved, the circuit is **not discretized** so the size of the matrices is relatively small and the code is consequently very fast.

## 4.4 Input-Output Equivalent Sources (IOES)

### 4.4.1 Introduction

The analysis of large distributed problems has been previously reported for BAW in [83] by taking advantage of the weak nonlinear behavior of these passive devices. In distributed problems, the field magnitudes are found at any point of the discretized circuit, and the nonlinear sources of a given H or IMD are calculated in the frequency domain to, finally, analyze the circuit at those frequencies and to obtain the output power at the load. Moreover, the generation of the H's or IMD's might be caused by direct generation involving only the fundamental frequencies or by the so-called remix effects meaning that, for example, a generated IMD2 can be mixed with a fundamental signal to create an IMD3.

The procedure of the IOES method can be outlined as follows:

1. The whole resonator is linearly evaluated at the fundamental frequencies without discretizing the regions (like explained in the previous section). The magnitudes of interest -independent variables of the nonlinear equations- are then found at the boundaries of each region, in this case the strain and the electric field.
2. Using these boundary magnitudes, the standing wave patterns -field magnitudes strain  $S(z)$  and electric field  $E(z)$  at each position along the propagation direction- are mathematically calculated following conventional circuit analysis [84].
3. The distributed nonlinear sources at each position are then calculated for a given H or IMD in the frequency domain (weak nonlinear approach).
4. The corresponding IOES sources applied at the boundaries of each region -producing the same effect as all the distributed nonlinear sources- are then calculated. This is the crucial step of the method and the one of the main contributions of this thesis.
5. The non-discretized circuit is then analyzed at the targeted IMD/H frequencies using these IOES sources.

The following sections applies the IOES method to SAW resonators providing further details for its analysis. The main key aspects can be summarized as follows:

- All the equations required to obtain the field magnitudes at any point as a function of the boundary magnitudes are provided.

- Details of the frequency-domain equations of the nonlinear sources, including remix effects are given.
- The reflectors and the IDT region are considered nonlinear.
- An analysis of the required minimum number of unit-cells is shown to get shape-independent nonlinear parameters.
- Validation of the procedure by comparing with ADS<sup>®</sup> simulations of simpler IDT structures.

#### 4.4.2 IOES method step-by-step

This subsection is destined to describe in further detail the previous IOES procedure steps.

##### Step 1. Analyzing the non-discretized circuit

The non-discretized circuit is characterized by its admittance matrix denoted as  $[\mathbf{Y}_\omega]$  where  $\omega$  refers to each frequency component of interest. This admittance matrix is created by joining the matrix of each different region, which are calculated independently as explained in section 4.2. Then, the circuit is linearly analyzed at each fundamental frequency to obtain voltages and currents at the boundaries of each region. It is important to outline that, as the circuit is not fully discretized, this step is faster in comparison with evaluating the full discretized circuit as it was done in [80] or typically done with a commercial simulator using HB techniques.

##### Step 2. Standing wave pattern calculation

The voltages obtained at the boundaries of each section of the equivalent circuit (each of the nodes of Fig. 3.37 (b)) are used to calculate the field distribution as a function of the position  $z$  inside a given nonlinear section. The number of discrete positions is called the discretization number  $N$ .

###### 1. Non-Metallized Region

By use of the conventional microwave analysis [84], it can be demonstrated that the voltage (force) distribution along the NMR sections, as it corresponds to a conventional transmission line (TL), will be:

$$V(z) = \frac{V_1 e^{\gamma z_2} - V_2 e^{\gamma z_1}}{2 \sinh(\gamma(z_2 - z_1))} e^{-\gamma z} + \frac{V_1 e^{-\gamma z_2} - V_2 e^{-\gamma z_1}}{2 \sinh(\gamma(z_1 - z_2))} e^{\gamma z} \quad (4.3)$$

being  $V_1$  and  $V_2$  the voltages at the far left and right sides (positions  $z_1$  and  $z_2$  and  $\Delta z = z_2 - z_1$ ) of the TL, that is input and output nodes of the NMR section, and  $\gamma$  is the propagation constant associated to the NMR region.

After that, the strain at each point of the NMR section  $S(z)$  can be found considering the voltage at the junction of the T-network of Fig. 3.36, which is denoted as  $V_c(z)$  and  $c^E$  following:

$$S(z) = -\frac{V_c(z)}{A_L c^E} = -\frac{\left(V\left(z - \frac{\Delta z}{2}\right) + V\left(z + \frac{\Delta z}{2}\right)\right)}{2 \cosh^2\left(\gamma \frac{\Delta z}{2}\right) A_L c^E} \quad (4.4)$$

where,  $A_L$  is the lateral resonator area, and  $c^E$  is the elastic constant.

## 2. Metallized Region

For the MR section we will consider four boundary nodes, the ones corresponding to the acoustic part ( $V_1$  and  $V_2$ ) and the ones of the electrical part ( $V_3$  and  $V_4$ ). First, the voltage at the acoustic part of the transformer (Fig. 3.35) is calculated by using

$$V_{Ta} = \pm \Phi V_{in} \quad (4.5)$$

where  $\Phi = we$  is the transformer ratio of the Mason model of Fig. 3.35,  $V_{in}$  corresponds to the electrical input port of the electrodes (port 3 in Fig. 3.37(b)), and the sign  $\pm$  depends on the polarization of the electrodes in a  $\lambda$ -section. Therefore, knowing 4.5 and introducing it into 4.3 we get  $V(z)$ :

$$V(z) - V_{Ta} = \frac{(V_1 - V_{Ta})e^{\gamma z_2} - (V_2 - V_{Ta})e^{\gamma z_1}}{2 \sinh(\gamma(z_2 - z_1))} e^{-\gamma z} + \frac{(V_1 - V_{Ta})e^{-\gamma z_2} - (V_2 - V_{Ta})e^{-\gamma z_1}}{2 \sinh(\gamma(z_1 - z_2))} e^{\gamma z} \quad (4.6)$$

and the strain  $S(z)$  is calculated as it was done before using (4.4).

The electric field is found directly from the input voltage since the opposite electrical port to the input port is grounded (see Fig. 3.37(c)),

$$E(z) = \pm \frac{1}{d} V_{in} \quad (4.7)$$

where  $d$  is the spacing between electrode centers (pitch). Note that we assume that the electric field distribution is constant below the metallized regions. This is of course a rough approximation to a real interdigital transducer, but as it will be shown in later sections, this approach is good enough to model the IMD3 of SAW resonators. The circuit model could be extended to account for non-uniform electric fields, as it will be explained in section 5.4.6, but at first, we will try to keep the circuit model as simple as possible.

At this point, it is worth mentioning that the process to obtain the standing wave patterns at a targeted frequency for remix purposes is slightly different. The

nonlinear generators at an intermediate frequency must be taken into consideration when calculating the standing wave pattern at this intermediate frequency. The intermediate frequencies are those that are remixed with the fundamental tones to generate a targeted IMD3. This process is completely described in Appendix C.

### Step 3. Distributed nonlinear sources

A method based on Volterra series analysis is used to simulate weak nonlinear circuits [29]. Frequency-domain equations in the steady state provide closed-form mathematical expressions of a given H or IMD for weak nonlinearities.

#### 1. Direct generation

In the SAW case, third-order nonlinear signals like IMD3 or H3 are the main concern in terms of nonlinear distortion as H2 (or IMD2) generation have less impact due to its own cancelling nature [85], [86]. In this example we restrict the analysis to the IMD3 but similar equations can be easily found for other IMD or H product. The nonlinear equations related to the directly generated IMD's products in the MR due to the third order terms of equation (3.55) are

$$\begin{aligned}\Delta T_{2\omega_2-\omega_1} &= \frac{1}{8}c_{3,MR}^E S_{\omega_2}^2 S_{\omega_1}^* - \frac{3}{8}X_{9,MR} S_{\omega_2}^2 E_{\omega_1}^* \\ &\quad + \frac{3}{8}X_{7,MR} E_{\omega_2}^2 S_{\omega_1}^* - \frac{1}{8}e_{3,MR}^E E_{\omega_2}^2 E_{\omega_1}^* \\ \Delta D_{2\omega_2-\omega_1} &= \frac{1}{8}e_{3,MR}^S E_{\omega_2}^2 E_{\omega_1}^* + \frac{1}{8}X_{9,MR} S_{\omega_2}^2 S_{\omega_1}^* \\ &\quad - \frac{3}{8}X_{7,MR} S_{\omega_2}^2 E_{\omega_1}^* + \frac{3}{8}e_{3,MR}^E E_{\omega_2}^2 S_{\omega_1}^*\end{aligned}\quad (4.8)$$

where  $\omega_1$  and  $\omega_2$  correspond to the fundamental frequencies in a standard two-tone experiment, and  $\omega_2 > \omega_1$ . A similar expression could be written for the terms  $2\omega_1 - \omega_2$  (swapping the subscripts) and  $2\omega_1 + \omega_2$ ,  $2\omega_2 + \omega_1$ . In these two later cases none of the phasors  $S$  and  $E$  are conjugated [33]. For the case of the NMR sections the equation is much simpler and becomes:

$$\Delta T_{2\omega_2-\omega_1} = \frac{1}{8}c_{3,NMR} S_{\omega_2}^2 S_{\omega_1}^* \quad (4.9)$$

#### 2. Remix generation

All the second order H's and IMD's that could remix to cause third order IMD3 must be calculated. Those terms correspond to the frequencies  $2\omega_1$ ,  $2\omega_2$ ,  $\omega_2 - \omega_1$ ,  $\omega_1 + \omega_2$ . For the H2 case we will use the following equations for the MR section:

$$\Delta T_{2\omega_1} = \frac{1}{4}c_{2,MR}^E S_{\omega_1}^2 + \frac{1}{4}\phi_{3,MR} E_{\omega_1}^2 + \frac{1}{2}\phi_{5,MR} S_{\omega_1} E_{\omega_1} \quad (4.10)$$

$$\Delta D_{2\omega_1} = \frac{1}{4}\varepsilon_{2,MR}^S E_{\omega_1}^2 - \frac{1}{4}\phi_{5,MR} S_{\omega_1}^2 + \frac{1}{2}\phi_{3,MR} S_{\omega_1} E_{\omega_1} \quad (4.11)$$

and for the NMR section:

$$\Delta T_{2\omega_1} = \frac{1}{4}c_{2,NMR} S_{\omega_1}^2 \quad (4.12)$$

For the case of the IMD2  $\omega_2 - \omega_1$  we will use the following equations for the MR section:

$$\Delta T_{\omega_2 - \omega_1} = \frac{1}{2}\phi_{5,MR}(S_{\omega_2} E_{\omega_1}^* + E_{\omega_2} S_{\omega_1}^*) + \frac{1}{2}c_{2,MR}^E(S_{\omega_2} S_{\omega_1}^*) + \frac{1}{2}\phi_{3,MR}(E_{\omega_2} E_{\omega_1}^*) \quad (4.13)$$

$$\Delta D_{\omega_2 - \omega_1} = -\frac{1}{2}\phi_{5,MR}(S_{\omega_2} S_{\omega_1}^*) + \frac{1}{2}\varepsilon_{2,MR}^S(E_{\omega_2} E_{\omega_1}^*) + \frac{1}{2}\phi_{3,MR}(E_{\omega_2} S_{\omega_1}^* + E_{\omega_1}^* S_{\omega_2}) \quad (4.14)$$

and for the NMR section:

$$\Delta T_{\omega_2 - \omega_1} = \frac{1}{2}c_{2,NMR} S_{\omega_2} S_{\omega_1}^* \quad (4.15)$$

The terms of  $\omega_1 + \omega_2$  are straightforward obtained avoiding conjugating any phasor.

Once the whole circuit is evaluated for those second order H's and IMD's, the sources of IMD3 due to remix effects can be calculated considering all the combinations of frequencies that might contribute to a given IMD3. For example, the sources of IMD3 at  $2\omega_1 - \omega_2$  will be:

$$\begin{aligned} \Delta T_{2\omega_1 - \omega_2} &= \frac{1}{2}\phi_{5,MR}(S_{2\omega_1} E_{\omega_2}^* + S_{\omega_2}^* E_{2\omega_1} + S_{\omega_1} E_{\omega_1 - \omega_2}^* + S_{\omega_1 - \omega_2}^* E_{\omega_1}) \\ &+ \frac{1}{2}c_{2,MR}^E(S_{2\omega_1} S_{\omega_2}^* + S_{\omega_1} S_{\omega_1 - \omega_2}^*) - \frac{1}{2}\phi_{3,MR}(S_{2\omega_1} S_{\omega_2}^* + S_{\omega_1} S_{\omega_1 - \omega_2}^*) \end{aligned} \quad (4.16)$$

$$\begin{aligned} \Delta D_{2\omega_1 - \omega_2} &= -\frac{1}{2}\phi_{5,MR}(S_{2\omega_1} S_{\omega_2}^* + S_{\omega_1} S_{\omega_1 - \omega_2}^*) \\ &+ \frac{1}{2}\varepsilon_{2,MR}^S(E_{2\omega_1} E_{\omega_2}^* + E_{\omega_1} E_{\omega_1 - \omega_2}^*) \\ &+ \frac{1}{2}\phi_{3,MR}(S_{2\omega_1} E_{\omega_2}^* + S_{\omega_2}^* E_{2\omega_1} + S_{\omega_1} E_{\omega_1 - \omega_2}^* + S_{\omega_1 - \omega_2}^* E_{\omega_1}) \end{aligned} \quad (4.17)$$

and, correspondingly, for the NMR sections:

$$\Delta T_{2\omega_1 - \omega_2} = \frac{1}{2}c_{2,NMR}(S_{2\omega_1} S_{\omega_2}^* + S_{\omega_1} S_{\omega_1 - \omega_2}^*) \quad (4.18)$$

## Step 4. Input-Output Equivalent Sources

The input-output equivalent nonlinear currents sources are found applying a rigorous mathematical procedure. As mentioned before, these equivalent nonlinear sources cannot lose the distributed nature of the problem. The powerful of the IOES method consists of calculating the equivalent sources at given boundaries that account for all the distributed nonlinear sources between these boundaries. This can be done without inverting big matrices and the procedure is based on a 2-port ABCD matrix description of the NMR sections and a 4-port ABCD matrix description of the MR sections. Note that this 4-port ABCD matrix is defined explicitly to solve this specific problem since it is not a conventional ABCD matrix.

We will illustrate some steps of the process with the very simple circuit of Fig. 4.16.

### 1. IOES of a Non-Metallized Region

The linear circuit is analyzed at the fundamental frequencies of a source connected to the port  $V_{out}$  (node 3 in Fig. 4.16) getting all the voltages and currents associated to each boundary node.

As an example, let us assume that we want to calculate the nonlinear contribution of the central NMR just between the electrodes, that is between nodes 4 and 5 of Fig. 4.16. By means of equations 4.3 and 4.4, it is possible to calculate the strain  $S_{\omega_1}(z)$  and  $S_{\omega_2}(z)$  and then, to find the distributed nonlinear sources  $T_{NL}(z)$  at a given IMD following 4.9.

Now, the conventional 2-port ABCD relation between the voltage-current vector at the input and at the output of a transmission line (NMR unit-cell) of length  $\Delta z$  at the position  $z_i$  must be modified to include the corresponding nonlinear source at that position:

$$\begin{bmatrix} V_{1,i} \\ I_{1,i} \end{bmatrix} = [ABCD]_{\Delta z} \begin{bmatrix} V_{2,i} \\ I_{2,i} \end{bmatrix} + \begin{bmatrix} -\frac{z_{s,i}}{z_{p,i}} \\ z_{p,i} \\ 1 \\ -\frac{z_{p,i}}{z_{p,i}} \end{bmatrix} T_{NL}(z_i) \quad (4.19)$$

where  $[ABCD]_{\Delta z}$  is the conventional ABCD matrix of a TL of length  $\Delta z$  and  $z_{s,i}$  and  $z_{p,i}$  are the series and shunt acoustic impedance of the T-network of Fig. 4.2. Note that both  $z_{s,i}$  and  $z_{p,i}$  are always the same (for any  $i$  value) and corresponds to one unit-cell, therefore from now on, they will be denoted as  $z_s$  and  $z_p$  for simplification, so equation 4.19 can be rewritten as

$$\begin{bmatrix} V_{1,i} \\ I_{1,i} \end{bmatrix} = \begin{bmatrix} \frac{z_s}{z_p} + 1 & \frac{z_s^2}{z_p} + 2z_s \\ \frac{1}{z_p} & \frac{z_s}{z_p} + 1 \end{bmatrix}_{\Delta z} \begin{bmatrix} V_{2,i} \\ I_{2,i} \end{bmatrix} + \begin{bmatrix} -\frac{z_s}{z_p} \\ z_p \\ 1 \\ -\frac{1}{z_p} \end{bmatrix} T_{NL}(z_i) \quad (4.20)$$

This description of an unit-cell allows to cascade  $N$  identical cells as pictured in Fig. 4.12, obtaining

$$\begin{aligned} \begin{bmatrix} V_1 \\ I_1 \end{bmatrix} &= [ABCD]_{\Delta z}^N \begin{bmatrix} V_{N+1} \\ I_{N+1} \end{bmatrix} \\ &+ \left( [ABCD]_{\Delta z}^{N-1} T_{NL,N} \right. \\ &\left. + [ABCD]_{\Delta z}^{N-2} T_{NL,N-1} + \dots + T_{NL,1} I_{2 \times 2} \right) [EF]_{\Delta z} \end{aligned} \quad (4.21)$$

where  $[EF]_{\Delta z}$  is a column vector having the coefficients (named  $E$  and  $F$ ) corresponding to the terms multiplying  $T_{NL}(z_i)$  in equation 4.20 and, we are denoting  $T_{NL}(z_i)$  as  $T_{NL,i}$ . The matrix  $I_{2 \times 2}$  refers to the 2-by-2 identity matrix. Note that in each side of the equation 4.21 there is only one input and output port, therefore the port sub-index can be omitted and the resulting equation shows only the cell-index.

Despite the mathematical procedure is not straightforward due to the addition of the nonlinear source, it results in a very simple expression that relates the V-I input vector with the V-I output vector as:

$$\begin{bmatrix} V_1 \\ I_1 \end{bmatrix} = [ABCD]_{\Delta z}^N \begin{bmatrix} V_{N+1} \\ I_{N+1} \end{bmatrix} + \begin{bmatrix} V_{eq} \\ I_{eq} \end{bmatrix} \quad (4.22)$$

where

$$\begin{aligned} \begin{bmatrix} V_{eq} \\ I_{eq} \end{bmatrix} &= \left( [ABCD]_{\Delta z}^{N-1} T_{NL,N} \right. \\ &\left. + [ABCD]_{\Delta z}^{N-2} T_{NL,N-1} + \dots + T_{NL,1} I_{2 \times 2} \right) [EF]_{\Delta z} \end{aligned} \quad (4.23)$$

The terms  $V_{eq}$  and  $I_{eq}$  accounts for the contribution of all the distributed nonlinear sources and note that the matrix  $[ABCD]_{\Delta z}^N = [ABCD]_{N\Delta z}$  of equation (4.22) is the one that corresponds to the conventional  $ABCD$  matrix of the whole section (a TL of length  $N\Delta z$ ), which can be easily calculated without multiplying the matrices of the  $N$  unit-cells.

Note that when we calculate the equivalent sources of equation (4.23), the powers of the  $ABCD$  matrix are not calculated by multiplying matrices but directly calculated changing the length of the TL as for example  $[ABCD]_{\Delta z}^{N-1} = [ABCD]_{(N-1)\Delta z}$ , which significantly reduces the computing time. Moreover, we use a matrix operation to calculate these equivalent sources of (4.23). In the case of the NMR section, this matrix operation is as follows:

$$\begin{bmatrix} V_{eq} \\ I_{eq} \end{bmatrix} = \begin{bmatrix} 1 & A_1 & \dots & A_{N-1} & 0 & B_1 & \dots & B_{N-1} \\ 0 & C_1 & \dots & C_{N-1} & 1 & D_1 & \dots & D_{N-1} \end{bmatrix} \begin{bmatrix} E \cdot T_{NL,1} \\ \vdots \\ E \cdot T_{NL,N-1} \\ E \cdot T_{NL,N} \\ F \cdot T_{NL,1} \\ \vdots \\ F \cdot T_{NL,N-1} \\ F \cdot T_{NL,N} \end{bmatrix} \quad (4.24)$$

where the parameters  $A_i, B_i, C_i, D_i$  are calculated accordingly to their subscript that indicates the length  $i\Delta z$ , where  $i = 1 \dots N$ .

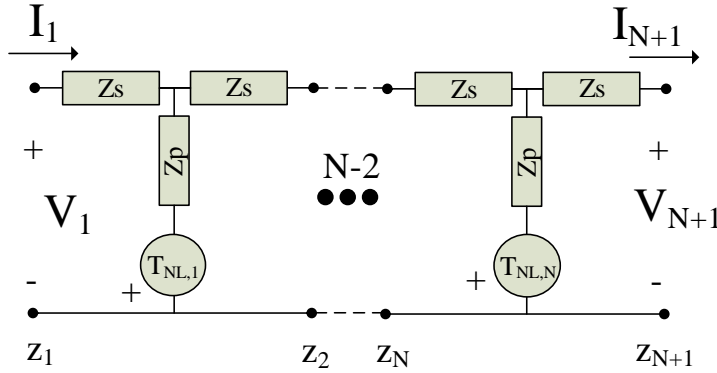


**Figure 4.12:** V-I definition for the ABCD matrix description of a non-metallized region. Example of connection of N unit-cells.

Certainly, 4.22 could be used to evaluate an equivalent circuit that concentrates all the nonlinearities in two equivalent sources (Fig. 4.13(a)). Nevertheless, and due to the use of the Y-matrix description of the whole circuit, it is more convenient to turn these two sources  $V_{eq}, I_{eq}$  into two current sources  $I_{e1}, I_{e2}$  as depicted in Fig. 4.13(b).



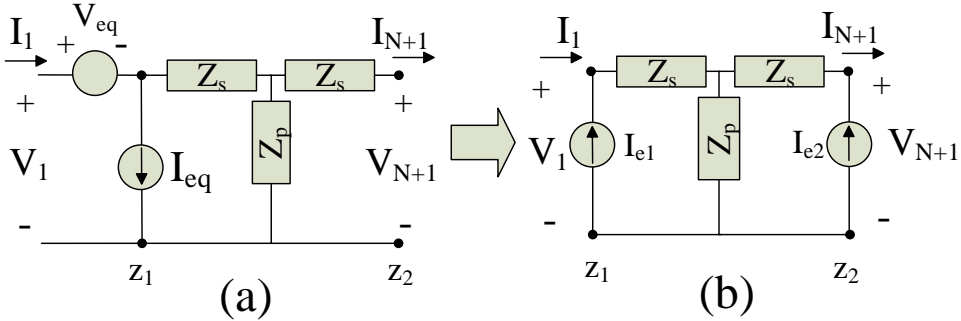


**Figure 4.13:** Equivalent current sources of a non-metallized region.

This can be done by means of

$$I_{e1} = \frac{1}{z_s + 2z_p} \left( 1 + \frac{z_p}{z_s} \right) V_{eq} - I_{eq} \quad (4.25)$$

$$I_{e2} = \frac{1}{z_s + 2z_p} \left( -\frac{z_p}{z_s} \right) V_{eq}$$

where  $z_s$  and  $z_p$  correspond to the whole section of length  $N\Delta z$ . Note that the impedance  $z_s$  and  $z_p$  of Fig. 4.12 has the same nomenclature but are different since it represent the impedance of a unit-cell and not the whole section  $N\Delta z$  as in this later case.

## 2. IOES of a Metallized Region

Analogously to the NMR sections, the voltages and currents that are found at the four nodes of the MR section (see Fig. 3.37 (b)) will allow to calculate the independent variables  $S(z)$  and  $E(z)$  (see section 4.4.2) to further find the nonlinear sources  $T_{NL}(z)$  and  $I_{NL}(z)$  for a given H or IMD following equations 3.57, 3.59 and 4.8.

The IOES of the MR sections and its associated pseudo-ABCD matrix equations are described bellow. The procedure is the same than the one described for the NMR sections and all the steps involved are detailed in the following equations for completeness of this chapter.

Firstly, as it was done for the NMR sections, we will use equation 4.26 as a result of the circuitual analysis of the crossed-Field Mason model of Fig. 4.14. This equation relates the input and output voltages and currents to define a so-called 4-port ABCD matrix following

$$\begin{aligned}
 \begin{bmatrix} V_{1,i} \\ I_{1,i} \\ V_{3,i} \\ I_{3,i} \end{bmatrix} &= \begin{bmatrix} \frac{z_{s'} + 1}{z_{p'}} & \frac{z_{s'}^2 + 2z_{s'}}{z_{p'}} & \frac{z_{s'}T}{z_{p'}} & 0 \\ 1 & z_{s'} + 1 & T & 0 \\ \frac{z_{p'}}{z_{p'}} & \frac{z_{p'}}{z_{p'}} & \frac{z_{p'}}{z_{p'}} & 0 \\ T & 0 & 1 & 0 \\ \frac{T}{z_{p'}} & \frac{z_{s'}T}{z_{p'}} & \frac{T^2}{z_{p'}} + j\omega C_0 & 1 \end{bmatrix} \begin{bmatrix} V_{2,i} \\ I_{2,i} \\ V_{4,i} \\ I_{4,i} \end{bmatrix} \\
 &+ \begin{bmatrix} -\frac{z_{s',i}}{z_{p',i}} \\ \frac{z_{p',i}}{z_{p',i}} \\ 1 \\ -\frac{z_{p',i}}{z_{p',i}} \\ 0 \\ T \\ -\frac{z_{p',i}}{z_{p',i}} \end{bmatrix} T_{NL}(z_i) + \begin{bmatrix} 0 \\ 0 \\ 0 \\ 1 \end{bmatrix} I_{NL}(z_i)
 \end{aligned} \tag{4.26}$$

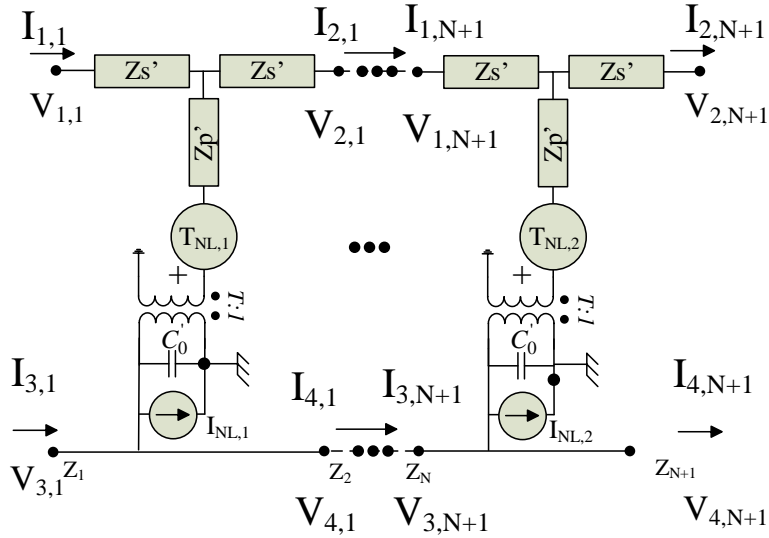


**Figure 4.14:** I-V definition of cascading 4-ABCD matrices of a MR section with only two unit-cells.

And we can rewrite equation 4.26 considering many unit-cells as in Fig. 4.14 following

$$\begin{aligned}
 \begin{bmatrix} V_{1,1} \\ I_{1,1} \\ V_{3,1} \\ I_{3,1} \end{bmatrix} &= [4ABCD]_{\Delta z}^N \cdot \begin{bmatrix} V_{2,N+1} \\ I_{2,N+1} \\ V_{4,N+1} \\ I_{4,N+1} \end{bmatrix} \\
 &+ \left( [4ABCD]_{\Delta z}^{N-1} T_{NL,N} + [4ABCD]_{\Delta z}^{N-2} T_{NL,N-1} \right. \\
 &\left. + \dots + T_{NL,1} I_{4x4} \right) [EFGH]_{\Delta z} + \left( \sum_{i=1}^N I_{NL,i} \right) \begin{bmatrix} 0 \\ 0 \\ 0 \\ 1 \end{bmatrix}
 \end{aligned} \tag{4.27}$$

where  $[4ABCD]_{\Delta z}^N$  is the lineal 4-port ABCD matrix of a differential  $\Delta z$  section of the  $N$   $\lambda$ -sections, and the right terms are added terms that affect the relation between input magnitudes (Port 1) with output magnitudes (Port  $N+1$ ) depending on the nonlinear sources  $T_{NL,i}$  and  $I_{NL,i}$ . Note that  $[EFGH]_{\Delta z}$  corresponds to a column vector multiplying  $T_{NL}(z_i)$  in equation 4.26 and,  $I_{4x4}$  refers to the 4-by-4 identity matrix. If we reformulate the equation 4.27 we obtain

$$\begin{bmatrix} V_{1,1} \\ I_{1,1} \\ V_{3,1} \\ I_{3,1} \end{bmatrix} = [4ABCD]_{\Delta z}^N \cdot \begin{bmatrix} V_{2,N+1} \\ I_{2,N+1} \\ V_{4,N+1} \\ I_{4,N+1} \end{bmatrix} + \begin{bmatrix} V_{1,eq} \\ I_{1,eq} \\ 0 \\ I_{3,eq} \end{bmatrix} \tag{4.28}$$

$$\begin{aligned}
 \begin{bmatrix} V_{1,eq} \\ I_{1,eq} \\ 0 \\ I_{3,eq} \end{bmatrix} &= \left( [4ABCD]_{\Delta z}^{N-1} T_{NL,N} + [4ABCD]_{\Delta z}^{N-2} T_{NL,N-1} \right. \\
 &\left. + \dots + T_{NL,1} I_{4x4} \right) [EFGH]_{\Delta z} + \left( \sum_{i=1}^N I_{NL,i} \right) \begin{bmatrix} 0 \\ 0 \\ 0 \\ 1 \end{bmatrix}
 \end{aligned} \tag{4.29}$$

Note that the previous formulation preserves  $V_{3,1} = V_{4,N+1}$  because the circuit is considered electrically small.

In this case, the corresponding equivalent sources are as shown in Fig. 4.15 left. As it was done for the NMR, we are interested in all current source's solution (Fig. 4.15 right).

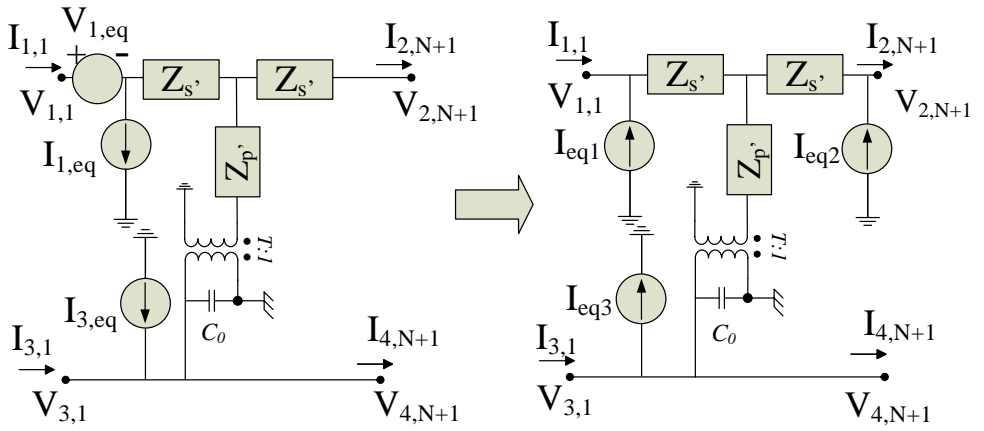


Figure 4.15: IOES of a MR section.

Therefore, the corresponding equations explaining the relation between the equivalent sources are as follows

$$I_{eq1} = \left( \frac{z_{p'}}{z_{s'}} + 1 \right) \frac{V_{1,eq}}{\left( \frac{z_{s'}^2}{z_{p'}} + 2z_{s'} \right)} - I_{1,eq} \quad (4.30)$$

$$I_{eq2} = - \frac{V_{1,eq}}{\left( \frac{z_{s'}^2}{z_{p'}} + 2z_{s'} \right)}$$

$$I_{eq3} = \left( \frac{Tz_{p'}}{z_{s'}} \right) \frac{V_{1,eq}}{\left( \frac{z_{s'}^2}{z_{p'}} + 2z_{s'} \right)} - I_{3,eq}$$

Finally, Fig. 4.16 shows the IOES of a  $\lambda$ -section (only sources of one MR and one NMR are shown for clearness of the figure). The currents that apply to the same boundary nodes (Fig. 3.37 (b)) are added to form a vector of source currents  $[I_\omega]_{7 \times 1}$ . This vector of currents is then used to get the node voltages at each node by means of the admittance matrix  $[\mathbf{Y}_\omega]_{7 \times 7}$ . Note that details of how this admittance matrix has been built up can be found in section 4.2 and Appendix A.

$$[V_\omega]_{7 \times 1} = [\mathbf{Y}_\omega]_{7 \times 7}^{-1} \cdot [I_\omega]_{7 \times 1} \quad (4.31)$$

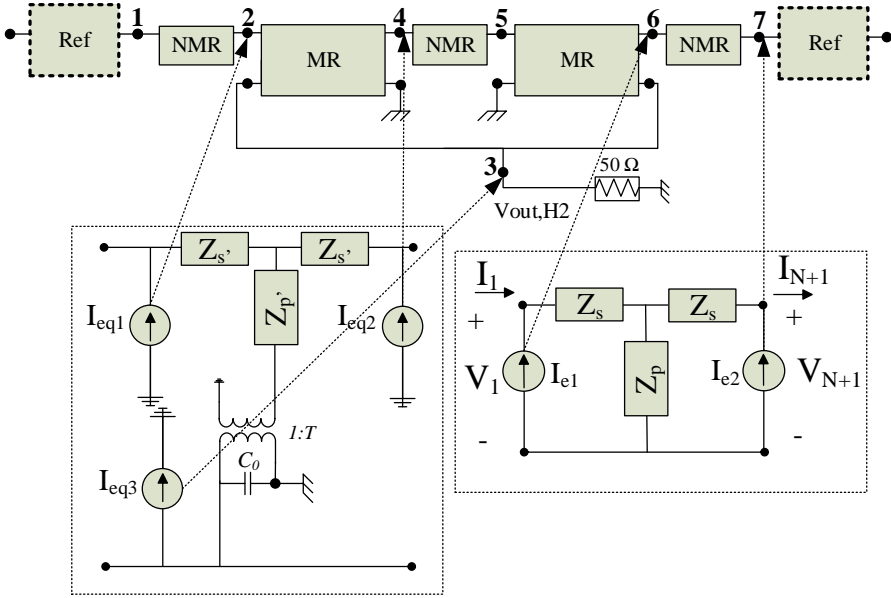


**Figure 4.16:** IOES of both MR and NMR applied to a  $\lambda$ -section.

### 3. IOES method for $M$ $\lambda$ -sections

Once the analysis of a  $\lambda$ -section has been derived, we can cascade  $M$  times the  $\lambda$ -section to analyze the full response of a given resonator. The result is a new admittance matrix  $[\mathbf{Y}_\omega]_{(5 \cdot M + 2) \times (5 \cdot M + 2)}$  that is built up from the admittance matrices of the  $\lambda$ -sections just considering that the last and first acoustic nodes of each consecutive section must be connected and all the electric nodes of each section must be connected to the same input node corresponding to the node 3 of Fig. 3.37.

When the whole non-discretized circuit is evaluated for the fundamental frequencies, the IOES equivalent sources of each section can be calculated as described in the previous sections. Note again, that the nonlinear current sources of two  $\lambda$ -sections that are connected to a given node must be added to get finally the  $5 \cdot M + 2$  vector of currents at a targeted IMD or H.

### 4. IOES method for SAW resonators: IDT and reflectors

Following the same process described for the IDT, we can cascade  $R$  times  $\lambda/2$ -sections of the reflector with 4 additional nodes per section. The result is a new admittance matrix  $[\mathbf{Y}_{(r,\omega)}]_{P \times P}$  of dimension  $P = 2(3 \cdot R + 1) + (5 \cdot M + 2) - (2)$  the first addend considers the reflectors on each side of the IDT, the second addend the IDT section, and the last addend accounts for the common nodes between IDT and reflectors.

At this point, we outline that the maximum dimension of the matrix to be inverted is  $P$ , instead of  $N \cdot P$  as it would correspond to the whole solution without using the IOES method, resulting in a drastic reduction of the computing time.

### 4.4.3 Matlab<sup>®</sup> nonlinear model

In this section the nonlinear solving work-flow will be summarized. As we have done previously with the linear solution, it is necessary to properly connect the nonlinear unit-cells of each MR and NMR and then, perform the calculations following the steps detailed in Section 4.4.2. Nevertheless, we will have to consider, in the case of the IDT zone, the conditions of polarization change between electrodes.

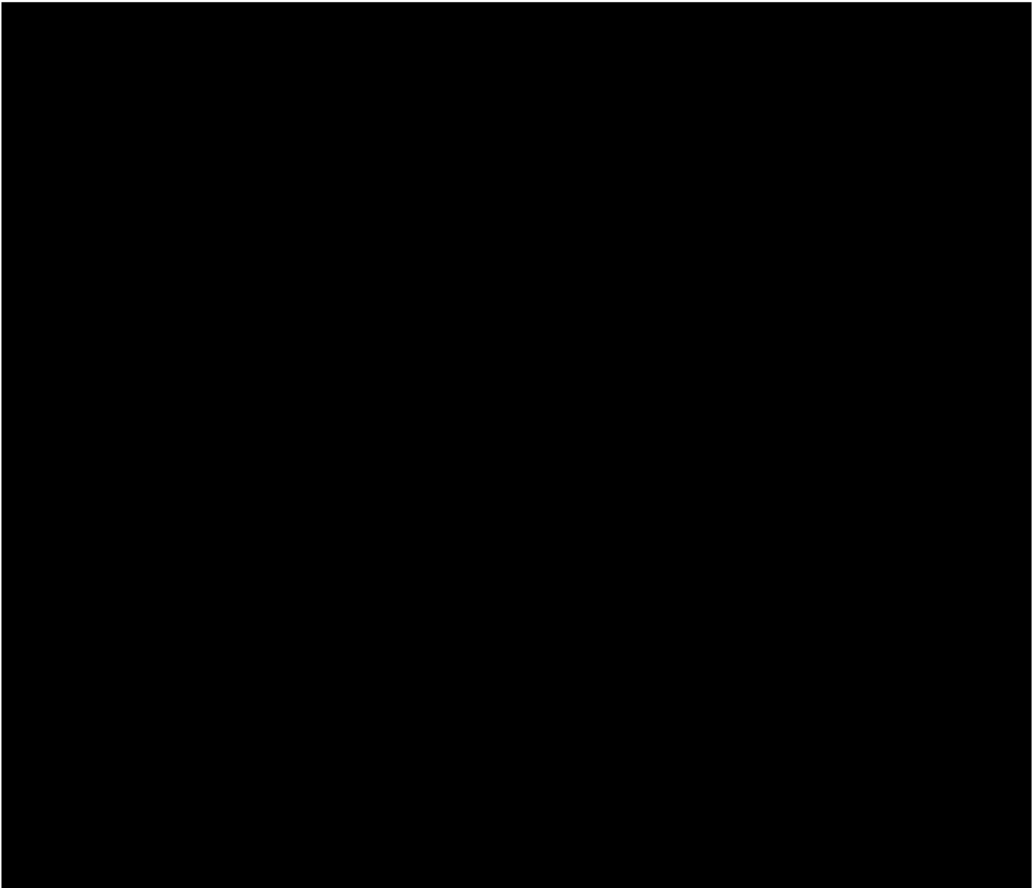


Figure 4.17: Nonlinear flow-chart algorithm.

Fig. 4.17 depicts the flow-chart of the algorithm for both the reflector and the IDT. Notice that for both regions the steps are identical but the calculations are different as the Y-block matrix are different (see Fig. 4.4 and Fig. 4.6). These for loops are started after the creation of the  $mY_{total}$  matrix (on Fig. 4.9 and Fig. 4.10) that has the full structure matrix. Therefore, the first step ("Define the nodes") becomes the most important as it will define, at each iteration, the position of the corresponding nodes for that iteration. It is important to highlight that, this node numbering sets-up different node position for the IOES calculation and, finally the current value for each node of the full structure.

#### 4.4.4 Full simulation process

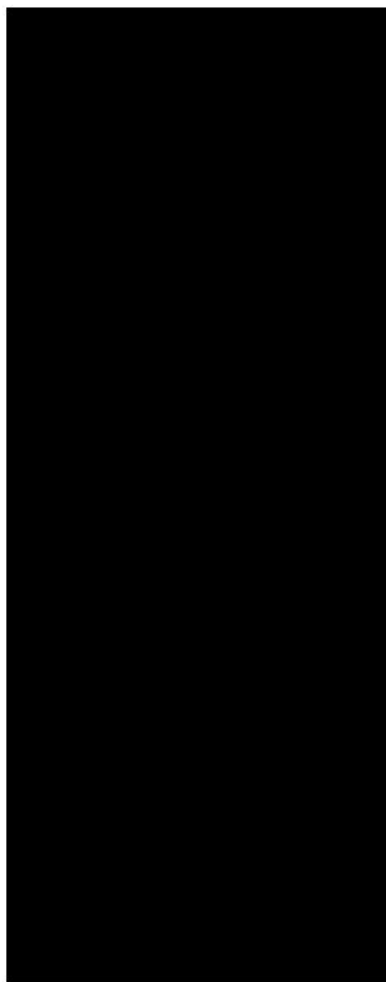


Figure 4.18: Full simulation process flow-chart.

The full simulation for SAW devices is briefly outlined following the flow-chart of Fig. 4.18. Moreover, the simulation process can be described as follows: the first step is devoted to define the device geometry and material parameters. After that, the linear analysis of Fig. 4.9 and Fig. 4.10 is performed. Now, the linear simulations are compared with the linear measurements. If the fitting results are not good the material parameters are changed and the simulation runs again. On the contrary, if the comparison is good enough the next step is to set the nonlinear parameters. Following that, the nonlinear analysis of Fig. 4.17 using the IOES method is performed. As done previously, nonlinear simulations are compared with the measurements. If the fitting results are satisfactory the nonlinear coefficient is determined. On the contrary, it is necessary to adjust the previous nonlinear parameters or to test a different one and run again the nonlinear analysis until obtaining a good agreement between measurements and simulations.

#### 4.4.5 IOES method validation

The IOES method has been validated through comparisons with Advanced Design System (ADS)<sup>®</sup> [87]. In all the cases a two-tone experiment with 51 frequency points is performed. For a fair comparison between both methods all the possible Hs and IMDs products were considered, including remix effects, as it was done in [83].

1. *Computing time comparison with ADS<sup>®</sup>*

Hereafter there are outlined a few examples of the time required for simulations performed with IOES method and commercial circuit simulator using HB techniques. Furthermore, we have evaluated the IOES method with two different scenarios, changing the number of unit-cells and changing the number of  $\lambda$ -sections to evaluate. In both cases, we have compared several examples using a general-purpose computer with an Intel<sup>®</sup> Core i7-10750Hz CPU @ 2.60 GHz and 32 GB RAM.

Table 4.1 shows an example of the computing time of simulations using IOES method considering only two electrodes. As it can be seen, it has been tested how it affects increasing the number of unit-cells. While for the ADS<sup>®</sup> simulator the computing time grows exponentially with the number of the discretization cells, computing time of the IOES linearly increases with the number of unit-cells.



**Table 4.1:** Computing time for 2 electrodes (one  $\lambda$ -section) and different unit-cells simulations using IOES method.

Experiment	# unit-cells	ADS <sup>®</sup> (s)	Matlab <sup>®</sup> (s)
$\lambda$ -section	100	105.7	1.5
	200	273.5	2.3
	300	545.7	3.1
	400	881.6	3.9
	500	1218.1	4.7

Moreover, we have progressively increased the number of  $\lambda$ -sections:  $M = 1, 5$  and 100 as depicted in Table 4.2. The discretization level was set to  $N = 100$  unit-cells per MR and NMR, which means 400 unit-cells per  $\lambda$ -section following the picture shown in Fig. 3.37. Note that all simulations are done with 51 frequency points, the reflector is also considered nonlinear and the remix effects are activated. Moreover, for the simulations of  $M = 1$  and 5 it has been previously checked that both ADS<sup>®</sup> and IOES traces perfectly overlap.

**Table 4.2:** Computing time for  $\lambda$ -sections simulations using IOES method.

Experiment	ADS <sup>®</sup> (s)	Matlab <sup>®</sup> (s)
1 $\lambda$ -section	130.3	1.5
5 $\lambda$ -sections	3330.1	3.3
100 $\lambda$ -sections	–	35.4

As it can be seen, ADS<sup>®</sup> simulations of 1 and 5  $\lambda$ -sections take 130.3 s and 3330.1 s respectively, whereas the IOES using Matlab<sup>®</sup> R2018b takes 1.6 s and 3.3 s respectively. Note that the IOES simulations are performed without using parallel computing. That is, the IOES method is around 80 and 1000 times faster than HB, being this difference more noticeable as the number of electrodes increases since the IOES method does not increase  $O(N^2)$  with the problem size. For the case of 100  $\lambda$ -sections, simulations using ADS<sup>®</sup> were unaffordable, whereas IOES takes 35.4 s.

## 2. Discussion about the minimum number of unit-cells

Although the discretization level  $N$  does not affect to the size of the matrix to be inverted when analyzing the circuit using the IOES method, it obviously has an impact on the computing time required to calculate the equivalent sources. In this subsection we discuss about the minimum number of unit-cells per region for both to achieve accurate results for the IMD3 and to minimize the computing time.

Fig. 4.19 shows simulations of a LSAW resonator with a duty factor of 50% and pitch of 950 nm. This resonator corresponds to the same as published in [88]. In this example, we have used a third order coefficient of the elastic

constant for the MR  $c_{3,MR}^E$ , and NMR  $c_{3,NMR}$  published in [77]. Black, blue, green and red dashed trace represents IOES simulations of the IMD3 with a discretization of 1, 2, 10 and 20 unit-cells per region respectively. As it can be seen, changes in the number of cells for the discretization leads to significant differences in the response below  $N = 10$  (green dashed trace). Note that for the case of  $N = 20$  (red dashed trace) the results are almost identical with  $N = 10$ , therefore 10 unit-cells is considered as a good number that provides a good compromise between computing time of the IMD3 and accuracy. Note that the required degree of discretization could be higher if the targeted frequency was higher, as it would be the case of the third harmonic for example.

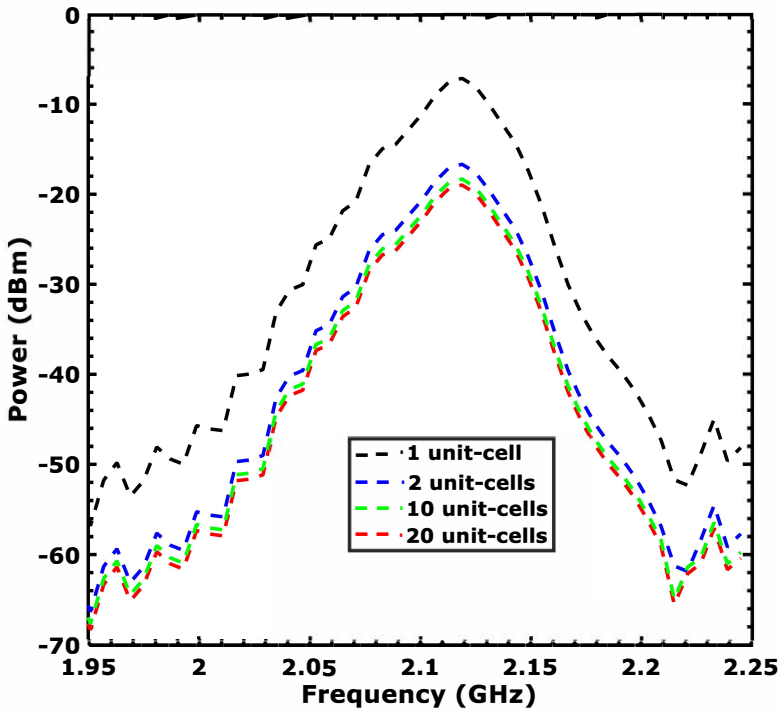


**Figure 4.19:** Simulated variation of 3rd order IMD response of a  $\eta = 50\%$  SAW resonator. Black, blue, green and red dashed trace correspond to a simulated  $(2f_2 - f_1)$  response with 1, 2, 10 and 20 unit-cells respectively.

Fig. 4.19 reveals that the shape of the frequency pattern of the IMD3 response within this narrow frequency range, is quite independent of the discretization level. However, the IMD3 level is overestimated unless the discretization level was high enough. This figure unveils the importance of the distributed models because the material parameter that causes a given nonlinear phenomenon must be independent of the discretization level. In fact, a given nonlinear

parameter of the local constitutive equations must be consistent with the nonlinear phenomena appearing in different resonators with other geometries. This is essential in order to predict the nonlinearities in new devices before manufacturing them.

Table 4.3 shows an analysis of the robustness of the distributed model. As a reference, let us consider a SAW resonator with a pitch of 950 nm and a duty factor of 50% simulated with  $N = 10$ . Then we have performed simulations of several resonators changing the pitch and the duty factor and we have obtained the corresponding  $c_{3,MR}^E$  parameter that provides the same IMD3 level than the one of the reference resonator. Furthermore, Table 4.3 shows the absolute percent variation of this parameter with respect to the value of the reference resonator changing the number of  $N$ . As it can be seen, the error considering only 1 cell can be almost 900%, and almost 40% for  $N = 2$  simulations.

The relative error is calculated with respect to the required value with the same number of cells of the reference resonator, and it quantifies the capability of the model to deal with different geometries. If we consider only 1 unit-cell per region, the term  $c_{3,MR}^E$  may change up to an 156% for different geometries. The shape-independent capability of the model is reduced up to almost 8% percent if just 2 unit-cells are considered.

This analysis allows to set the value of  $N = 10$  per region (which corresponds with 40 unit-cell per  $\lambda$ ) as a conservative value that guarantees independence of the model with the discretization level and the shape of the resonator.

**Table 4.3:** Variation of  $N_L$  coefficient  $c_{3,MR}^E$  with the number of cells with respect of a 10 cell case.

Resonator		Absolute Error [%]		Relative Error [%]	
Pitch [nm]	$\eta$ [%]	2 cells	1 cell	2 cells	1 cell
950	40	30.3	155.59	1.14	34.31
	45	25.0	198.80	5.16	23.21
	50	31.8	289.11	–	–
	55	35.7	433.33	2.93	37.07
	60	39.7	632.82	5.96	88.34
850	65	21.3	896.68	7.95	156.15
	50	30.2	332.81	1.26	11.23
900	50	30.2	319.57	1.26	7.83
1000	50	30.8	318.12	0.80	7.46
1100	50	30.8	313.81	0.80	6.35

Note that a full simulation of a SAW resonator composed by an IDT region of 100 pair of electrodes and each reflector region with 20 electrode pairs and a discretization of 10 unit-cells per section results in a 5600 cells non-linear problem. This results in an unfeasible large problem to be evaluated using conventional HB techniques, whereas the IOES method spends 35.4 s

(51 frequency points) to evaluate all the possible nonlinear harmonics and intermodulation products up to a third order.

### 3. IOES method validation of simulations

This subsection outlines an example and compares its results between the IOES method and ADS<sup>®</sup> simulations. In both cases the simulations are done considering a two-tone experiment with 23 dBm input sources, whose frequencies are separated by 2 MHz, directly connected to the input electrical port of the resonator. The central frequency of both signals is swept from 0.91 GHz to 0.92 GHz with 200 KHz steps, resulting in 51 frequency points.

The circuit was simulated with HB limiting the maximum order of each fundamental frequency (and maximum mixing order) to three and is further compared with the IOES method. For a fair comparison between both methods, the same frequency components and remix effects are included. Furthermore, in all the simulations it was set an arbitrary value only considering the  $c_{3,MR}^E$  nonlinear constant.

Example: simulations of a three  $\lambda$ -sections resonator

Fig. 4.20 depicts a comparison between the HB simulations using commercial software ADS<sup>®</sup> in solid traces versus the proposed IOES method in dashed traces. Moreover, it shows an example of both the IMD3 response on the left and the H3 response on the right of simulations considering three  $\lambda$ -sections. As it can be seen in both plots, HB (dashed) and IOES (continuous) traces perfectly overlap. With this example we can conclude that the IOES method is validated and well implemented since it obtains the same results as the HB simulations on ADS<sup>®</sup>.

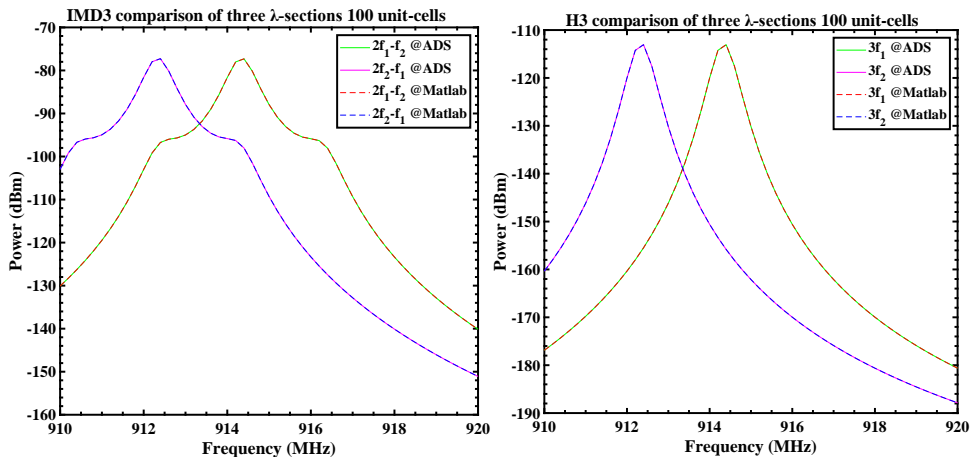


**Figure 4.20:** Example of three- $\lambda$  section simulations of ADS (magenta and green solid traces) versus IOES method (red and blue dashed traces). IMD3 response on the left and H3 on the right.

As remarking concussions of this chapter, the proposed application of the IOES method has demonstrated to be extremely useful for the analysis of large distributed nonlinear circuits, as it is the case of SAW resonators. Considering a simple structure composed by five  $\lambda$ -section in both IDT and reflector regions with 400 nonlinear unitary cells per  $\lambda$ -section and 51 frequency points the IOES method is 1000 times faster than a commercial software using HB. For more  $\lambda$ -sections the improvement is drastically enhanced since the computing time of the proposed method does not increase exponentially with the problem size, in fact, the improvement is enhanced with more sections. For example, the computing time required by the analysis of a resonator with 100 and 20  $\lambda$ -sections for the active region and each reflector respectively, is less than 35.4 s (51 frequency points) while these simulations are practically unaffordable using HB techniques.

# Chapter 5

## Nonlinear characterization

### 5.1 Introduction

One of the main topics of this thesis is the accurate nonlinear characterization of SAW devices. The characterization process plays an important role since it is necessary to develop models capable of predicting the linear and nonlinear behavior and, at the same time, to fully understand the generation mechanism of nonlinearity. In particular, the development of appropriate measurement methods is essential to obtain a proper characterization of the devices since nonlinearities of SAW devices are relatively weak and those can be masked by the own nonlinearity of the measurement equipment.

Taking into account the aspects that have been previously commented, the main objectives to be achieved in this chapter are the following:

- Verify that an unique set of nonlinear parameter allows to describe the in-band IMD3 and H3 nonlinear behavior independently of the in-plane geometry of the device for a given technology (or stack).
- Obtaining an accurate broadband linear characterization for a better prediction of the H3.
- Out-of-band verification of the developed model, adding additional nonlinear parameters if required.
- Analysis of the H2 generation and its modeling.
- After that, the objective is to extend towards the analysis of devices with different stack configurations or technologies.

Each of these aspects will be analyzed and validated from measurements of resonators with different typologies.

The sequence of the contents of this chapter is as follows:

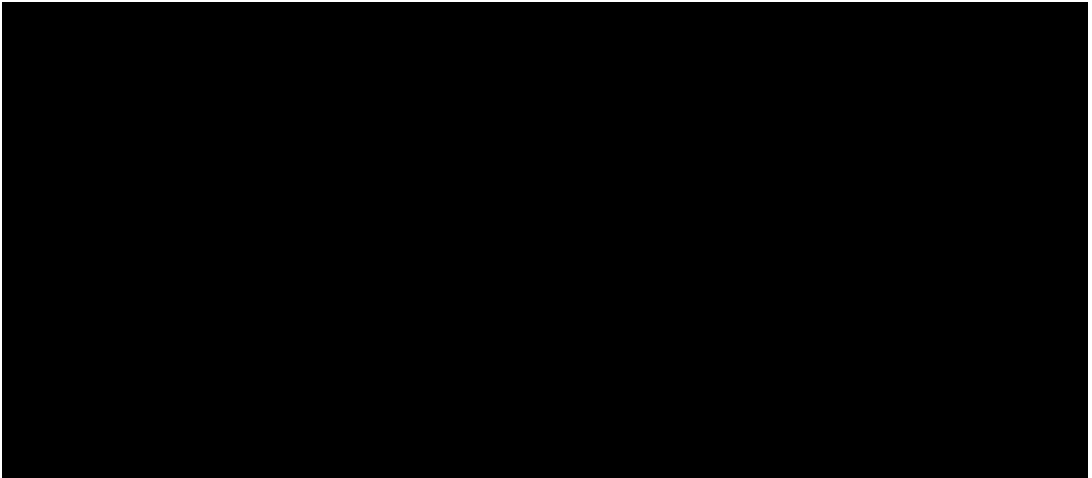
- Description of the resonator measurements with two technologies, LSAW and TC-SAW.
- Characterization process, which includes the linear and nonlinear simulations to match the measurements and upgrading of the models when required. This is done also for both LSAW and TC-SAW.
- A brief summary of this significant chapter of this thesis.

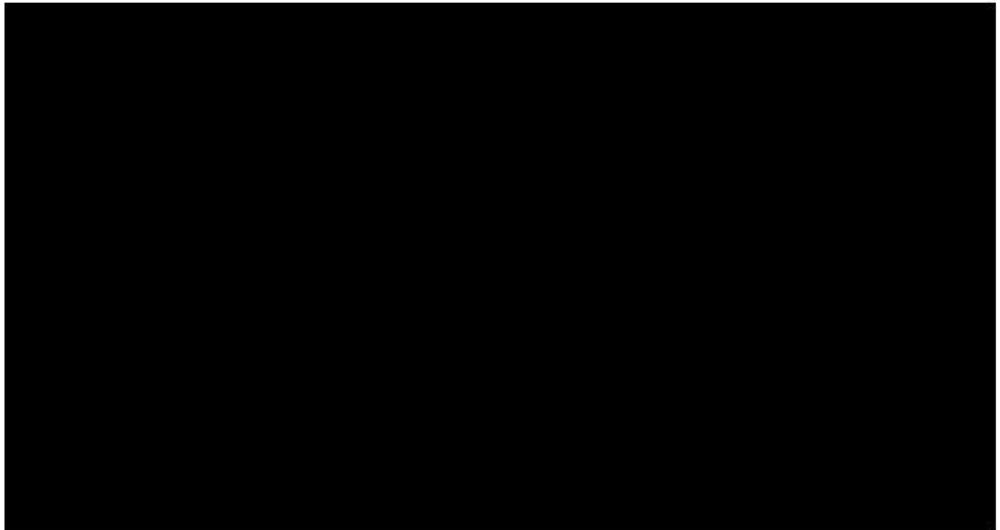
## 5.2 LSAW resonators measurements

This section is devoted to the LSAW resonators measurements. To make it easier for the reader, below it is a summary with the main points of this section:

- Description of the evaluated set of LSAW resonators.
- The measured IMD3 and H3 nonlinear response is outlined, including a description of the two-tone measurement system.
- The measured H2 and H3 nonlinear response is discussed, including a one-tone measurement system specific for harmonic measurements.

### 5.2.1 Description of resonators





### 5.2.2 IMD3 and H3 measurement system

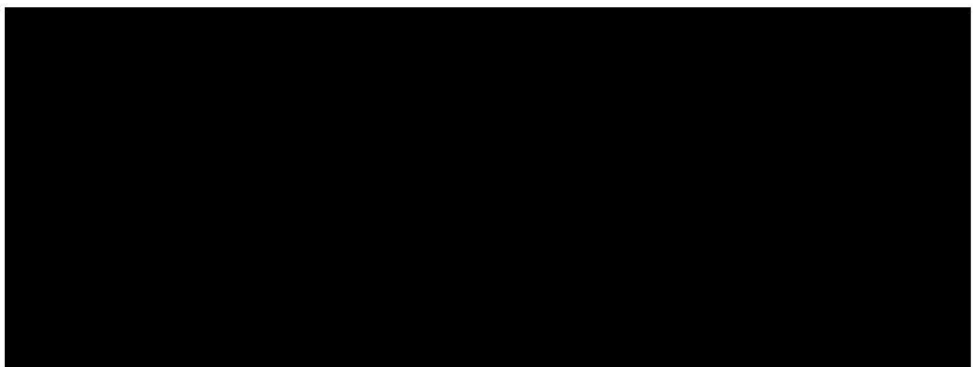
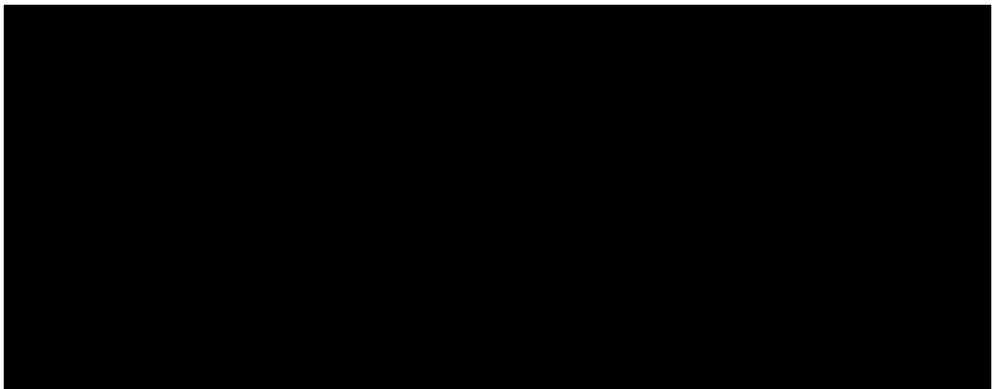


**Figure 5.1:** Schematic diagram of the IMD3 and H3 measurement system. The set-up is based on a conventional two-tone experiment.



The fundamental tones have around 24 dBm of power (input power to the device) and a constant tone spacing of  $\Delta f = f_2 - f_1 = 10$  MHz. The central frequency was swept from 1.950 GHz to 2.250 GHz for the Set 1 measurements with 76 frequency points, and from 1.680 GHz to 2.468 GHz for the Set 2 depending on the device with a span of 300 MHz and 76 frequency points.

Besides, to ensure that the measured IMD3 and H3 products of the DUT can be clearly separated from those of the own set-up IMD3 and H3 floor level, a measurement with the probes set on air is always done. Fig.5.2 shows the measured IMD3 (left) and H3 (right) level response, resulting in -84 dBm for the IMD3 level and -86 dBm for the H3 floor level. In the figure the x-axis represents the frequency corresponding to the sweep of the central frequency  $f_0$  and the y-axis the reflected measured power in dBm. In order to have uniformity in the graphs and make it easier for the reader, from now on this axes criterion will be used in all the graphs, otherwise it will be remarked.

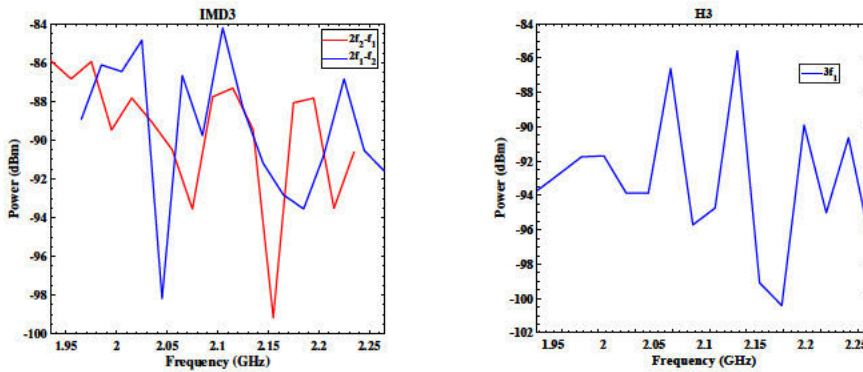
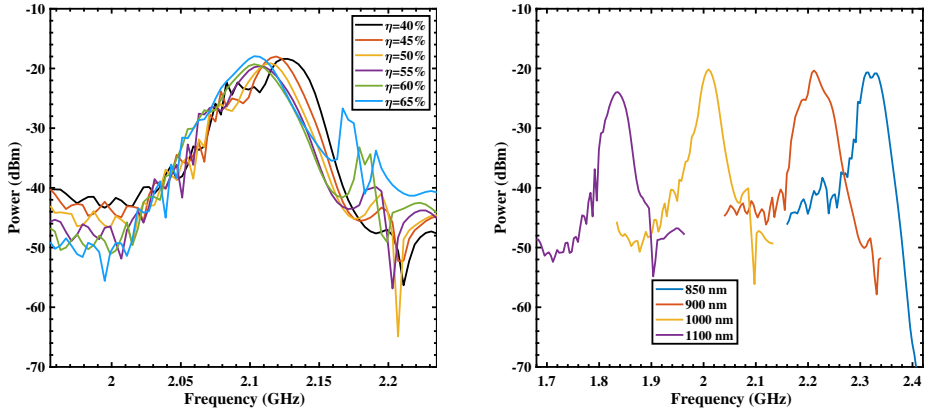


Figure 5.2: Measured IMD3 (left) and H3 (right) response of the measurement system intermodulation and harmonic floor level.

### 5.2.3 IMD3 measurements

Figure 5.3 shows the measured IMD3 response of Set 1 (left) and Set 2 (right) resonators with 24 dBm of input power to the DUT. The measurements were performed over a frequency sweep of the central frequency  $f_0$ . For simplicity we have only plotted the IMD3 corresponding to  $2f_1 - f_2$  and the H3 to  $3f_1$  respectively.



**Figure 5.3:** Measured IMD3 response of Set 1 (left) and Set 2 (right) resonators.

As seen in Fig. 5.3, all the measurements show a maximum IMD3 at a frequency between the series and shunt resonances. An example of the IMD3 and the input admittance of a resonator of  $\eta = 50\%$  and pitch 950 nm can be seen together in Fig. 5.4. In the figure, the x-axis corresponds to the  $f_0$ , the right y-axis represents the reflected IMD3 power in dBm and the left y-axis the measured input admittance magnitude.

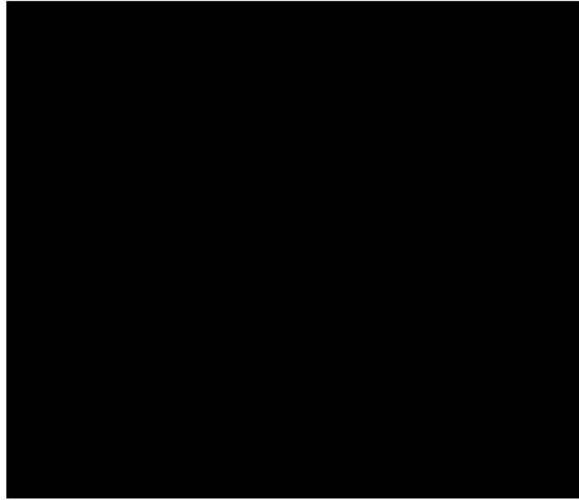
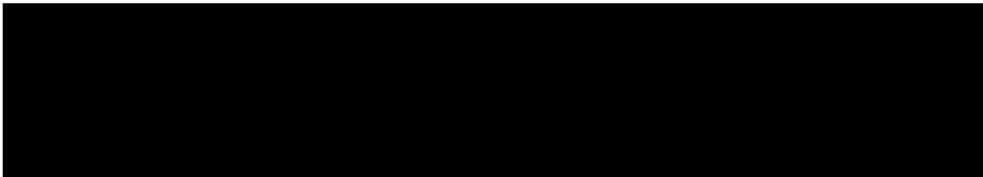


Figure 5.4: Measured IMD3 of resonator  $\eta = 50\%$  and pitch 950 nm versus its measured input admittance magnitude  $|Y|$ .

Note that, in Fig. 5.3 smaller peaks appear at higher frequencies that correspond to the frequencies of the SBUE around 2.2 GHz after the shunt resonances already unveiled into the linear response. This is very clear in Fig. 5.4 at 2.21 GHz.



#### 5.2.4 H3 measurements

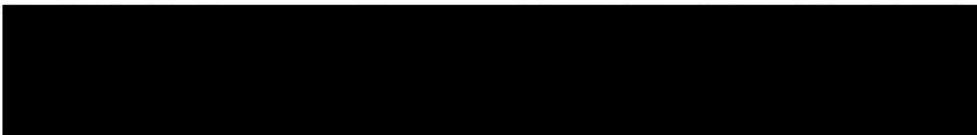




Figure 5.5: Measured H3 response of Set 1 (left) and Set 2 (right) resonators.

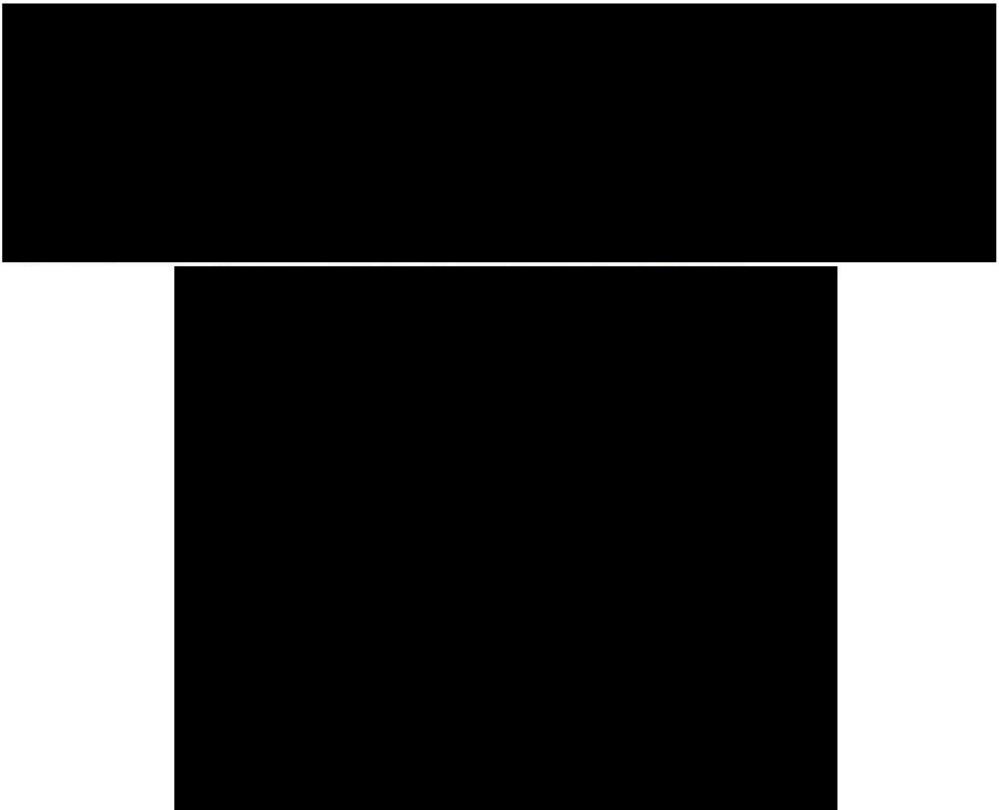
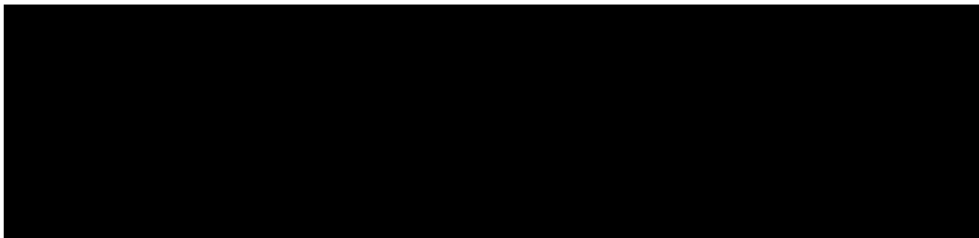
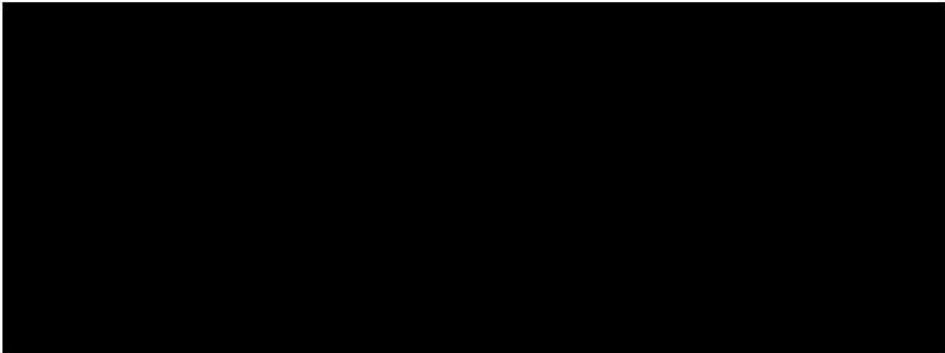


Figure 5.6: Measured H3 of resonator [redacted] versus its measured input admittance magnitude  $|Y|$ .

Figure 5.5 (right) shows the H3 response of Set 2 resonators. In this case, since all the resonators have a constant duty factor of  $\eta = 50\%$ , the H3 levels for all of them remains almost the same. The narrow high peaks at the right zone of each trace correspond to the previously mentioned spurious modes associated to the SBUE. Note that in the case of pitch 850 nm (blue trace) the peak is not present because of a frequency limitation of the LPF in the measurement system.

### 5.2.5 H2 measurement system

With the purpose of characterizing as much as possible the nonlinear behavior of SAW resonators, several measurement systems were developed during this thesis. Figure 5.7 shows the harmonics measurements system. The main idea is to perform a single-tone harmonic measurement under large continuous wave (CW) signal to later obtain the reflected power of the different test resonators. Basically, the methodology



To accomplish reliability and repeatability of the nonlinear measurement, the impact of the set-up needs to be considered. The measurement system has been calibrated and characterized with a 3-port broadband S-parameter measurement and was stored in a Touchstone file format. The calibration planes have been set at the SG output, before the DUT and the SA corresponding to ports 1, 2 and 3 respectively.

To ensure that the measured harmonics of the DUT can be clearly separated from the harmonic floor level of the measurement system, a measurement was obtained with the probes on air as depicted in Fig. 5.8, resulting in -75 dBm for the H2 level and -80 dBm for the H3 floor level. In this case, the x-axis represents the frequency corresponding to  $2f_1$  (left) and  $3f_1$  (right) and the y-axis the reflected measured power in dBm. The same axis criteria will be employed in the measurements plots of this subsection. Moreover, Fig. 5.8 present a strong ripple due to the isolator voltage standing wave ratio (VSWR) generated by the port mismatch of the broadband isolator.

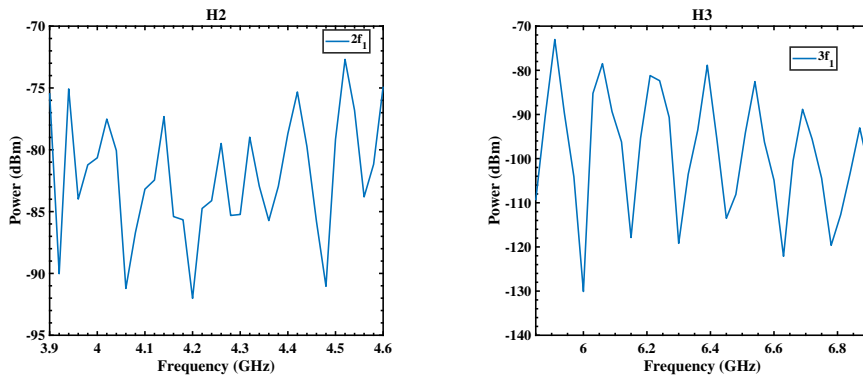


**Figure 5.8:** Measured H2 (left) and H3 (right) response of the measurement system harmonic floor level.

Again, it is necessary to perform a power calibration of the system. Both input and reflected power levels are calibrated and monitored to the end of the probe tip. Specifically, the total amount of power reaching the DUT is measured by connecting the SA at the plane where the DUT was previously located and setting the remaining circulator port with a  $50 \Omega$  load. Knowing the value of the input power reaching the DUT gives us information to set properly the desired power value in the simulations. This fact is specially relevant when measuring SAW devices since their power handling capability is limited and, commonly, the imposed maximum power of SAW devices is around 33 dBm.

### 5.2.6 H2 and H3 measurements

Figure 5.9 depicts the measured H2 and H3 response of Set 1 resonators with 23 dBm of input power to the DUT. The measurements were performed over a frequency sweep of the fundamental tone  $f_1$ . In the figure, the x-axis represents the frequency corresponding to the H2 ( $2f_1$ ) or H3 ( $3f_1$ ), and the y-axis the reflected measured power. The same criterion will be used in all the H2 and H3 measurements of this subsection but in Fig. 5.10.



Figure 5.9: Measured H2 (left) and H3 (right) response of Set 1 resonators.

As it can be seen, both measurements present levels above the measurement system floor level showed in Fig. 5.8, indicating that the nonlinear response is coming only from the DUT nonlinearities. In the H2 case (left), because of the SAW

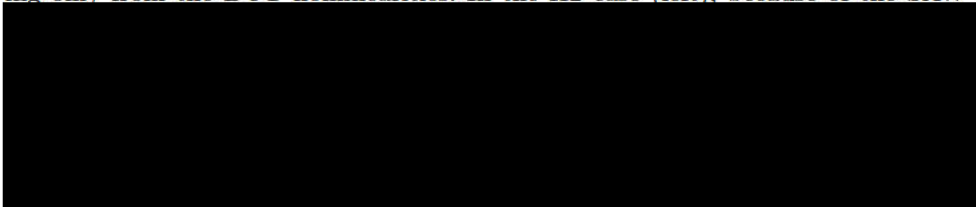


Figure 5.10: Measured H2 of resonator  $\eta = 50\%$  and pitch 950 nm versus its measured input admittance magnitude  $|Y|$ .

[REDACTED]

[REDACTED]

[REDACTED]

### H2 measurements changing the gap between IDT and reflectors

[REDACTED]



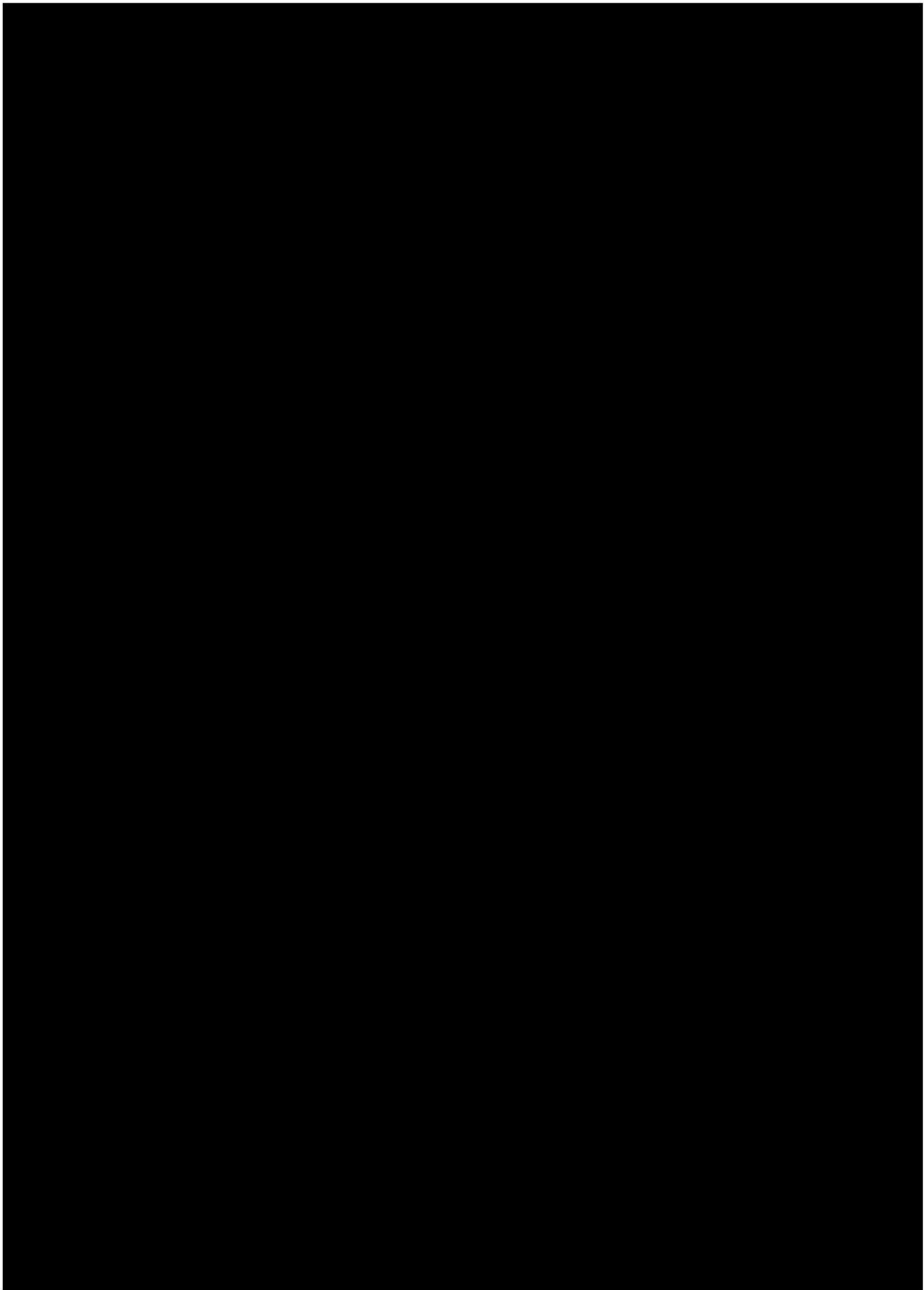


Figure 5.11: Measured H2 response of [REDACTED] from top to bottom respectively of Set 1 resonators. Each trace corresponds to different measurements changing the edge gap between the electrode and the dummy structure.

[REDACTED]

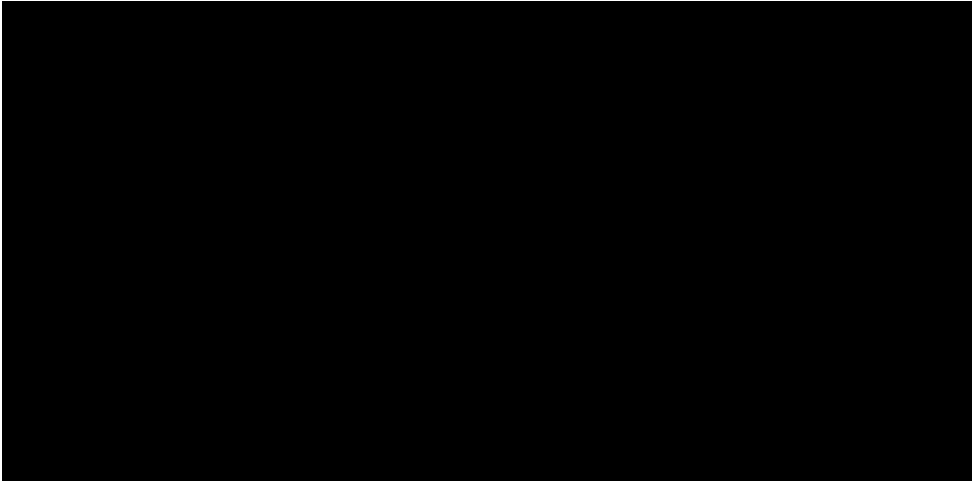
### 5.3 TC-SAW resonator measurements

This section is devoted to the TC-SAW resonator measurements. The procedure to analyze them follows the same steps as done previously with LSAW resonators.

#### 5.3.1 Description of resonators

We have also measured TC-SAW resonators to test if the model will be able to reproduce also the nonlinear response of resonators with different stack configuration.

[REDACTED]



### 5.3.2 IMD3, H3 and H2 measurement system

The measurement system is the same as the one shown in Fig. 5.1 but considering new circulators and LPF's whose cut-off frequency are conveniently chosen to measure the new resonators. The procedure of considering the measurement system and the calibration of the fundamental tones power is also performed and described in section 5.2.2.

At first, we performed the measurement campaign for all the TC-SAW resonators with a 2140 nm pitch. The fundamental tones had 19 dBm of power (input power to the device) and a constant tone spacing of  $\Delta f = f_2 - f_1 = 10$  MHz. To ensure that the measured intermodulation and harmonics products of the DUT can be clearly separated from the own set-up IMD3 and H3 floor level, a measurement was obtained with the probes on air. The central frequency was swept from 700 MHz to 1 GHz with 76 frequency points. Fig. 5.12 shows the measured IMD3 (left) and H3 (right) level response, resulting in -82 dBm for the IMD3 level and -93 dBm for the H3 floor level respectively.

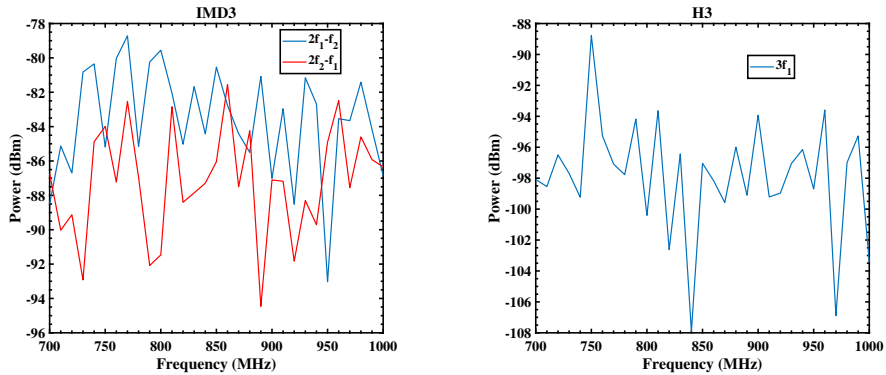


**Figure 5.12:** Measured IMD3 (left) and H3 (right) response of the measurement system intermodulation and harmonic floor level for 2140 nm pitch TC-SAW resonators.

Then, we measured the other TC-SAW resonators, corresponding to a 1980 nm and 1830 nm pitch. For these specific pitch values we decided to increment the fundamental tones power having 22 dBm of power (input power to the device) and a constant tone spacing of  $\Delta f = f_2 - f_1 = 10$  MHz. The central frequency was swept from 750 MHz to 1.1 GHz with 76 frequency points. Again, a measurement of the IMD3 and H3 floor level with the new power value was obtained with the probes on air. Fig.5.13 shows the measured IMD3 (left) and H3 (right) level response, resulting in -78 dBm for the IMD3 level and -93 dBm for the H3 floor level. The red circle shown in Fig. 5.13 left is plotted to highlight that the measurements system has a limitation at 1.02 GHz because of the employed LPF, affecting some of the measurements whose frequency sweep is above the LPF band value.

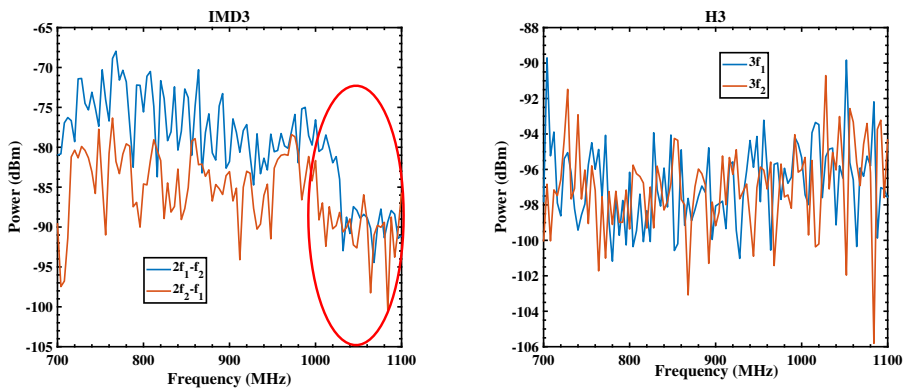


**Figure 5.13:** Measured IMD3 (left) and H3 (right) response of the measurement system intermodulation and harmonic floor level for 1980 nm and 1830 nm pitch TC-SAW resonators.

In accordance of the characterization process established before, we have also performed H2 measurements of these TC-SAW resonators. In this case, we are not using a specific harmonic measurement system but the same as the two-tone measurement system used for the IMD3 and H3. Fig. 5.14 shows the H2 levels obtained with the probes on air. Note that as stated previously, the input power reaching the DUT for resonators with pitch of 2140 nm was different in comparison with those of pitch 1980 and 1830 nm respectively, which explains the differences between the H2 values of left and right plots.

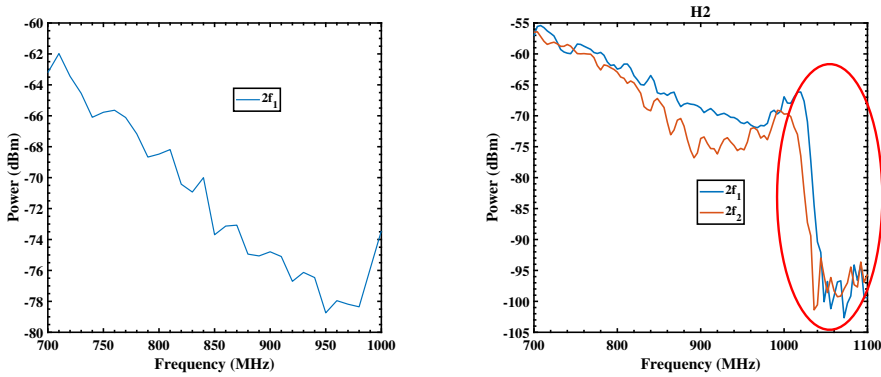


**Figure 5.14:** Measured H2 response of the measurement system harmonic floor level for TC-SAW resonators with configuration of pitch of 2140 nm (left) and pitch 1980 and 1830 nm (right) respectively.

Moreover, Fig. 5.14 right shows marked with a red circle the LPF frequency limitation which also affects the H2 measurements. In general terms, the obtained H2 noise floor levels are quite significant in comparison for example with those obtained in Fig. 5.8. The reason behind this H2 level increase is directly related to the new employed circulators, whose H2 behaviour is worst than expected. Note that, higher H2 levels would imply possible problems when measuring the H2 response of TC-SAW resonators.

### 5.3.3 IMD3 measurements

The next step is to proceed with the IMD3 measurements of the TC-SAW resonators. Figure. 5.15(a) to Fig. 5.15(c) depict the measured IMD3 response of Set 3, Set 4 and Set 5 resonators respectively. The measurements were performed over a frequency sweep respect the central frequency  $f_0$ , in the figure the x-axis represents the frequency corresponding to the IMD3 ( $2f_2 - f_1$ ) and the y-axis the reflected measured power in dBm.

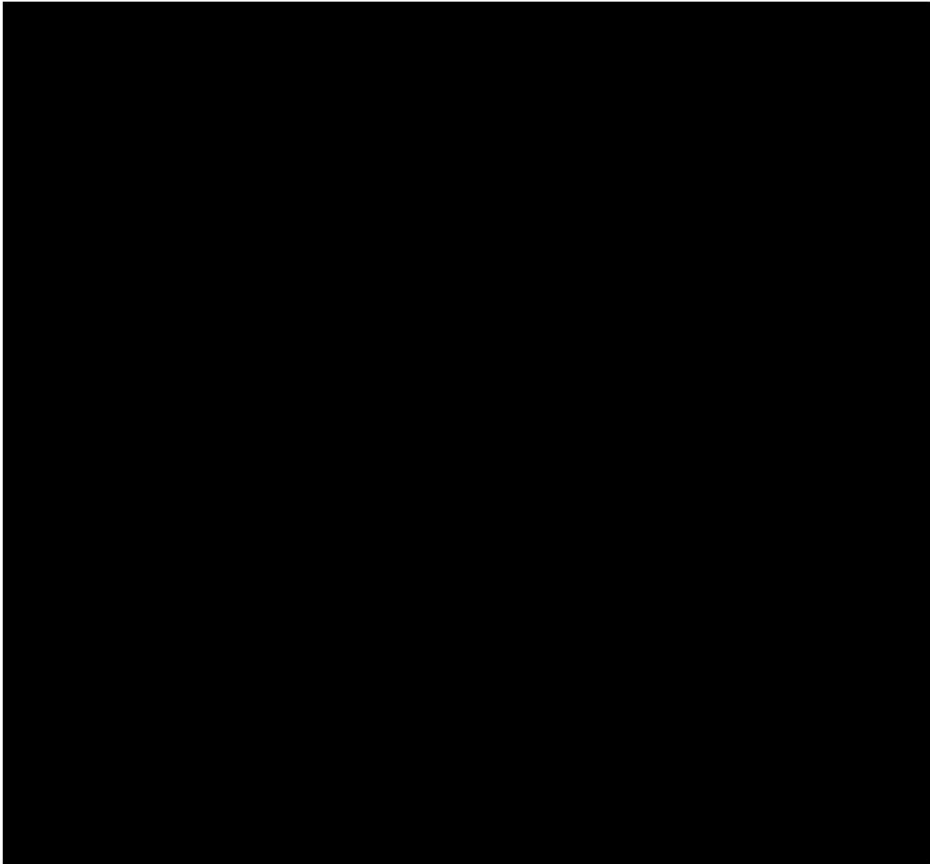
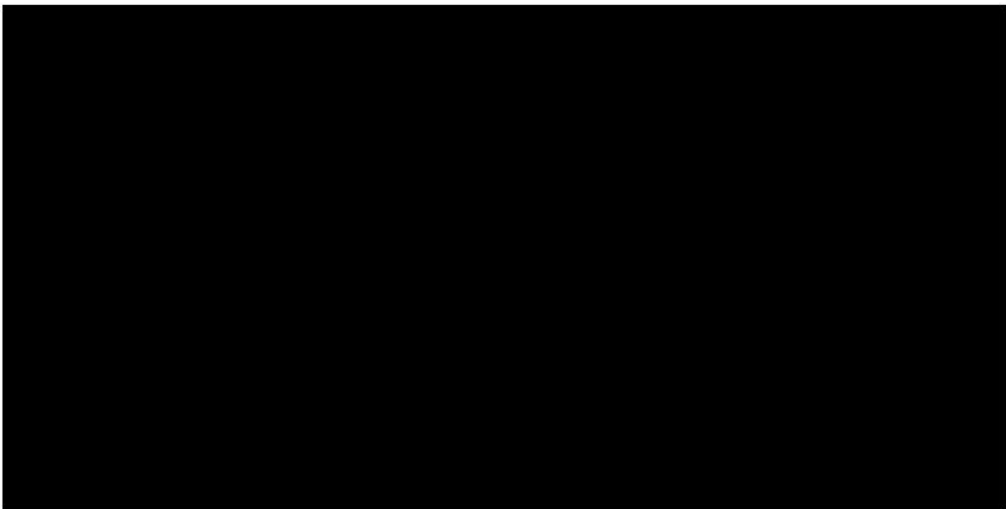


Figure 5.15: Measured IMD3 response of TC-SAW resonators.



### 5.3.4 H3 measurements

Fig. 5.16(a) to Fig. 5.16(c) depict the corresponding measured H3 response for Set 3, Set 4 and Set 5 resonators. Again, all the measurements show a maximum H3 level at a frequency between the series and shunt resonances. Also, at lower frequencies, it can also be observed a H3 plateau between [REDACTED] because of the measurement system.

Moreover, in all the cases the resonators exhibit [REDACTED]

[REDACTED]

[REDACTED]

[REDACTED]

[REDACTED]

[REDACTED]

[REDACTED]

[REDACTED]

[REDACTED]



Figure 5.16: Measured H3 response of TC-SAW resonators.



### 5.3.5 H2 measurements

Finally, Fig. 5.17(a) to Fig. 5.17(c) depict the corresponding measured H2 response for Set 3, Set 4 and Set 5 resonators respectively. As previously unveiled in Fig. 5.14, the H2 noise floor level of the measurement system is quite significant obtaining -62 dBm and -58 dBm for resonators of pitch [redacted] respectively. These high H2 levels imply problems if the measured H2 response of the resonators is not high enough to overcome the H2 levels of the measurement system.

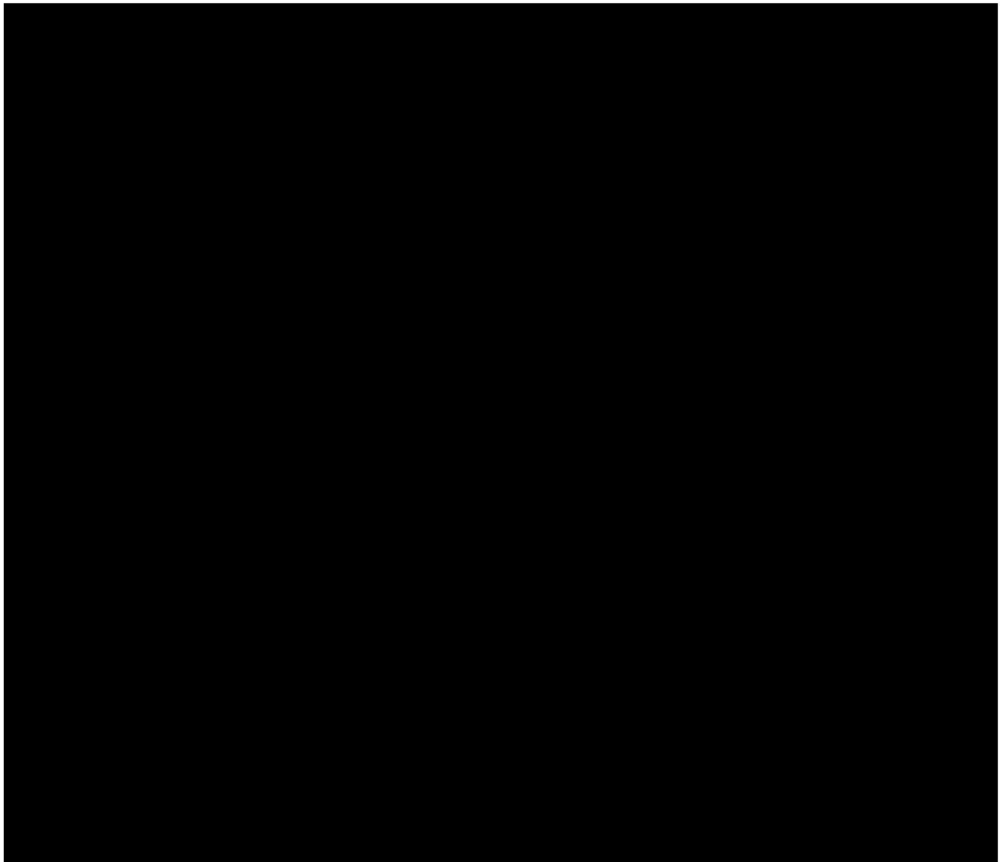


Figure 5.17: Measured H3 response of TC-SAW resonators.



Definitely, all the measurements present levels around or at the same level as the H2 measurement system floor level and thus, is not possible to distinguish whether the H2 response comes from the DUT or the measurement system itself. Since the resonators measured H2 response cannot be clearly separated from those of the harmonic floor level of the measurement system, the previous H2 measurements are discarded and not considered for the characterization process. Defining large signal nonlinear measurement systems with high dynamic range is very important for reliable measurements and, in this case, the new circulators call into question the effectiveness and trustworthiness of the measurements.


## 5.4 LSAW resonators response analysis

This section analyzes the response of LSAW resonators. Below the main points of this analysis are summarized:

- Linear modeling: once the narrowband linear model was validated in Chapter 3, broadband linear measurements will be presented.
- IMD3 characterization: an extensive characterization process of the IMD3 response is described to figure out which is the nonlinear parameter that better agrees with the measured in-band IMD3 of a reference resonator.
- IMD3 validation: this characterization process is validated with simulations and measurements of other resonators with different geometry.
- [REDACTED]
- [REDACTED]
- [REDACTED]
- [REDACTED]

### 5.4.1 Broadband linear response measurements versus simulations

As commented previously, a proper characterization of both the linear and nonlinear response is indeed crucial when determining the nonlinear manifestations of the resonators. Broadband linear measurements provide useful information about resonator response at higher frequencies. Although it might not sound quite relevant regarding the nonlinear response, it is completely the opposite, since the harmonic generation for example H2 and H3 are relevant at twice and third times respectively the resonant frequency. One thing to point out is that nonlinear simulations can only be accurate if the simulations predict the wide-band linear behavior accurately.



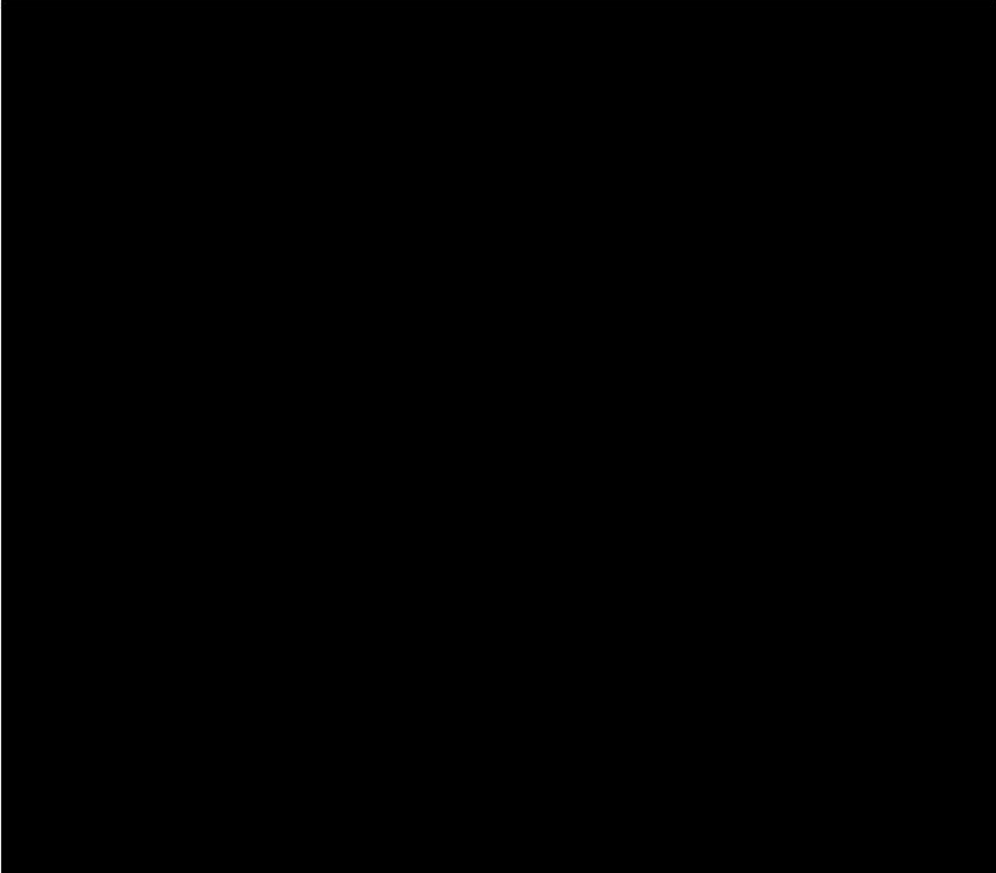


**Figure 5.18:** Measured (blue trace) and simulated (red trace) broadband input admittance magnitude response of Set 1 resonators (on top) and Set 2 resonators (on bottom). Zoomed input admittance close to three times the resonance frequency on the right respectively.

## 5.4.2 IMD3 nonlinear characterization

### Identification of potential contributors

An accurate analysis of the contribution of each nonlinear constant to the nonlinear IMD3 response is presented. The main goal is to identify the potential contributors responsible of the IMD3 manifestation. Here we analyze a so-called reference resonator and the results are further tested on other resonators. Specifically, the frequency pattern of the second-order and third-order nonlinear derivatives of the stiffness, dielectric and piezoelectric constants are compared.

We decided to use as a reference resonator the one with pitch 950 nm and 50% of duty factor, whose measured IMD3 is shown in Fig. 5.19 with continuous green trace.

The upper plots of Fig. 5.19 show the simulated IMD3 response considering only the individual contribution of the third-order coefficients of equation 3.55, namely:  $c_{3,MR}^E$  (red circle),  $\varepsilon_{3,MR}^S$  (cyan dotted),  $\chi_{7,MR}$  (magenta dotted) and  $\chi_{9,MR}$  (black dot-dashed). The value of those coefficients was arbitrary set to provide a maximum IMD3 level comparable to the one measured to facilitate the comparison of their frequency pattern with the measurements. Note that here the subscript MR refers to the metallized zone and NMR to the non-metallized zone.

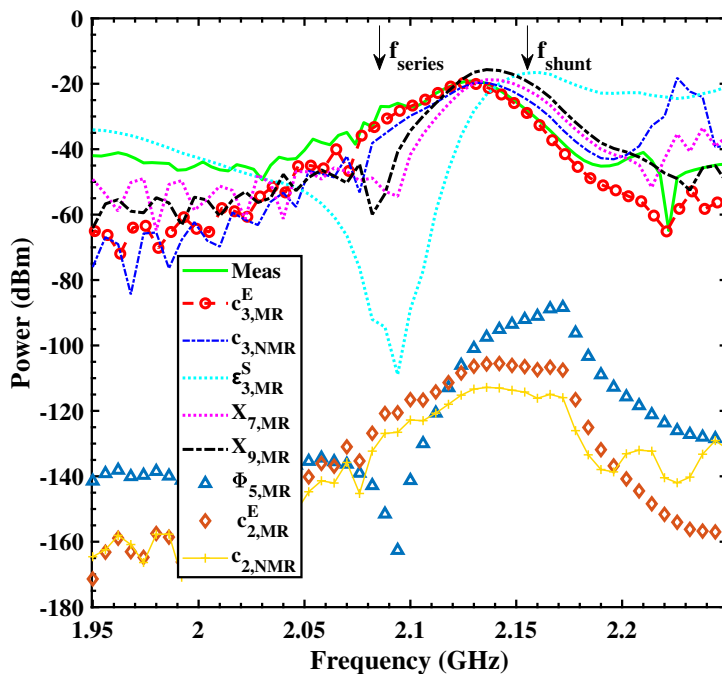


**Figure 5.19:** Analysis example of a SAW reference resonator. Simulated 3rd order IMD response of a SAW resonator. Green solid line corresponds to measured  $2f_1 - f_2$  and red circle line to the best fitted data.

Note that the pattern of the values  $\varepsilon_{3,MR}^S$ ,  $\chi_{7,MR}$  and  $\chi_{9,MR}$  exhibit a notch at the series resonance frequency and the one that provides the most similar frequency pattern is  $c_{3,MR}^E$ . Between the series and shunt resonances -marked with arrows into the figure- the value of  $c_{3,MR}^E = -110c^E$  reproduces the same measured IMD3 very well.

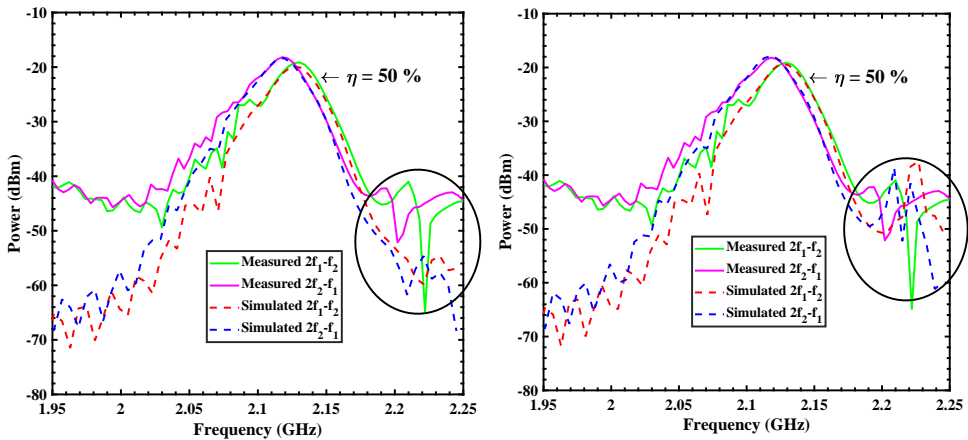
Figure 5.19 also includes the trace for  $c_{3,NMR} = -2100c$  of the NMR (blue dashed). As it can be seen, though the frequency pattern is very similar (except at higher frequencies where larger peaks appear) to the one caused by  $c_{3,MR}^E$ , it is necessary to force a very big value of  $c_{3,NMR}$  to obtain the same maximum of IMD3. Certainly, these values could be slightly different in both regions since the

mass loading of the electrodes could affect to them. However, it seems there is no physical reason to force big differences between  $c_{3,MR}^E$  and  $c_{3,NMR}$ . From now on, in all our simulations we will set the same value for both nonlinear constants.

It has been reported in several articles [81], [82] that the contribution of remix effects to the generation of IMD3 might be not negligible in comparison with the direct generation. At the bottom of Fig. 5.19 we have considered the second-order terms of the MR,  $\phi_{5,MR}$  (blue triangles), and  $c_{2,MR}^E$  (orange diamonds), and the  $c_{2,NMR}$  (yellow crosses) parameter of the NMR. Their values are arbitrary low for the clearness of the figure. It is clear that the frequency patterns that these parameters provide are not well correlated with the one measured, so we could conclude that, at least in this case, remix effects do not have an important effect on the IMD3 response and could be neglected.

### Reflector effects

In this subsection the contribution to the nonlinear IMD3 response with regard the nonlinear constant of the reflectors is considered. Fig. 5.20 left shows with more detail the agreement between simulations and measurements of the IMD3 response of the reference resonator using the values  $c_{3,MR}^E = c_{3,NMR} = -110c^E$  we had got from the previous characterization process. Red and blue dashed traces correspond to computed  $2f_1 - f_2$  and  $2f_2 - f_1$  respectively, and measured response in green ( $2f_1 - f_2$ ) and magenta ( $2f_2 - f_1$ ) traces. Note that although simulations show very good in-band results there are still some peaks around 2.2 GHz that the simulations are not being able to reproduce and, therefore it comes from another non-linear constant or constants not considered yet.



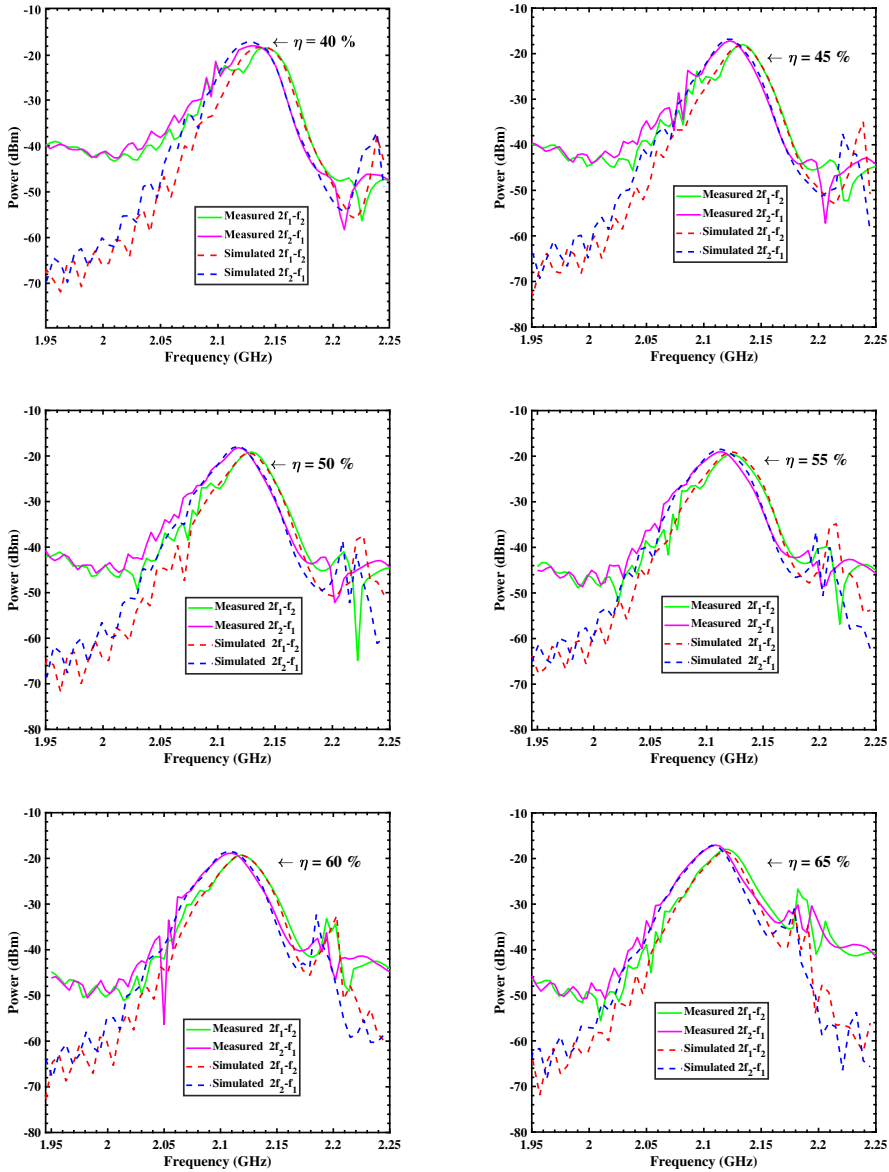
**Figure 5.20:** IMD3 response of reference resonator with  $\eta = 50\%$ . Left shows simulations only considering nonlinear coefficients of the IDT area. Contrarily, right shows simulations adding the reflector nonlinear coefficients.

Figure 5.20(right) depicts the IMD3 response when apart from the previous  $c_{3,MR}^E$  and  $c_{3,NMR}$  nonlinear constants of the IDT section, their corresponding counterparts of the reflector section  $c_{3r,MR}^E$ ,  $c_{3r,NMR}$  are activated. As evidenced in Fig. 5.20 (right) and marked with a black circle, some peaks appear now around 2.2 GHz so it seems that those peaks on the IMD3 come from the reflectors and are therefore associated to the SBUE.

Note also that the measured out-of-band IMD3 at lower frequencies unveils than an additional nonlinear term should be included to increase the IMD3 since the terms  $c_{3,MR}^E$  and  $c_{3,NMR}$  clearly underestimate the IMD3. At a first glance, this out-of-band IMD3 could be adjusted using a nonlinear term that accompanies the electric field into the constitutive equations, such as,  $e_{3,MR}^E$  or  $\varepsilon_{3,MR}^S$ . However, we checked with additional experiments that the slope of the IMD3 at those frequencies does not follow the characteristic scaling factor of 3 as a function of the input power, even at moderate input power levels, at which saturation effects are not expected. Therefore, we are not confident that those terms are the responsible of the measured out-of-band IMD3 and further investigation must be done.

### 5.4.3 IMD3 characterization process validation

Once identified the potential contributors of the in-band IMD3 nonlinear response of the reference resonator, the characterization process is validated testing the same nonlinear parameters  $c_{3,MR}^E = c_{3r,MR}^E = c_{3,NMR} = c_{3r,NMR} = -110c^E$  in both Set 1 and Set 2 resonators. In all the following plots it is shown the simulated 3rd order IMD response. Red and blue dashed traces correspond to simulated  $2f_1 - f_2$  and  $2f_2 - f_1$  respectively, and measured response in green ( $2f_1 - f_2$ ) and magenta ( $2f_2 - f_1$ ) traces. As it can be seen in Fig. 5.21, the proposed nonlinear parameters are consistent for all the resonators with different duty factor.



**Figure 5.21:** Measured IMD3 response (green and magenta solid trace) and simulations (blue and red dashed trace) for Set 1 resonators corresponding to  $2f_1 - f_2$  and  $2f_2 - f_1$  respectively. From top to bottom resonators with  $\eta = 40\%$  to  $\eta = 65\%$  respectively.

Furthermore, Fig. 5.22 depicts the results for the Set 2 resonators. Again, the tested values are consistent with the measurements. Note that although simulations show pretty good results for both Set 1 and Set 2 in the in-band frequency response, there are still some discrepancies between simulations and measurements at lower

and higher frequencies as commented previously and, further investigation would be needed for modeling the out-of-band IMD3.

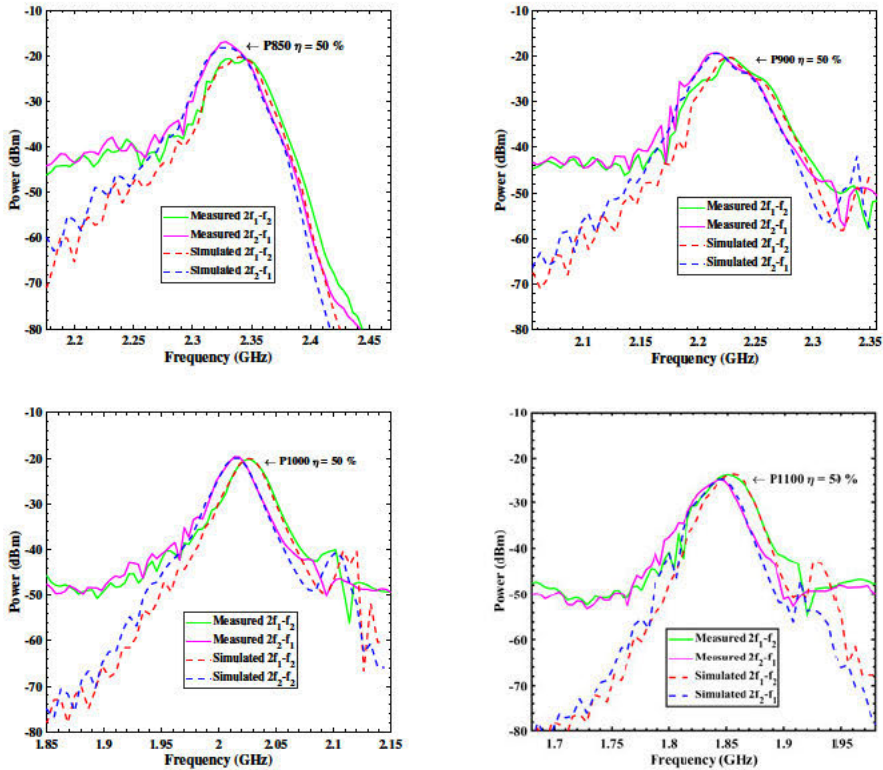


Figure 5.22: Measured IMD3 response (green and magenta solid trace) and simulations (blue and red dashed trace) for Set 2 resonators corresponding to  $2f_1 - f_2$  and  $2f_2 - f_1$  respectively. From top to bottom resonators with pitch of 850 nm to 1100 nm respectively.

#### 5.4.4 H3 characterization

##### Identification of potential contributors

Following the same procedure as done with the IMD3 response, we check the individual contributions of the nonlinear constants in the H3 response with the same reference resonator. Remix effects are discarded since they are not considered relevant in this particular case based on the results obtained in the previous Fig. 5.19



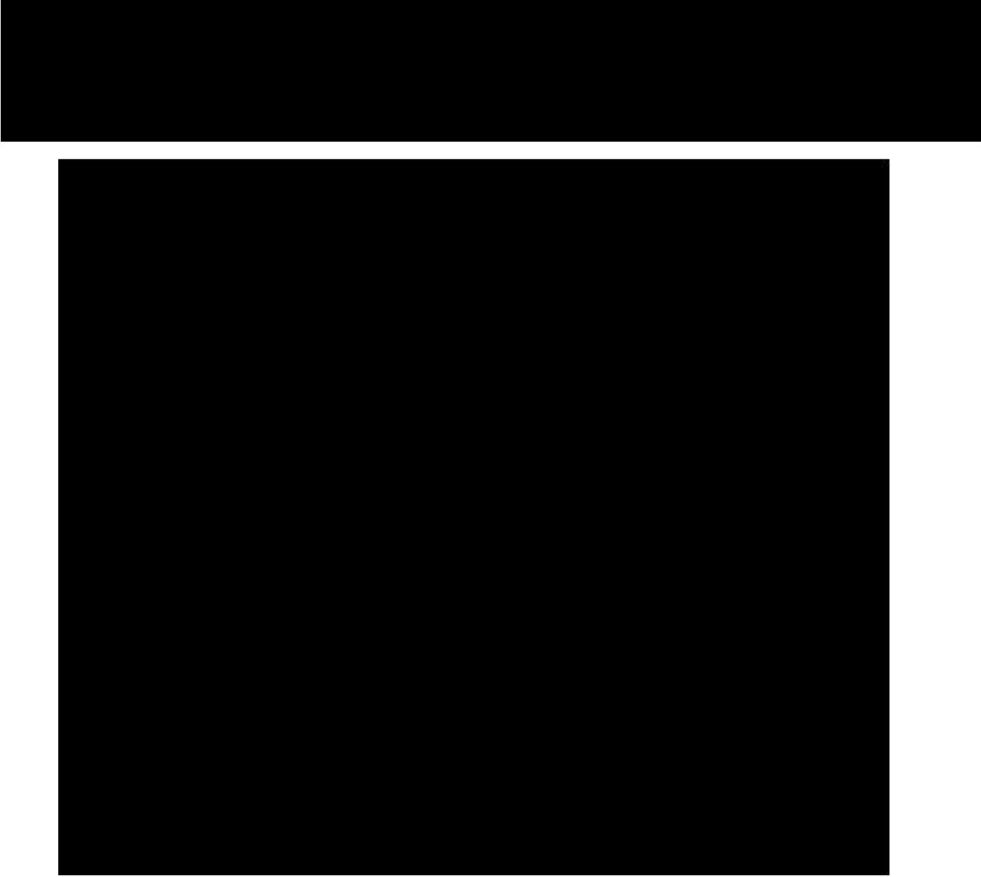
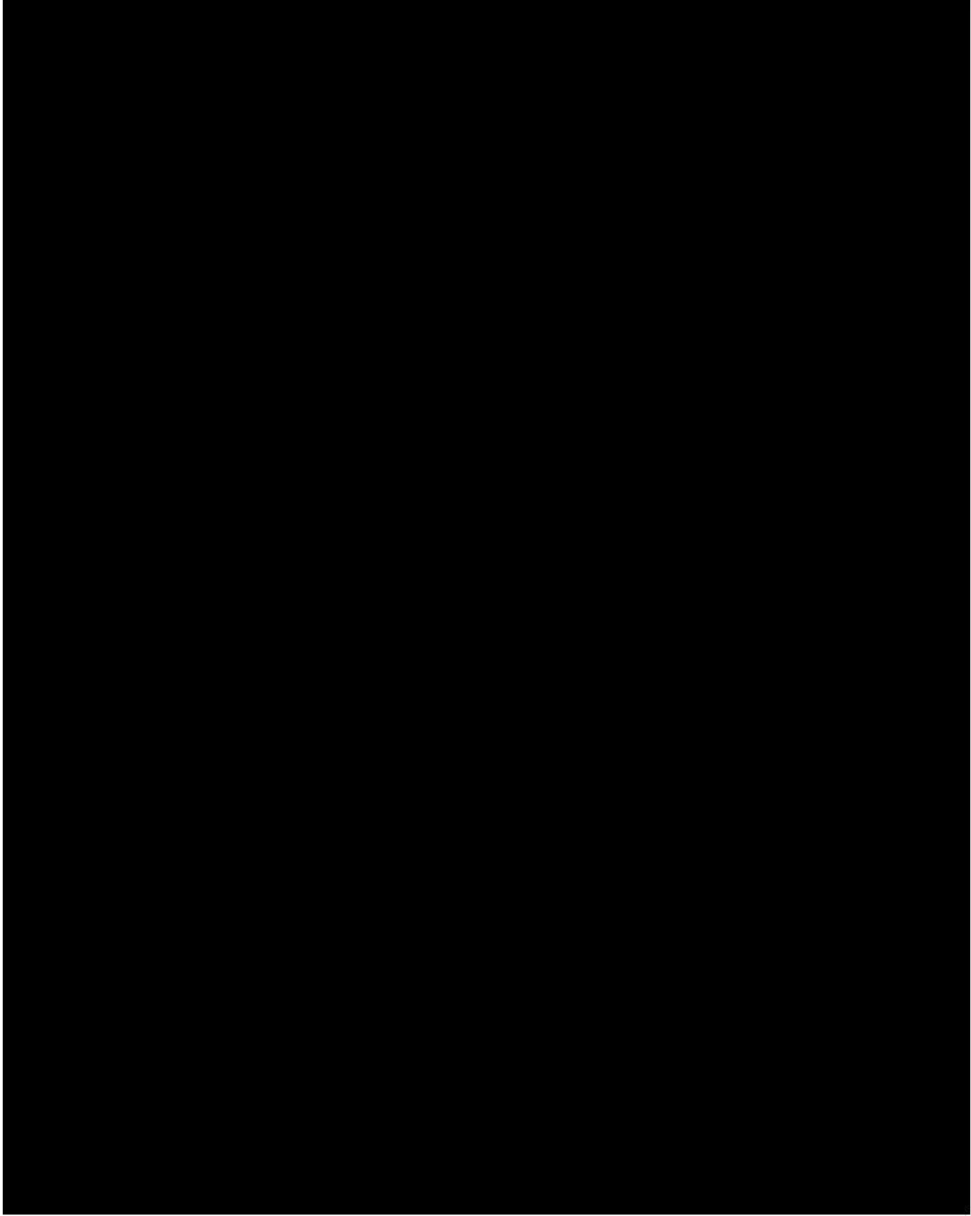


Figure 5.23: Analysis example of a SAW reference resonator. Simulated 3rd order harmonic response of a SAW resonator. Green solid line corresponds to measured  $3f_1$  and red circle line to the best fitted data.

### 5.4.5 H3 characterization process validation

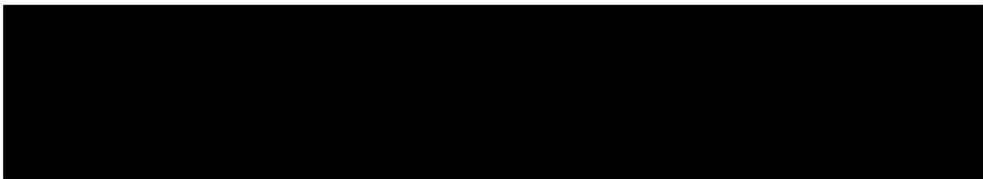
For completeness, we show the simulated H3 considering only the same value of the  $c_{3,MR}^E$  nonlinear constant. Plots of Fig. 5.24 and Fig. 5.25 show the H3 response of the Set 1 and Set 2 resonators respectively. As it can be seen, the simulated response is not consistent for any resonator.



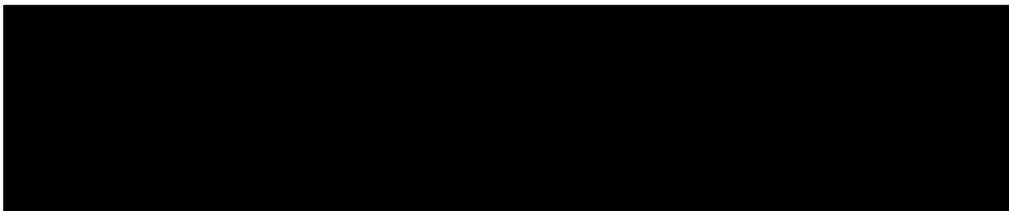
**Figure 5.24:** Measured H3 response (green solid trace) and simulations (red dashed trace) for Set 1 resonators. Red dashed trace represents simulations considering  $c_{3,MR}^E$  nonlinear constant of both the MR and NMR of the IDT and reflector activated. From top to bottom resonators with [REDACTED]



Figure 5.25: Measured H3 response (green solid trace) and simulations (red dashed trace) for Set 2 resonators. Red dashed trace represents simulations considering  $c_{3,MR}^E$  nonlinear constant of both the MR and NMR of the IDT and reflector activated. From top to bottom resonators with [redacted] respectively.



#### 5.4.6 Non-uniform electric field: edge-E linear model

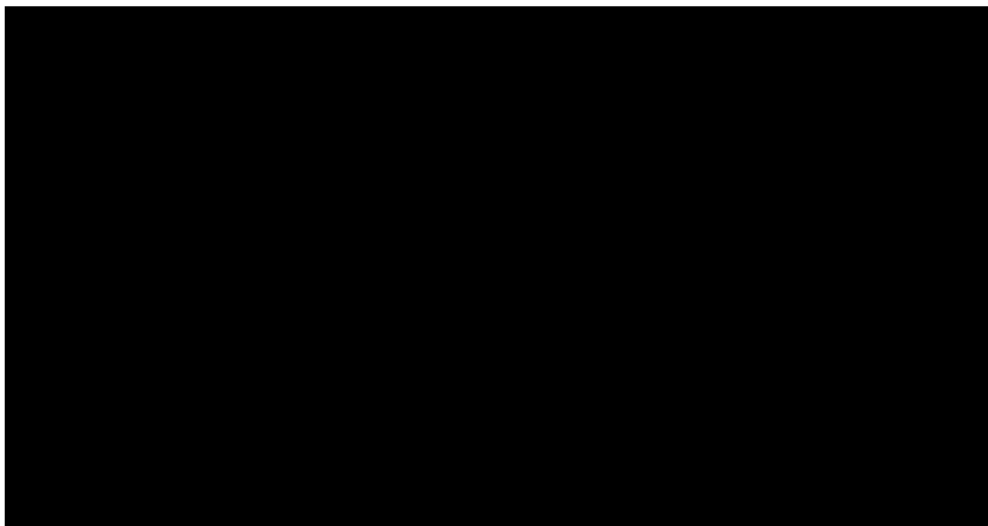
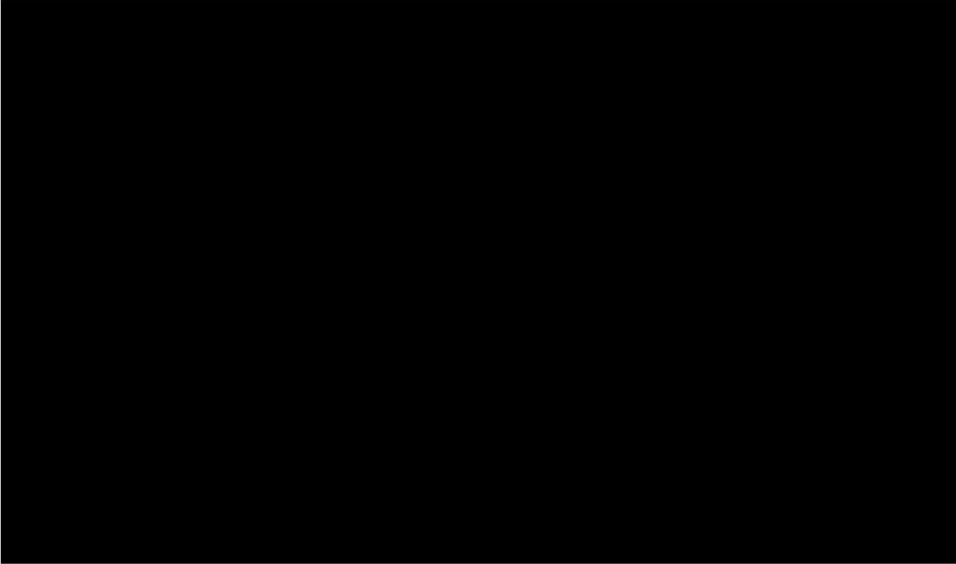


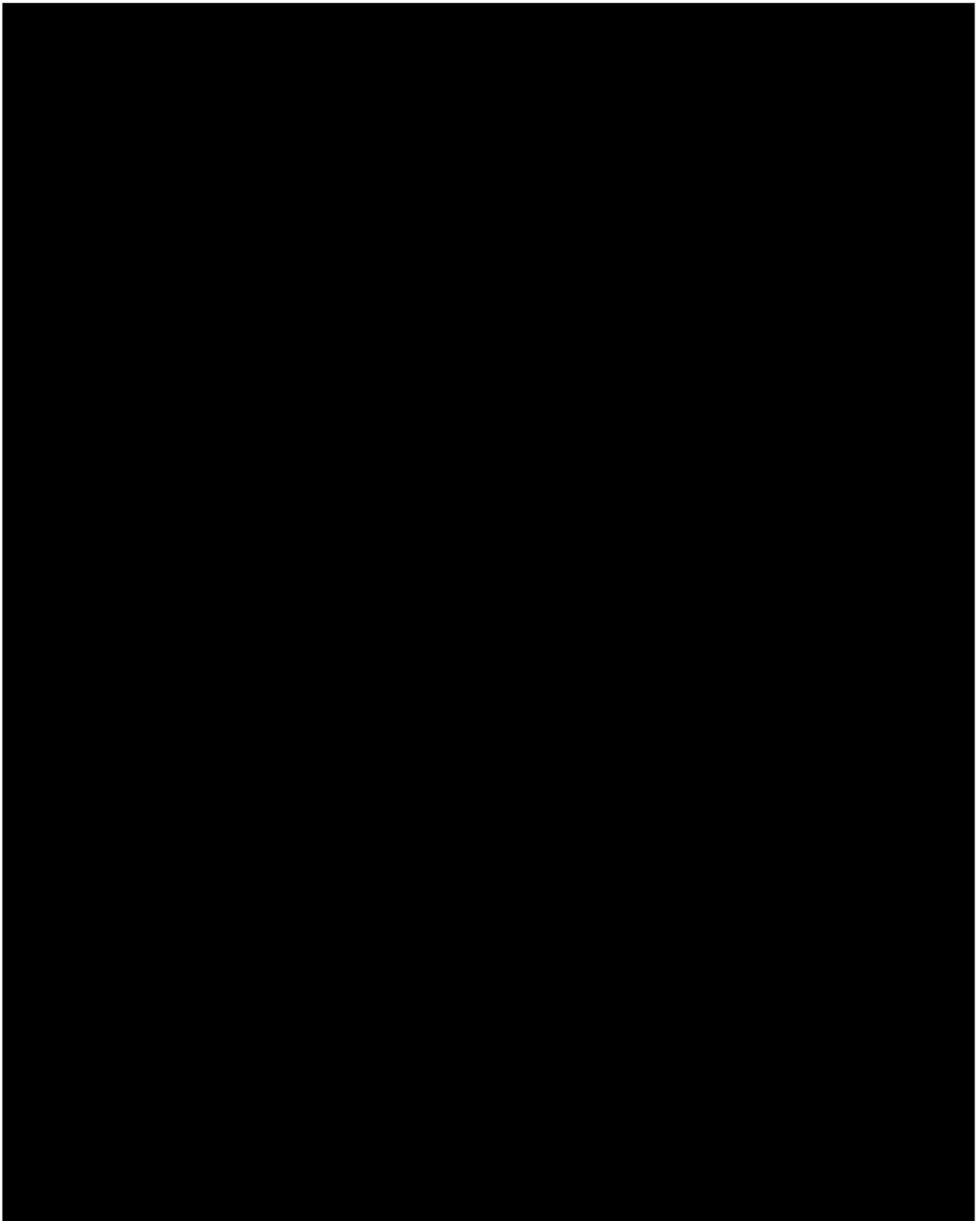
[REDACTED]

[REDACTED]

[REDACTED]

[REDACTED]





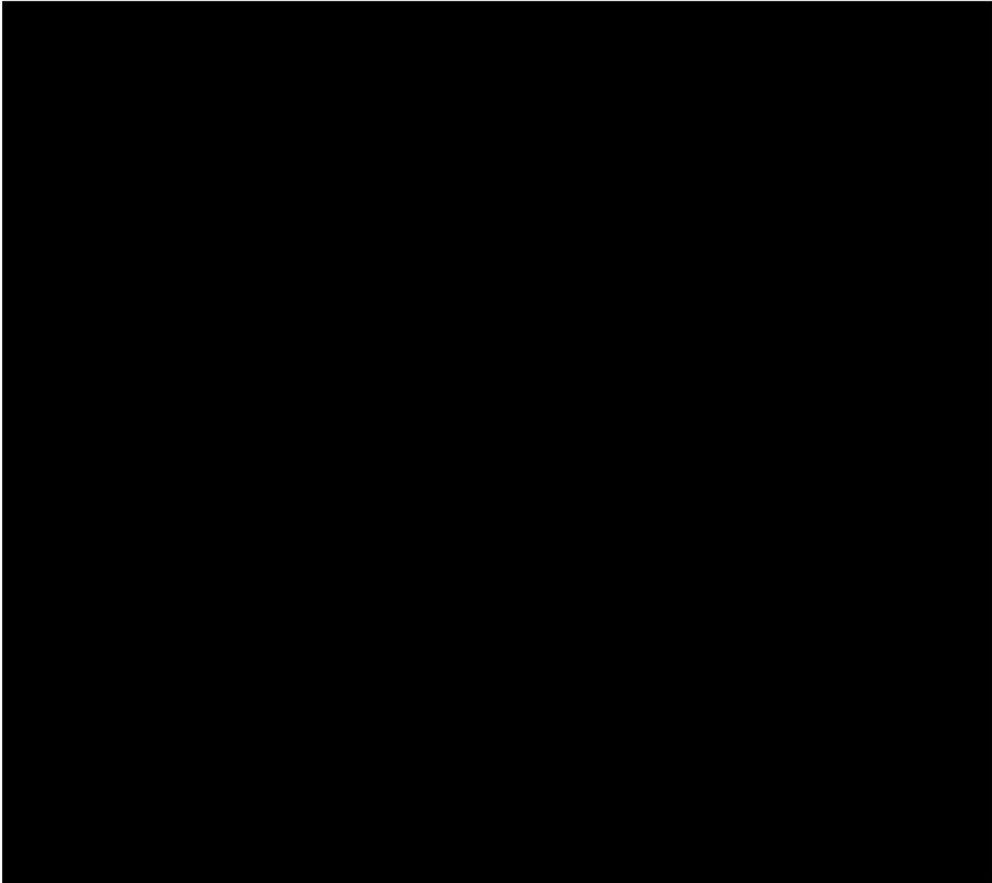
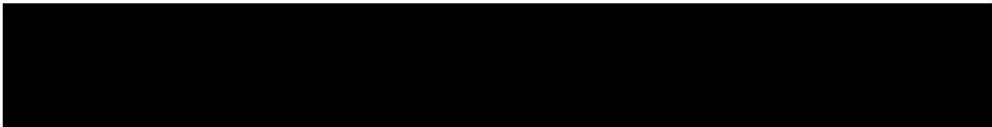


**Figure 5.31:** Measured (blue trace) and simulated (red trace) broadband input admittance magnitude response of Set 1 resonators (on top) and Set 2 resonators (on bottom). Zoomed input admittance close to three times the resonance frequency on the right respectively.



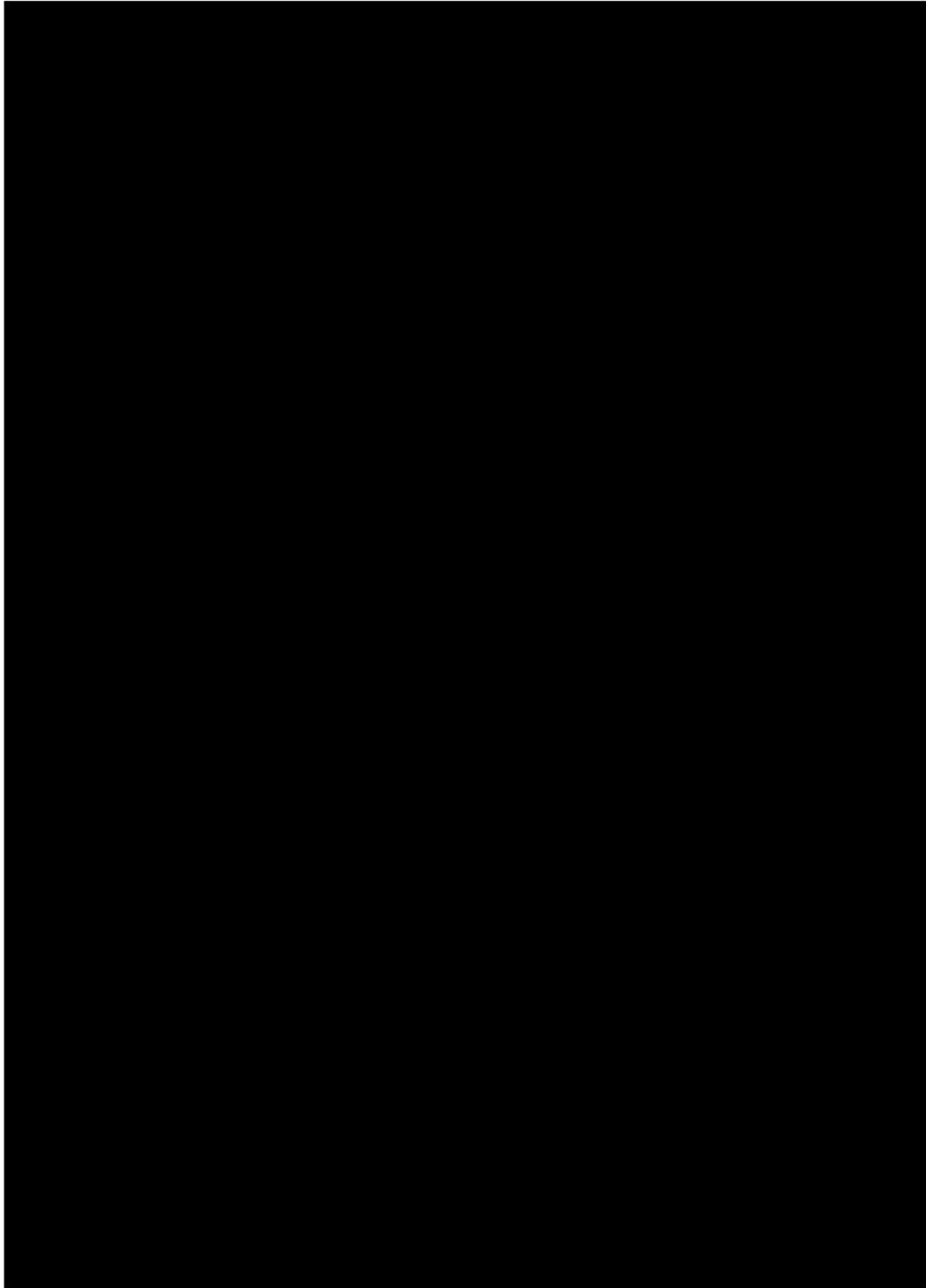
H3 nonlinear simulations considering edge-E linear model

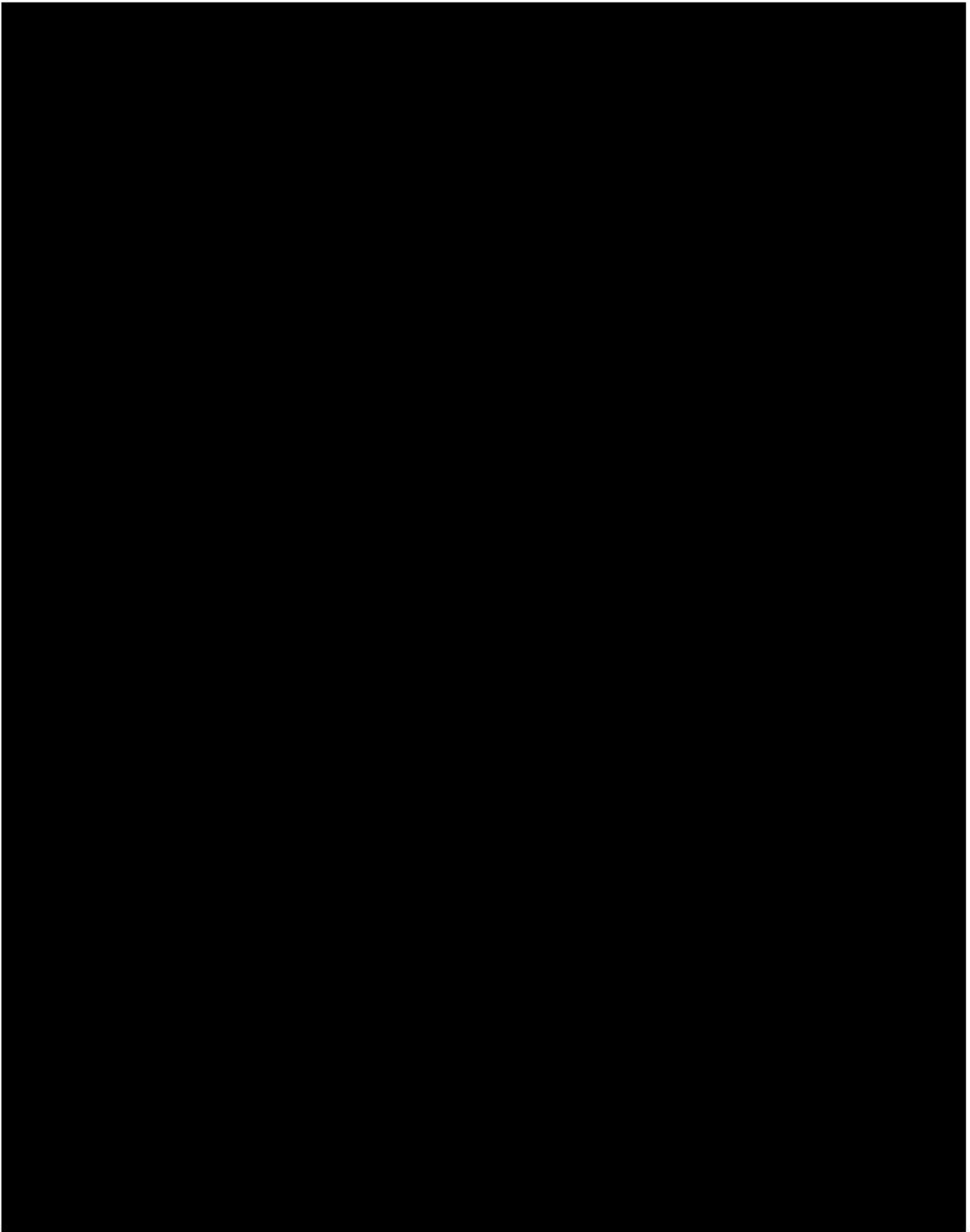
[REDACTED]

[REDACTED]

[REDACTED]







### Edge-E linear model IMD3 verification

Finally, the last step is to verify if the IMD3 response of the resonators remains unaltered in comparison with the previous results. Fig. 5.34 shows the IMD3 simulation results considering the edge-e linear model (non-uniform electric field) for Set 1 and Set 2 resonators.

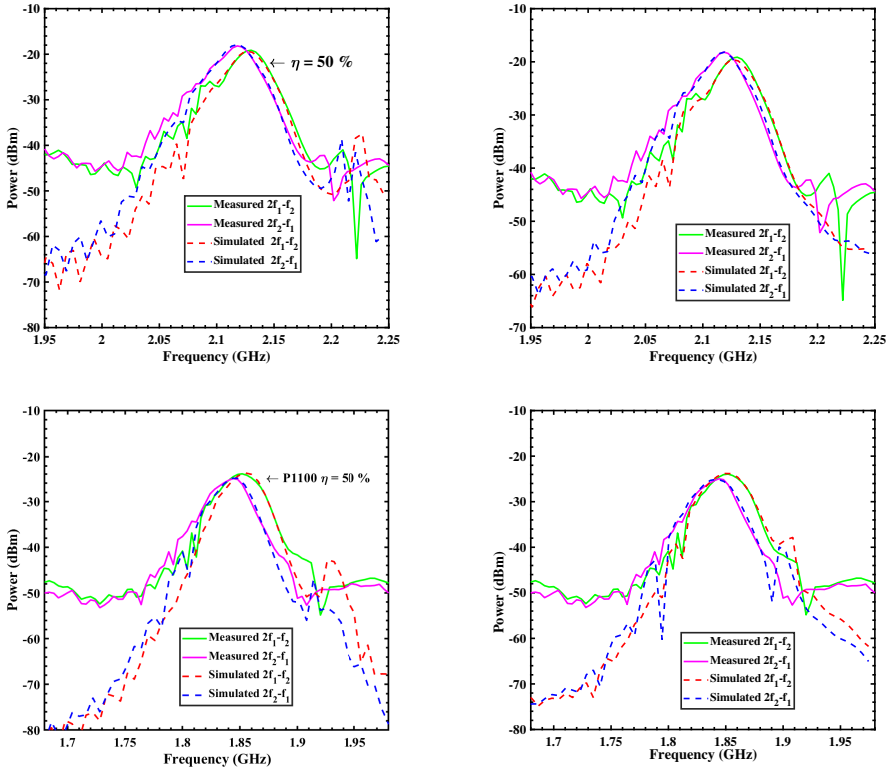


**Figure 5.34:** Measured IMD3 response (green and magenta solid trace) and simulations (blue and red dashed trace) for Set 1 (top) and Set 2 (bottom) resonators corresponding to  $2f_1 - f_2$  and  $2f_2 - f_1$  respectively. Left plot represents simulations with uniform electric field whereas right plot represents simulations with edge-E electric field.

As we can see in all the figures, the IMD3 response is still consistent with this new model in both Set 1 and Set 2.

### 5.4.7 Out-of-band IMD3 characterization

This subsection describes a new out-of-band IMD3 characterization set-up. The motivation to develop an out-of-band IMD3 set-up arises from the need of fully understand the origin and the behavior of the IMD3 response in zones just below and up series and shunt resonances of the measured resonators. [REDACTED]

[REDACTED]

[REDACTED]

#### Proposed two-tone cancellation system

Figure 5.35 shows the proposed two-tone cancellation system with the aim of improving the dynamic range of the measurement system. The general purpose of using a feed-forward cancellation system [91],[92], is to provide a mechanism able to suppress the excitation used before going into the SA. Basically, a feed-forward system uses a copy of the excitation signal (the fundamental tone) with same amplitude and opposite phase, and combines both the reflected signal coming from the DUT with the feed-forward signal to cancel out the first one. Iterative, gradient descent algorithms [93] are able to provide high levels of cancellation by finding the gain and phase shift to be applied to the cancelling signal that minimizes the power of the fundamental frequency going into the SA. The main drawback of this approach is that sometimes, a high number of iterations are needed to get the desired cancellation level.

This system consists of a conventional two tone test setup, with the addition of a feed-forward cancellation branch for one of the tones, which employs a variable attenuator and a Vector Modulator (VM). The system is automated using a Matlab application, with a graphical user interface (GUI) that allows to control the instru-



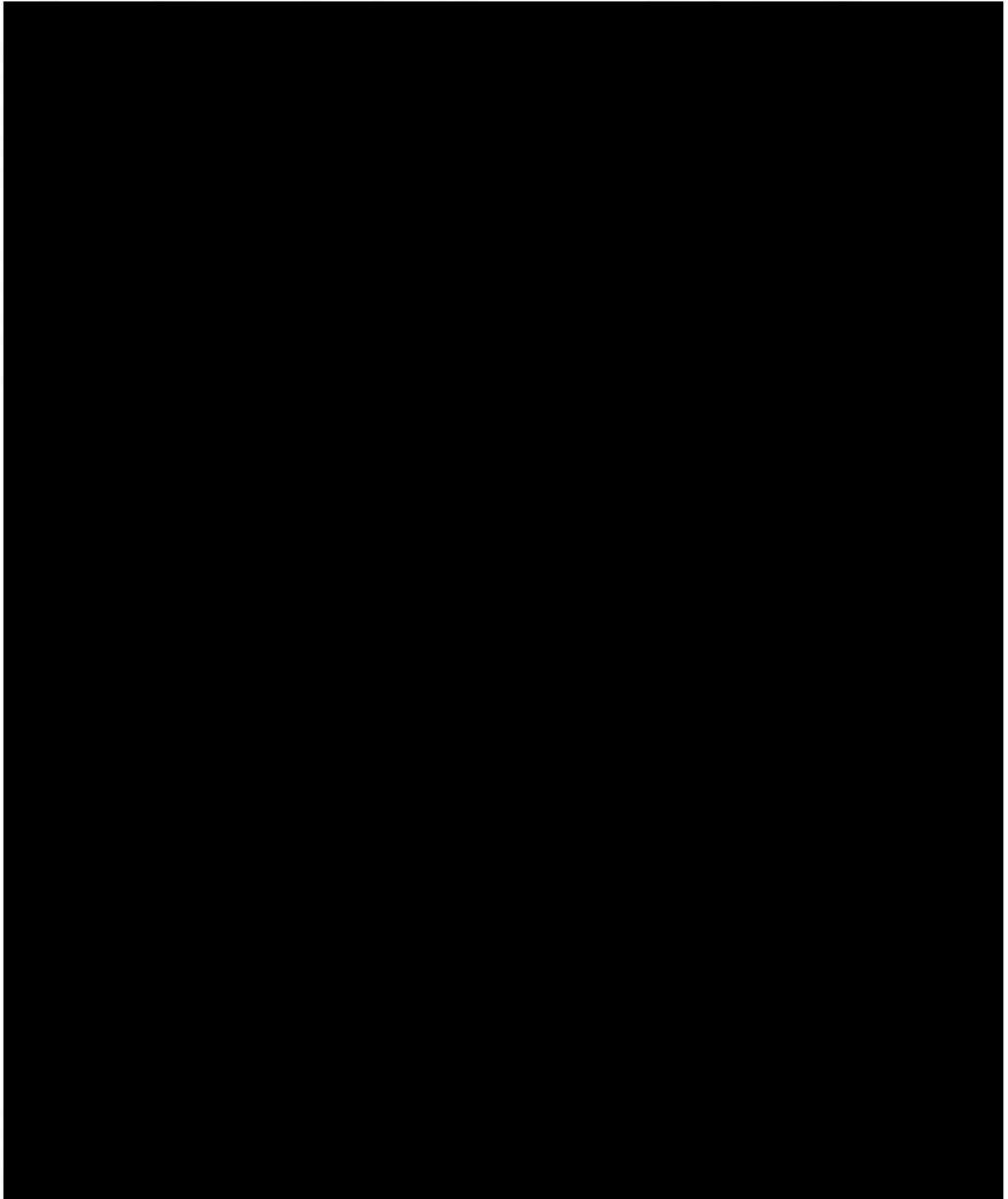
Figure 5.35: Schematic diagram of the proposed two-tone cancellation system. The experiment has been used to measure the out-of-band IMD3.

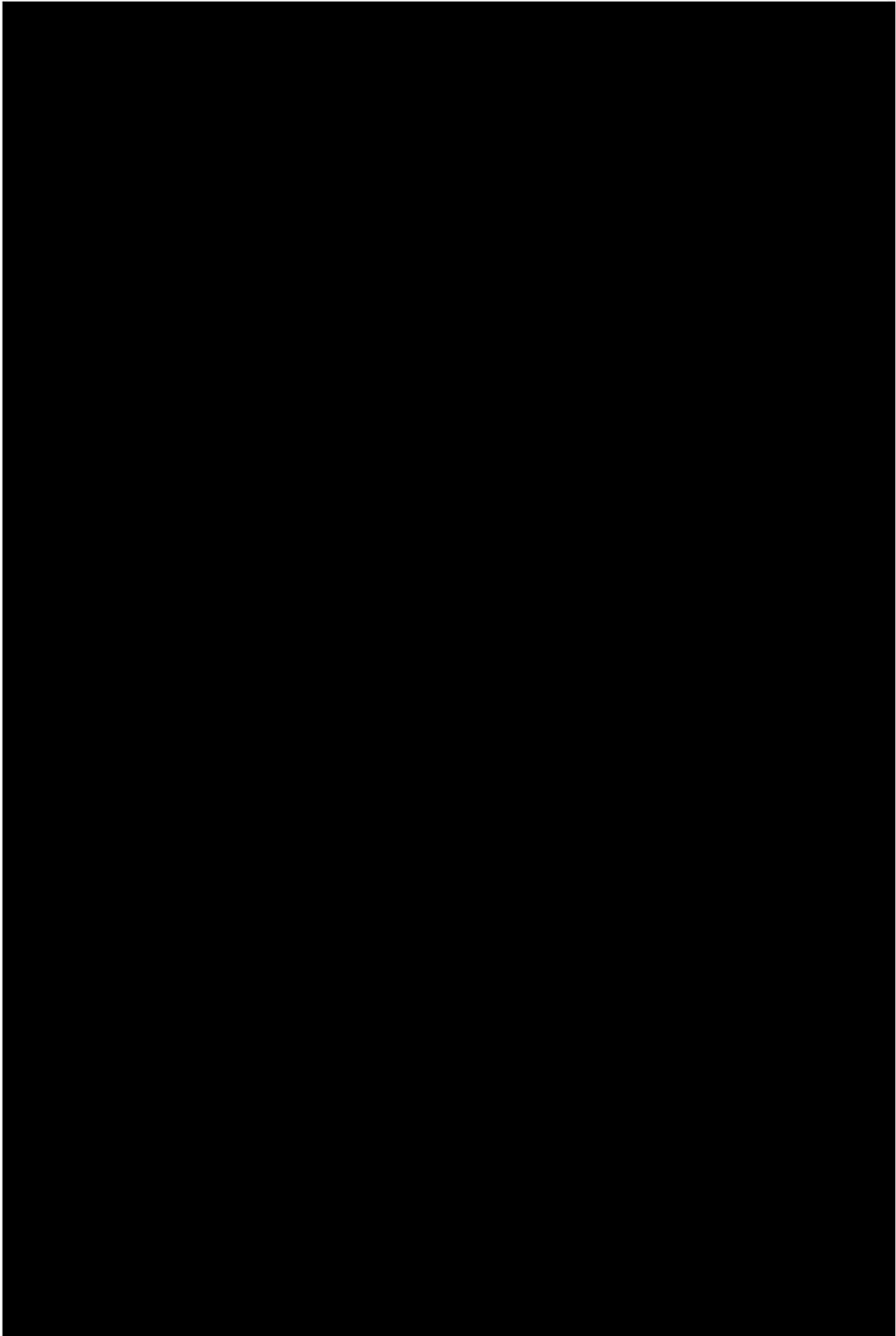
[REDACTED]

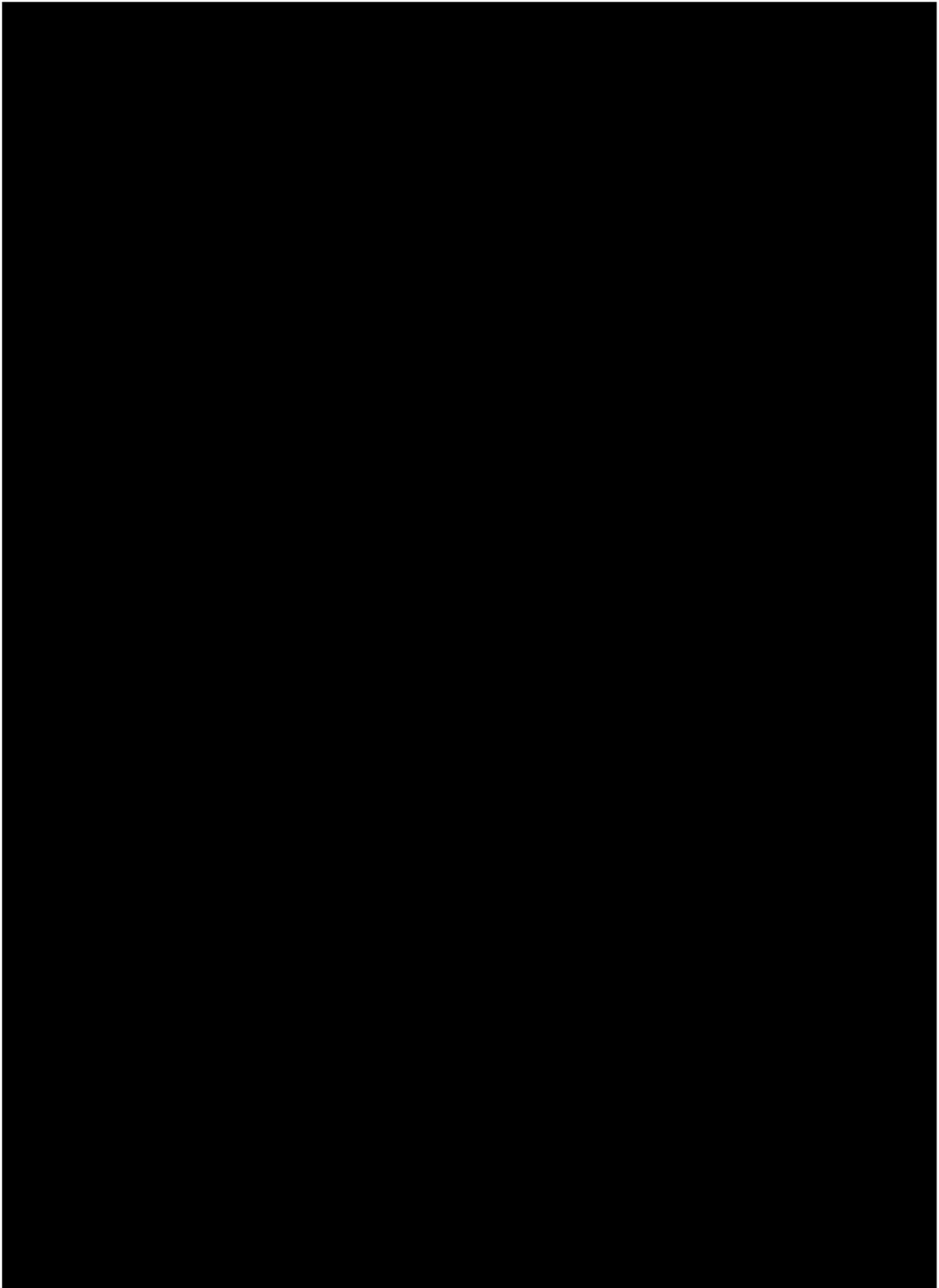
[REDACTED]

### Power sweep IMD3 characterization

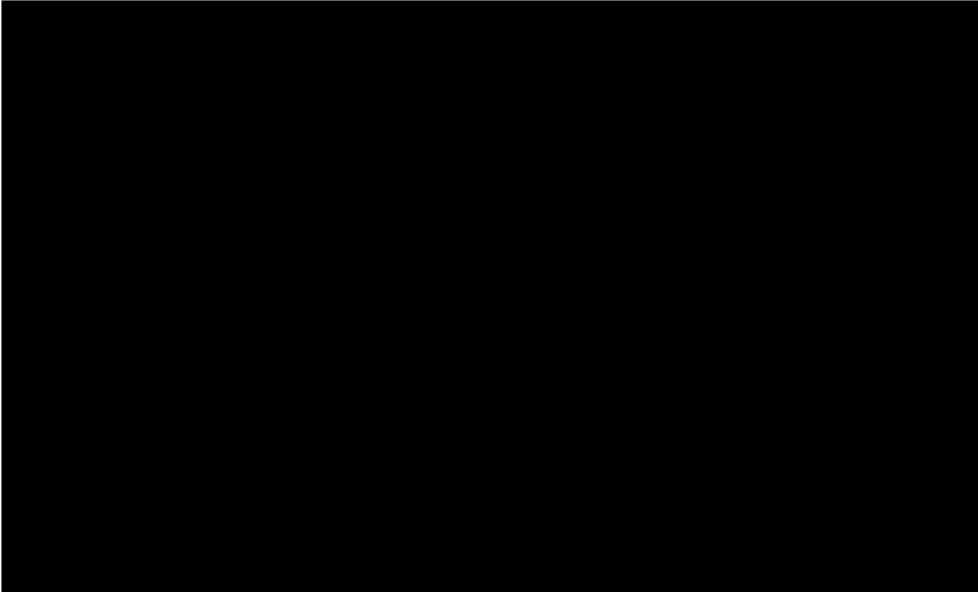
As it can be seen in Fig. 5.36, we previously obtained a disagreement between IMD3 measurements (magenta and green solid traces) and simulations (red and blue dashed traces) corresponding to  $2f_1 - f_2$  and  $2f_2 - f_1$  respectively on the left zone of the IMD3 response. This Fig. 5.36 corresponds to a 900 nm pitch and  $\eta = 50\%$  resonator. The main objective here is to understand the cause of this disagreement.











#### Out-of-band IMD3 characterization

Once the nonlinear scenario of section 5.4.7 is decided, we need to evaluate the measurement system at those frequencies. The measurement system employed is the same as the one depicted in Fig. 5.35 and the power calibration of the fundamental tones is also performed resulting in 17 dBm for  $f_1$  and 15 dBm for  $f_2$  respectively. Then, the next step is to ensure that the measured IMD3 of the DUT can be separated for those corresponding to the system. Fig. 5.40 shows the IMD3 response floor level with the probes set on air. Note that regarding the IMD3 results, we can observe a -90 and -100 dBm for the IMD3 floor level.

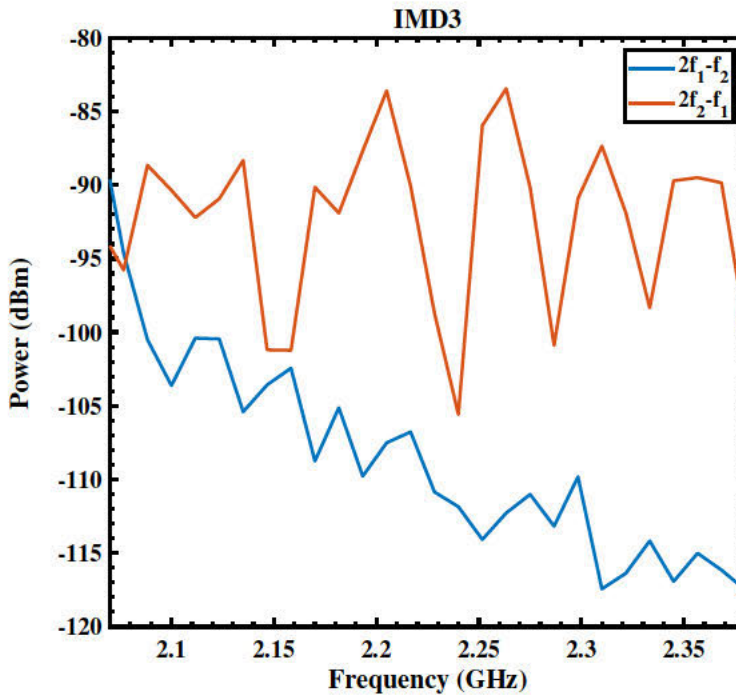
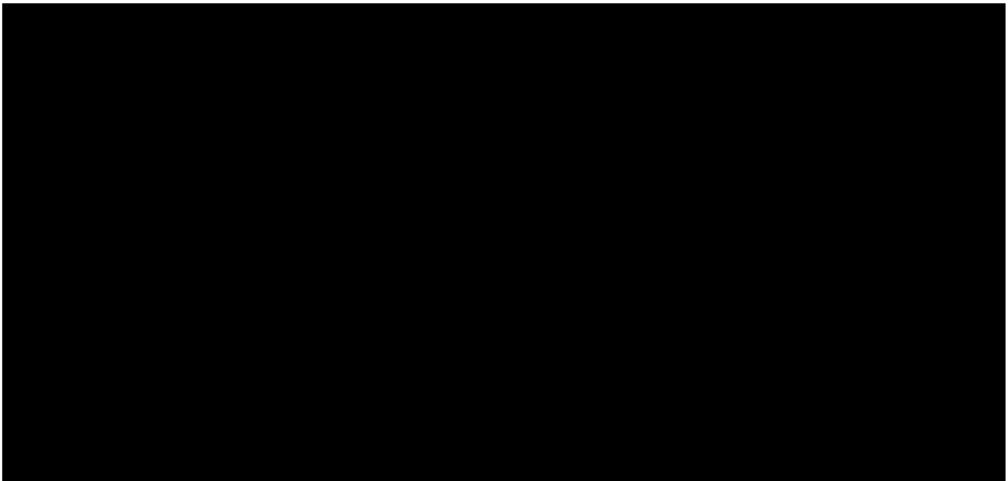
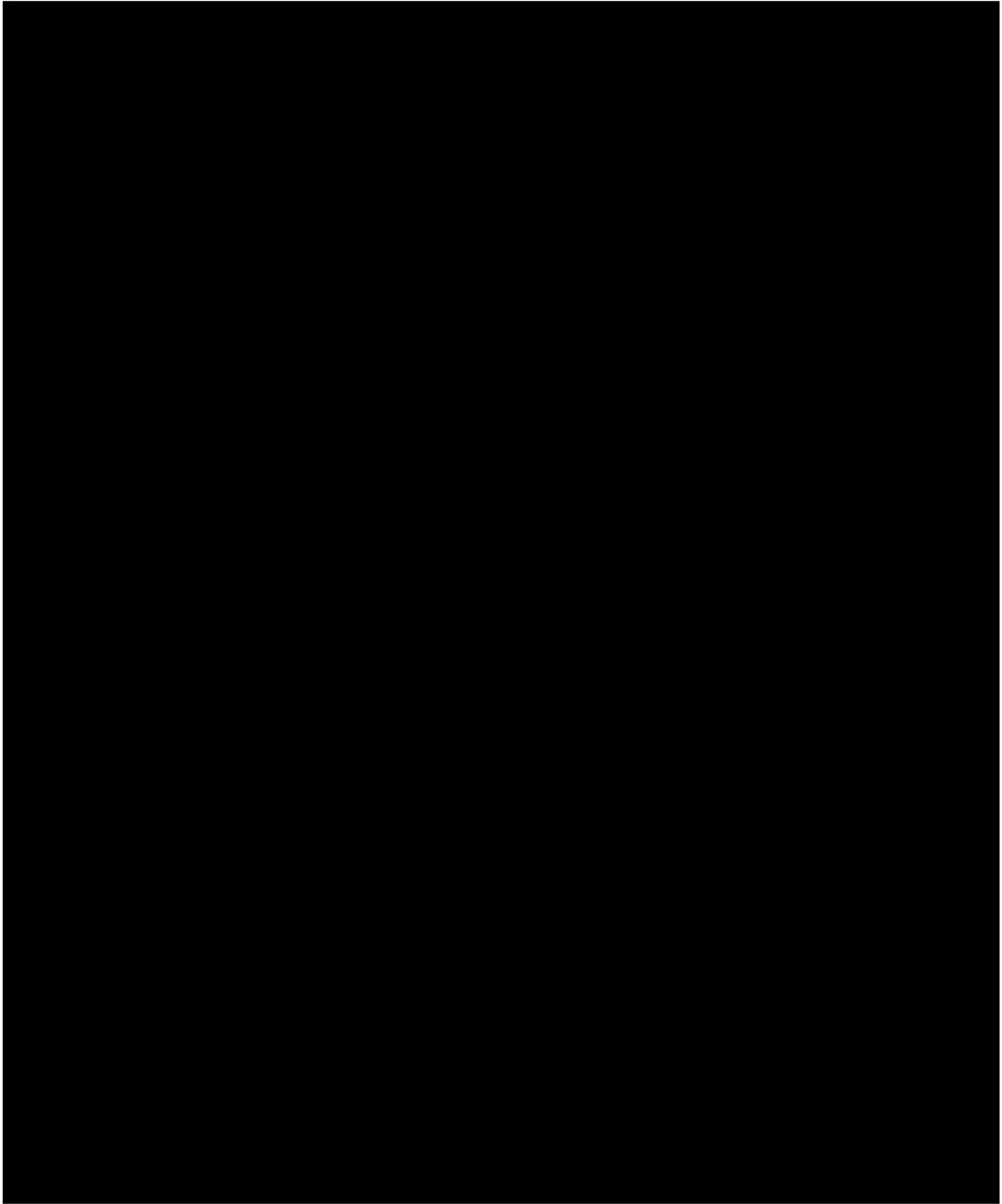
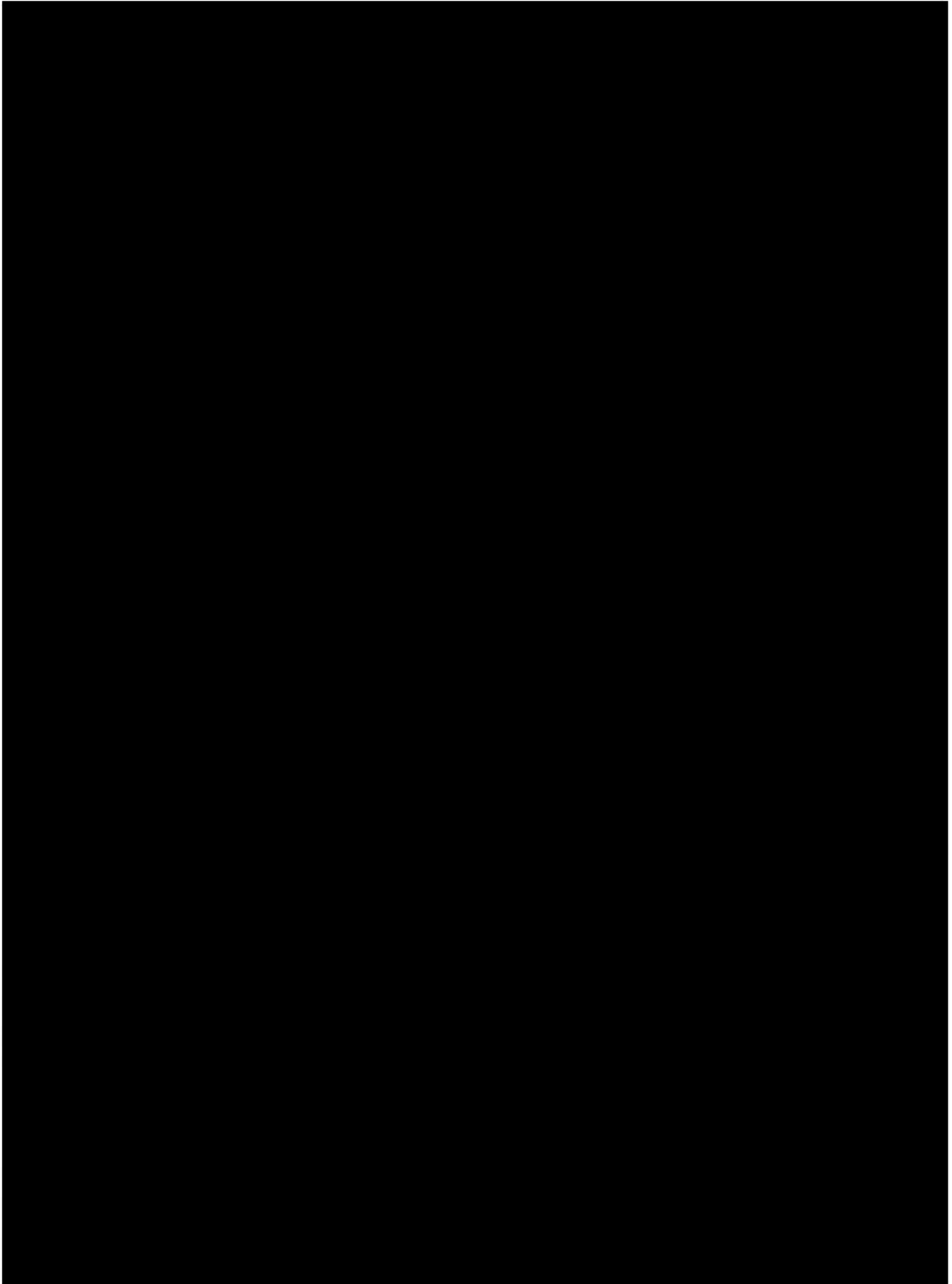


Figure 5.40: Measured IMD3 response of the measurement system of the out-of-band IMD3 of 1000 nm pitch and  $\eta = 50\%$  resonator.

Fig. 5.41 shows the measured IMD3 response of the pitch 1000 nm and  $\eta = 50\%$  resonator. Specifically, green and magenta solid traces ( $2f_1 - f_2$  and  $2f_2 - f_1$  respectively) are measured IMD3 and red and blue dashed traces correspond to simulations.



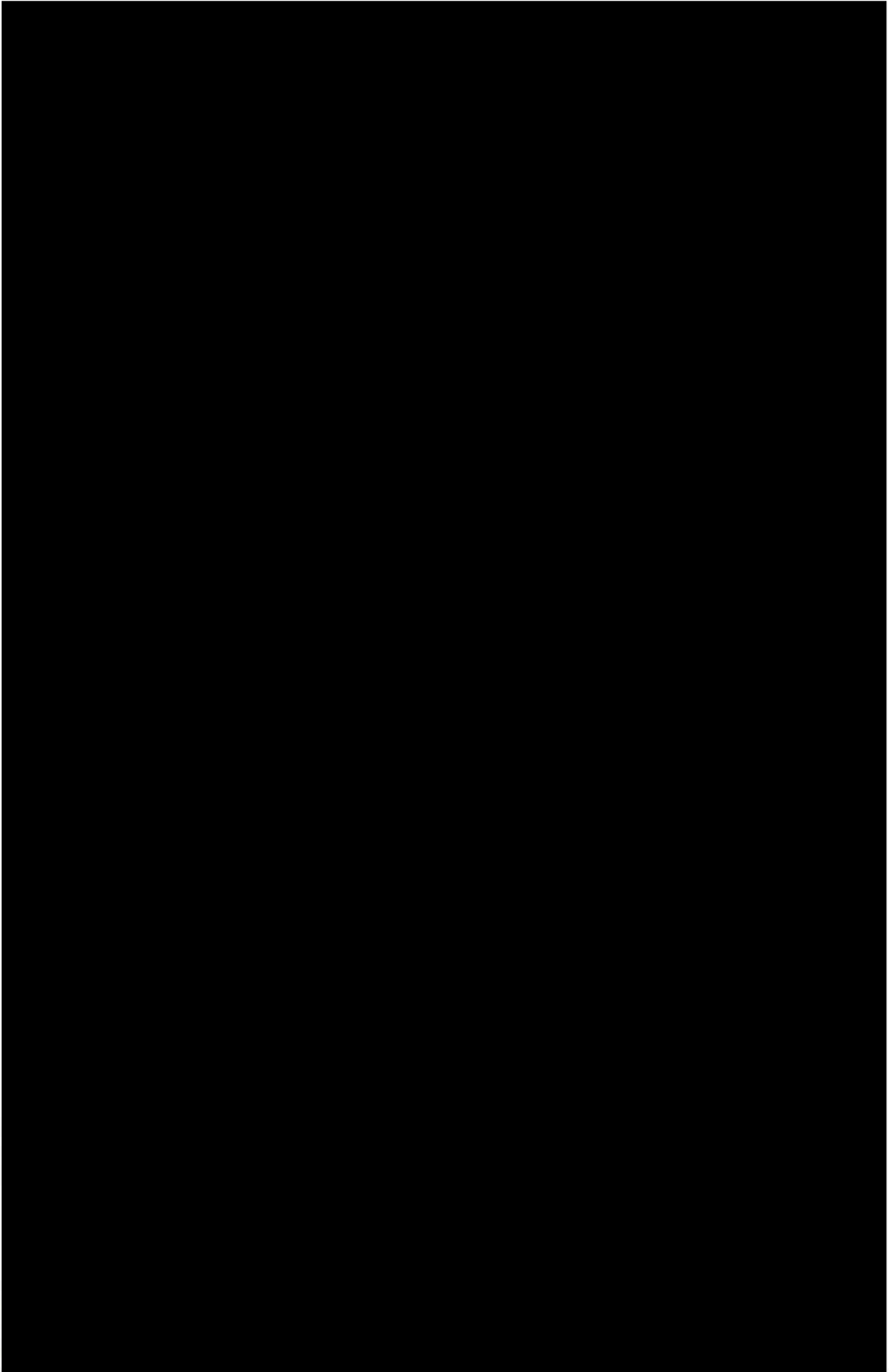


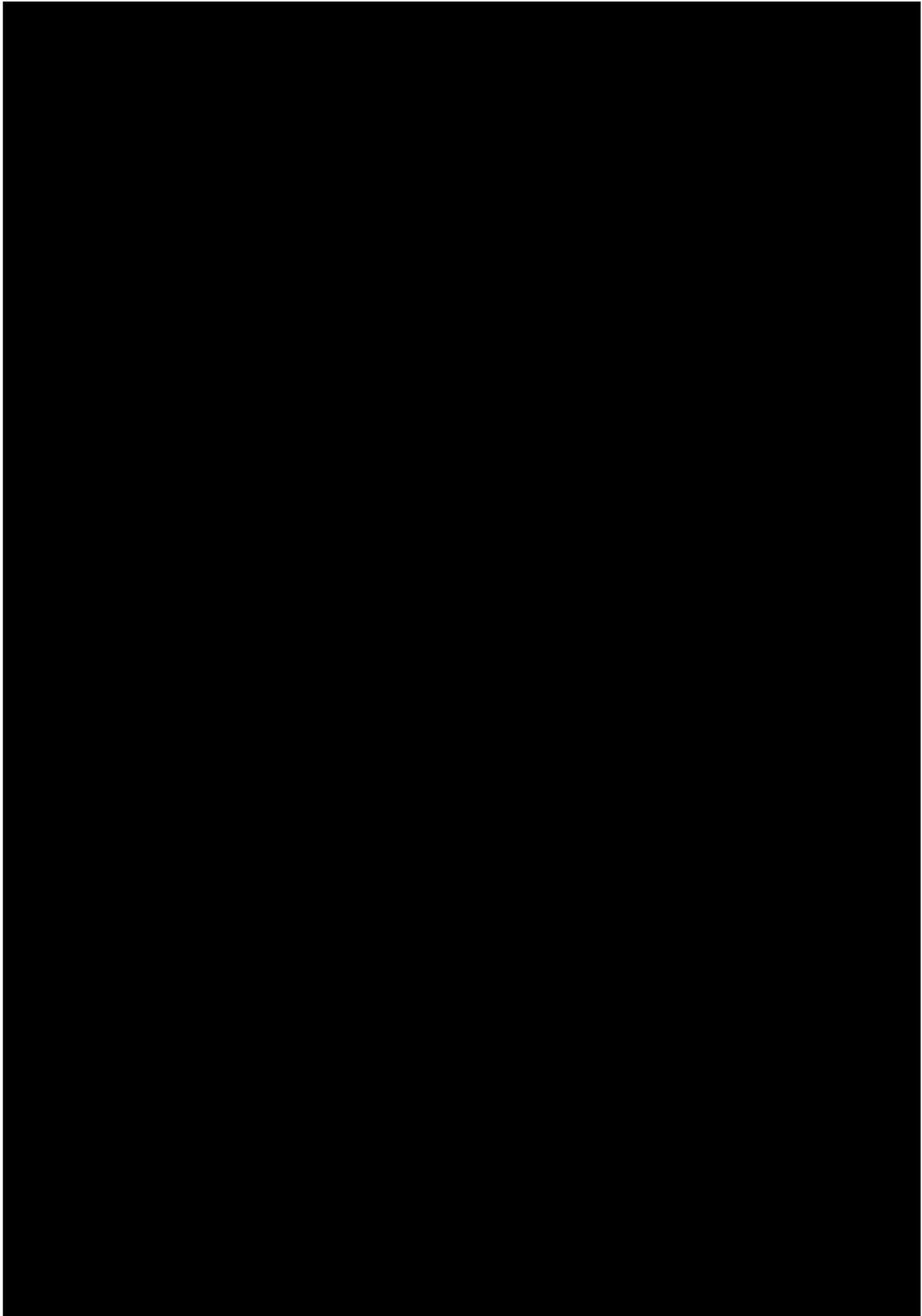


### 5.4.8 H2 nonlinear fitting and characterization

[REDACTED]

[REDACTED]





[REDACTED]

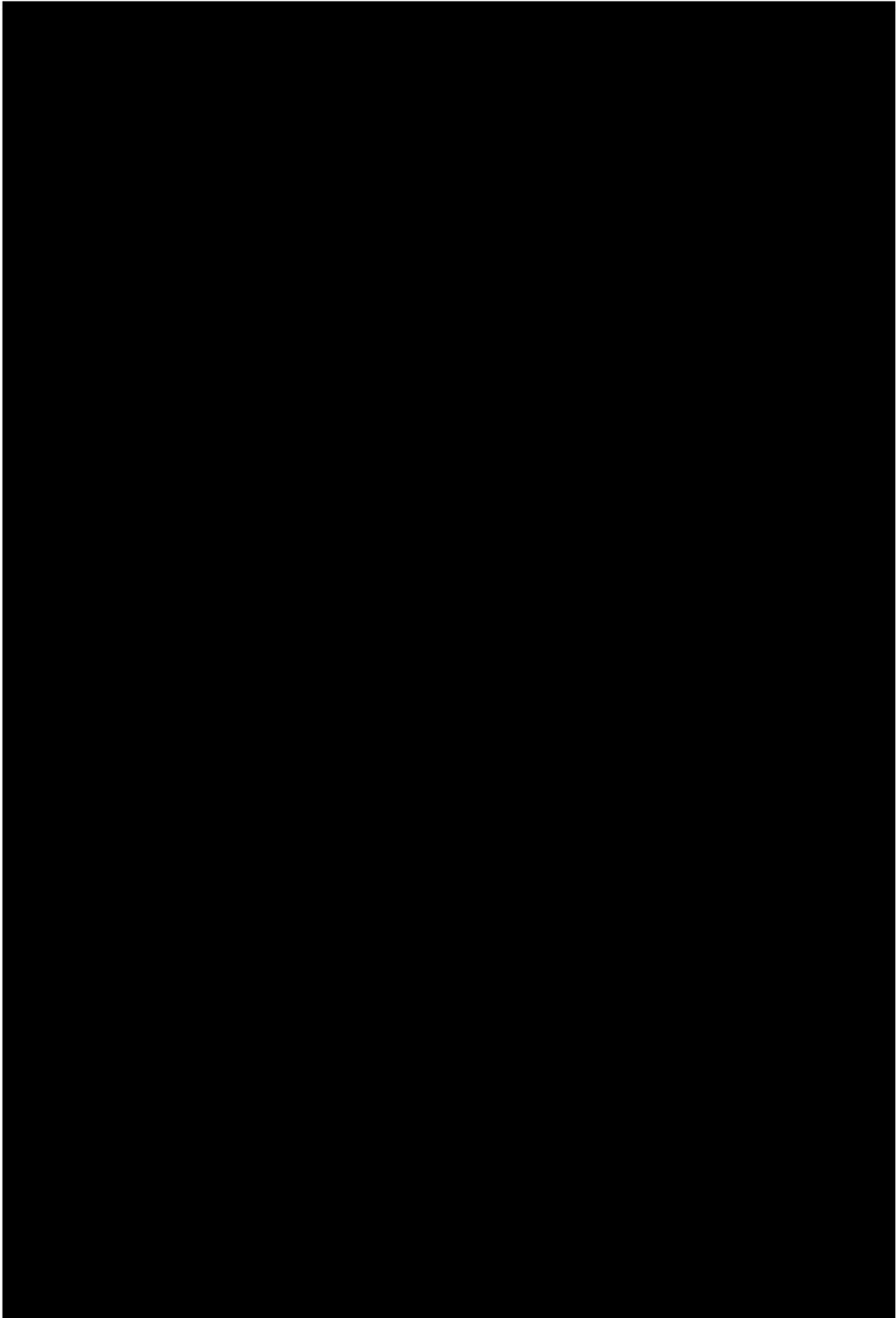
[REDACTED]

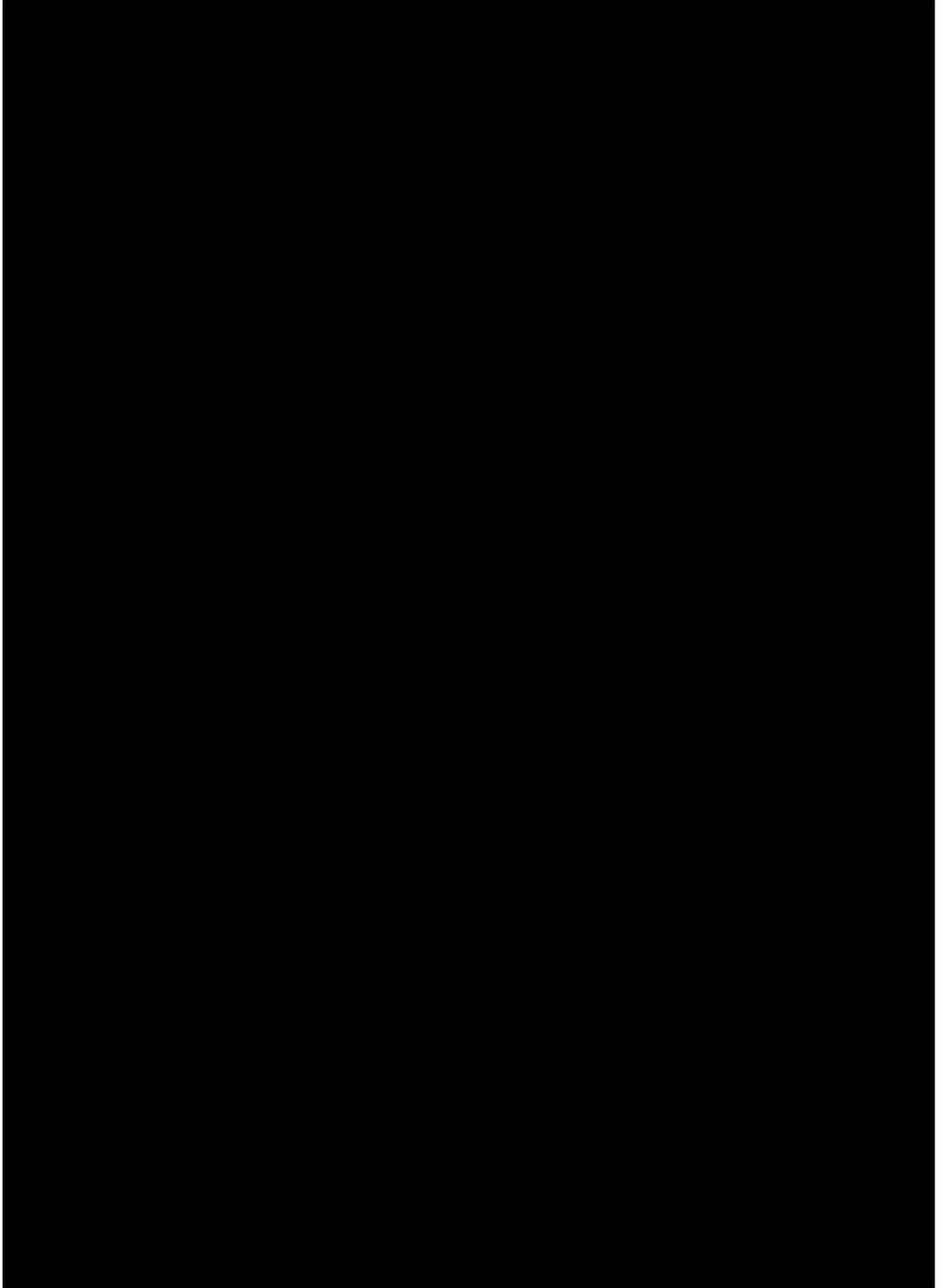
[REDACTED]

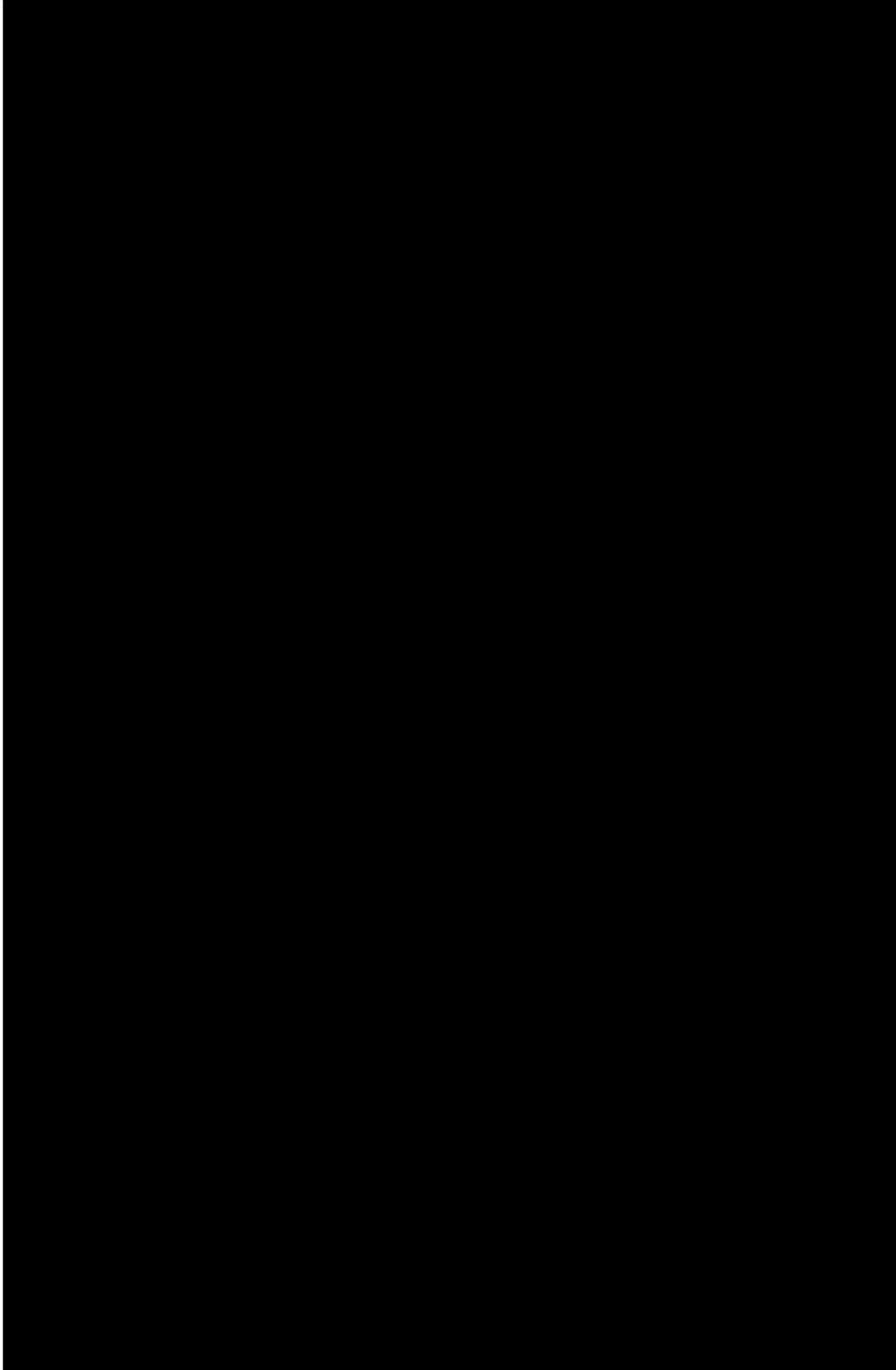
[REDACTED]	[REDACTED]
[REDACTED]	[REDACTED]
[REDACTED]	[REDACTED]
[REDACTED]	[REDACTED]
[REDACTED]	[REDACTED]
[REDACTED]	[REDACTED]
[REDACTED]	[REDACTED]
[REDACTED]	[REDACTED]
[REDACTED]	[REDACTED]
[REDACTED]	[REDACTED]

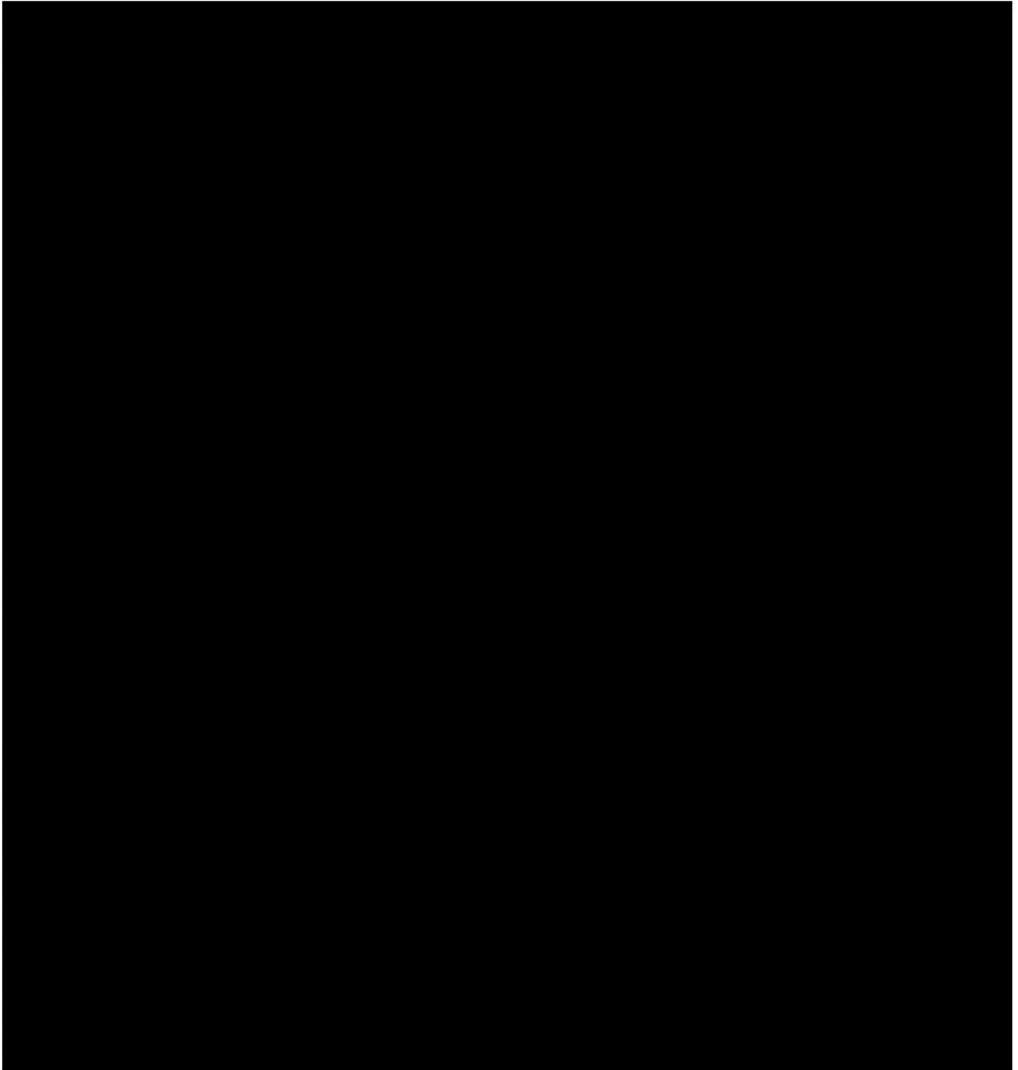
[REDACTED]

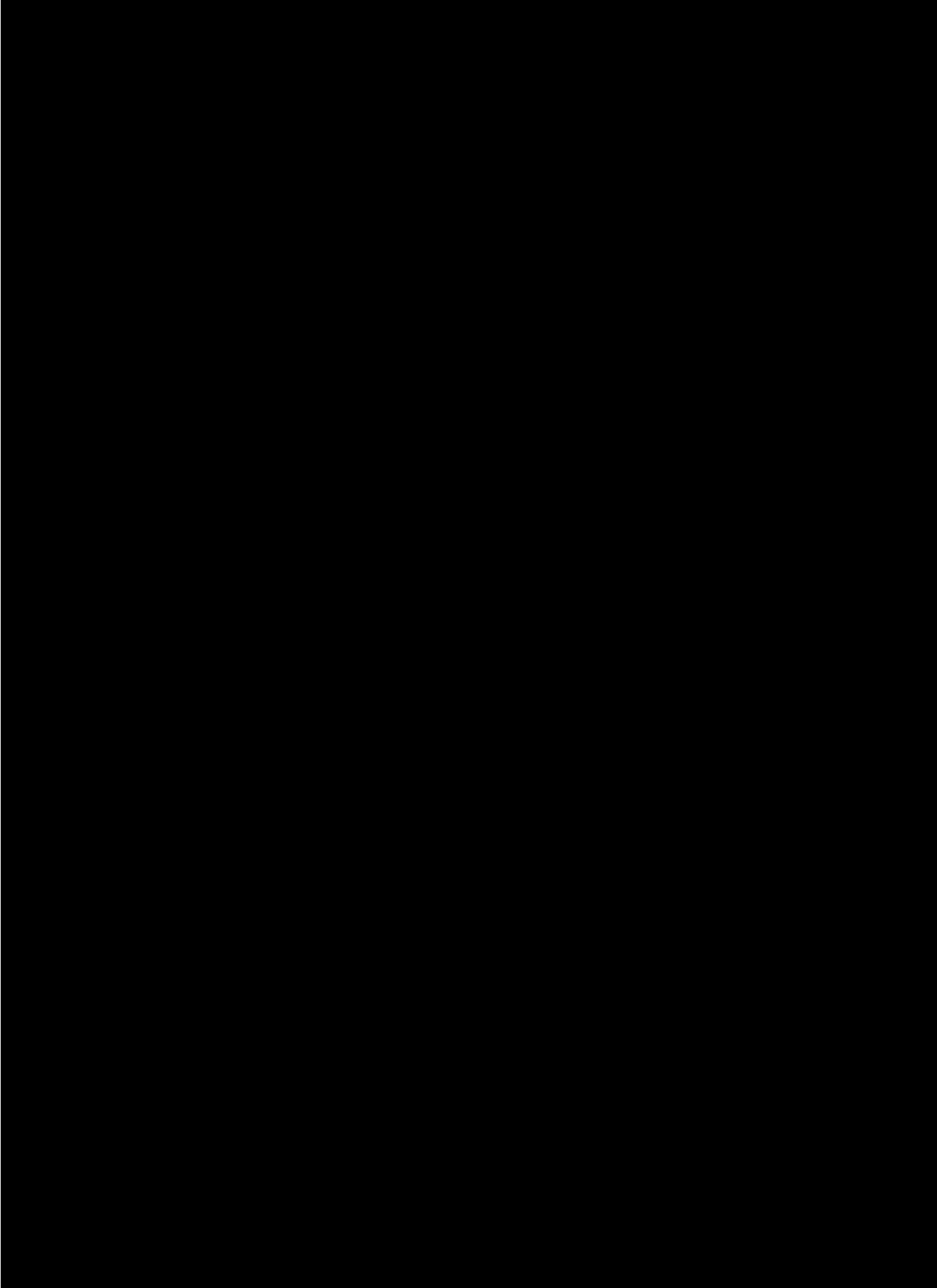












## 5.5 TC-SAW resonators response analysis

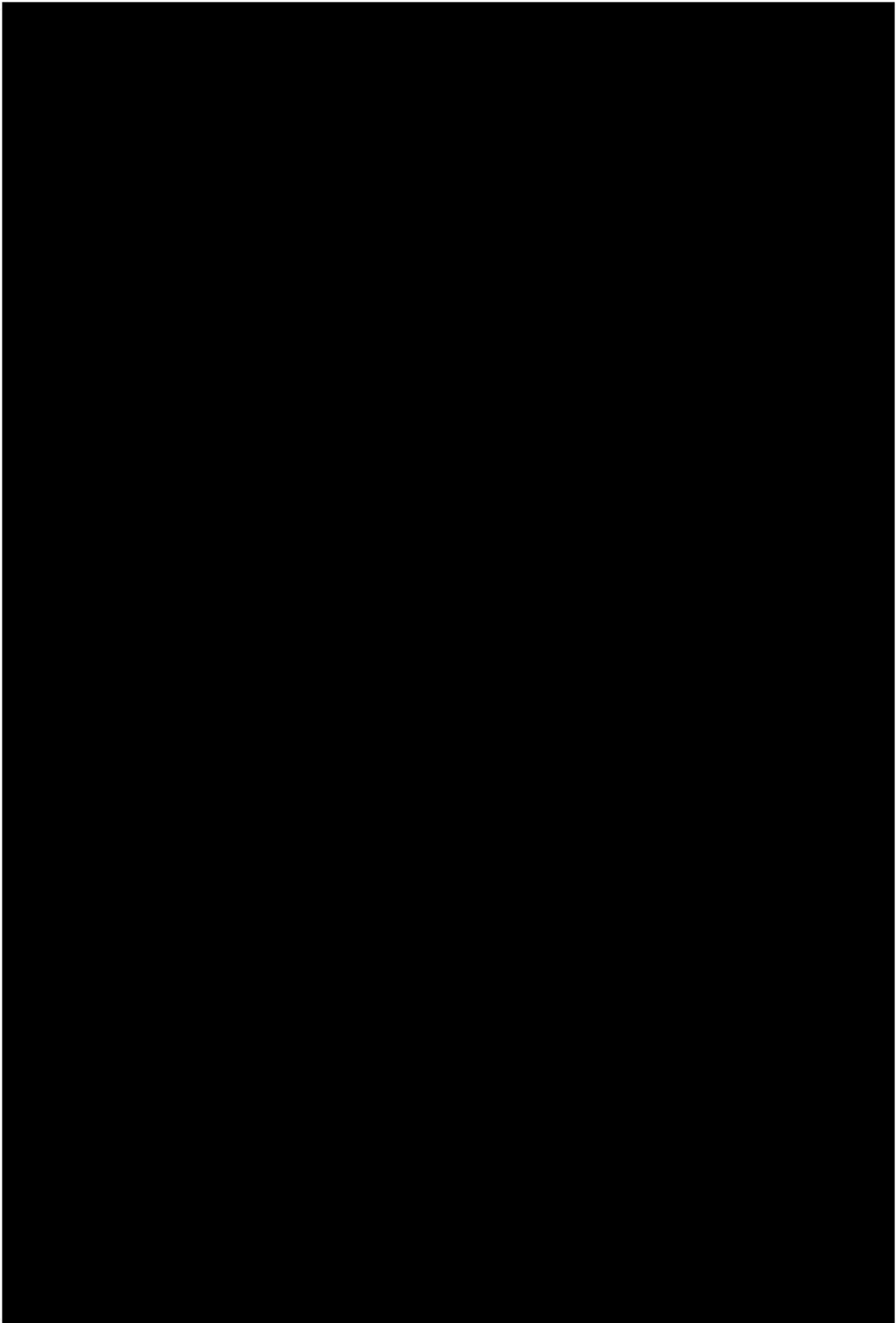
This section analyzes the TC-SAW resonators response. Due to the limitations of the measurements system (IMD3 and H3 floor level in Fig. 5.12 and H2 floor level in Fig. 5.14) the analysis of these resonators is reduced to the following steps:

- Analysis of the linear response, comparing measurements versus simulations.
- Use of the IOES method to proceed with the IMD3 and H3 nonlinear simulation of TC-SAW resonators, considering uniform electric field model and only a single shape-independent nonlinear parameter.



### 5.5.1 Broadband linear response measurement versus simulations

Once the narrowband linear measurements were validated in section 3.2.4, we proceed to carry out broadband measurements of the corresponding set of TC-SAW resonators. Fig. 5.52 shows the broadband linear response of measured TC-SAW resonators of variable pitch and fixed duty factors [redacted] respectively. Note that in Fig. 5.52 an artificial offset (a factor 1/10 per resonator) was added for easy viewing of the traces. Furthermore, details about the parameters used for the linear and nonlinear simulations of the TC-SAW resonators can be found in Appendix D section D.2.



[REDACTED]

### 5.5.2 IMD3 and H3 nonlinear characterization of TC-SAW resonators

An accurate analysis of the contribution of the 3rd-order nonlinear constant to the nonlinear IMD3 and H3 response of an example TC-SAW resonator is presented. The idea is as done previously with the LSAW resonators, identify the major contributors for the IMD3 and H3 nonlinear response.

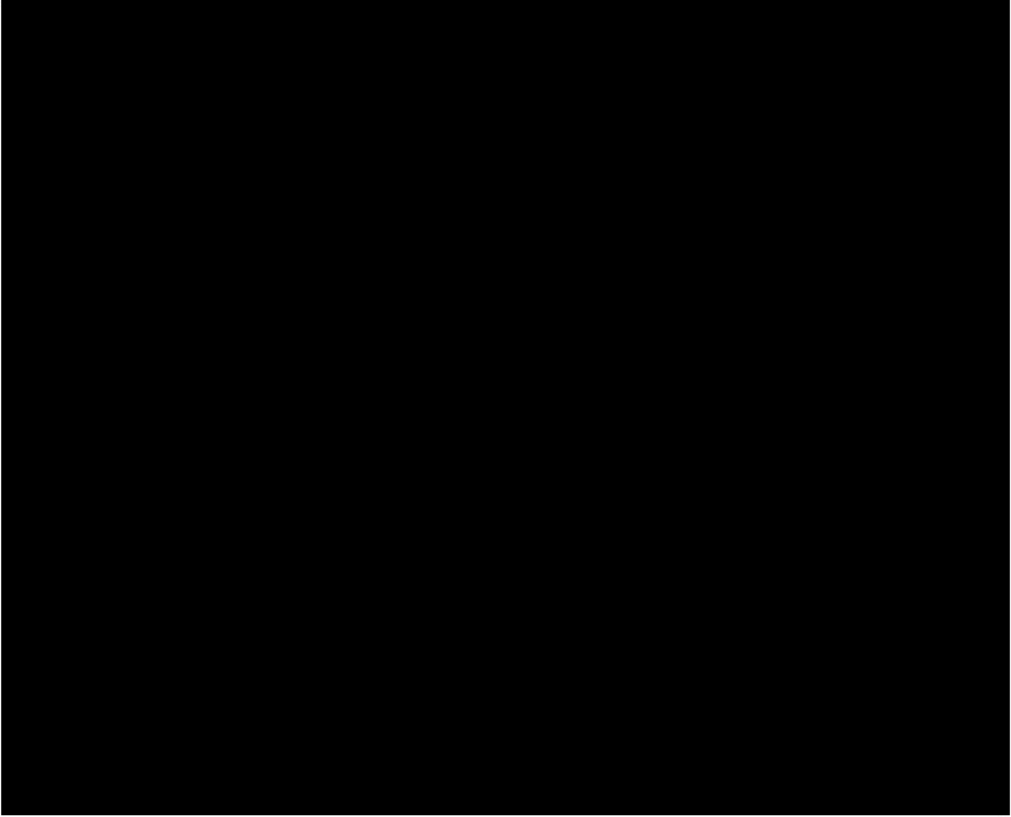
#### Identification of potential contributors

Following the same procedure as done in sections 5.4.2 and 5.4.4, we check the individual contributions of the nonlinear constants in the IMD3 and H3 response with the same reference resonator. Remix effects are discarded since they are not considered relevant in this particular case based on the results obtained in the previous Fig. 5.19

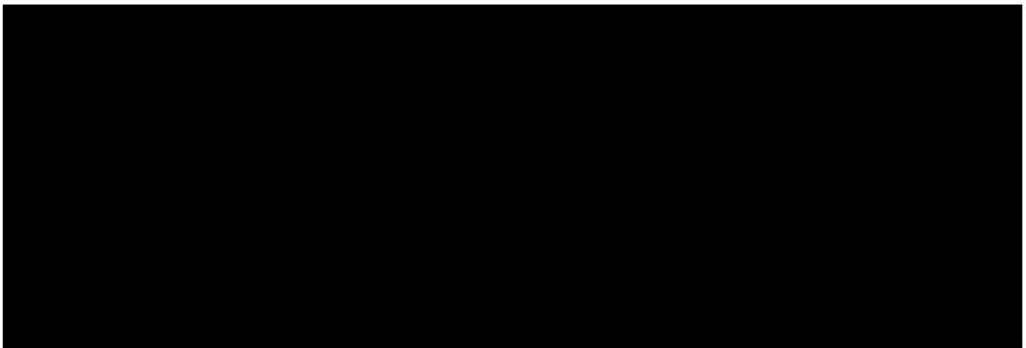
[REDACTED]

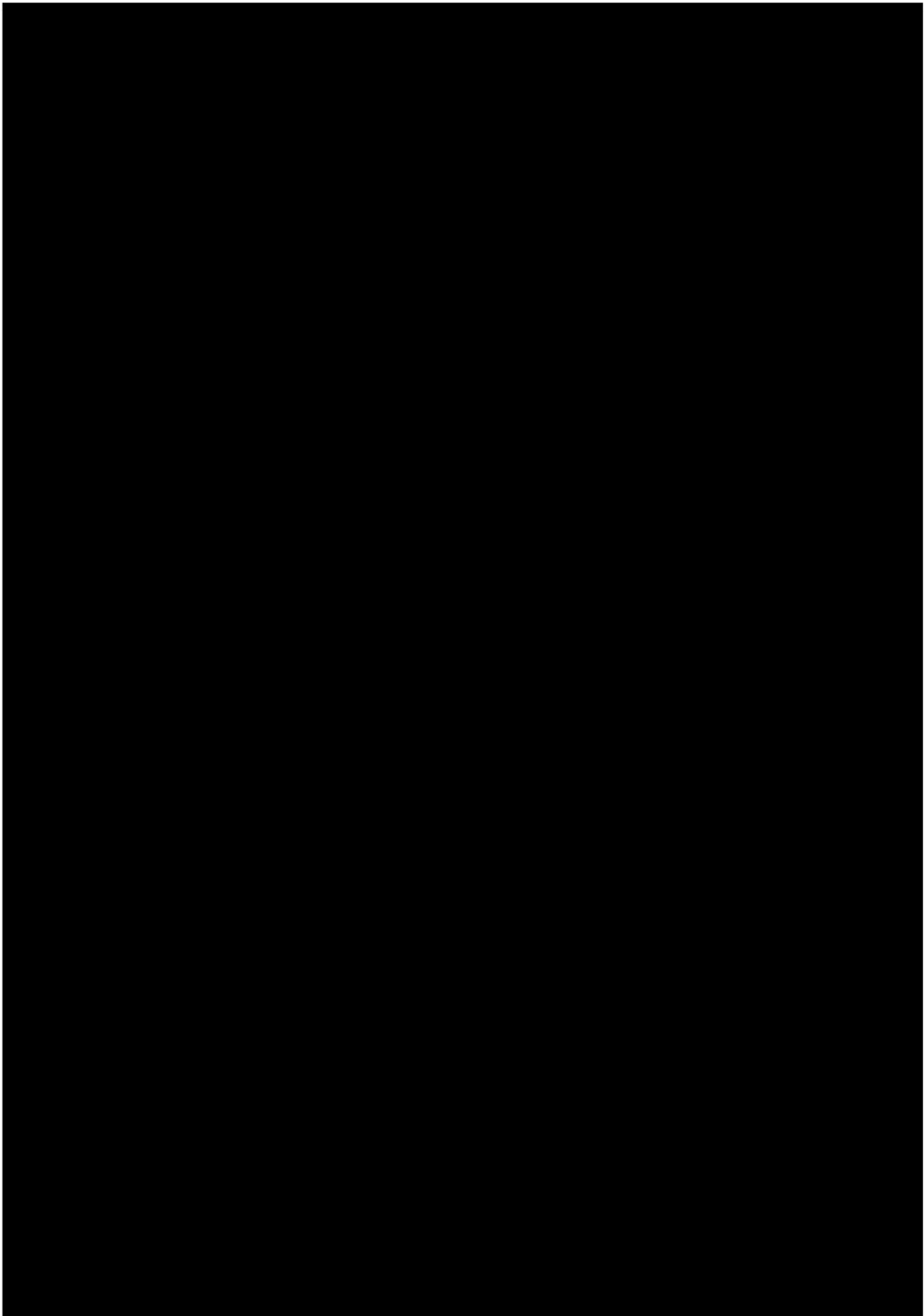






### 5.5.3 IMD3 and H3 nonlinear fitting of TC-SAW resonators

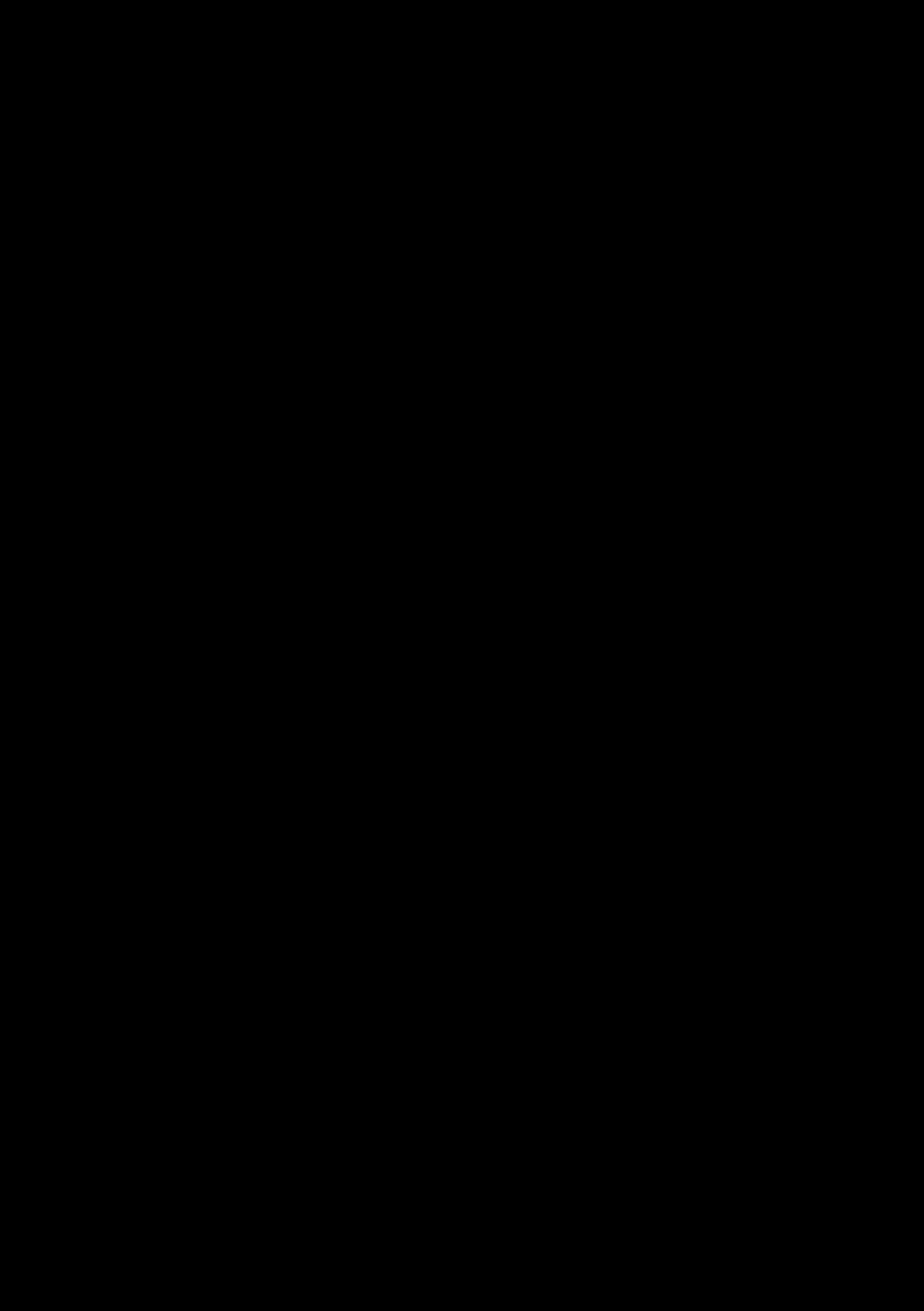


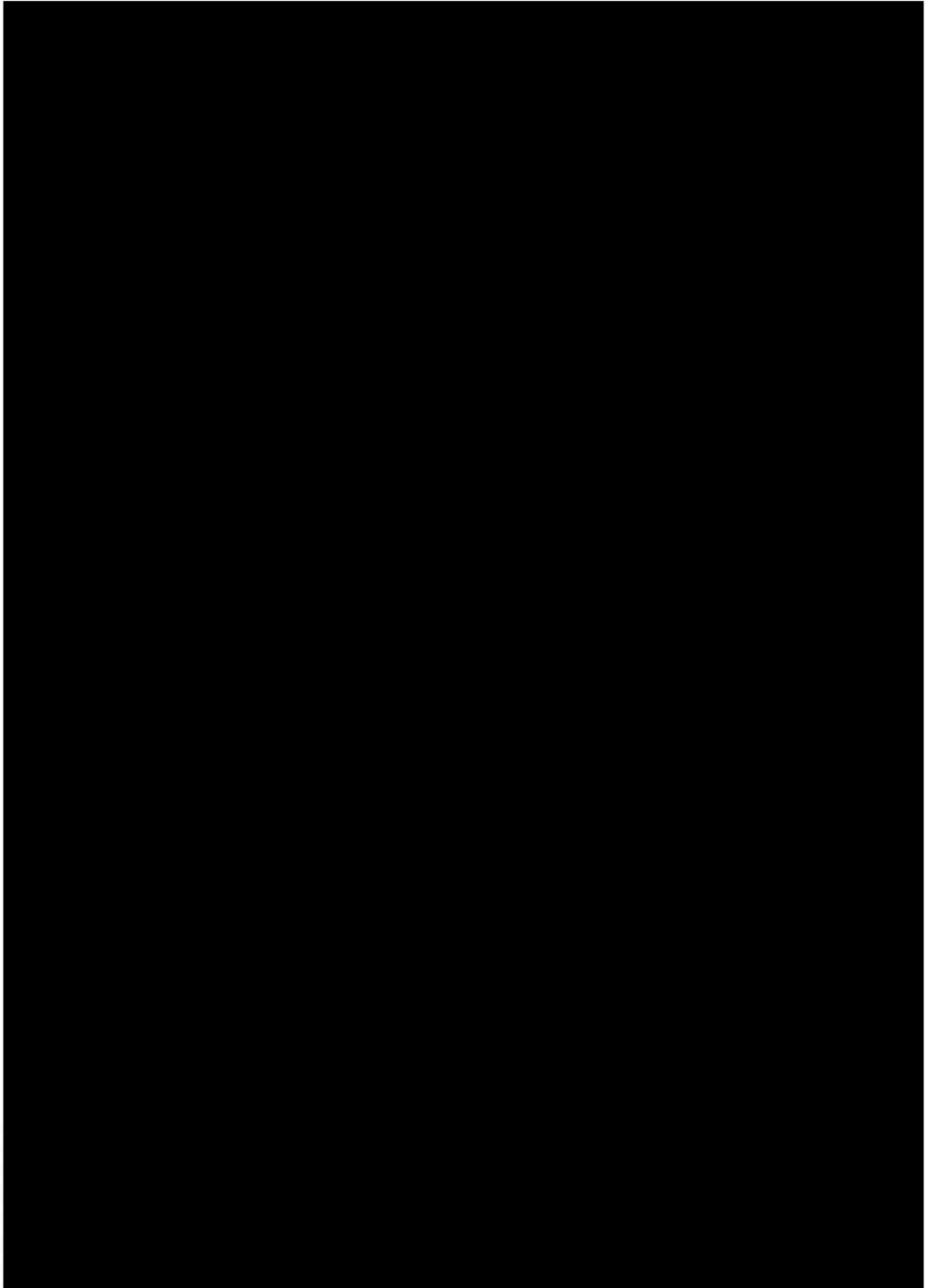


[REDACTED]

[REDACTED]

[REDACTED]

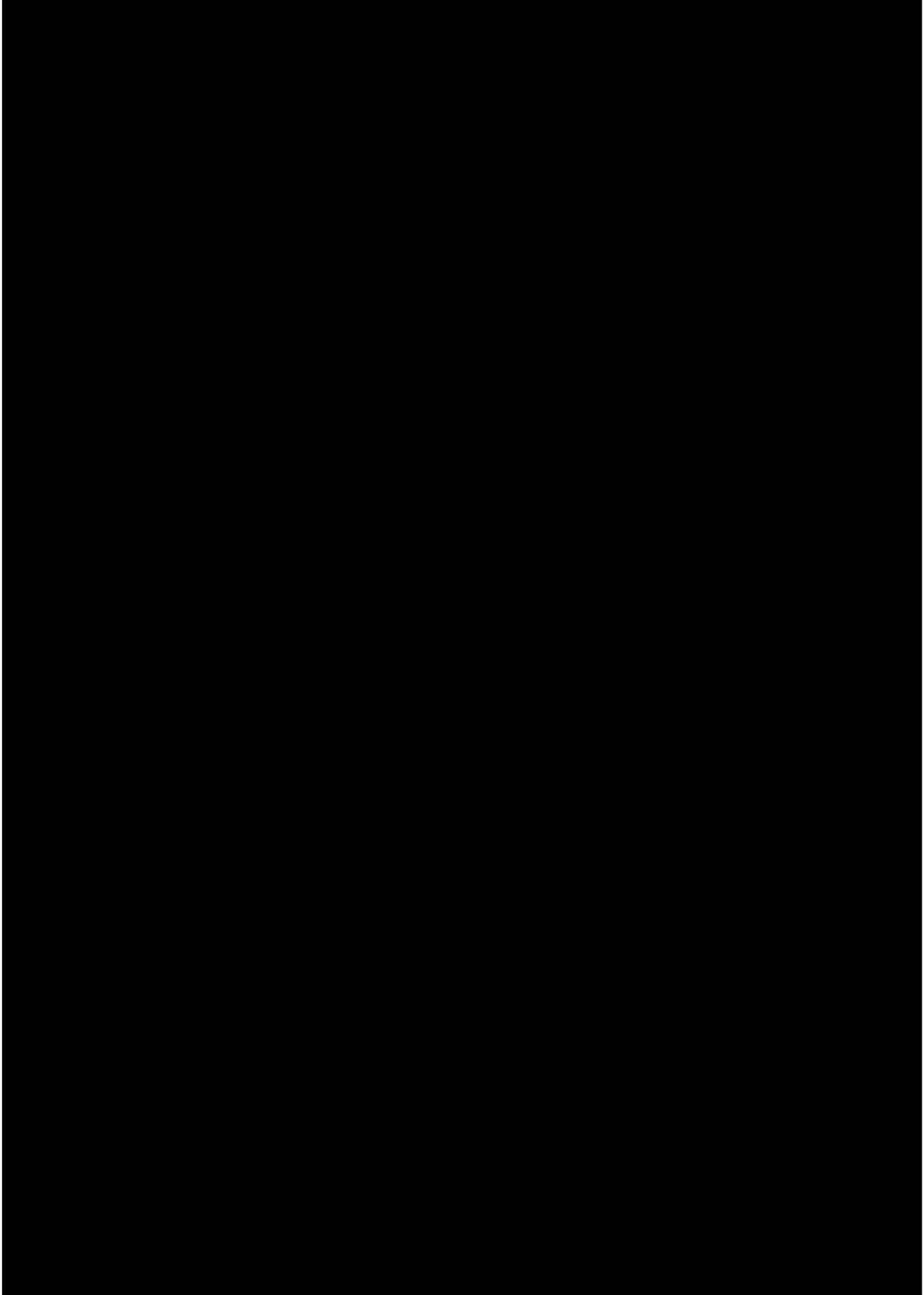




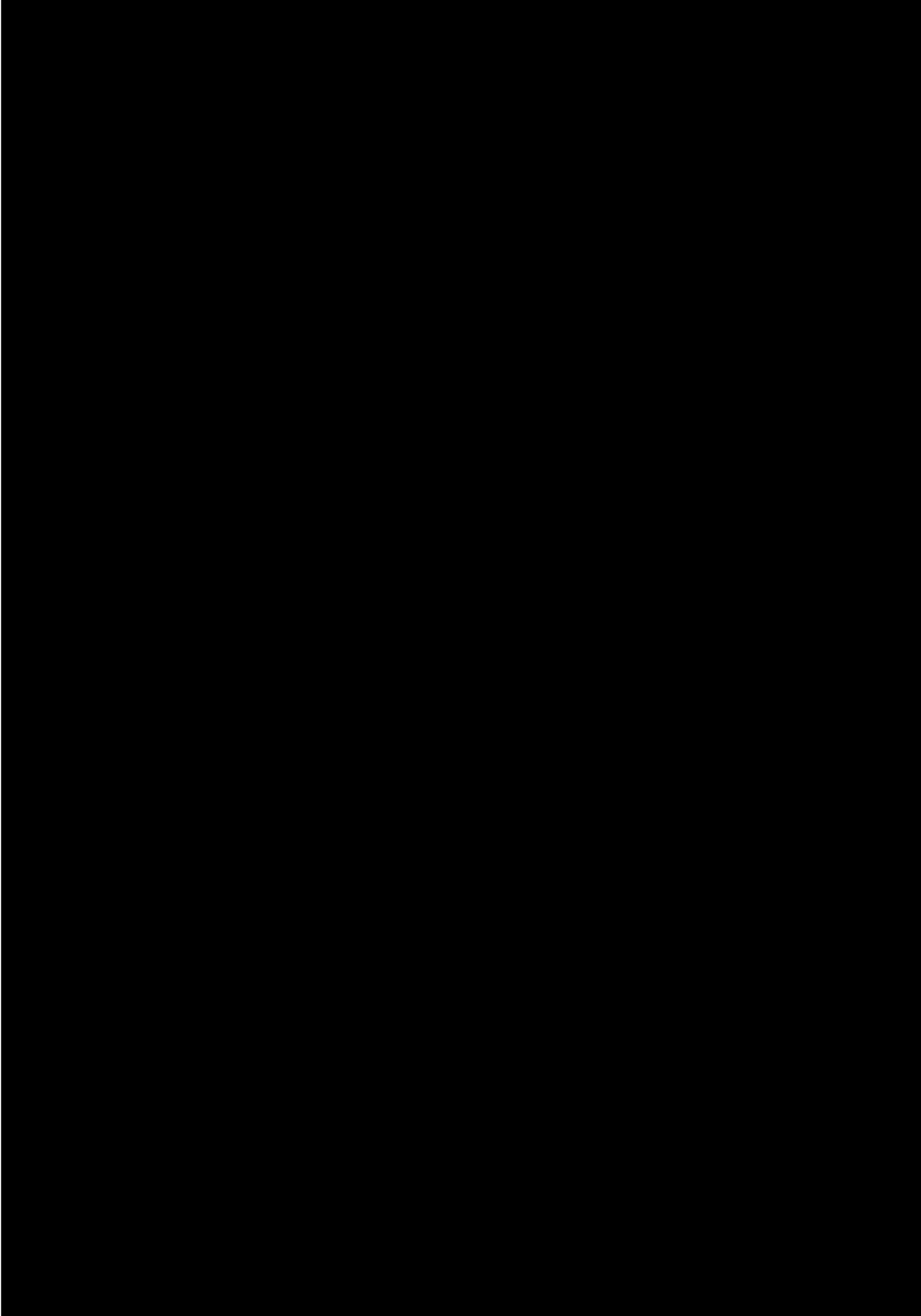
[REDACTED]

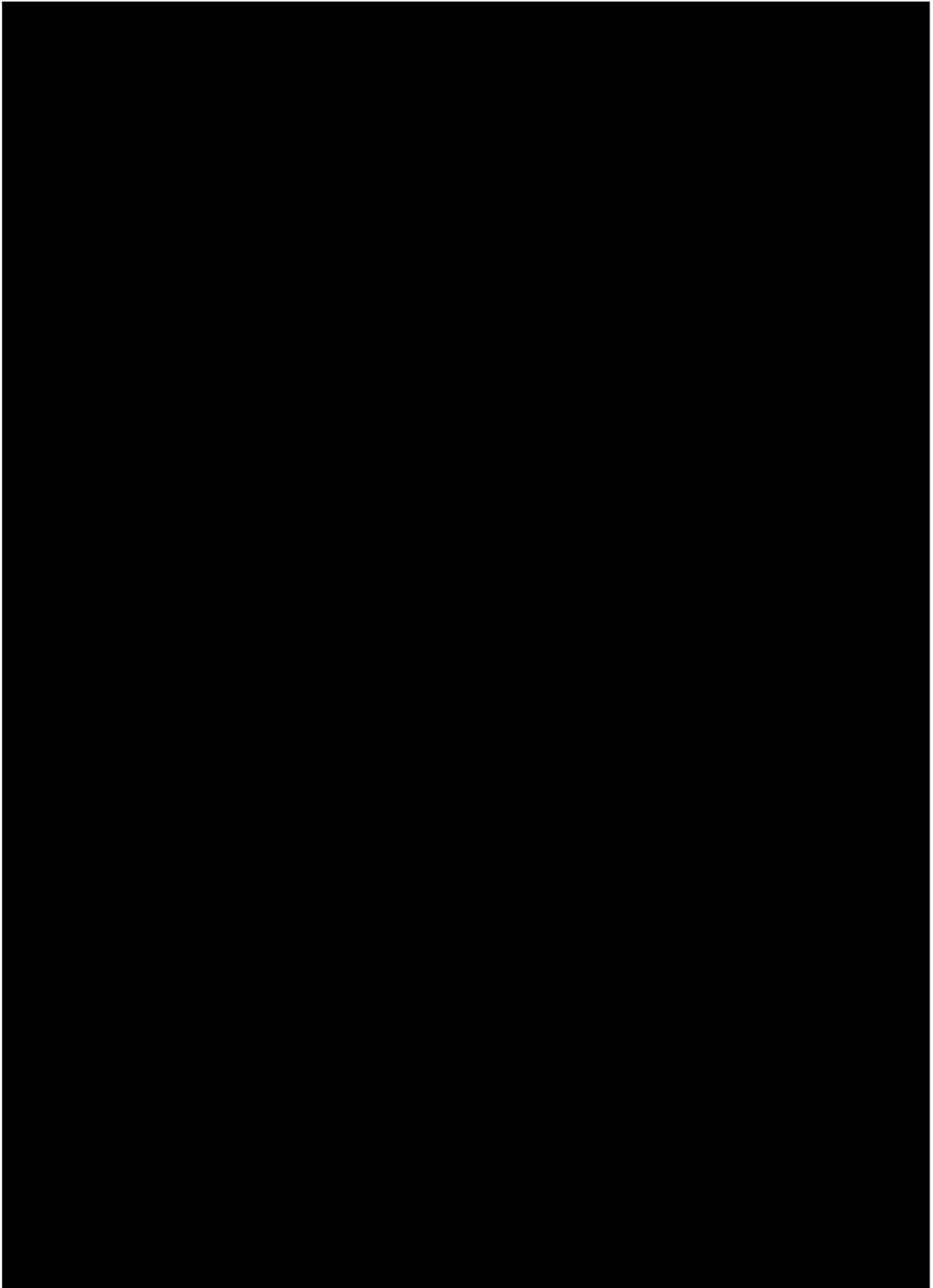
Edge-E linear model

[REDACTED]









[REDACTED]

## 5.6 Summary measurements results

The main conclusions extracted from the measurements carried out in this chapter are described in this section. The summary of the results is presented as they appear in the chapter.

### 5.6.1 LT-SAW

At first, an accurate analysis of the contribution of each nonlinear constant to the nonlinear IMD3 response is presented. With this analysis, it has been possible to identify the potential contributors responsible of the IMD3 manifestation. Once identified the potential contributors for the in-band IMD3 response, a characterization process has been performed and validated. [REDACTED]

[REDACTED]

The distributed model of a SAW resonator described in Chapter 3 and the IOES method of Chapter 4 has been applied to analyze the measured IMD3 and H3 of ten different LSAW resonators with different pitch and duty factor, concluding that only one shape independent parameter, the third order derivative of the elastic constant with a value of  $c_{3,MR}^E = -110c^E$ , can explain all the measured in-band IMD3 around resonance within an error of  $\pm 0.5$  dB. Under our knowledge there are no previous works showing such degree of agreement between simulations and measurements for different in-line geometries using the same nonlinear parameter. This validates the idea that a distributed model governed by local constitutive equations is fundamental to predict the in-band IMD3 of other resonators before manufacturing. [REDACTED]

[REDACTED]

[REDACTED]

[REDACTED]

[REDACTED]

### 5.6.2 TC-SAW

Regarding the IMD3 and H3 nonlinear response of TC-SAW resonators, in view of the results, we can finally conclude that if we use the same value of [REDACTED] for all the TC-SAW resonators, the model is able to adjust both measurements and simulations of the main peak of the IMD3 response and is the best candidate found to explain the nonlinear in-band IMD3 response of measured TC-SAW resonators. The same value of  $c_{3,MR}^E$  have been tested for both different pitch and duty factors resonators. [REDACTED]

[REDACTED]

[REDACTED]

[REDACTED]

Finally, it has been demonstrated that the IOES method is not restricted to a specific in-plane geometry and it is possible to properly simulate the nonlinearities of resonators employing a different technology. Specifically, the nonlinear distributed model has been also applied to analyze the measured IMD3 and H3 of nine TC-SAW resonators with different pitch and duty factor. [REDACTED]

[REDACTED]

The next step, as it will be further discussed in Chapter 6, is to analyze with the IOES method the nonlinearities of more complex structures such as ladder filters or coupled resonators filters.

# Chapter 6

## Application of the IOES to SAW filters

### 6.1 Introduction

This chapter is devoted to analyze using the IOES method, the linear and non-linear response of more complex structures such as ladder-type filters or coupled resonators filters. In both cases, the analyzed test structures are composed by TC-SAW resonators. After that, the chapter will be focused on introducing other non-linear model called the lumped nonlinear model. This model has been designed to reduce the computational time and as an alternative to solve the nonlinear problem of complex structures avoiding the discretization of the models.

Taking into account the aspects that have been previously commented, the main objectives to be achieved in this chapter are the following:

- Linear analysis of ladder and CRF filter measurements and its corresponding linear simulations with IOES.
- Analysis of ladder and CRF nonlinear measurements.
- Characterization process of the nonlinear results and validation with IOES.
- A summary of the main conclusions for both ladder and CRF results.

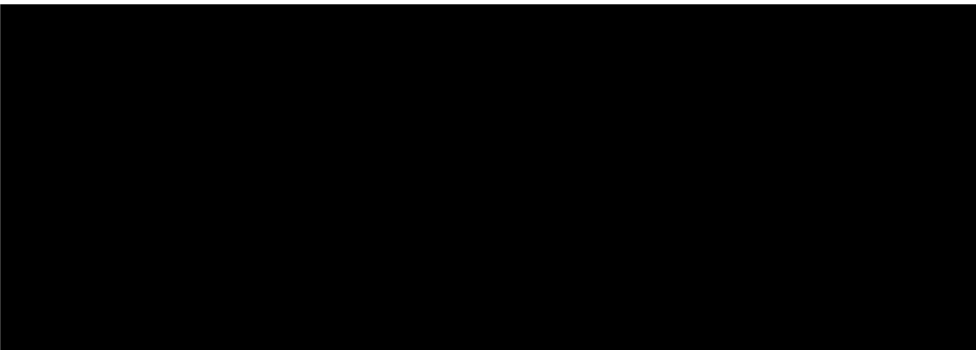
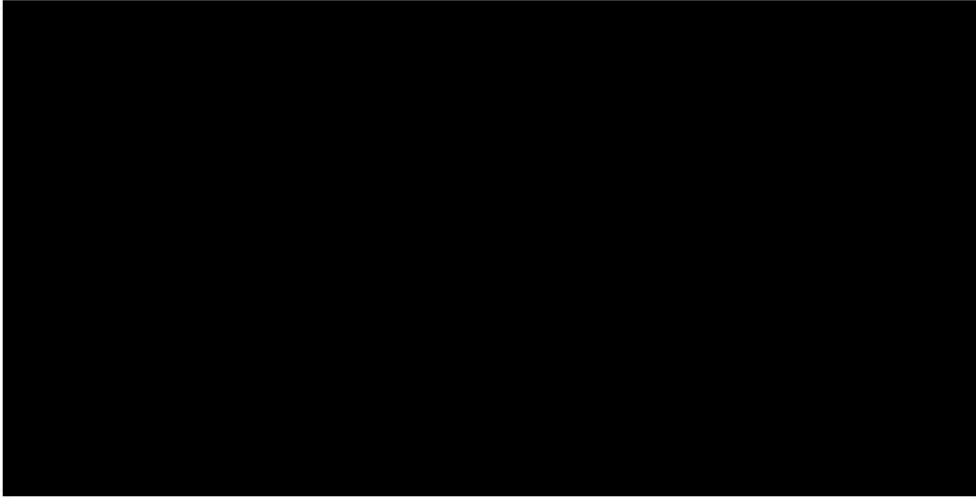
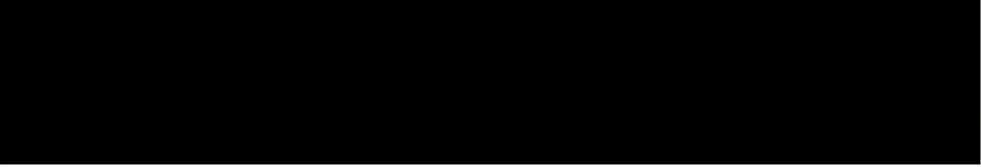
■ [REDACTED]

■ [REDACTED]

Each of these aspects will be analyzed and validated from measurements of resonators with different typologies.

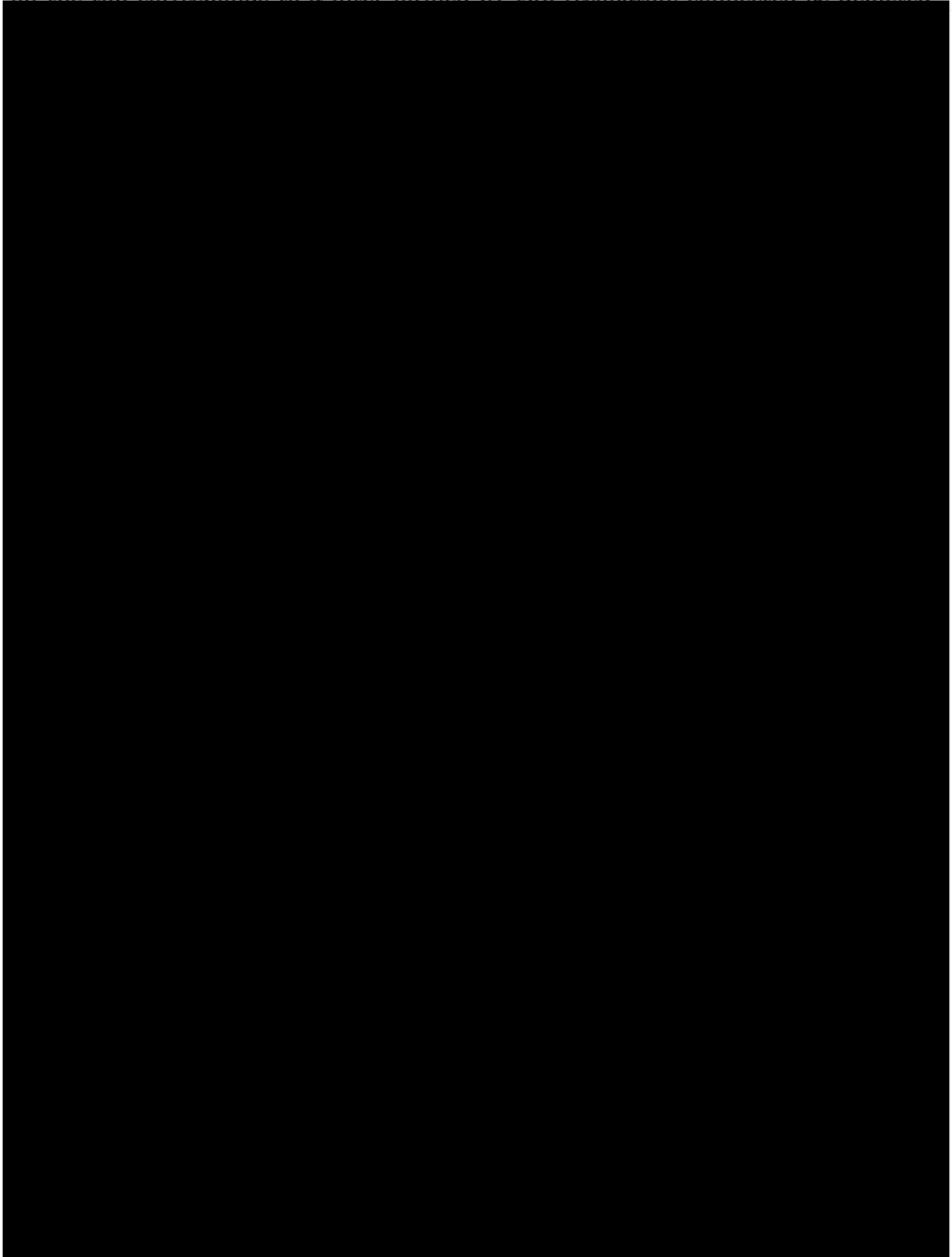
## 6.2 Ladder filters

Filters used in SAW technology can be grouped into two major categories: the electrically coupled and the acoustically coupled filters. Ladder filters are a type of configuration where the resonators are electrically coupled. Besides, are commonly used in high-end communication systems because of their steep skirt selectivity and very selective transmission band due to the presence of transmission zeros at each side of the pass-band. Fig. 6.1 (left) shows the schematic representation of the

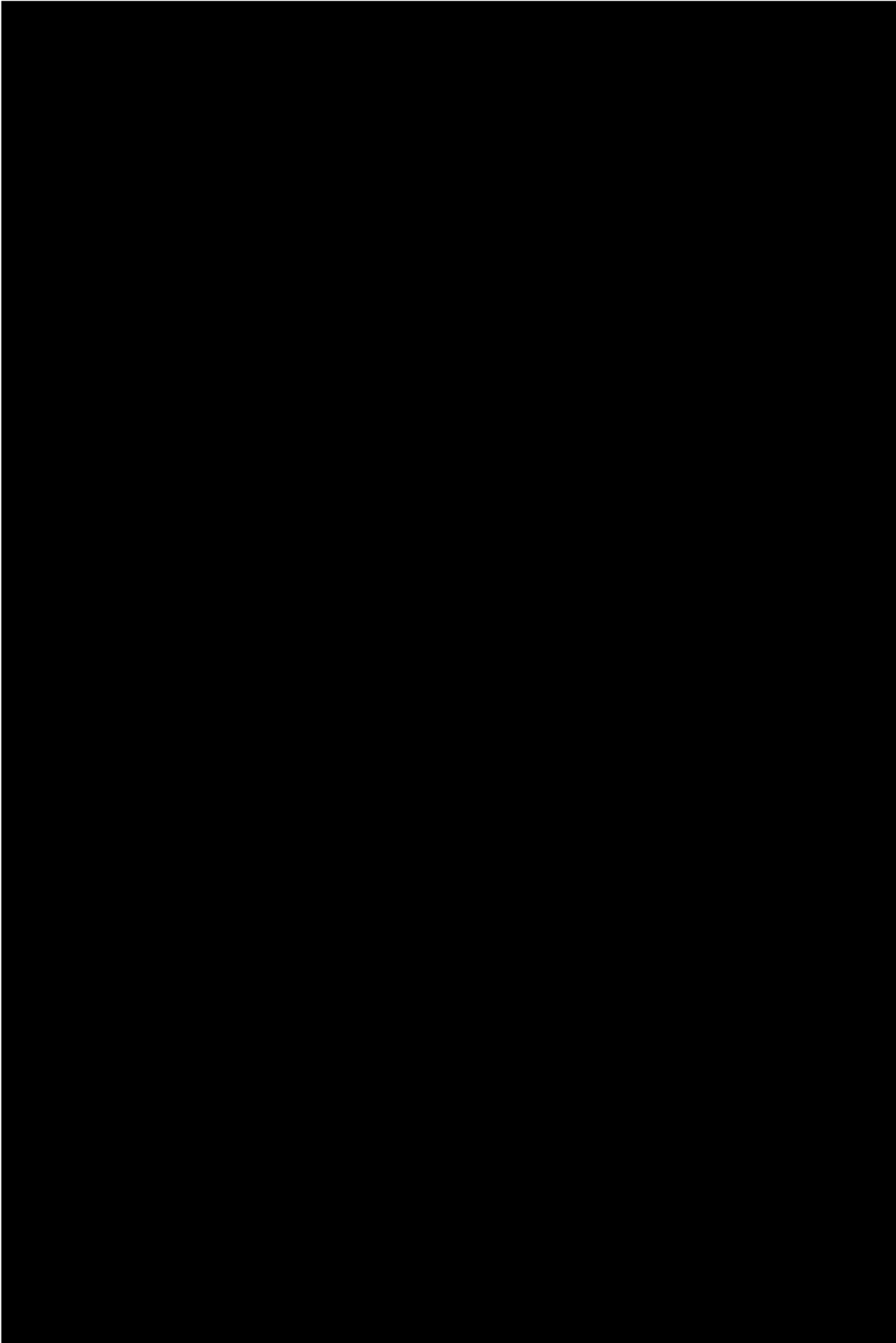


### 6.2.1 Linear measurements

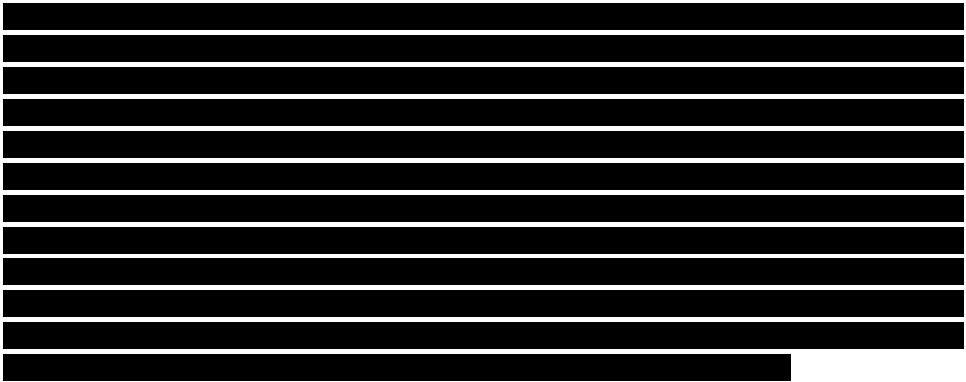
Once the ladder-type filters has been outlined, the next step is to proceed with linear measurements. Fig. 6.2 shows the narrowband (left) and broadband (right) measured scattering response of two different ladder filter structures. The structure on the top corresponds to a filter formed by two resonators connected as depicted







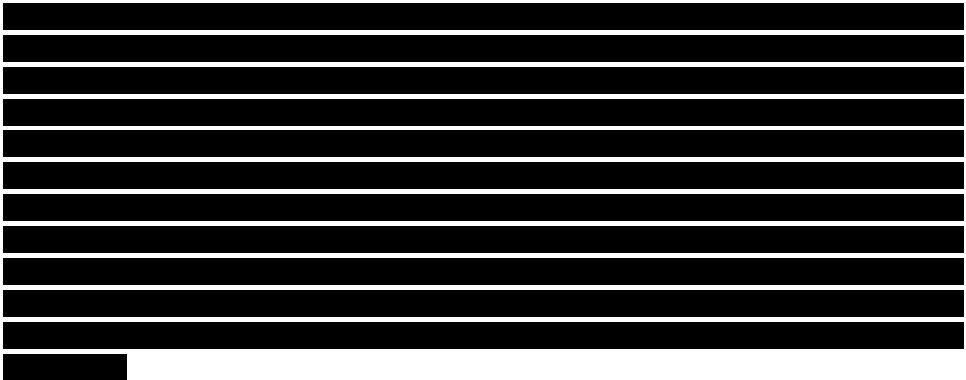
Specifically, left plots represent the admittance  $|Y|$  response and right plots the admittance real part. Blue solid traces represent the measurements and red dashed traces the simulations. As it can be seen, the linear simulations show an overall good agreement between measurements and simulations.

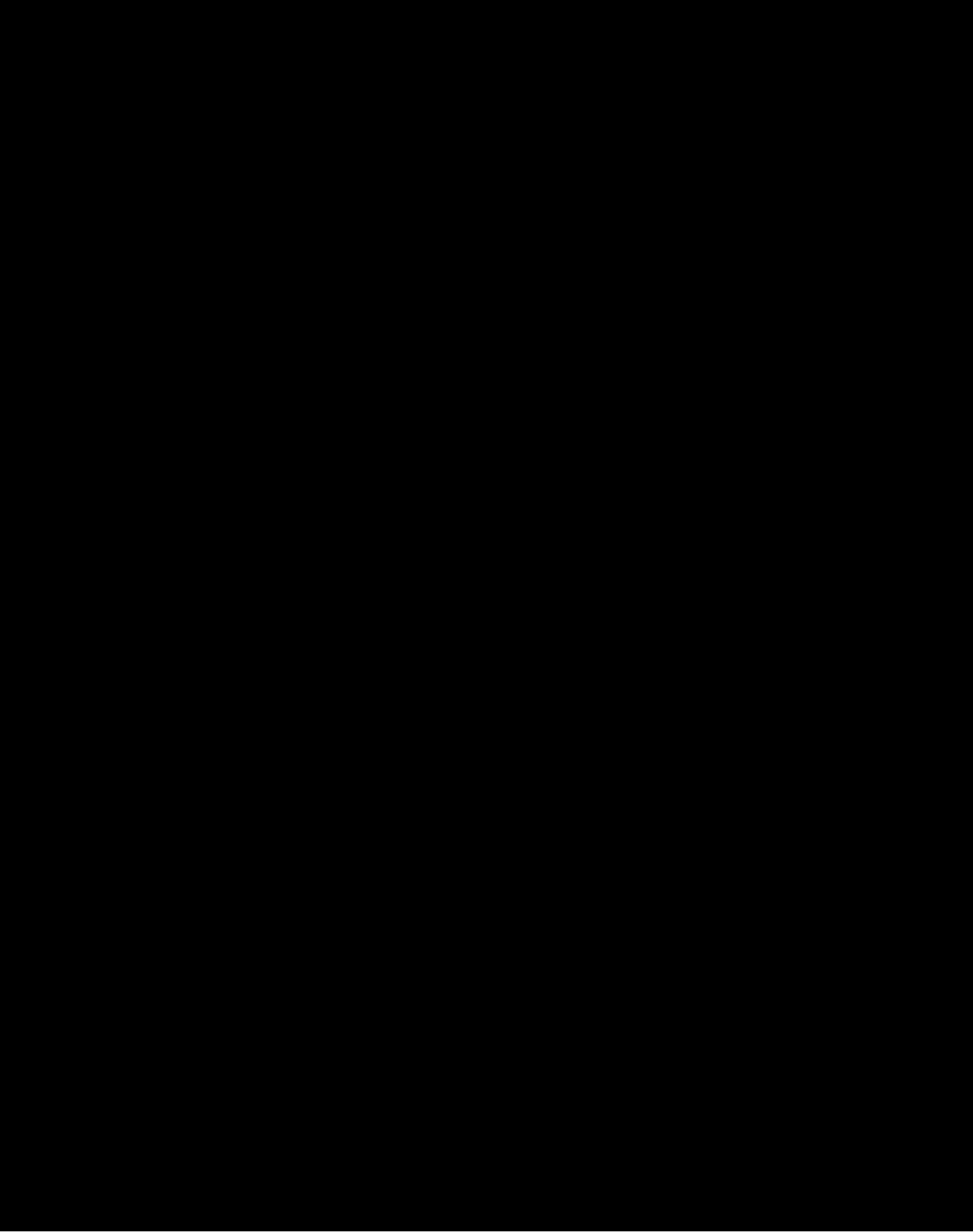


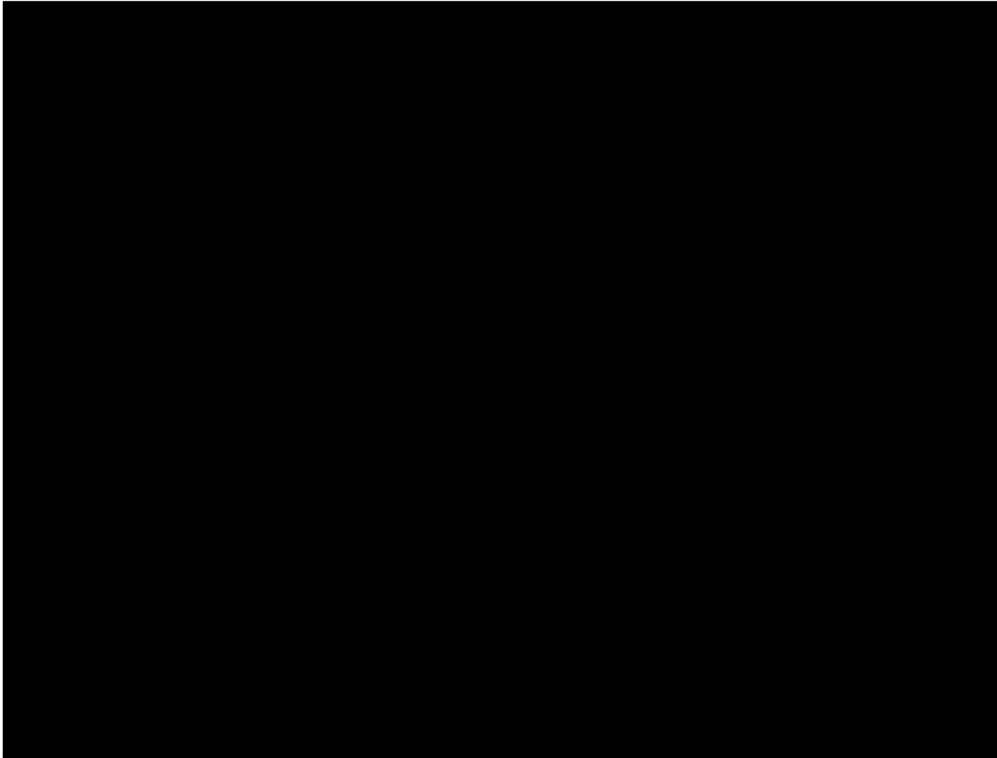
In any case, for a first approximation the linear model will be kept as simple as possible and therefore considering these results we can move forward to simulate the filter.

### 6.2.2 Matlab<sup>®</sup> linear simulations of ladder filters

[Redacted text]







### 6.2.3 Nonlinear measurements of ladder filters

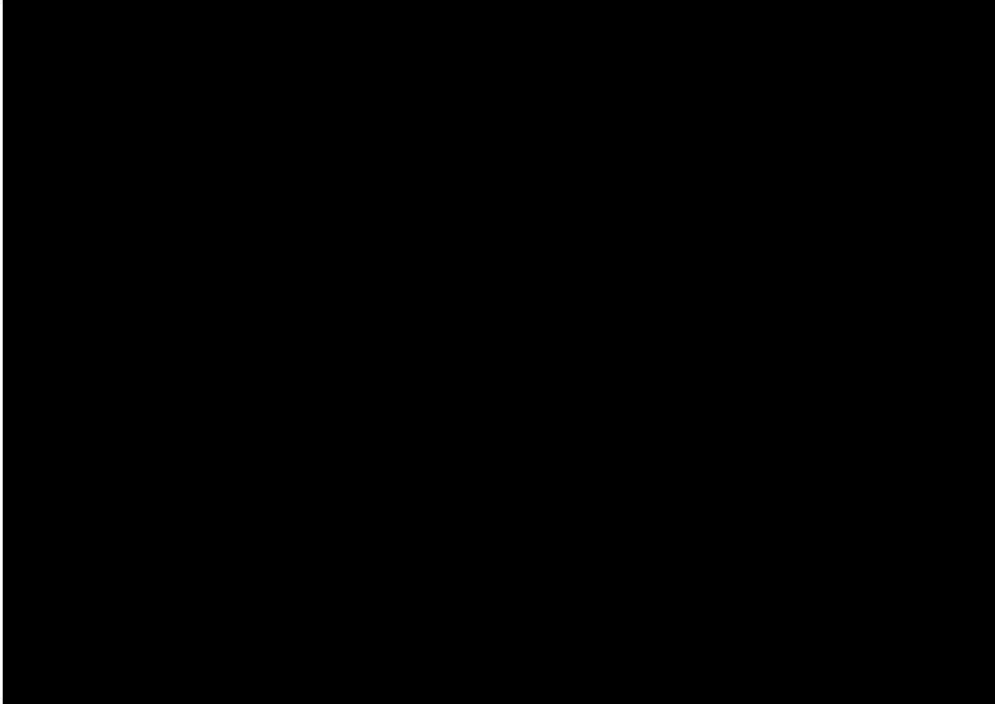
Once it has been verified that linear modeling of the filters can be carried out, efforts are now focused on verifying the nonlinear modeling. As it has been done in previous chapters, the three main steps we describe in this subsection are:

- Present the measurement set-up.
- Nonlinear measurements of isolated resonators which are present on the filters structures.
- Nonlinear measurements of the ladder filters.

#### IMD3, H3 and H2 measurement system

The two-tone measurement system will follow the schematic of Fig. 6.6. Basically, the configuration is mostly the same as the set-up used for the resonators measurements with the particularity that now, instead of a reflection configuration we have the filter on a cascade configuration and therefore the hybrid coupler is not needed. Considering this, now we need two different Touchstone files to include the measurement system into the simulations. The first one is characterized as a 3-port

broadband S-parameters measurement (marked with red dashed box) with the calibration planes set at just both SG outputs and just after the combiner output, and the second is another 2-port broadband S-parameter measurement (marked with dotted blue box) whose calibration planes are located to measure the cable that joins the output of the filter structure with the SA.



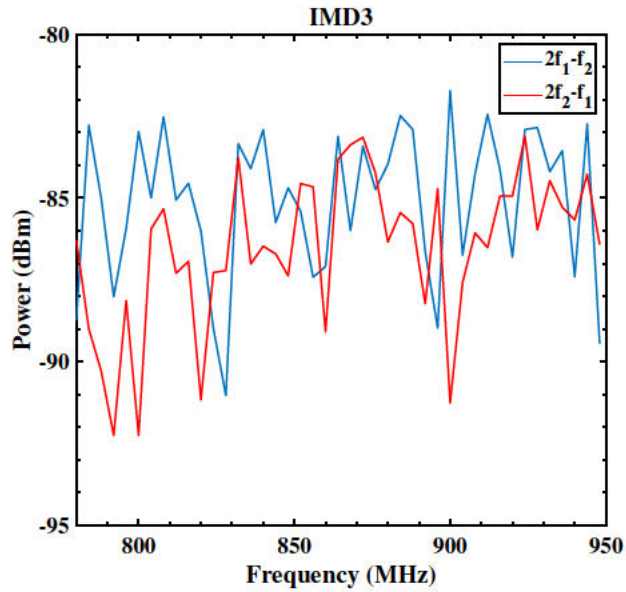


Figure 6.7: Measured IMD3 response floor level of a thru structure.

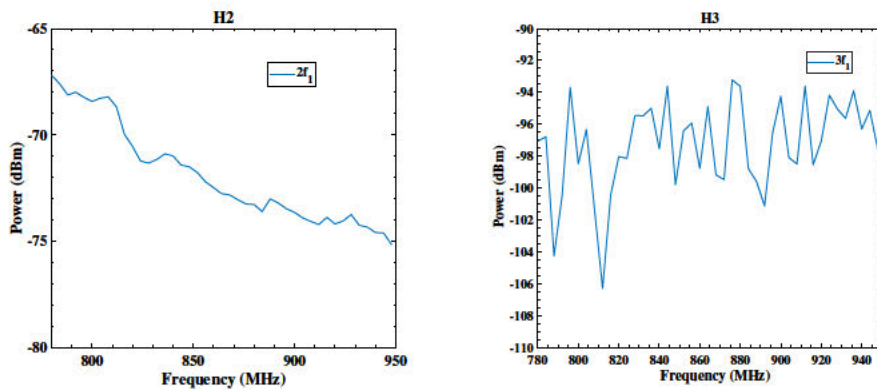
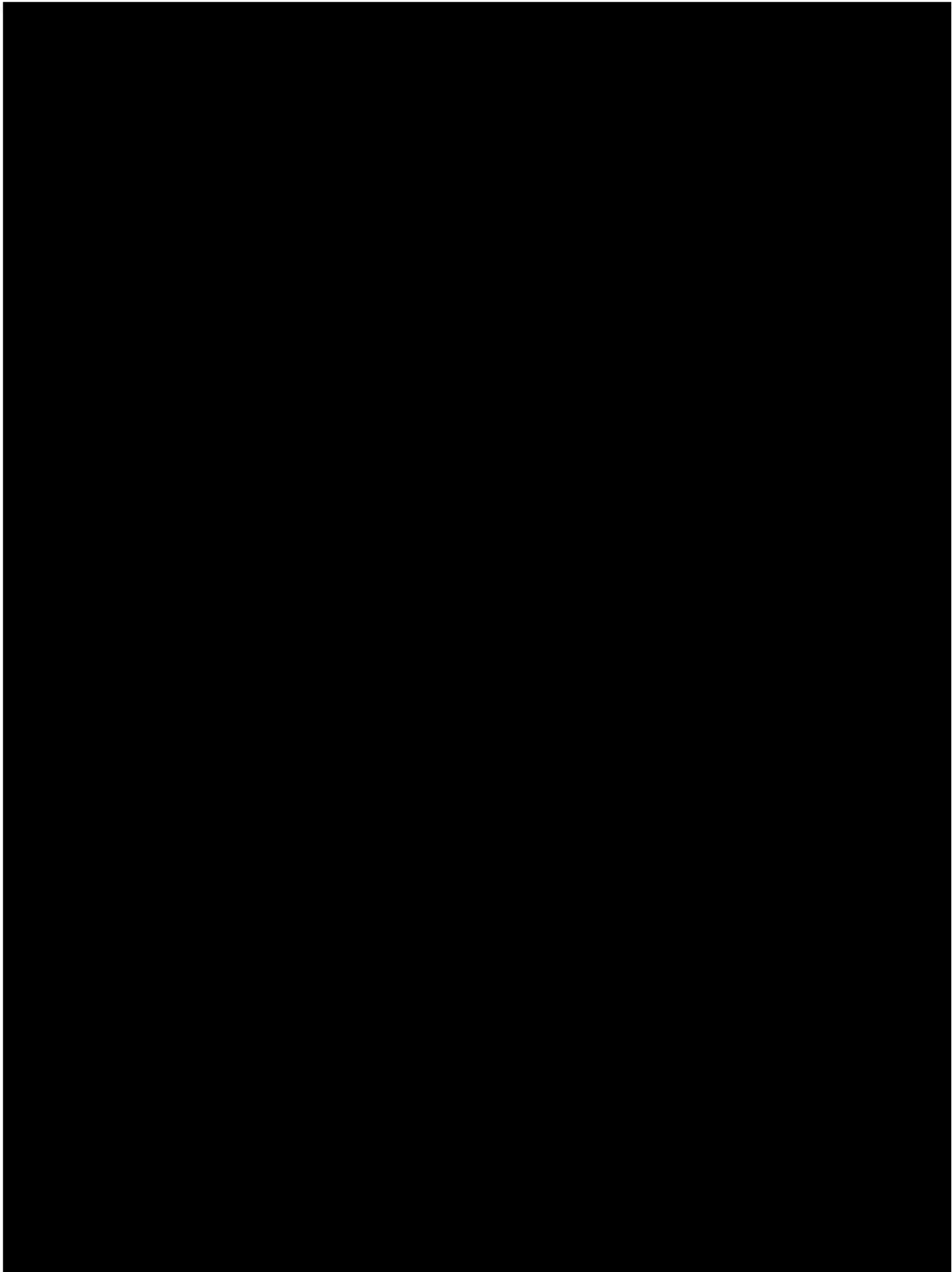
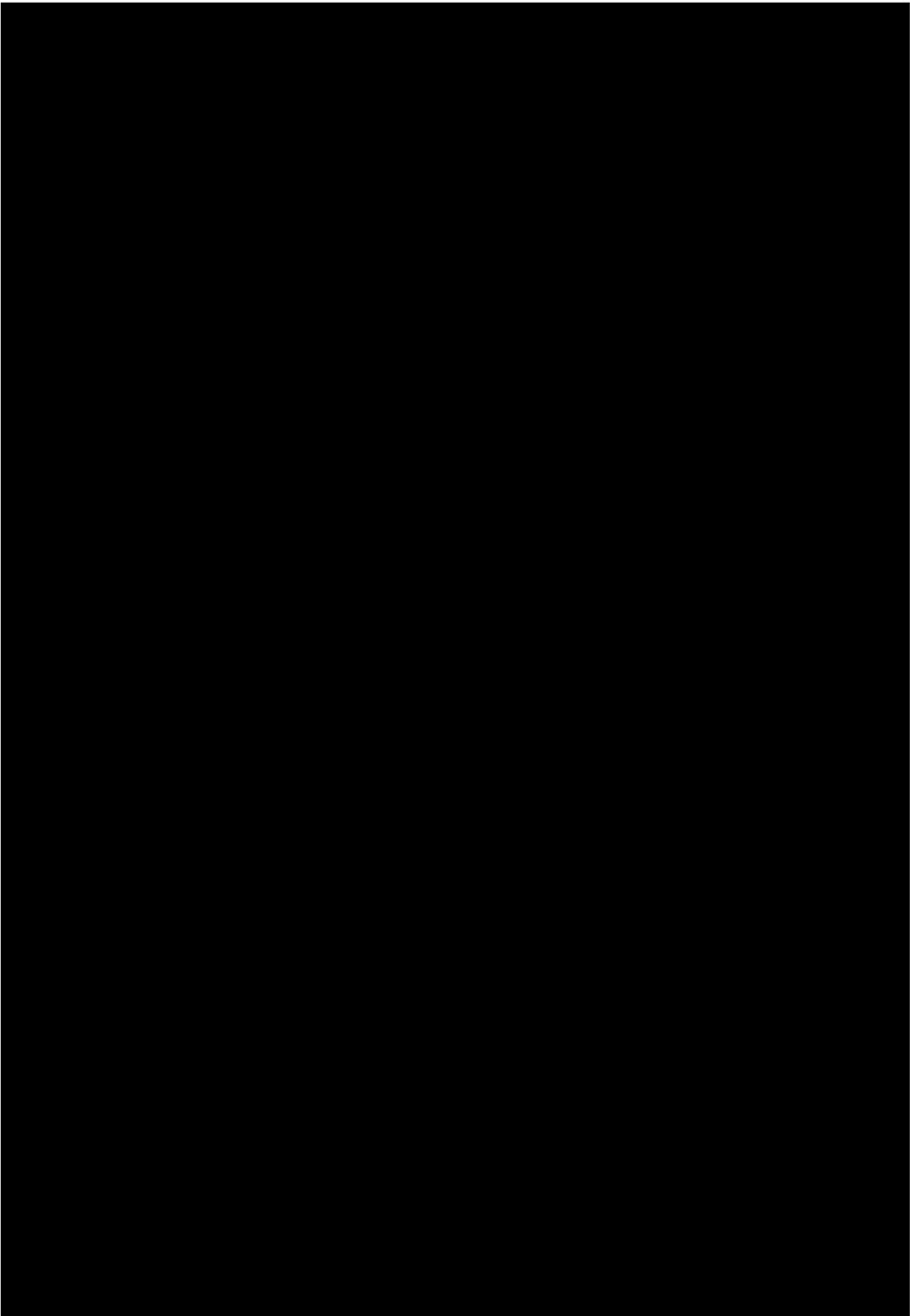


Figure 6.8: Measured H3 response (right) and H2 (left) noise floor level of a thru structure.

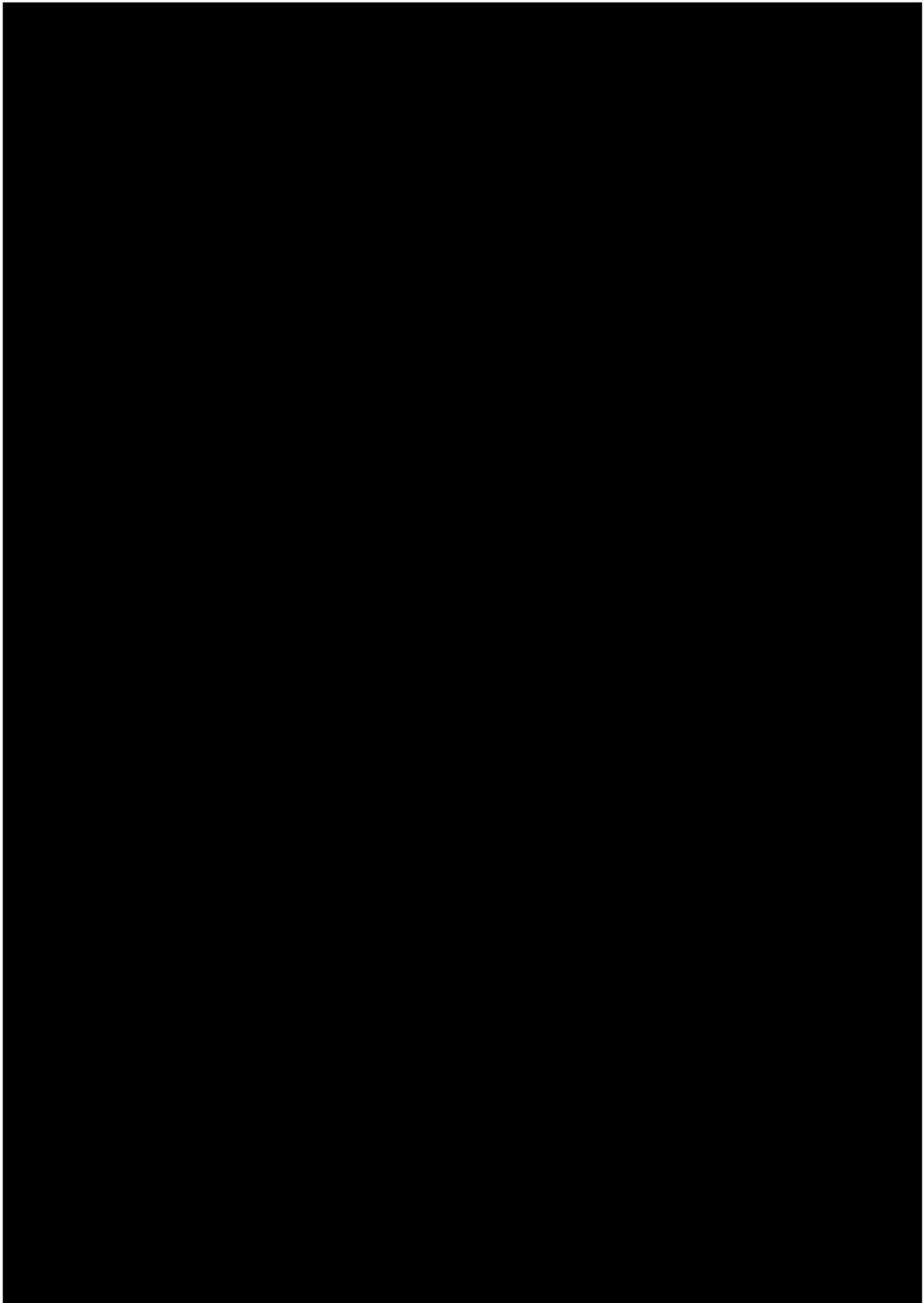
As it can be seen, it results in -84 dBm for the IMD3 floor level and -67 and -94 dBm for the H2 and H3 floor levels respectively. Note that again the H2 response is very high because of the circulators.

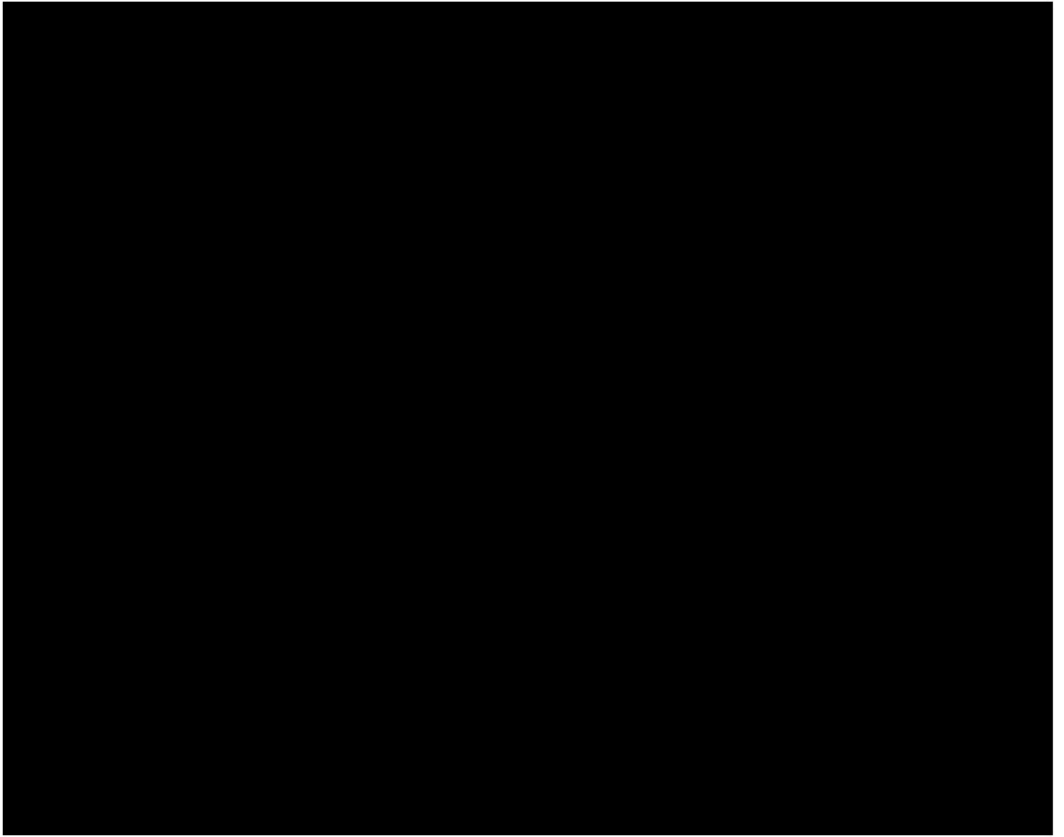
**IMD3 and H3 Nonlinear measurements of isolated resonators**

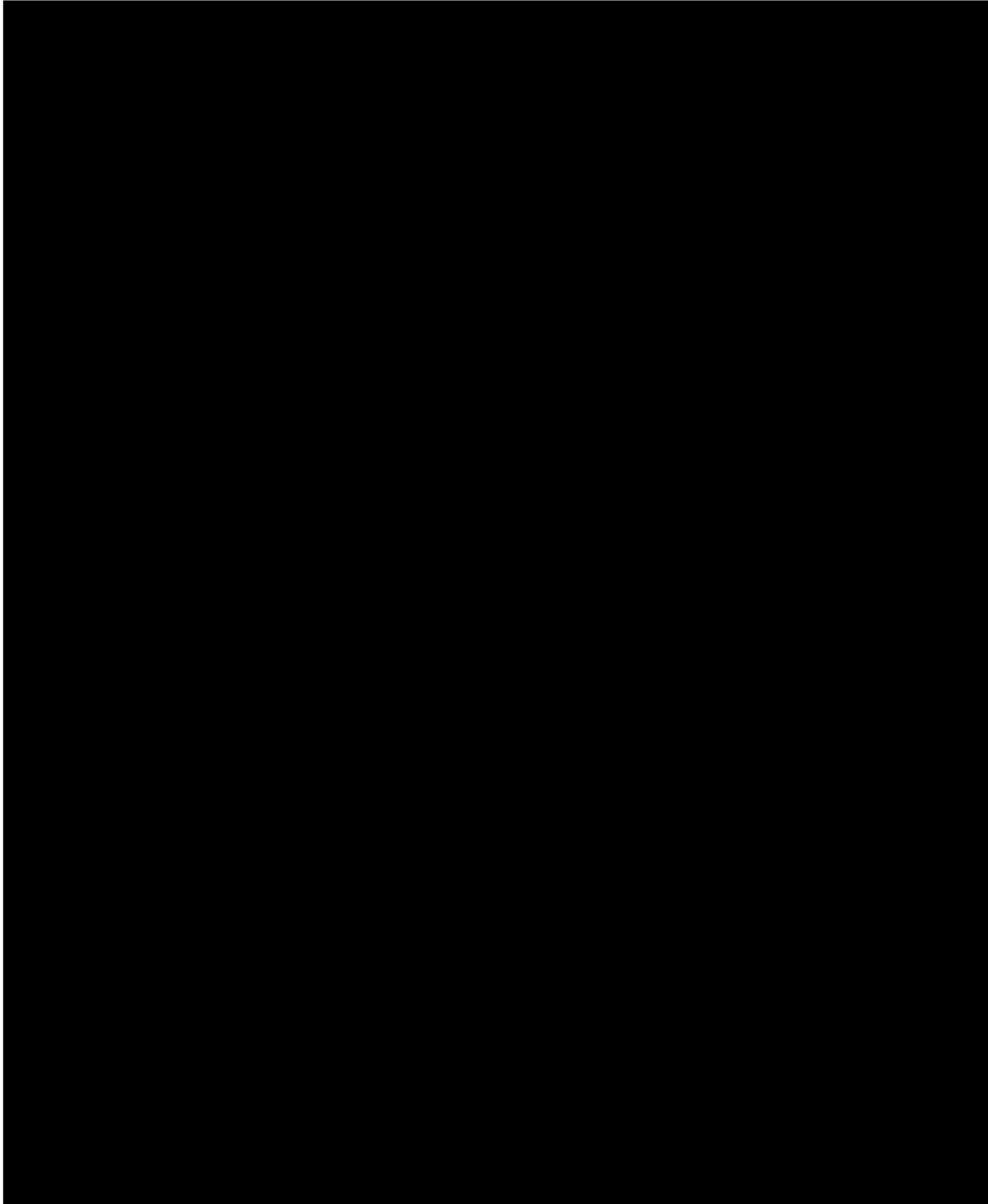
Nonlinear measurements of ladder filters

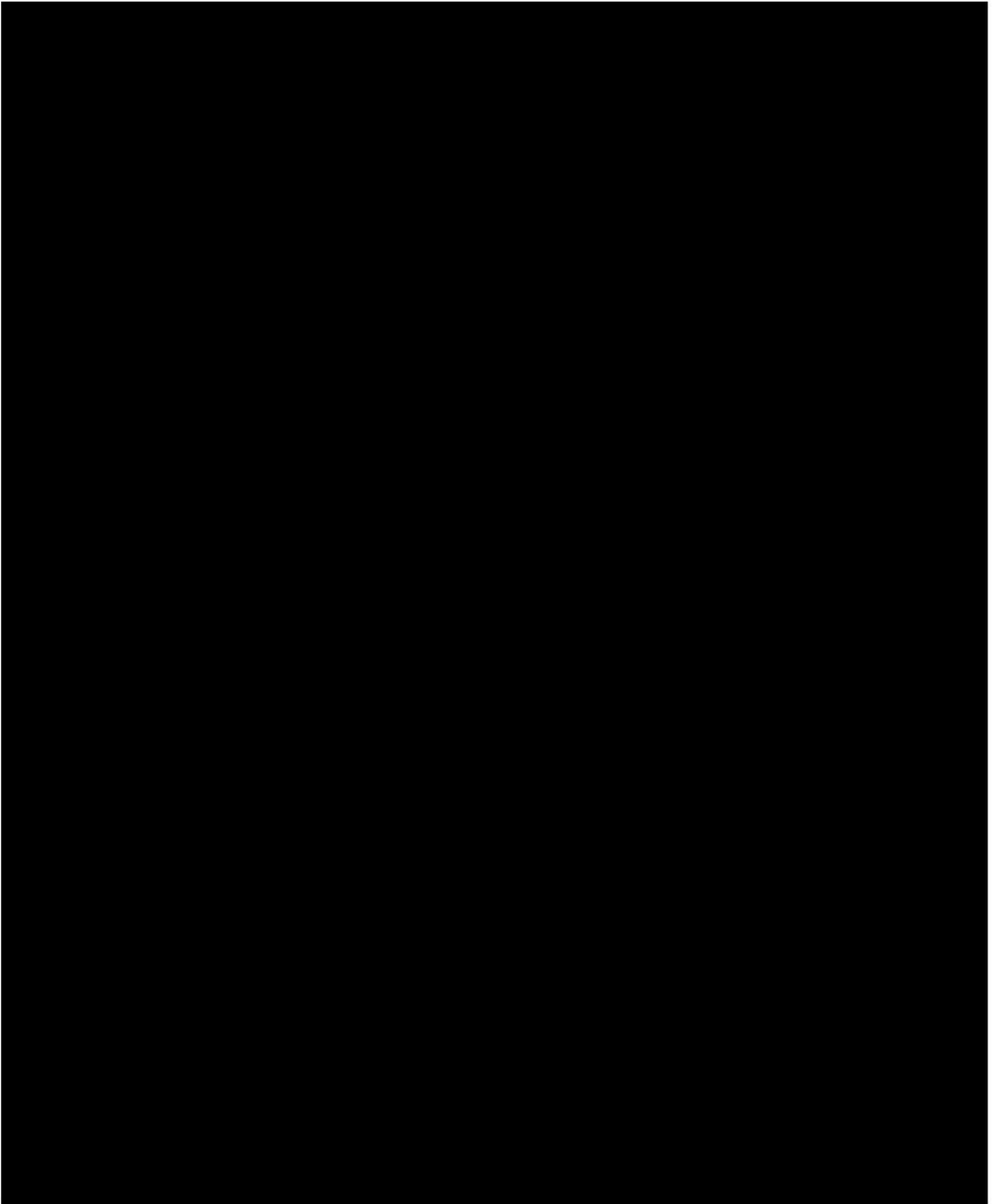






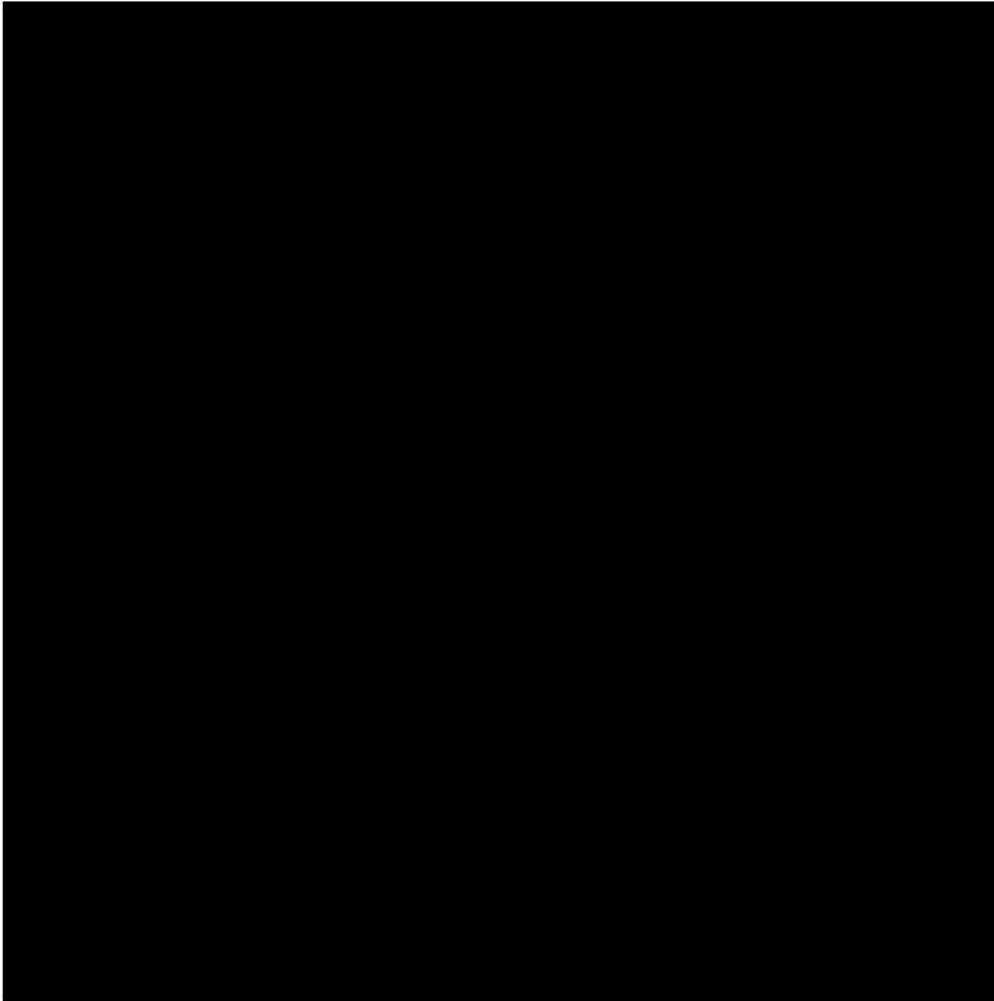


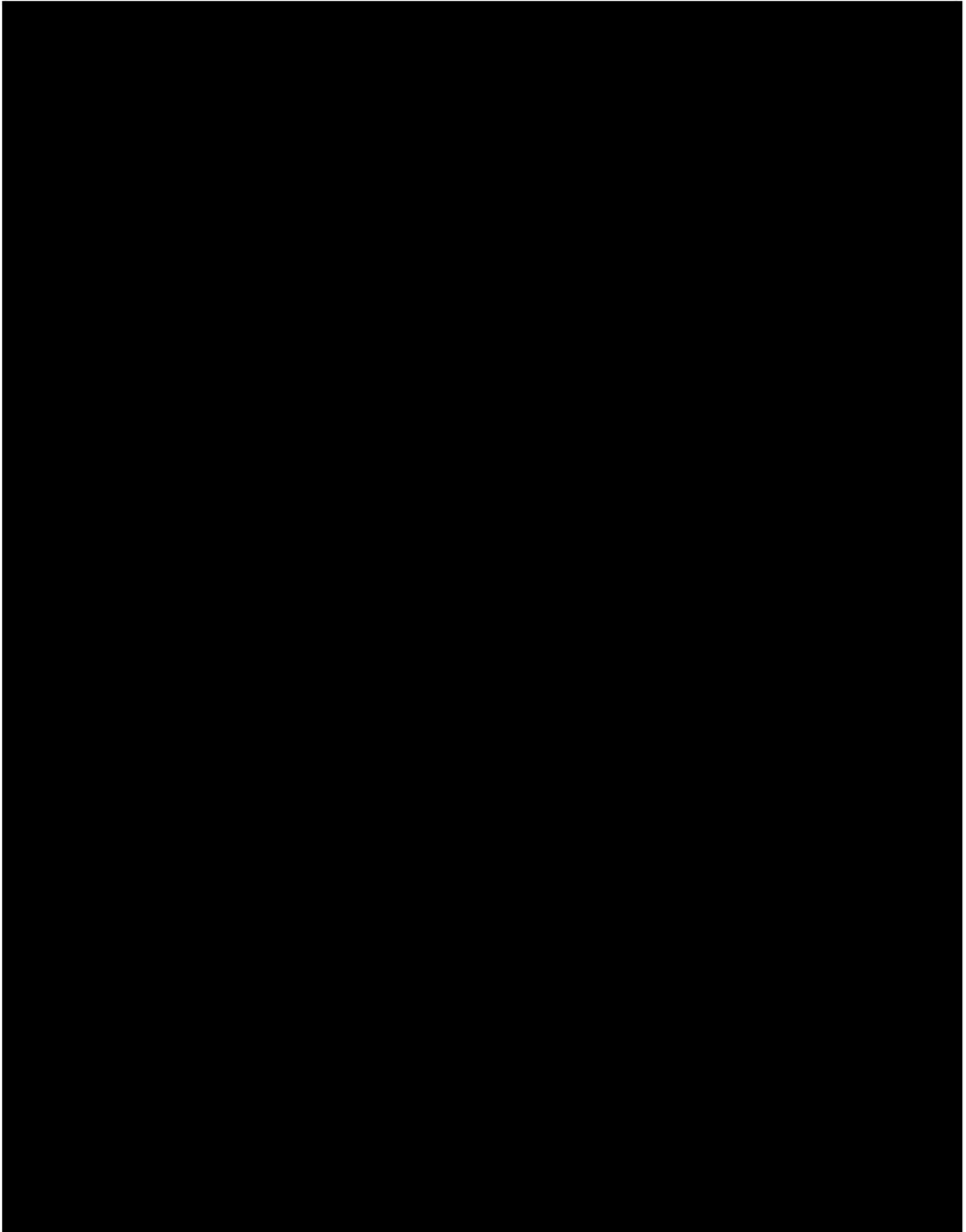




### 6.2.4 Nonlinear simulations of ladder filters

Hereafter, the corresponding nonlinear simulations of the ladder structures are presented. The order in which the data is presented follows the same structure as in the previous subsection.





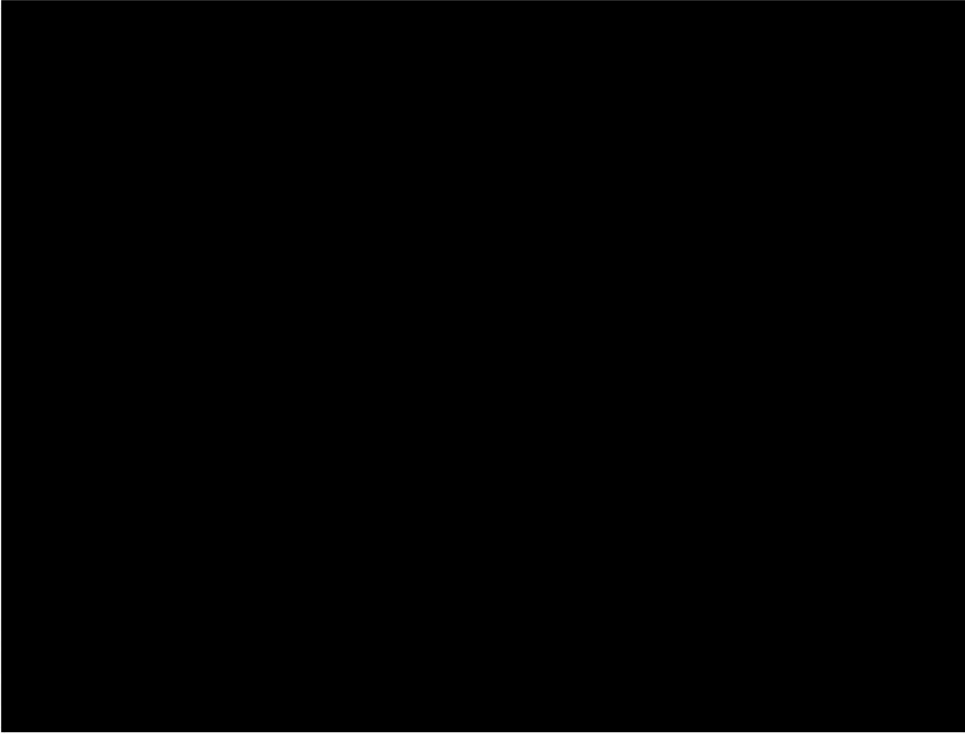


Figure 6.20 shows the IMD3, on the left, and H3, on the right, simulated response versus the measurements of the ladder filter. Red and blue lines correspond to computed  $2f_1 - f_2$  and  $2f_2 - f_1$  respectively, and measured response in green ( $2f_1 - f_2$ ) and magenta ( $2f_2 - f_1$ ) traces.

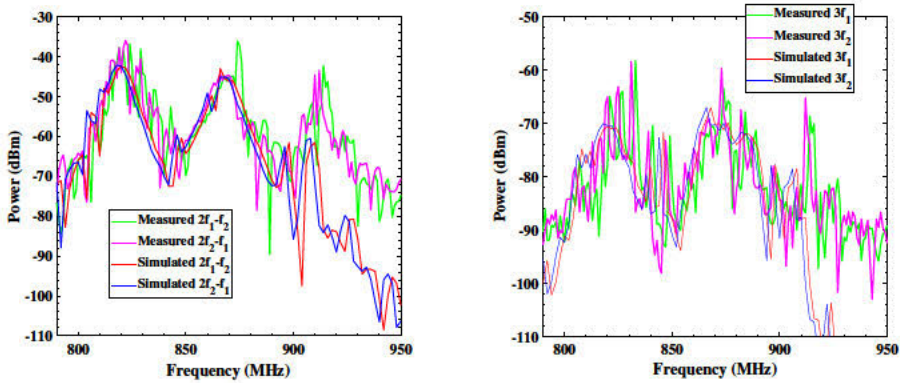
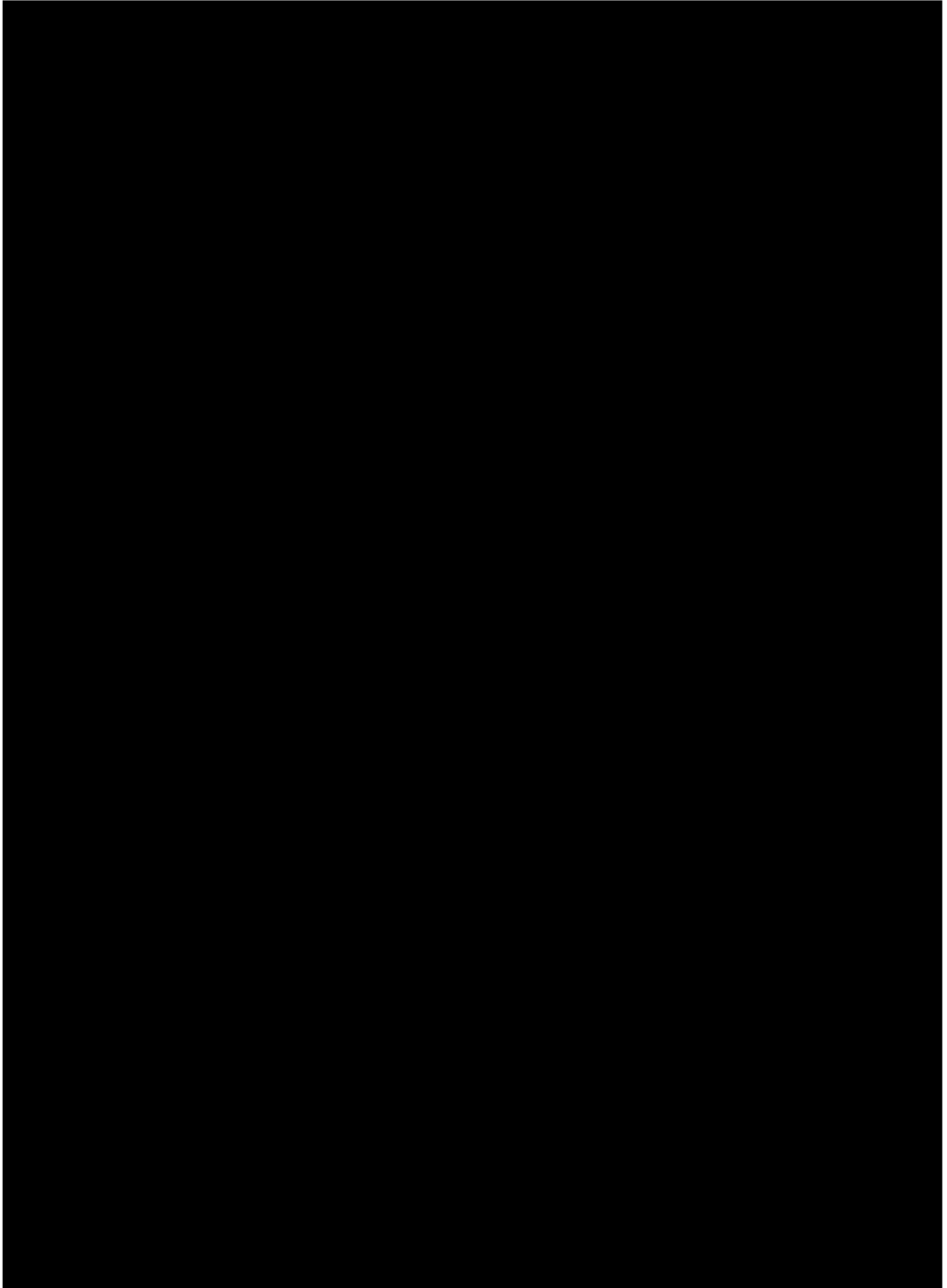
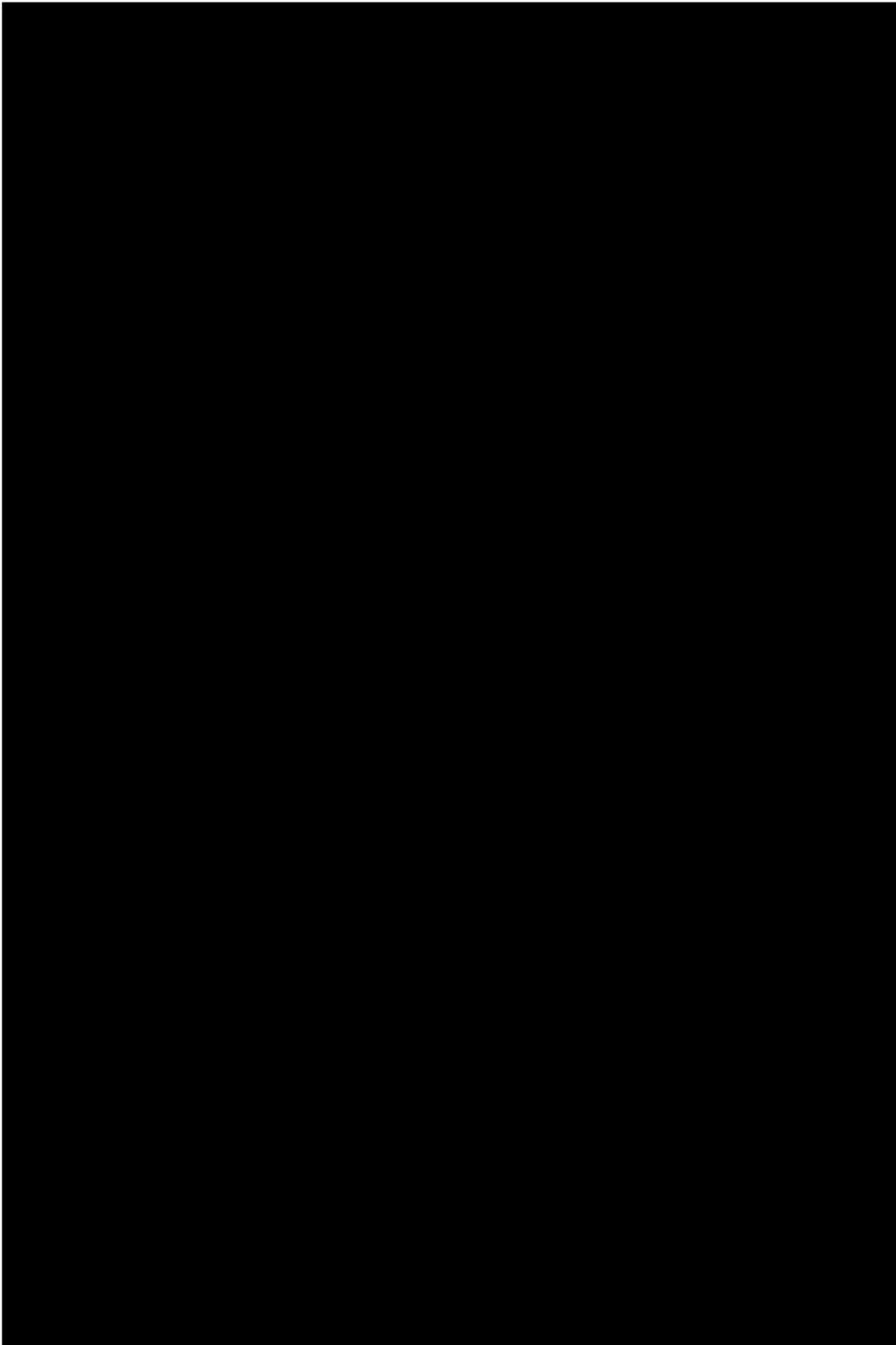
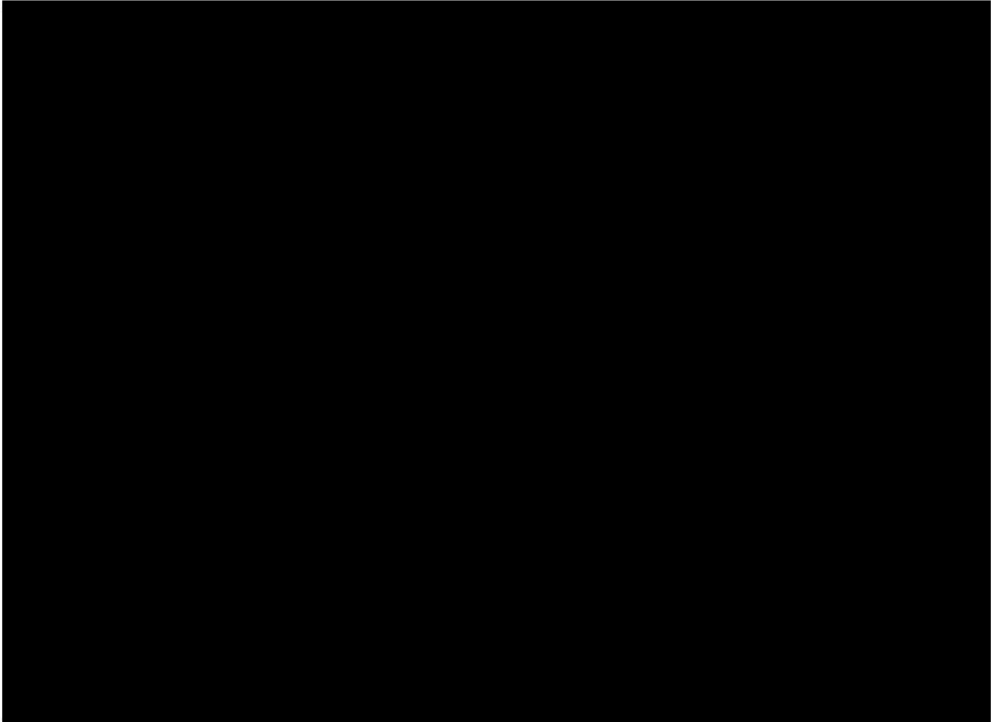


Figure 6.20: Ladder-type TC-SAW structure with IMD3 (left) and H3 (right) nonlinear response. Red and blue dashed traces correspond to computed  $(2f_1 - f_2)$  and  $(2f_2 - f_2)$  respectively, and measured response in green ( $2f_1 - f_2$ ) and magenta ( $2f_2 - f_1$ ) traces on the left. On the right, green and magenta correspond to measured  $3f_1$  and  $3f_2$  response and in red and blue their corresponding simulations.





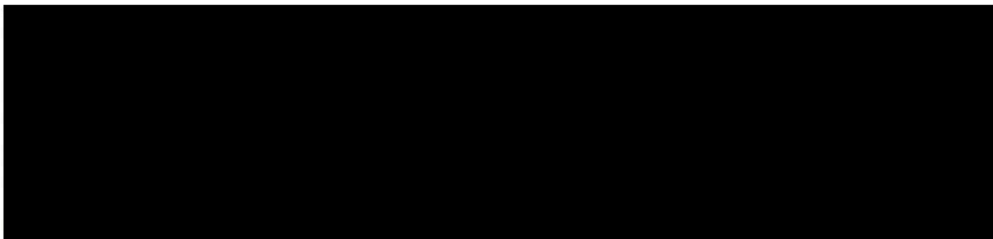




### 6.2.5 Analysis of the nonlinear response of ladder filters

An accurate analysis of the nonlinear contribution of each resonator separately is presented. After that, the individual analysis of each of the nonlinear constants employed and its contribution to the ladder filter nonlinear response is outlined.

#### IMD3 and H3 nonlinear contribution of each resonator



These simulations are obtained switching off the nonlinearities of one resonator while switching on those of the other resonator. Similarly, right plot depicts the H3 response, where green and magenta traces correspond to measured  $3f_1$  and  $3f_2$  response and in black solid and dashed traces the H3 individual contribution of the series and shunt resonator respectively.

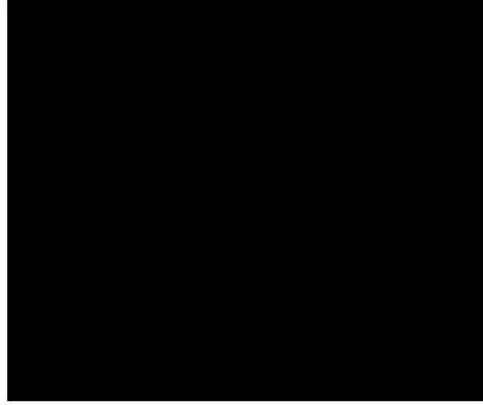
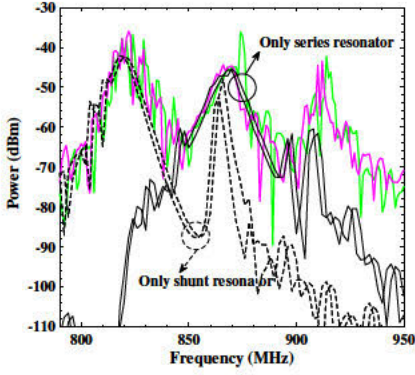
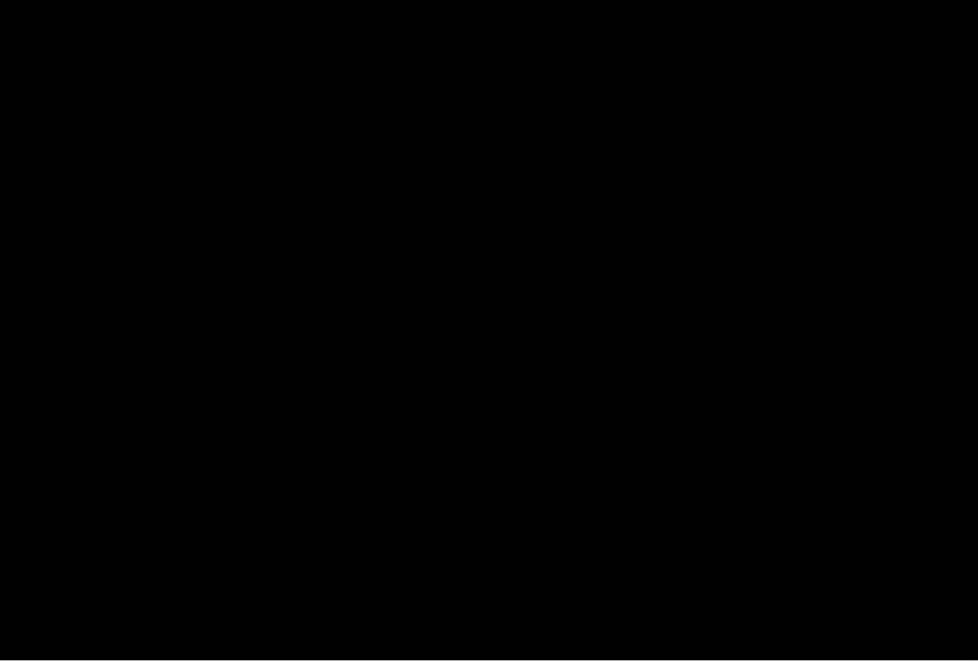
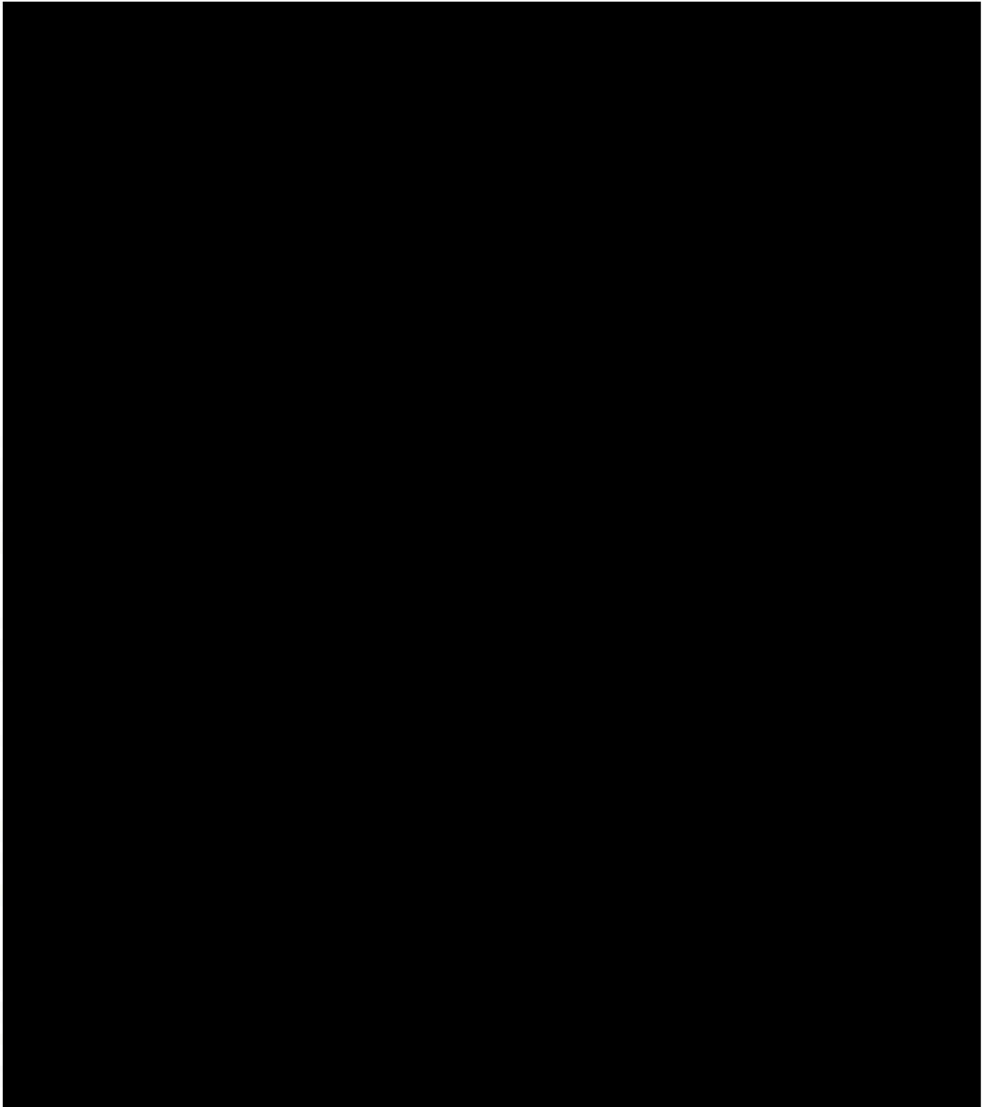


Figure 6.24: Ladder-type TC-SAW structure [redacted] with IMD3 (left) and H3 (right) nonlinear response. Green ( $2f_1 - f_2$ ) and magenta ( $2f_2 - f_1$ ) traces correspond to measured response. Black solid lines represent the nonlinear contribution of series resonator individually and black dashed lines the shunt resonator respectively.





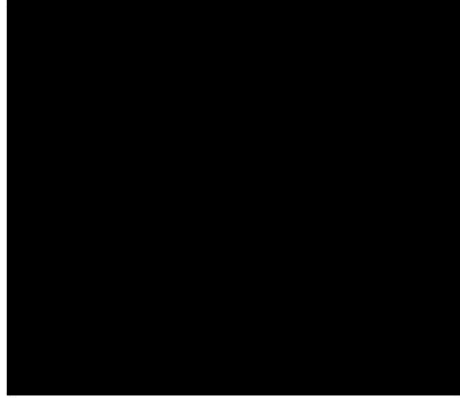
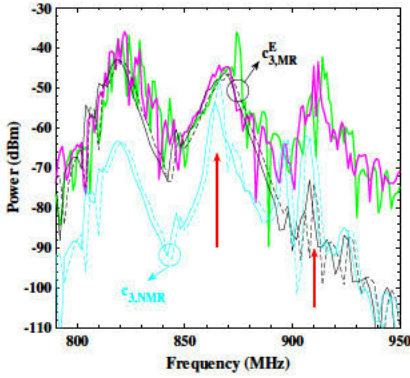
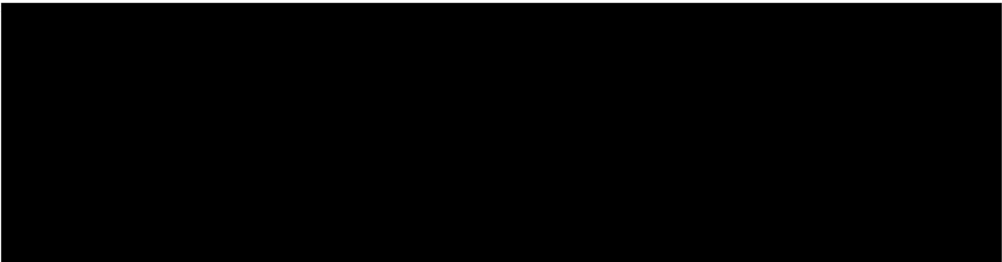
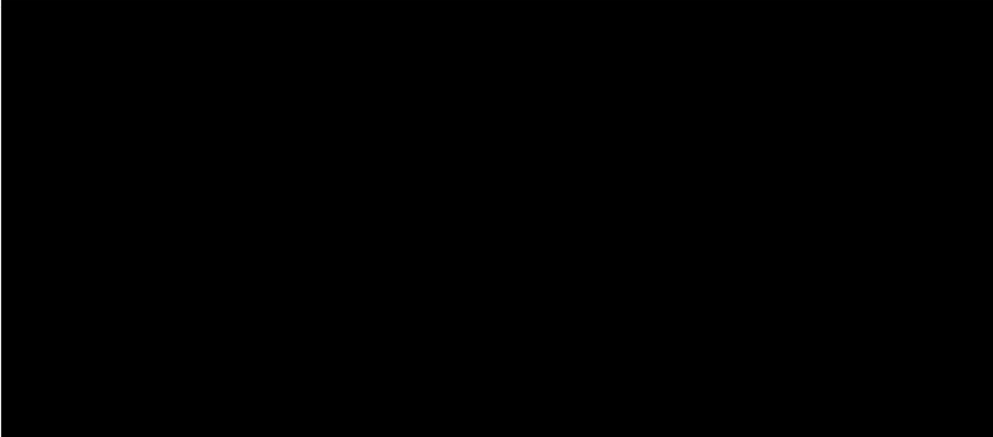
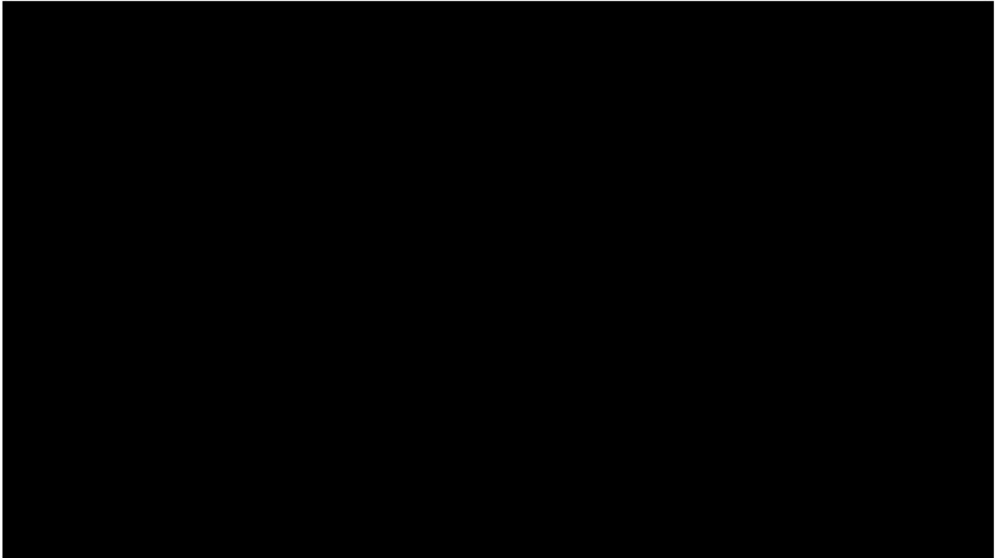


Figure 6.26: Ladder-type TC-SAW structure [redacted] with IMD3(left) and H3(right) nonlinear response. Green ( $2f_1 - f_2$ ) and magenta ( $2f_2 - f_1$ ) traces correspond to measured response. Black dashed and solid lines represent the nonlinear contribution considering only  $c_{3,MR}^E$  and cyan solid and dashed considering  $c_{3,NMR}$  respectively.

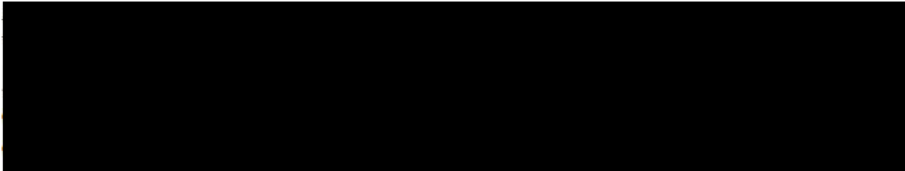
Moreover, Fig. 6.26 (right) depicts the H3 response where the green and magenta traces correspond to the measured  $3f_1$  and  $3f_2$  response. Black solid and dashed traces the H3 individual contribution of the  $c_{3,MR}^E$  and in solid and dashed cyan the corresponding nonlinear contribution of  $c_{3,NMR}$  respectively.

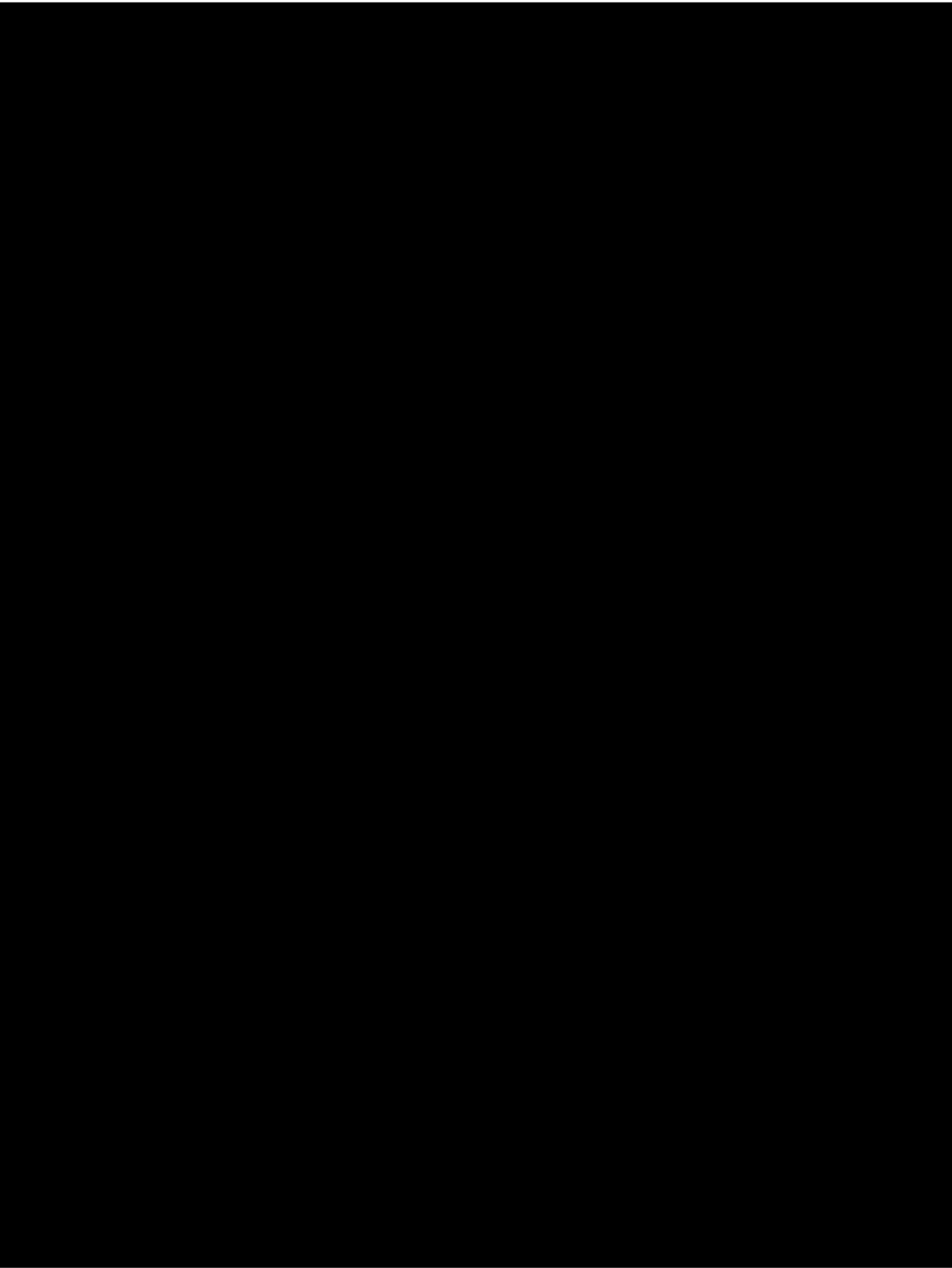




### 6.2.6 Conclusions

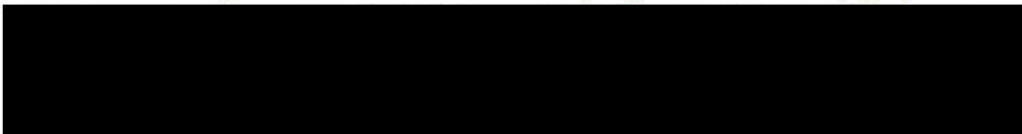
Finally, the main conclusions that can be drawn are the following:

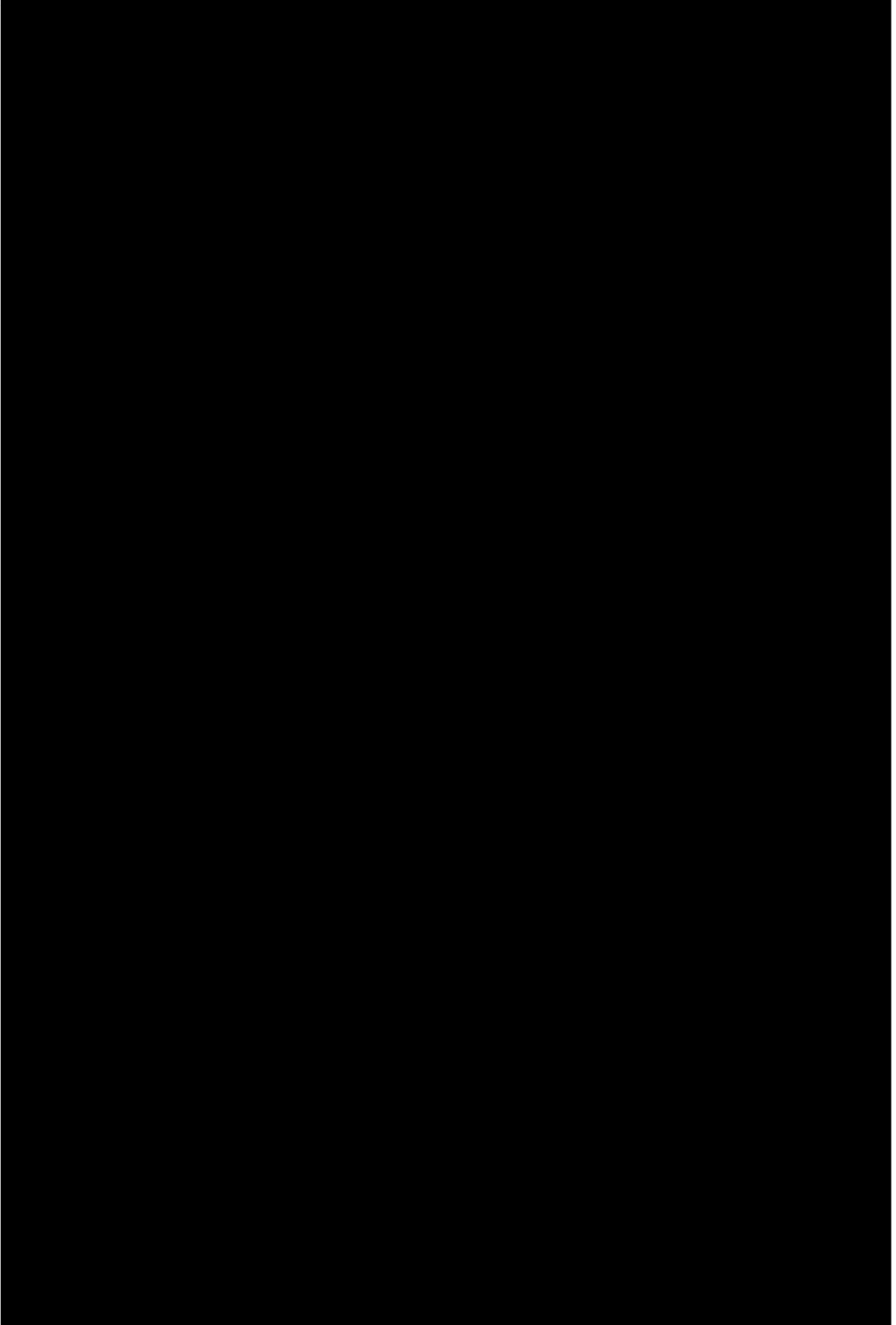
- It has been possible to verify that the main peaks of the ladder filter nonlinear response are due to  $c_{3,MR}^E$  nonlinear constant.
- Using the same  $c_{3,MR}^E$  and  $c_{3,NMR}$  values for the resonator simulations is also possible to fit the IMD3 and H3 of the ladder filter.
- With regard to the observed high spurious peaks due to  $c_{3,NMR}$  nonlinear constant, further investigation is required.
- 
- The simulation time considering 81 frequency points and 3220 nonlinear unit-cells was 12 seconds.



### 6.3.1 Linear measurements

Once the CRF filter has been outlined, the next step is to proceed with the linear measurements. Fig. 6.29 shows the narrowband (left) and broadband (right) mea-







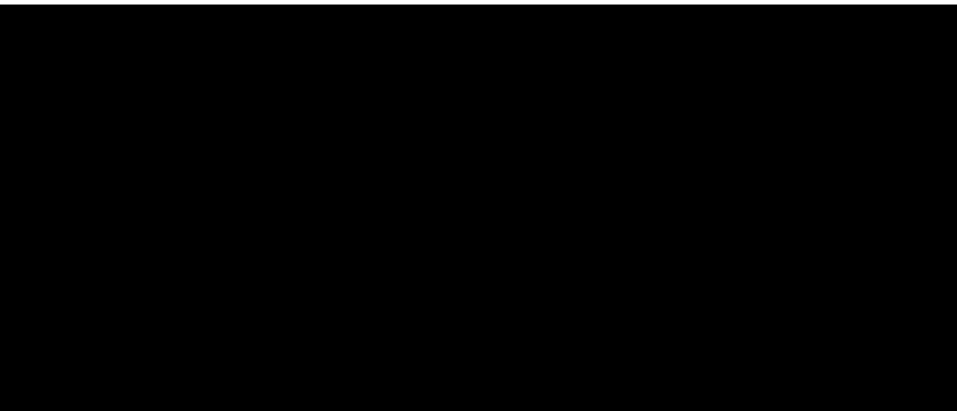
24.0 $\lambda$ . In this case, three different modes can be observed. This is because although using the same number of transducers, their lengths are shorter in comparison between the previous CRF, and less different pitches compose the whole structure.


### 6.3.2 Matlab<sup>®</sup> linear simulations of CRF filters

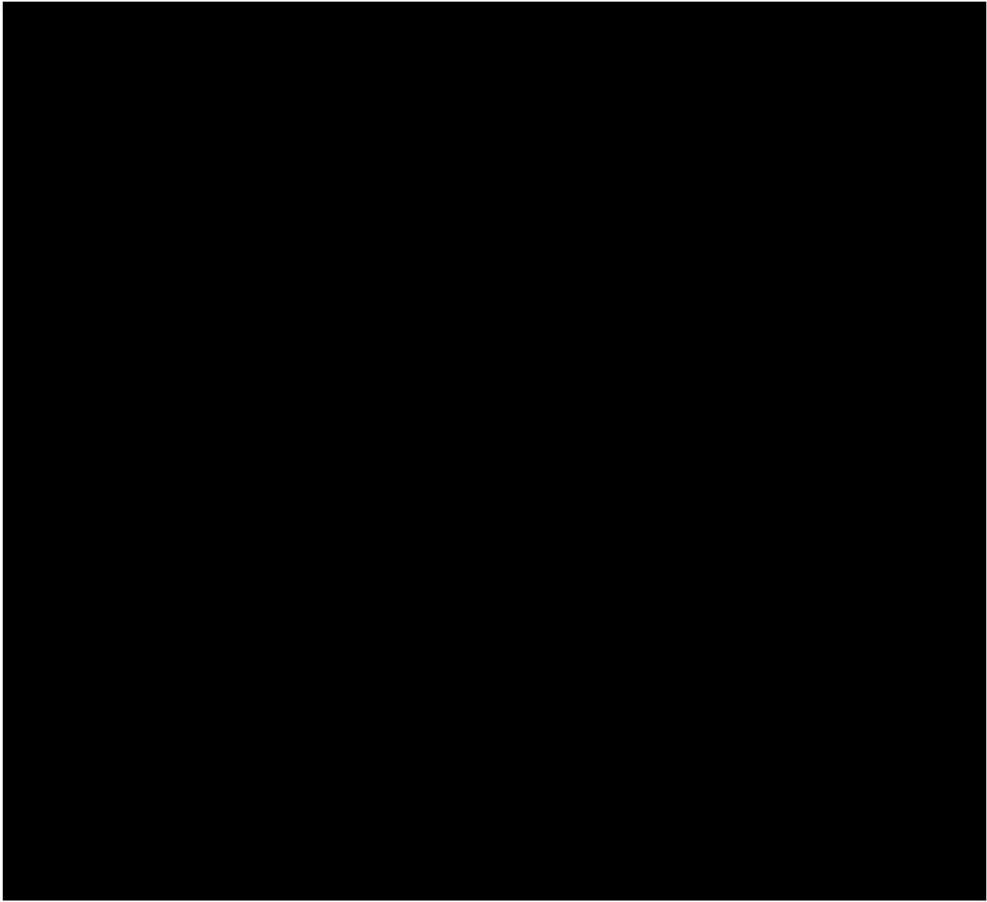
After the linear CRF measurements have been outlined, linear simulations were performed. In the same way as with the ladder filter, the IOES method has been employed to analyze the CRF filter and the procedure can be summarized in the following steps:



Figure 6.30 shows the narrowband (left) and broadband (right) simulations versus measurements, respectively. Green and magenta solid traces correspond to measured  $|S_{21}|$  and  $|S_{11}|$  scattering parameters and red solid and blue solid to their corresponding simulations.



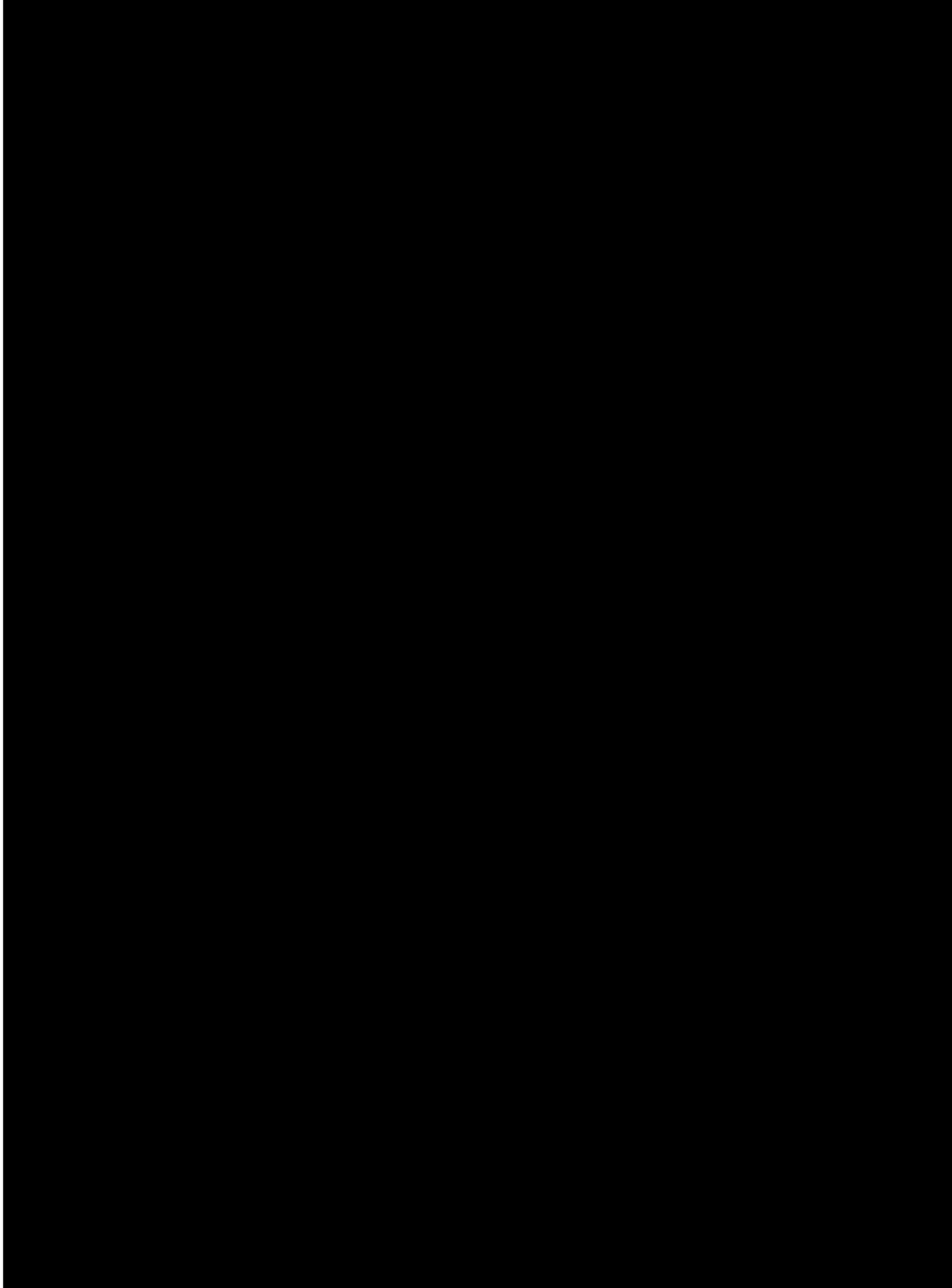
**Figure 6.30:** CRF-type TC-SAW filter structure  simulated narrowband (left) and broadband (right) linear response. Green and magenta solid traces correspond to the measured  $|S_{21}|$  and  $|S_{11}|$  scattering parameters and red and blue solid to their corresponding simulations.

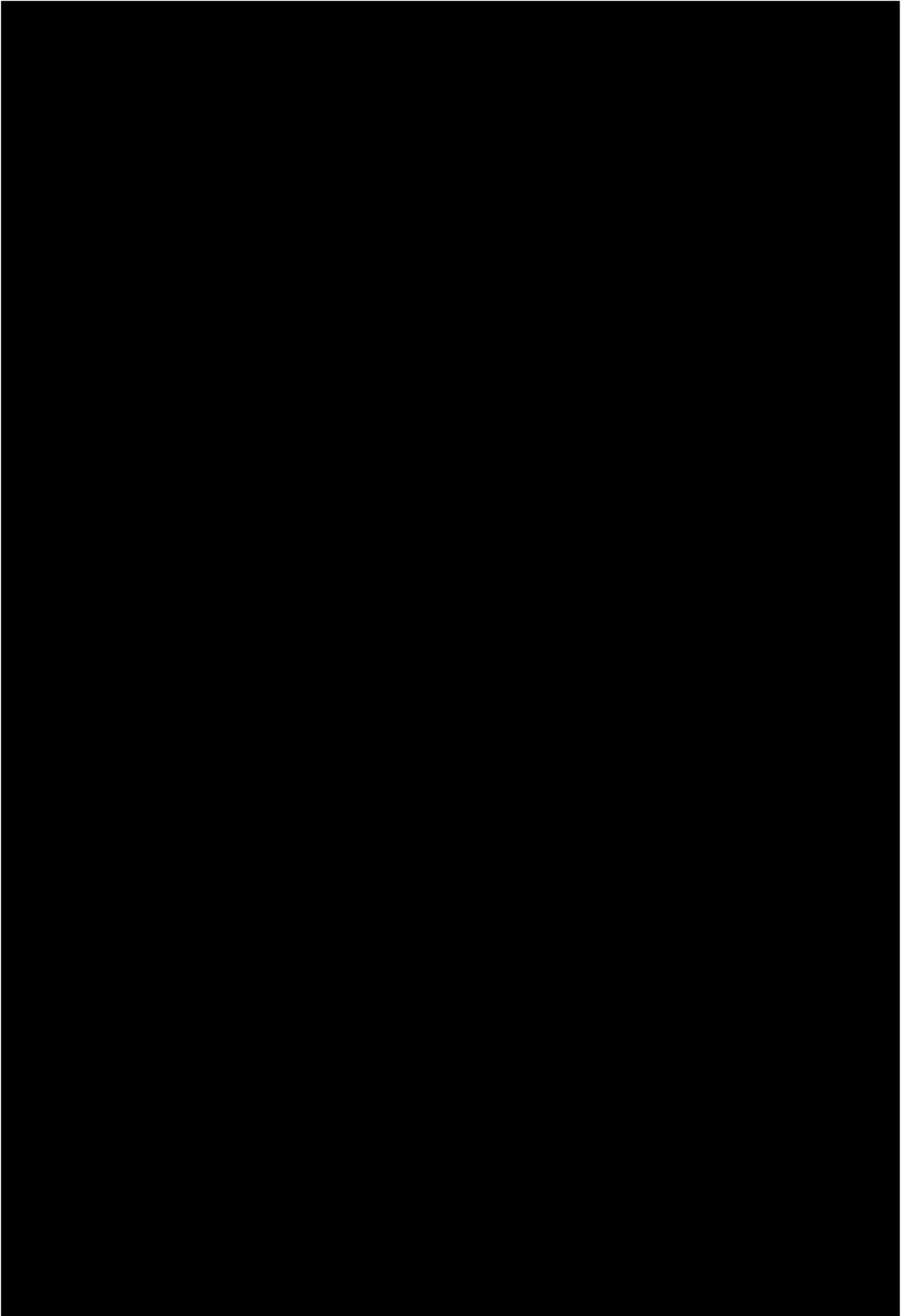


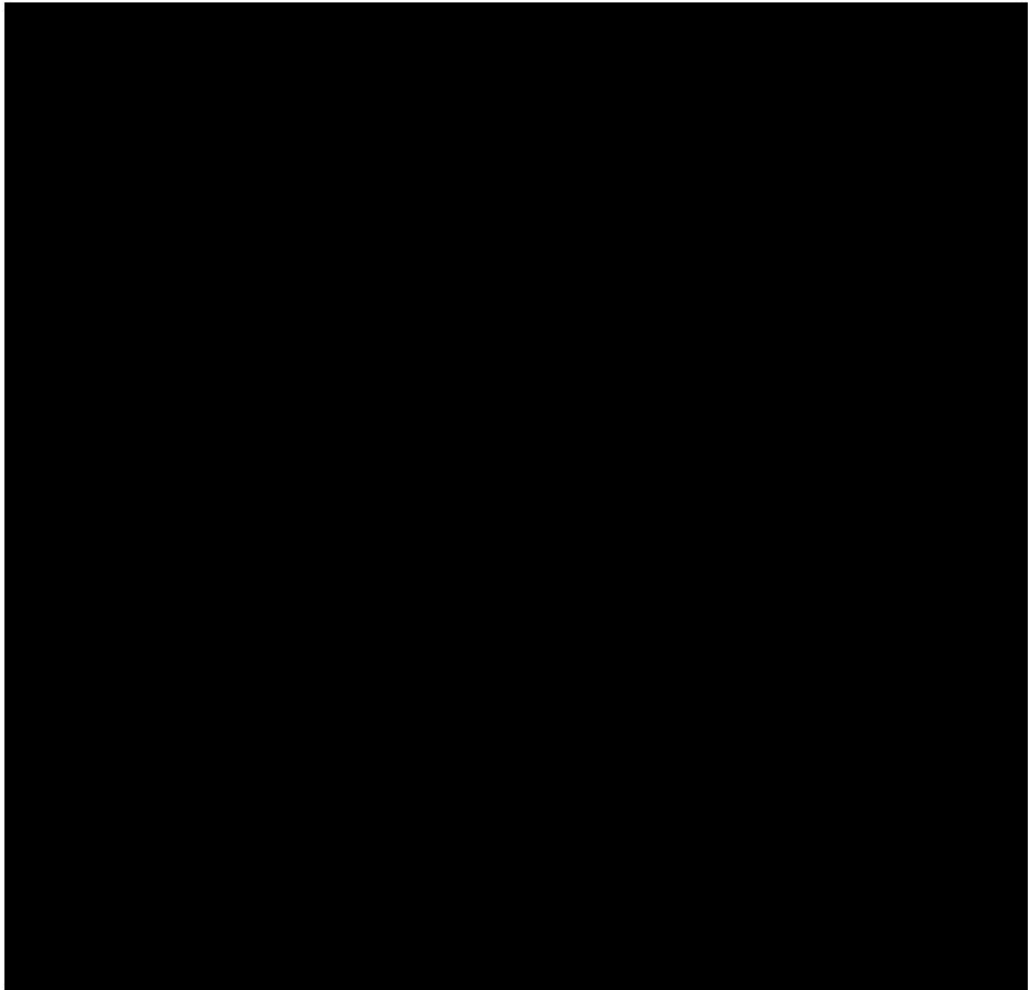
**Figure 6.31:** CRF-type TC-SAW filter structure [redacted] simulated narrowband (left) and broadband (right) linear response. Green and magenta solid traces correspond to the measured  $|S_{21}|$  and  $|S_{11}|$  scattering parameters and red solid and blue solid to their corresponding simulations.

### 6.3.3 Nonlinear measurements of CRF filters

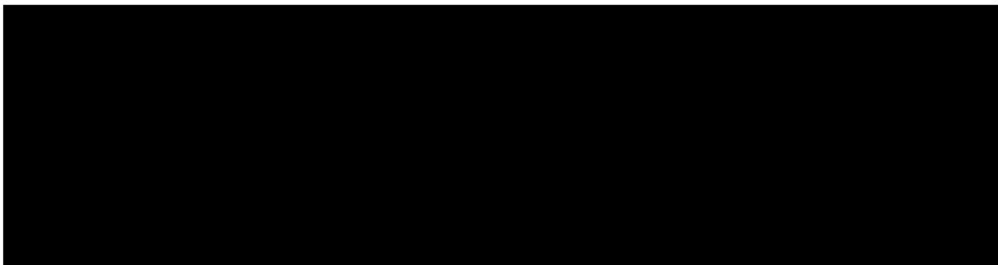
Hereafter an overview of the nonlinear measurements of the CRF structures. Fig. 6.32 and Fig. 6.33 shows the measurements over a frequency swept respect the central frequency  $f_0$  corresponding to the x-axis, whereas the y-axis corresponds to

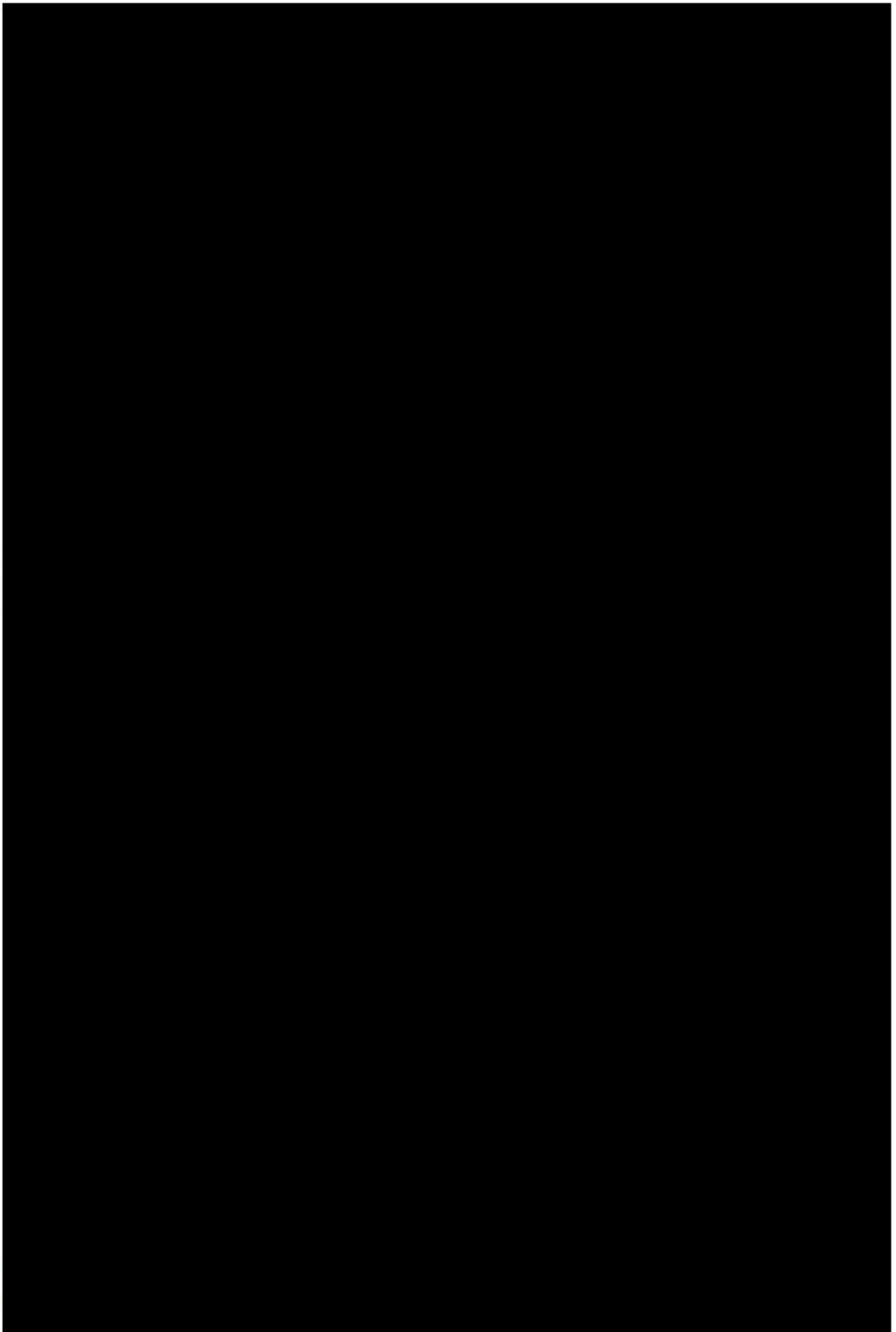






#### 6.3.4 Nonlinear simulations of CRF filters





IMD3 and H3 analysis of CRF filters



Figure 6.38 shows the IMD3 on the left and H3 on the right simulated nonlinear response versus the measurements of the on-wafer CRF filter P2140M40A240 (without matching network). Red and blue lines correspond to computed  $2f_1 - f_2$  and  $2f_2 - f_1$ , respectively, and measured response in green ( $2f_1 - f_2$ ) and magenta ( $2f_2 - f_1$ ) traces.

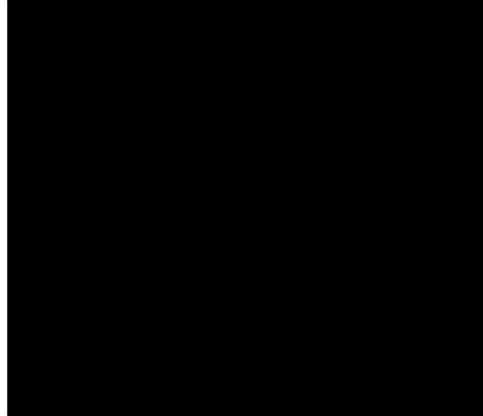
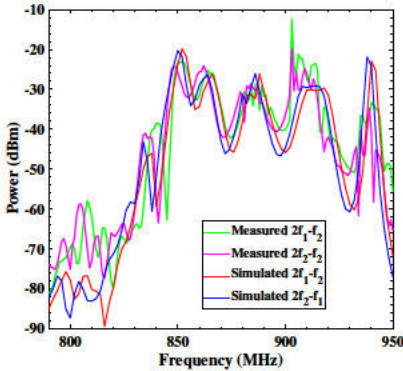
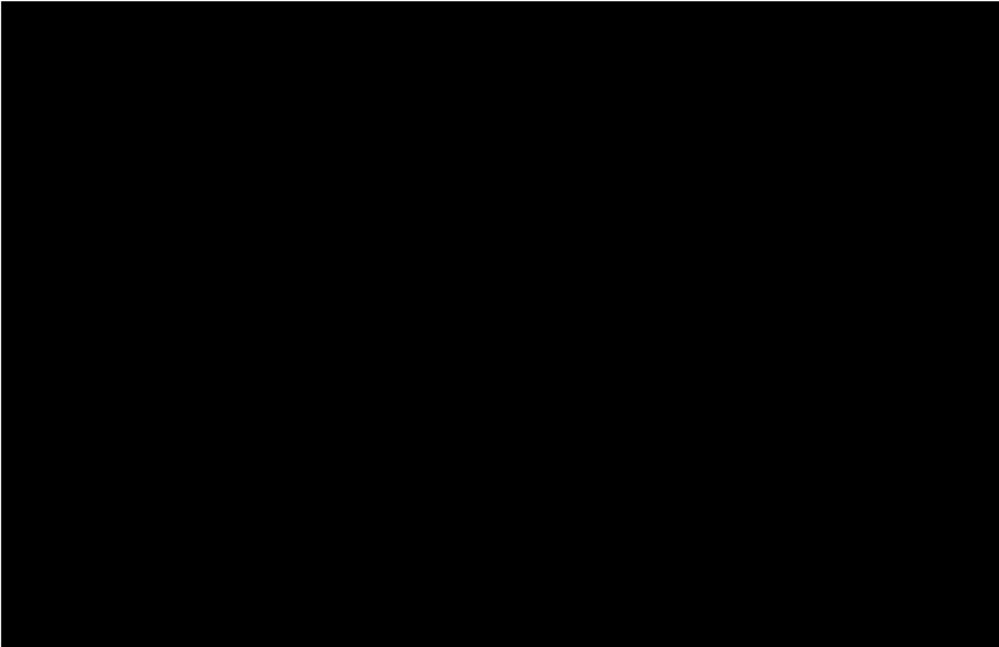
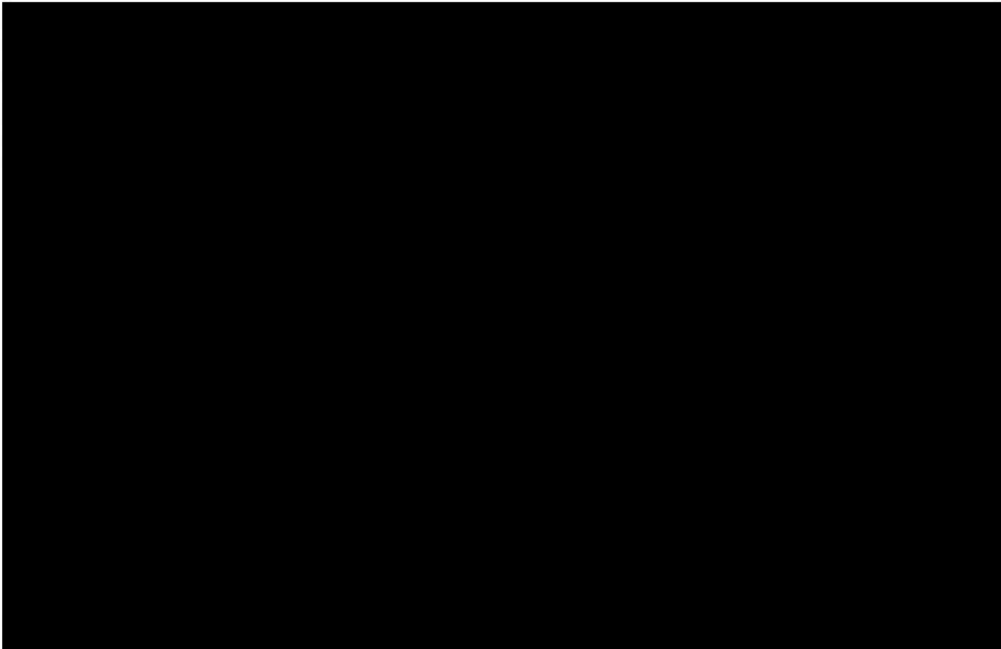


Figure 6.38: CRF structure P2140M40A240 with IMD3 (left) and H3 (right) nonlinear response. Red and blue traces correspond to computed  $(2f_1 - f_2)$  and  $(2f_2 - f_1)$  respectively, and measured response in green  $(2f_1 - f_2)$  and magenta  $(2f_2 - f_1)$  traces.





response. Red and blue traces correspond to computed  $(2f_1 - f_2)$  and  $(2f_2 - f_1)$  respectively, and measured response in green  $(2f_1 - f_2)$  and magenta  $(2f_2 - f_1)$  traces.

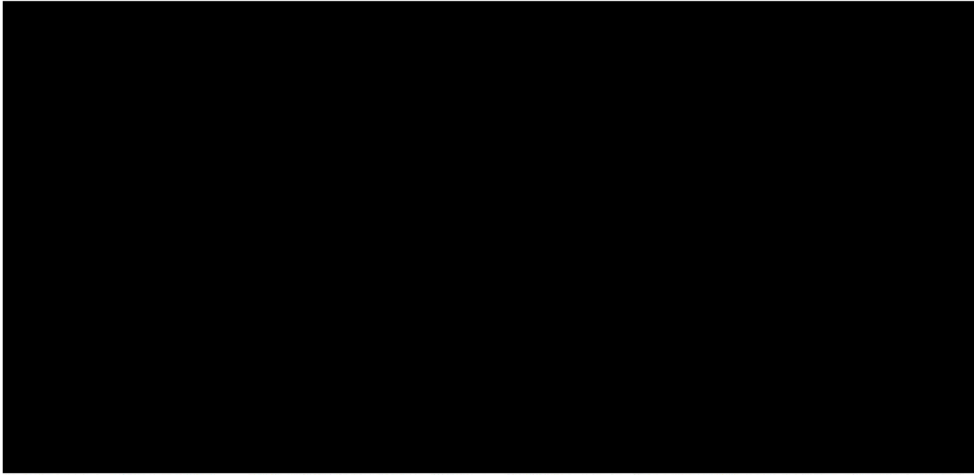
### 6.3.5 Analysis of the nonlinear response of CRF filters

This subsection is devoted to the analysis of the nonlinear contribution of each IDT composing the CRF structures separately is presented. After that, the individual analysis of each of the nonlinear constants employed and its contribution to the CRF filter nonlinear response is outlined.

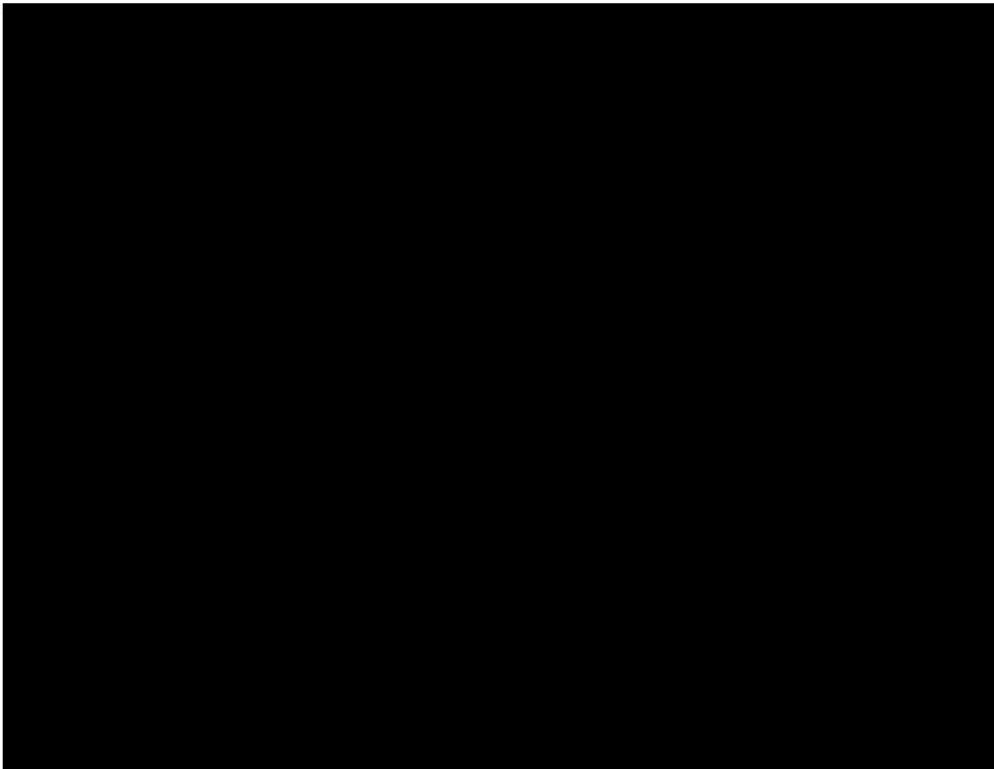
#### IMD3 and H3 nonlinear contribution of each IDT on the CRF

As done previously with the ladder filter, Fig. 6.40 presents the nonlinear contribution of each transducer composing the CRF structure separately. Left plot represents the IMD3 response with green  $(2f_1 - f_2)$  and magenta  $(2f_2 - f_1)$  traces corresponding to measured response. Moreover, black solid lines represent the nonlinear contribution of IDT1 resonator individually and black dashed lines the IDT2 resonator respectively. On the other hand, right plot depicts the H3 response, green and magenta traces correspond to measured  $3f_1$  and  $3f_2$  response and in black solid and dashed traces the simulated H3 individual contribution of the IDT1 and IDT2 respectively.





response. Green ( $2f_1 - f_2$ ) and magenta ( $2f_2 - f_1$ ) traces correspond to measured response. Black solid lines represent the nonlinear contribution of IDT1 individually and black dashed lines the IDT2, respectively.



response. Green ( $2f_1 - f_2$ ) and magenta ( $2f_2 - f_1$ ) traces corresponds to measured response. Black solid lines represent the nonlinear contribution of IDT1 individually and black dashed lines the IDT2 respectively.

IMD3 and H3 nonlinear contribution considering separately  $c_{3,MR}^E$  or  $c_{3,NMR}$

After the previous analysis, now the individual analysis of each of the nonlinear constant employed, being  $c_{3,MR}^E$  or  $c_{3,NMR}$ , and its contribution to the CRF filter nonlinear response is outlined. Figure 6.42 depicts the nonlinear contribution of the three IDT's but considering the third order nonlinear constants  $c_{3,MR}^E$  or  $c_{3,NMR}$  individually. On the left plot, green ( $2f_1 - f_2$ ) and magenta ( $2f_2 - f_1$ ) traces correspond to measured IMD3 response. In addition, black solid and dashed lines represent the IMD3 nonlinear contribution if only the  $c_{3,MR}^E$  nonlinear constant is activated. Instead, cyan solid and dashed lines represent the nonlinear contribution if only the  $c_{3,NMR}$  nonlinear constant is activated.

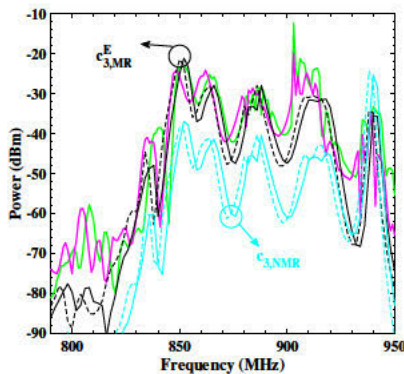
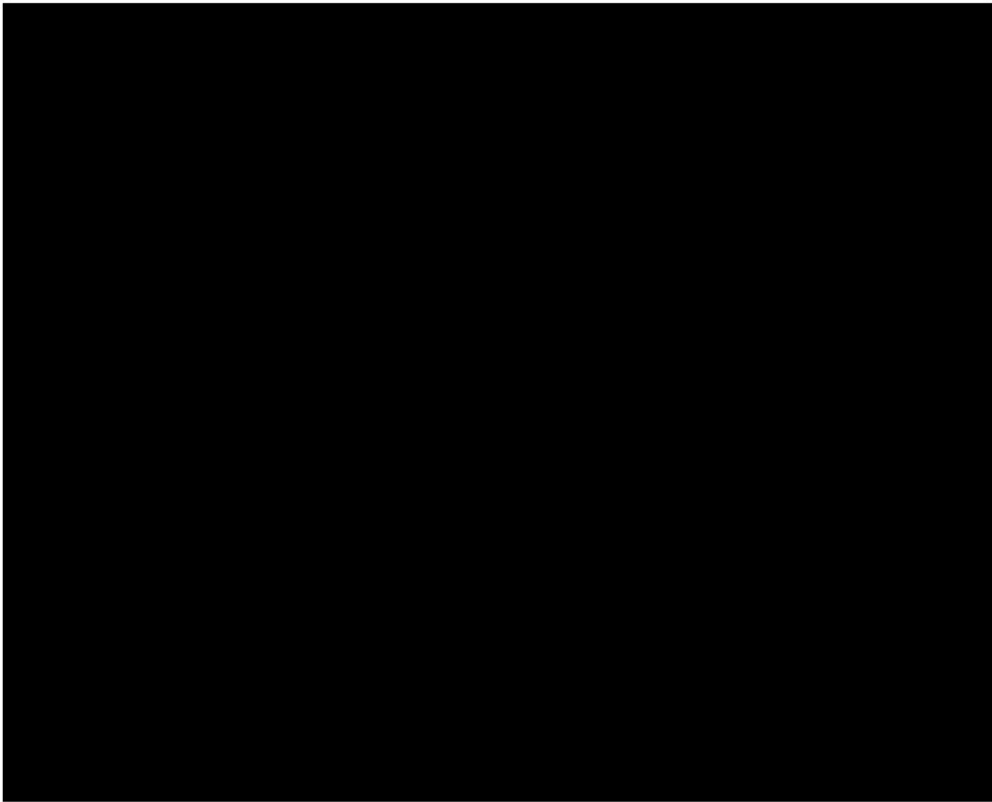


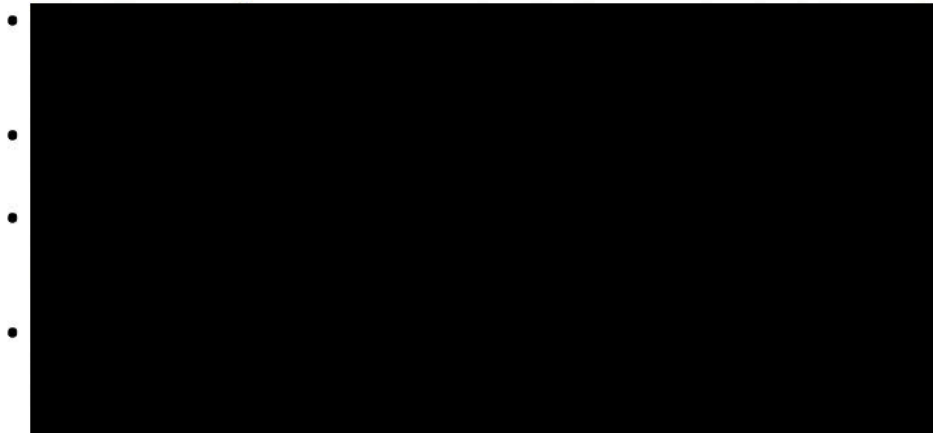
Figure 6.42: CRF structure [redacted] with IMD3 (left) and H3 (right) nonlinear response. Green ( $2f_1 - f_2$ ) and magenta ( $2f_2 - f_1$ ) traces correspond to measured response. Black dashed and solid lines represent the nonlinear contribution considering only  $c_{3,MR}^E$  and cyan solid and dashed considering  $c_{3,NMR}$  respectively.



### 6.3.6 Conclusions

Finally, the main conclusions that can be extracted for the CRF structure are the following:

- The use of the distributed crossed-field model reproduces the linear narrow-band measurements.



## 6.4 Nonlinear lumped model

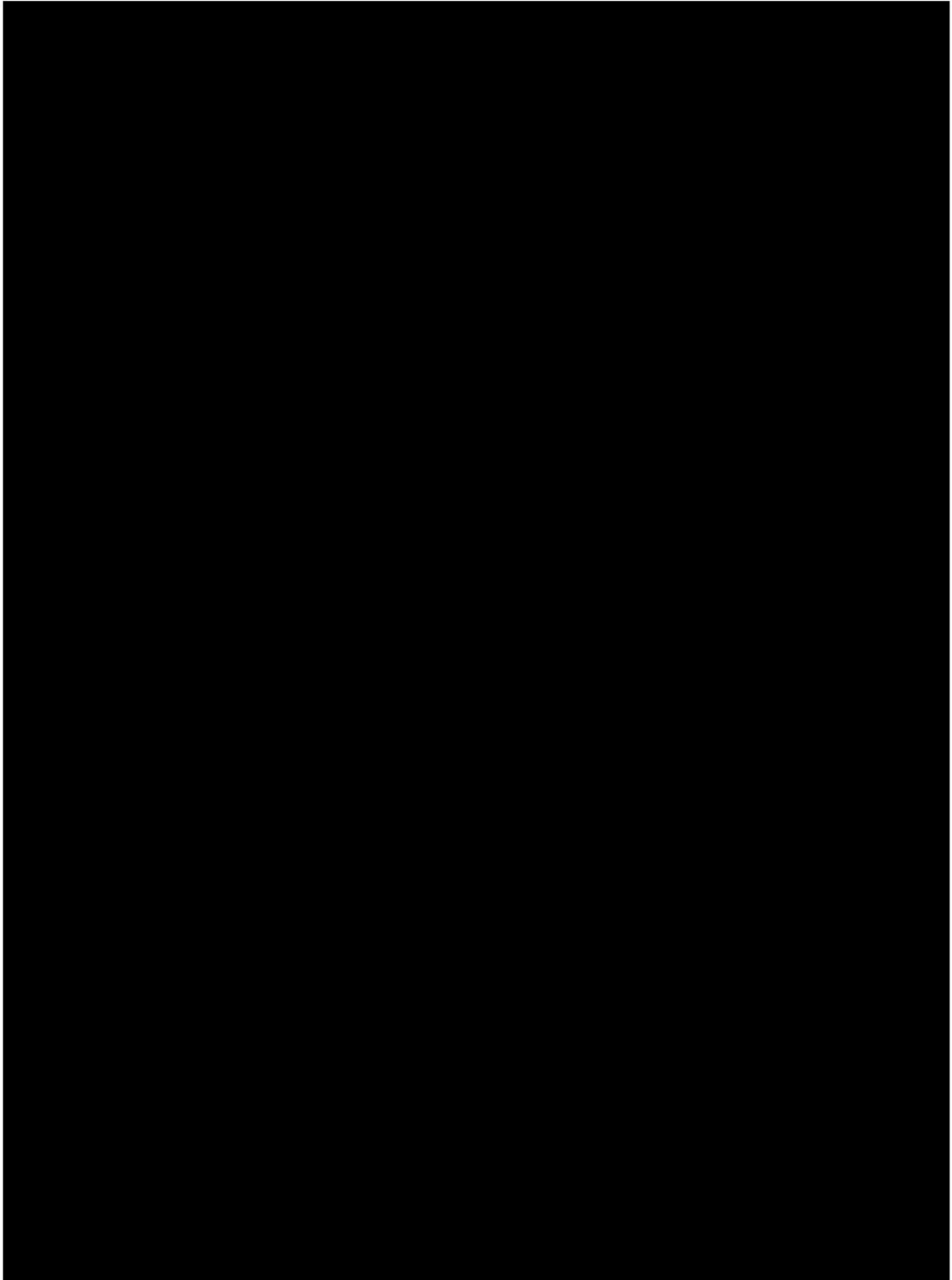
The main drawback of using distributed circuit models is their high computational time required when analyzing nonlinearities in more complex structures like multiplexers. A very hot topic is to find a nonlinear lumped model able to calculate for example the main peak of the IMD3 response in a faster way than the previous distributed model, which would be possible reducing the number of the required nonlinear sources.

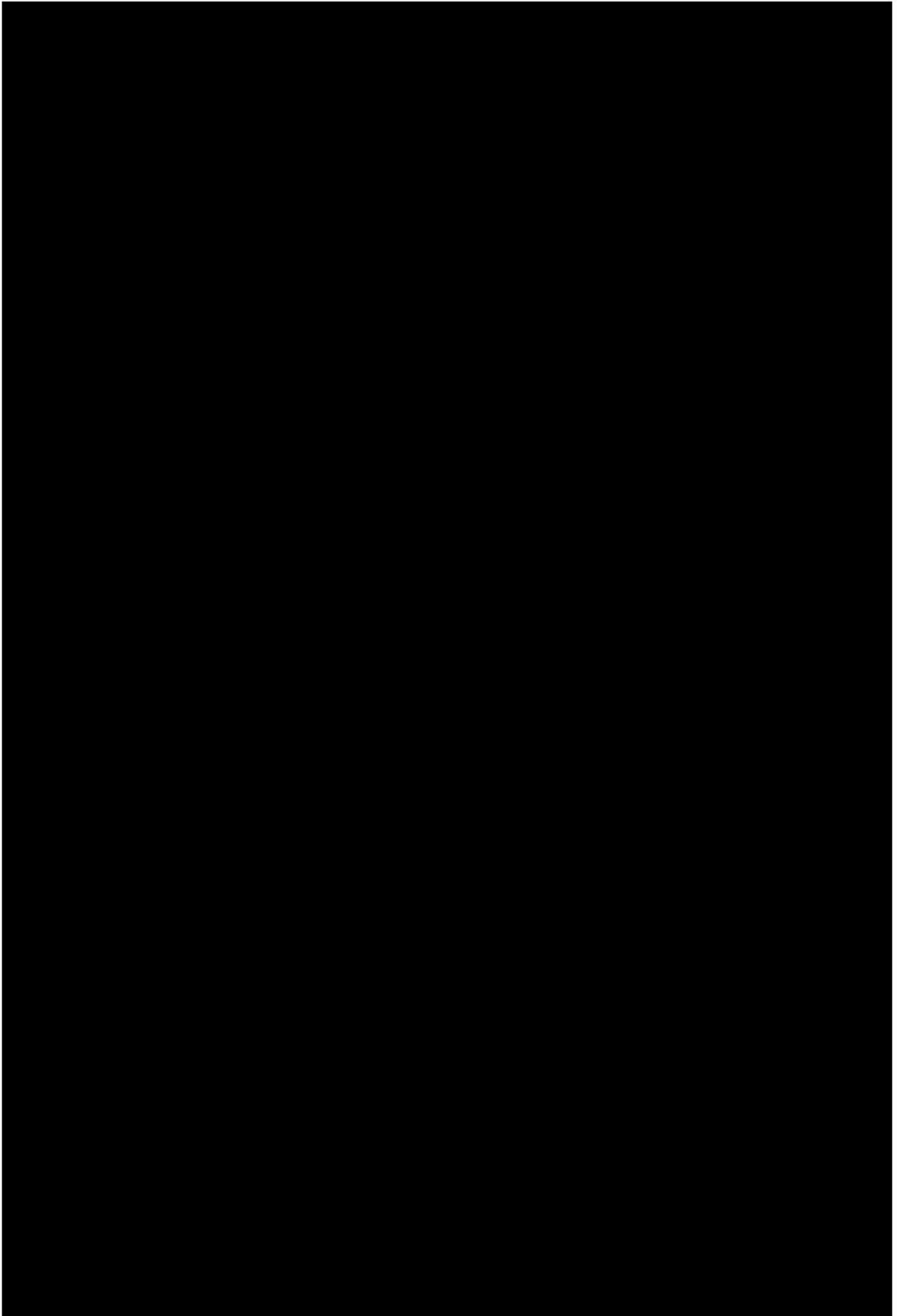
[REDACTED]

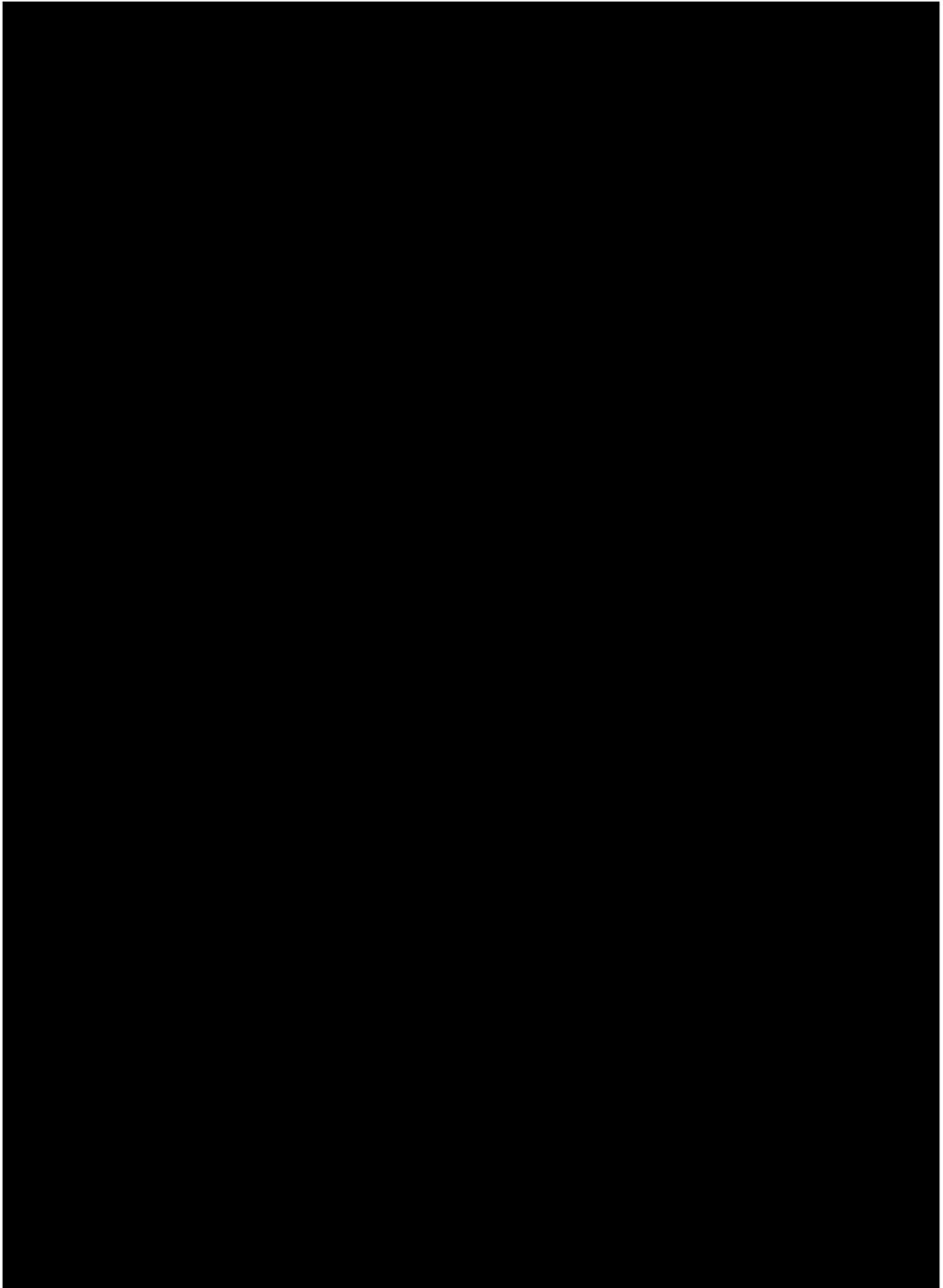
[REDACTED]

[REDACTED]

[REDACTED]







With this lumped model the admittance matrix analysis will be simplified and the nonlinear analysis will be easier since less nonlinear sources are required. Of course, there are many assumptions we have done through the process for going from a distributed model with many nonlinear sources to a lumped model with only two sources. Next section compares the lumped model with a full discretized model to evaluate its limitations.

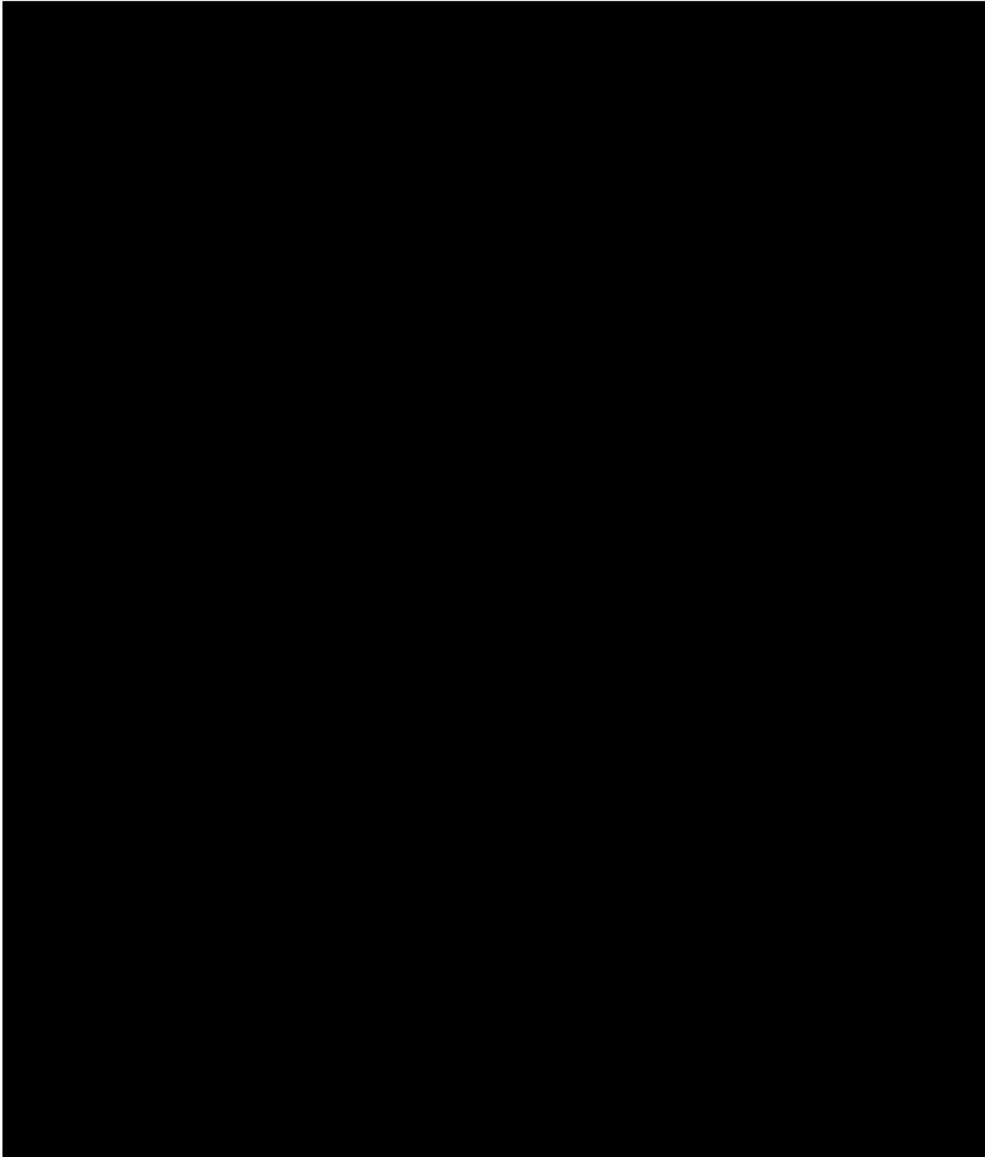
## 6.5 Nonlinear simulations with lumped model

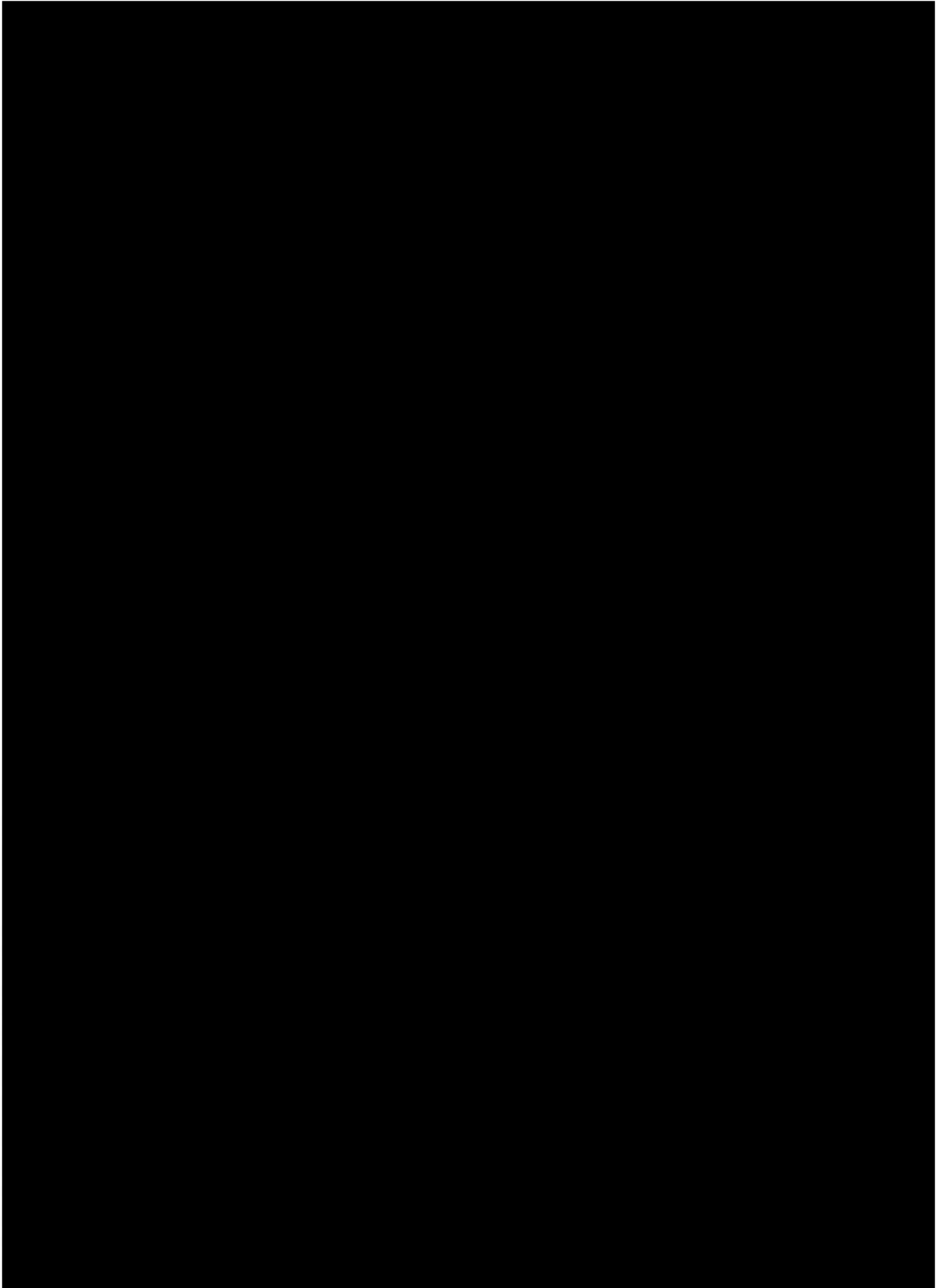
To validate the new developed lumped model, IOES simulations have been performed on resonators with different technologies as well as in a ladder-type filter. The corresponding measurement system is also included into the simulations. Specifically, the simulations were performed considering different duty factor, pitch, number of electrodes and nonlinear constants.

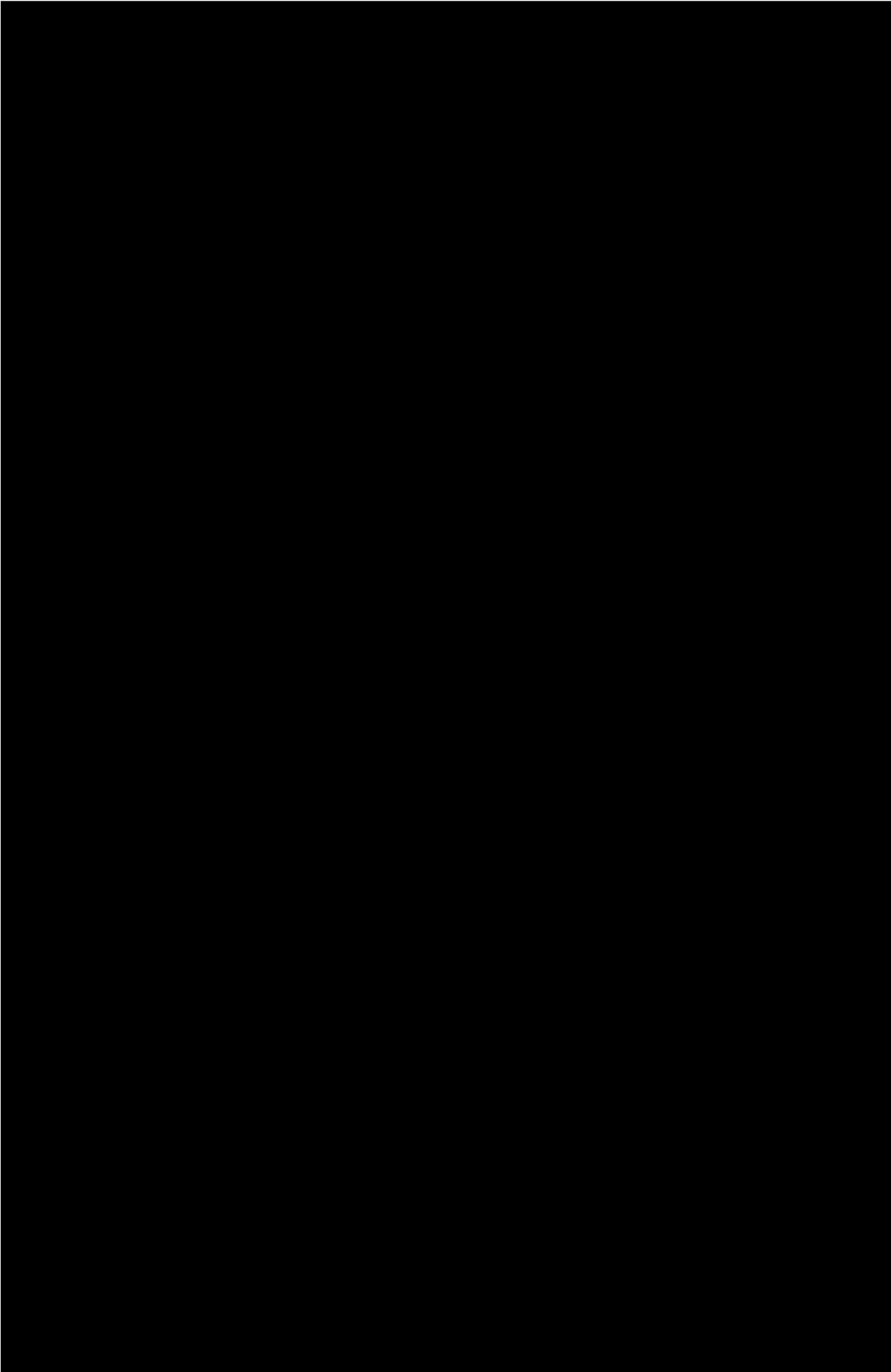
[REDACTED]

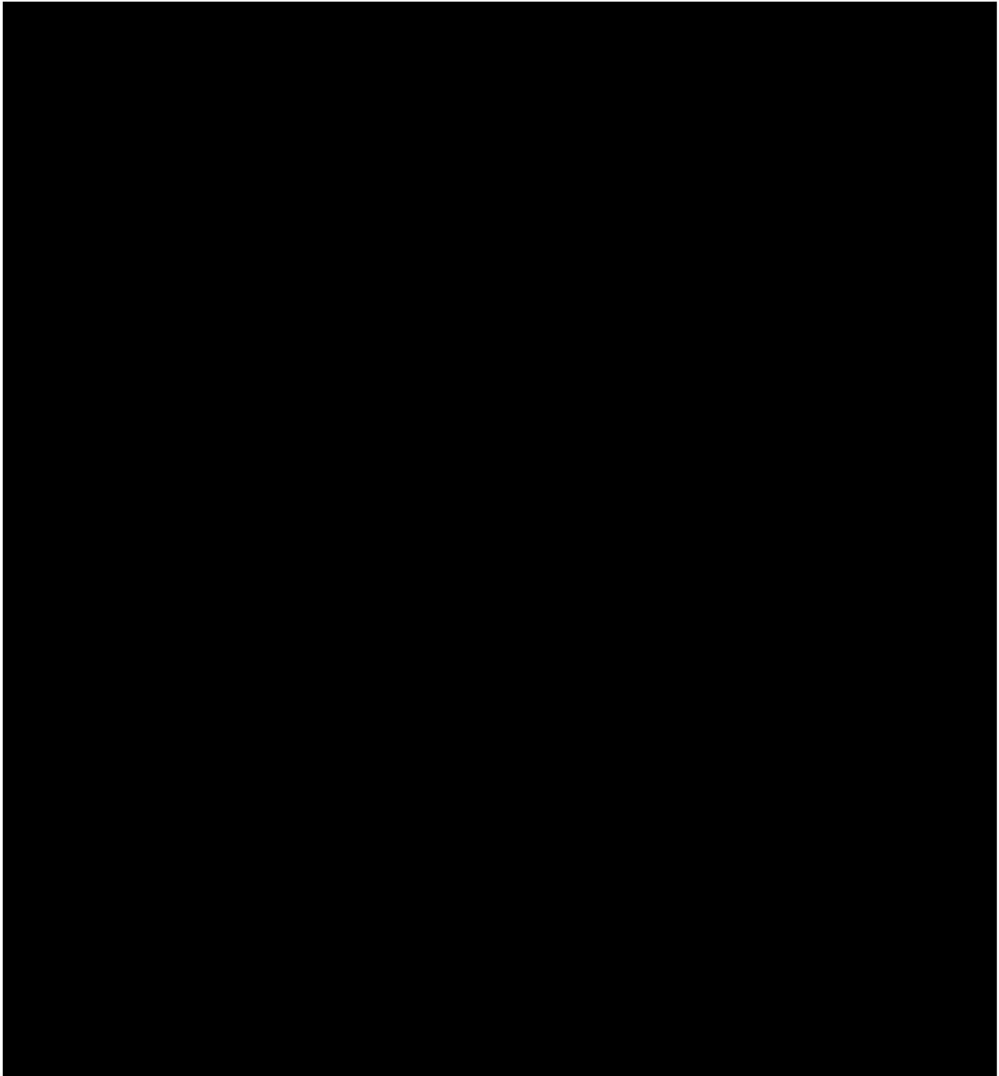
[REDACTED]

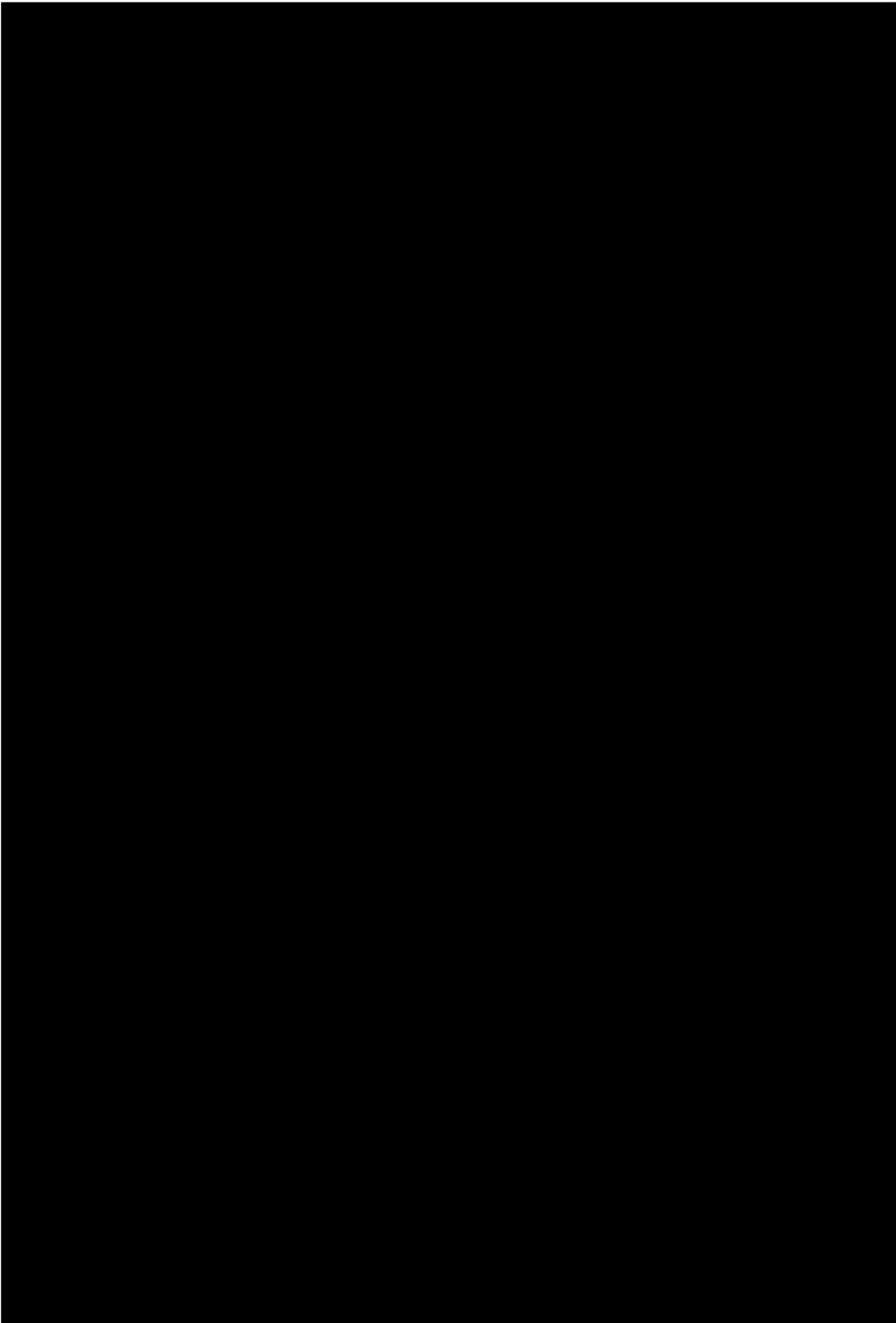


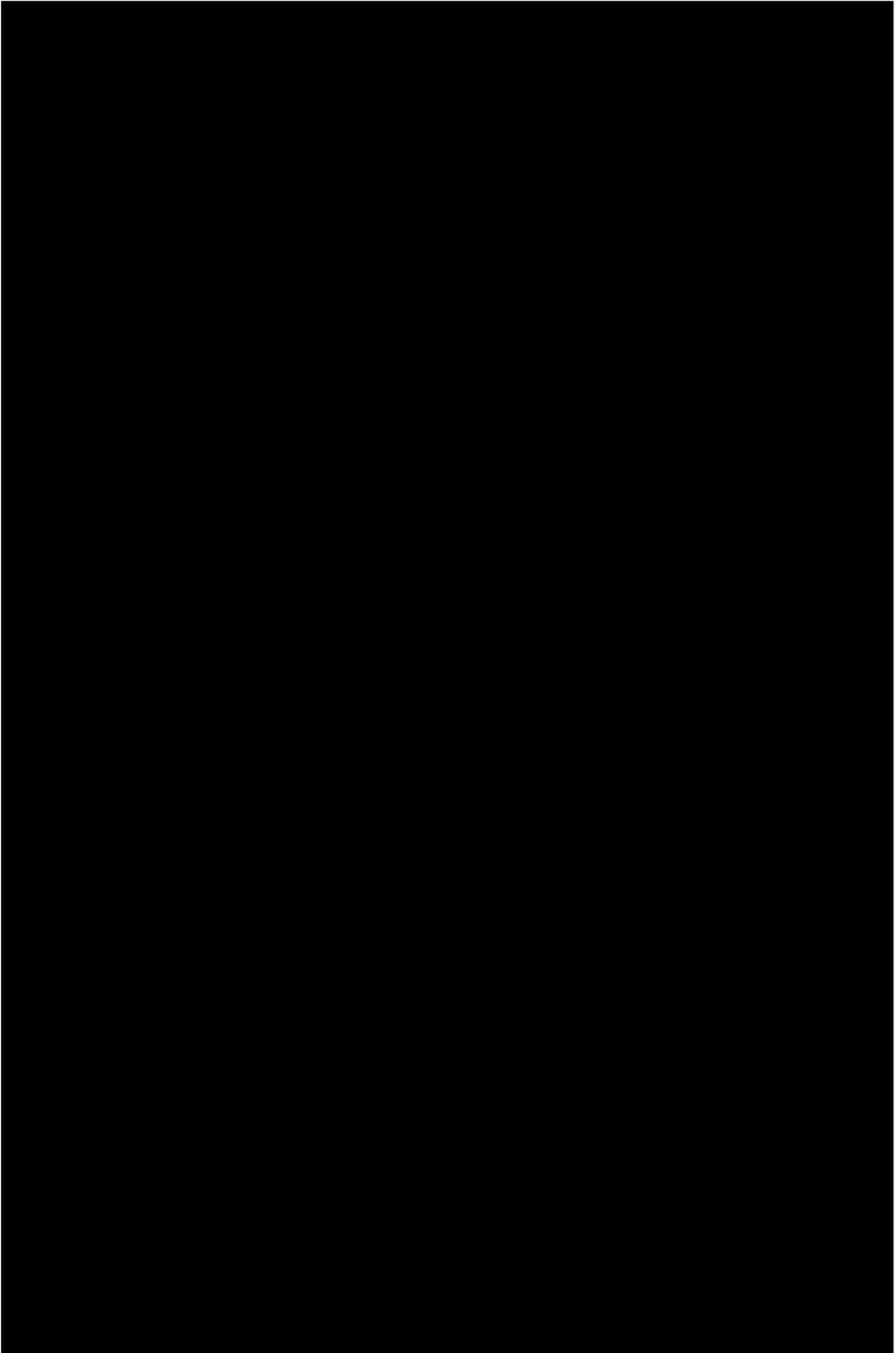


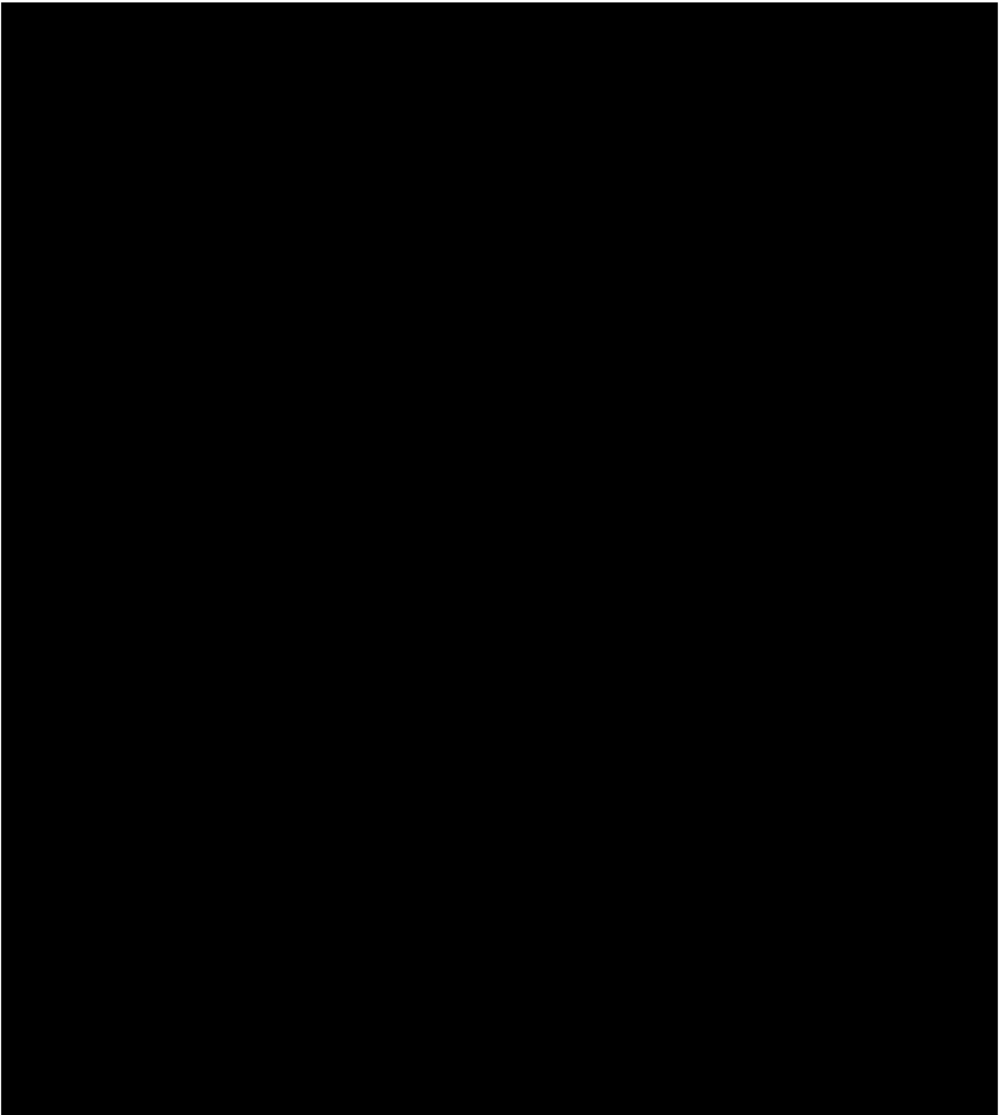












**Conclusions**

[Redacted text block]

[Redacted text block]

[Redacted text block]





## Chapter 7

# High-power characterization and other set-ups

This chapter is focused on introducing other characterization set-ups that have been developed during the thesis. Specifically, a feed-forward based cancellation technique is used to measure S-Parameters of devices under CW high-power (HP) signals. The developed test system will be further used to characterize a set of SAW resonators under HP conditions. Finally, based on the same concept of feed-forward technique, a tone-injection based measurement system has been developed to prove that the same concept can be applied to cancel-out effects with modulated signals in BAW resonators.

### 7.1 Feed-forward cancellation

#### 7.1.1 Introduction

The evolution of mobile devices imposes the use of new and miniaturized RF front-ends. In addition to that, actual demands of circuit integration of RF modules leads to increased power densities and temperatures into the components. Temperature stability is a crucial aspect in the design chain as may lead to a frequency shift of the filter transfer function and is a good example of the increasing interest in characterizing devices when they are driven by high power signals [95].

Power durability and low temperature drift are among the most demanded and challenging features for SAW devices [96], [97], [98], [99]. It is well known that SAW devices can handle less power than BAW devices due to the very thin cross-section of the IDT fingers. As a CW is applied to the resonator, there is a heat dissipation that involves a temperature rise in the resonator leading to changes on resonator performance. Overloading the resonators with high-power levels may

lead to an excessive current density affecting the electrodes, being degradation of the metallization due to acoustically-induced migration one of the possible failure mechanism [100],[101].

The motivation of develop this measurement system is to monitor and characterize the resonator behavior even at high powers levels that can damage the device. Monitoring the performance of the resonators under high power CW signals at different frequencies provides useful information for a better understanding of the failure mechanisms. The method is based on a feed-forward-based technique to measure the reflection coefficient of one-port SAW resonators under a fixed-frequency High-Power (HP) heating signal. The HP signal is cancelled more than 60 dB and that guarantees a precise measurement of the reflection coefficient using a conventional Vector Network Analyzer (VNA). The measurement system is protected against high power levels even when the devices fails causing sudden changes of its reflection coefficient.

### 7.1.2 Proposed method description

The proposed method is based on a feed-forward loop technique to measure the reflection coefficient of SAW resonators under a fixed-frequency HP signal. Feed-forward architectures have been successfully used in the past to measure for example PIM [91] cancelling the HP fundamental tone before reaching the SA or to measure the reflection coefficient of a device when this device is driven by a HP CW signal [94] at a given frequency. The idea behind this is to drive a jamming signal in the DUT to heat the device and measure changes in its small-signal S-parameters. This HP signal will be monitored with the SA, while the changes in the S-parameters of the device will be measured with the VNA. Nevertheless, the injected signal can compromise the integrity of the instrumentation, specifically the VNA and affect to the measurement of the small-signal parameters. A way to avoid that, is to apply a feed-forward cancellation technique before the HP signal goes into the VNA. Specifically, this technique consists on taking a reference of the heating signal before driving the device. This cancellation signal branch can change the attenuation and phase of the reference signal using a controlled VM.

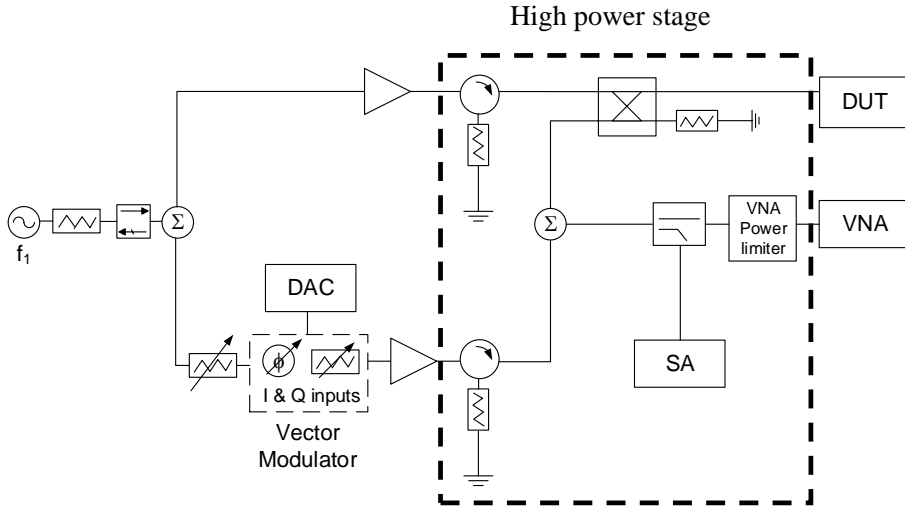


**Figure 7.1:** Feed-forward developed cancellation set-up.

Fig. 7.1 shows the proposed measurement system, where a CW signal is split into two paths. Upper branch provides a HP stimulus signal to the DUT whereas the bottom branch generates a feed-forward signal that cancels out the HP reflected signal from the DUT so that the undesired tone is suppressed and, in the ideal case, total cancellation occurs. The cancelled signal is monitored using a conventional SA.

As it can be seen on Fig. 7.1, isolators protect in both branches the high-power amplifiers (HPA) from reflected signals. The variable attenuator is placed before the VM of the cancellation branch, to adequate the level of the cancellation signal to the reflected power at the DUT, which is useful when dealing with very reflective DUTs. The attenuation and phase of the output VM signal are controlled by an in-phase ( $V_i$ ) and quadrature ( $V_q$ ) DC voltages generated by the digital-to-analog converter (DAC). The values of these voltages are found and adjusted in real time using a cancellation algorithm whose input is the power level measured at the SA.

With regard of the DUT branch, the amplified cancellation signal is connected to a  $90^\circ$  hybrid coupler that can separate the incident and the reflected power at the DUT input. Then, both the reflected and cancellation signals are added using a high power Wilkinson power combiner. As explained in [94], the power of the canceled signal depends on the unbalanced phase and magnitude between the signals of both cancellation and DUT branch, therefore the cancellation level is maximum when both signals add each other, having equal magnitude and opposite phase. The inputs of the algorithm are the power measured by the SA and the desired cancellation level.

Furthermore, the cancellation level is defined as the ratio of the power of the HP signal reflected from the DUT with no cancellation considered over the power of the cancellation branch, both measured at the output of the combiner. The algorithm uses an iterative gradient descent-based method [93]. Because of its iterative nature, the algorithm is prepared for small variations in the reflection coefficient with the power or the time. Moreover, the gradient direction is calculated with numerical derivatives of the obtained power samples. The magnitude and phase of the cancellation signal whose search domain is defined by the VM DC voltages, are modified in real time to find the proper cancellation signal that will later destructively interfere with the reflected one at the DUT. More details about the cancellation algorithm and its particularities can be found in [94].

At the same time, at the combiner output, a HP directional coupler is placed to probe the power level of the canceled HP signal at the coupled port using a SA. The through port of the directional coupler is connected to a power limiter used to protect the VNA when no cancellation is achieved. Finally, if cancellation occurs the scattering parameters of the DUT can be obtained avoiding that the HP signal goes into the VNA.

### 7.1.3 High-power measurements and results

The proposed application is validated with measurements of the input impedance of a set of on-wafer based on Lithium Tantalite LSAW resonators with different duty factors. All the measurements were made setting the heating source at three different frequencies corresponding to series, shunt and maximum stress resonant frequency. Specifically, the HP tone is set at a desired fixed frequency along the measurements with the power being swept in steps of 1 dB. For every power step, the HP is cancelled each time, and then the S-parameters are taken.

Fig. 7.2 (top) shows the measured input impedance of a  $\eta = 50\%$  duty factor resonator and with the HP signal set at series resonant frequency, Fig. 7.2 (middle) and Fig. 7.2 (bottom) show the corresponding measured impedance with the HP signal set at shunt and the maximum stress resonant frequency respectively. The input HP signal is swept from 5 to 33 dBm, leaving one minute between each power step to allow the device to obtain a proper steady state temperature. Once the HP signal is cancelled, the  $S_{11}$  parameter is measured.

As depicted in the inset of the figures (right side of the plots), as the power increases, there is a frequency shift of the response towards lower frequencies. Last trace of each figure corresponds to 33 dBm power before the electrodes got damaged. It is also noticeable that apart from the frequency shift, the resonator response becomes more unstable since the sharp series resonant frequency becomes less pronounced and some waving appears making clearly appreciable that is suffering a severe degradation. Specifically, Fig. 7.2 (top) and (bottom) depict more clearly the degradation effect. This degradation in some cases is reversible as in Fig. 7.2 (top) but on the contrary, the degradation could lead to a fatal failure of the device as in Fig. 7.2 (bottom) where the resonator was destroyed.

Furthermore, Fig. 7.3 shows the measured results for the  $\eta = 45\%$  LSAW resonator. In this case, for the series and shunt resonant frequencies the power was swept from 5 to 30 dBm and only when the HP was located at maximum stress resonant frequency the power arrived to 33 dBm, which is when the resonator was severely damaged. Additionally, Fig. 7.4 shows the results for the  $\eta = 60\%$  LSAW resonator. In this case, for the series and shunt resonant frequencies the power was swept from 5 to 33 dBm. Besides, when the HP was located at maximum stress resonant frequency the power arrived to 32 dBm to avoid fatal resonator electrodes damage.

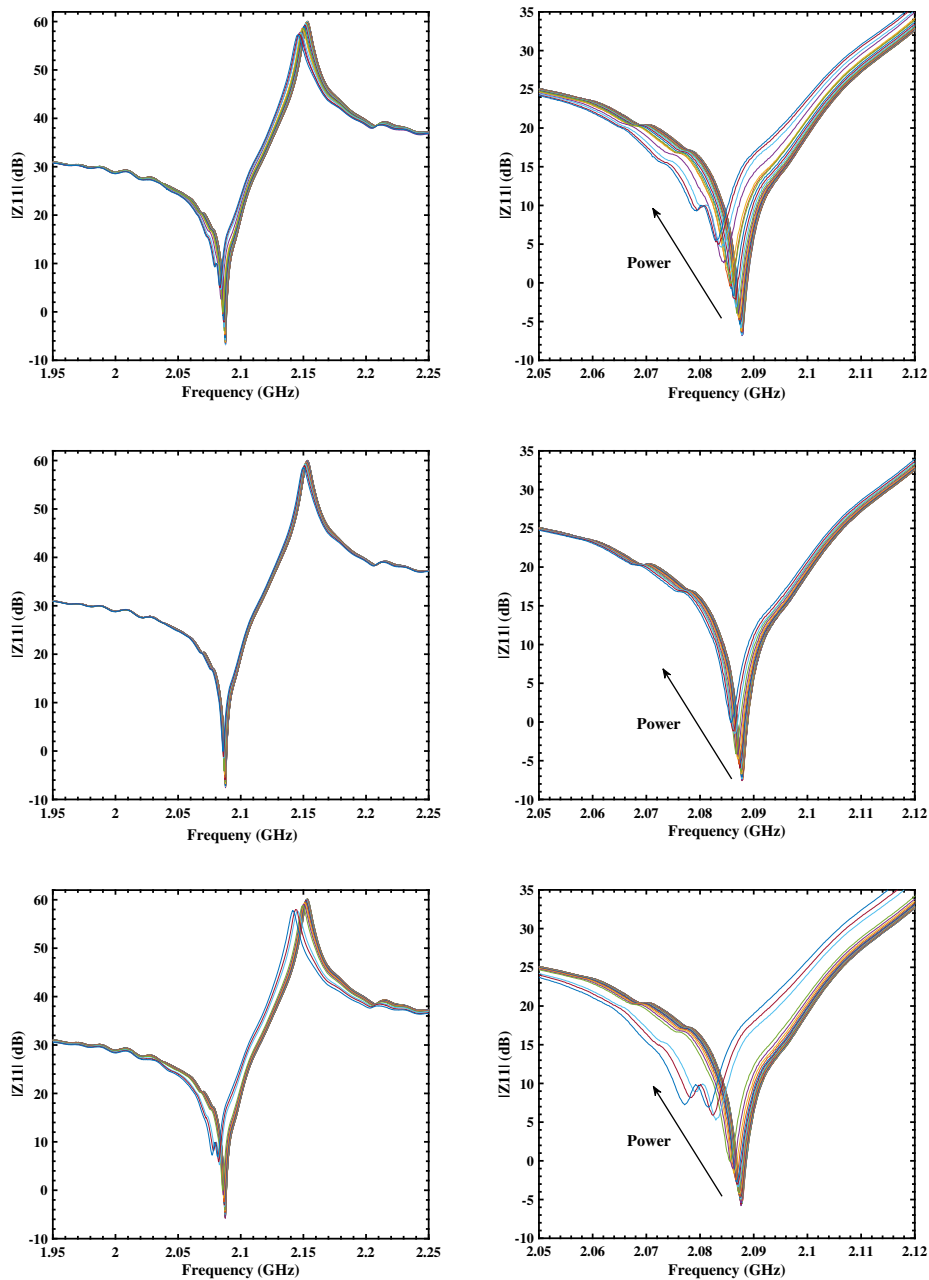


**Figure 7.2:** Measured input impedance of  $\eta = 50\%$  LSAW resonator. (Top) HP cancelling tone is set at series resonant frequency located at 2.088 GHz. (Middle) HP cancelling tone is set at shunt resonant frequency located at 2.153 GHz. (Bottom) HP cancelling tone is set at maximum stress resonant frequency located at 2.118 GHz. Right plots show the zoomed insets.

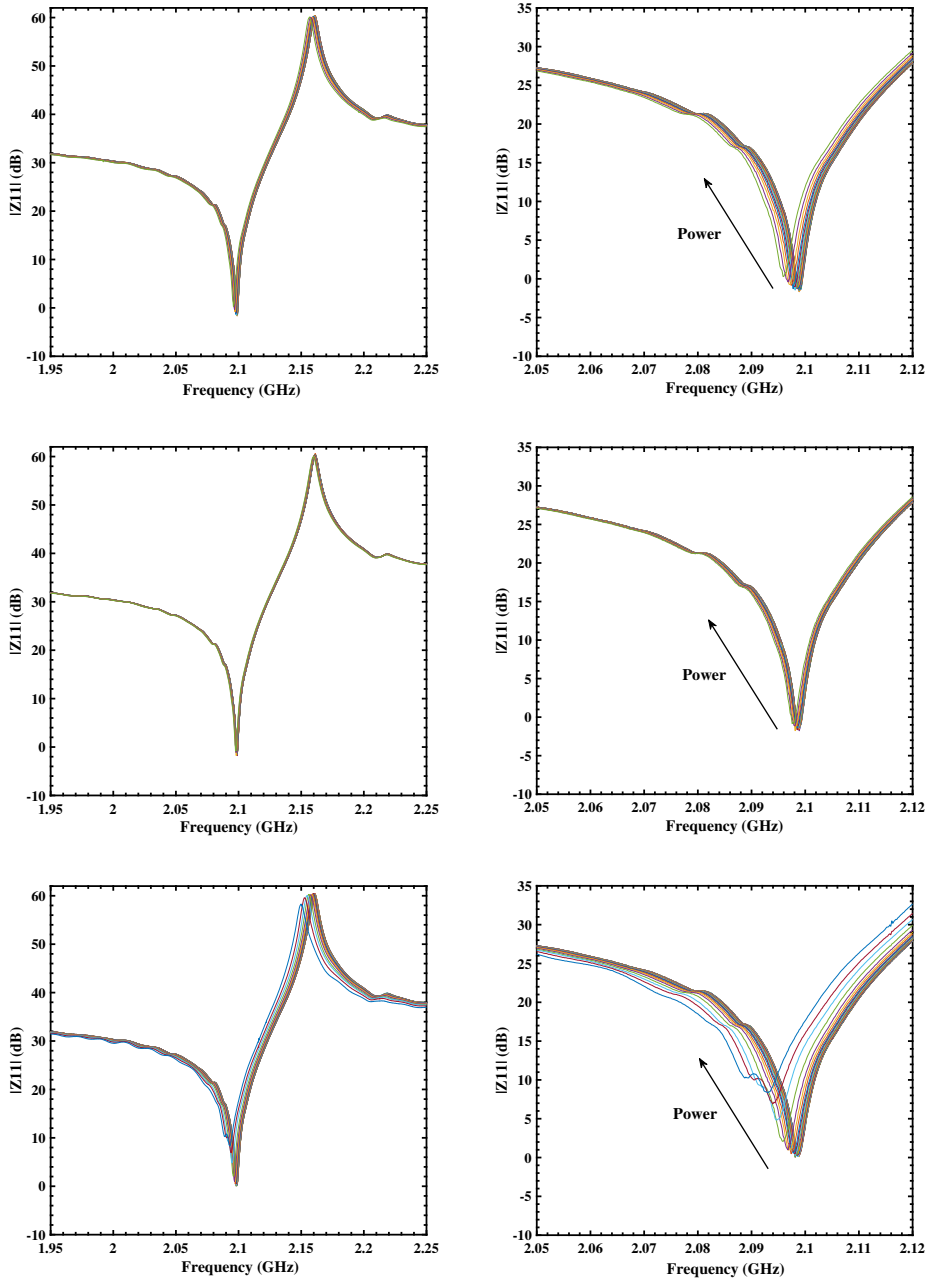


**Figure 7.3:** Measured input impedance of  $\eta = 45\%$  LSAW resonator. (Top) HP cancelling tone is set at series resonant frequency located at 2.097 GHz. (Middle) HP cancelling tone is set at shunt resonant frequency located at 2.159 GHz. (Bottom) HP cancelling tone is set at maximum stress resonant frequency located at 2.122 GHz. Right plots show the zoomed insets.



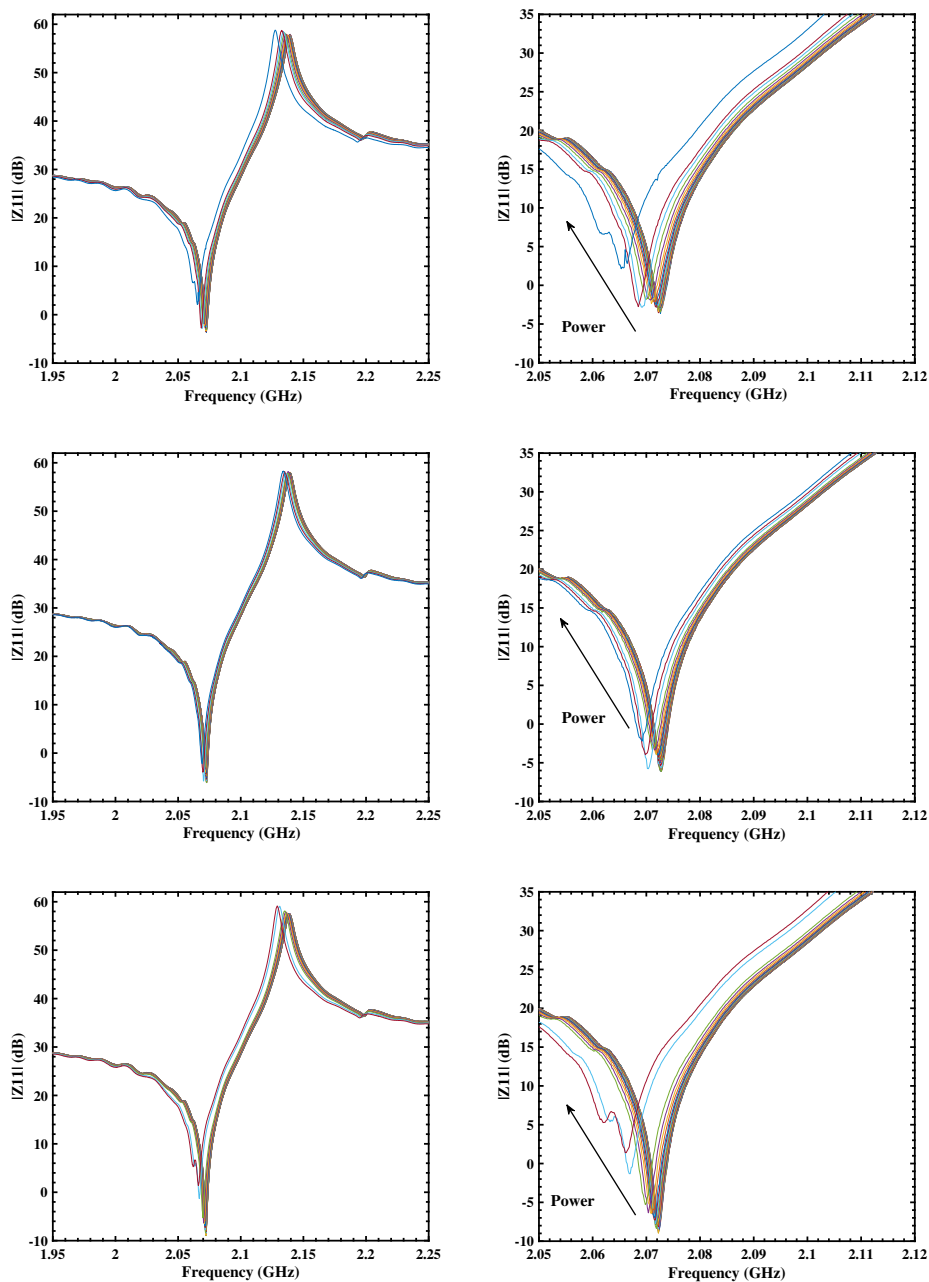


**Figure 7.4:** Measured input impedance of  $\eta = 60\%$  LSAW resonator. (Top) HP cancelling tone is set at series resonant frequency located at 2.072 GHz. (Middle) HP cancelling tone is set at shunt resonant frequency located at 2.141 GHz. (Bottom) HP cancelling tone is set at maximum stress resonant frequency located at 2.110 GHz. Right plots show the zoomed insets..

The previous data can be used for setting useful information. For example, Fig. 7.5 shows an example of the evolution of series and shunt frequency shift of  $\eta = 50\%$  LSAW resonator over power, having a maximum value of 5 and 8 MHz frequency shift respectively.

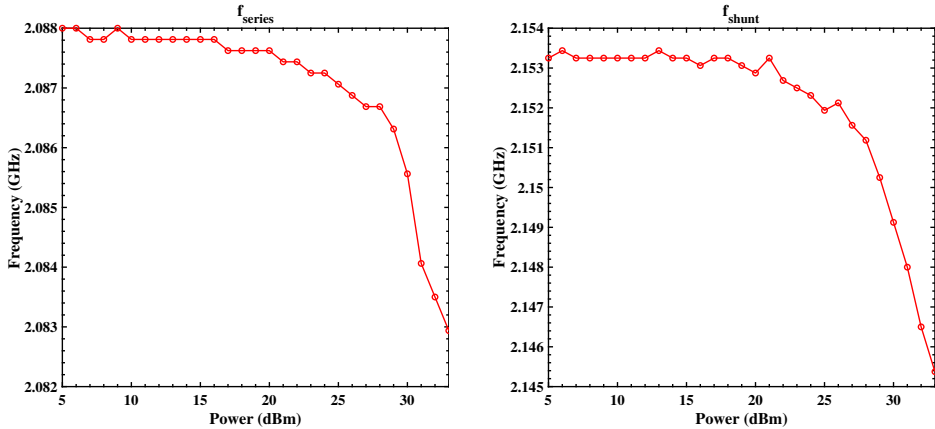


**Figure 7.5:** Example of evolution of series and shunt frequency shift of  $\eta = 60\%$  LSAW resonator with HPH tone located at series resonant frequency on the left and shunt resonant frequency on the right.

Table 7.1 summarizes the measurements of the previous set of resonators. Specifically, the frequency shift column shows the corresponding shift at the series, maximum stress and shunt resonant frequency respectively. Furthermore, we can see the biggest frequency shift suffered when the HP signal is located at maximum stress resonant frequency for each of the duty factors. In addition, we have evaluated how much power the resonators can deal without losing structural integrity. In all the cases, the devices can afford high power values up to 33 dBm prior to breaking. Moreover, for all the resonators the maximum degradation point was found when the HP was located at the maximum stress resonant frequency as depicted in Fig. 7.2, Fig. 7.3 and Fig. 7.4 (bottom) respectively.

**Table 7.1:** Evaluated LSAW resonators frequency shift and maximum input power overview.

Resonator $\eta$ (%)	Frequency shift (MHz)			Maximum input power (dBm)
	Series	Stress	Shunt	
45	3	6	1.3	33
50	3	5	2	33
60	6	8	3.4	33

As it could be expected, the device response is more degraded when the HP signal is set at the series resonance and at a frequency where the stress is maximum. Because of the nature of the SAW resonator, formed by tiny line IDT structures and spacing between them, stress induced migration and heat dissipation may prone the electrodes to be affected severely, being degradation of the metallization one of the common failure modes [102].

### 7.1.4 Performance evaluation

Afterwards, from the previous measurements the resonators are modeled using the mBVD model [52], whose input parameters are power dependent. As an example, Fig. 7.6 depicts as a function of power from 5 to 30 dBm, the series resistance  $R_{ss}$ , the static capacitance  $C_0$  and the motional  $L_m$ ,  $C_m$ , and  $R_m$  mBVD parameters of a measured  $\eta = 50\%$  resonator.

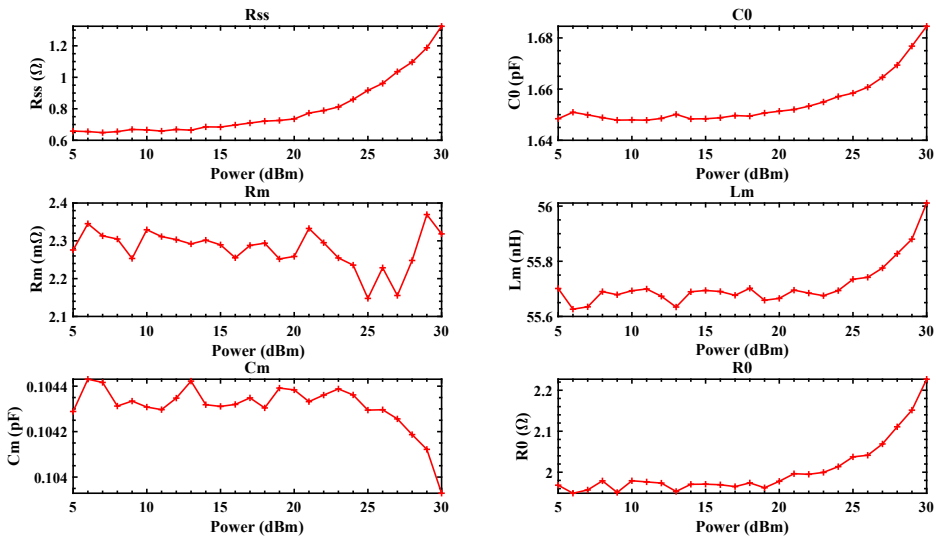


**Figure 7.6:** Example of algorithm mBVD circuital parameters dependence over power of  $\eta = 50\%$  LSAW resonator with HPH tone located at series frequency.

Note that the  $R_{ss}$  parameter degradation due to increase of losses shows a quadratic dependence with the input power. This could be related to the dissipated power (heat) involving a temperature rise in the resonator and therefore leading to changes on its performance.

Furthermore, with our algorithm we can also extract data about how the input power affects the Q-values. Fig. 7.7 shows the power dependence of the resonator in terms of the Q-factor. Each of the traces corresponds to algorithm-fitted Q-factor values extracted from the measurements. The proposed algorithm is based on a least-squares algorithm in which a proper set of mBVD parameters are extracted to

fit the measured input impedance. After that, the stored energy and the dissipated energy is calculated and the fitted Q-factor value is extracted. As we can see, the influence of power on Q-values is less noticeable up to a very high power levels. In fact there is a reversible Q-factor degradation point (black dotted trace) but at the same time there is a power level at which the resonator suffers a severe

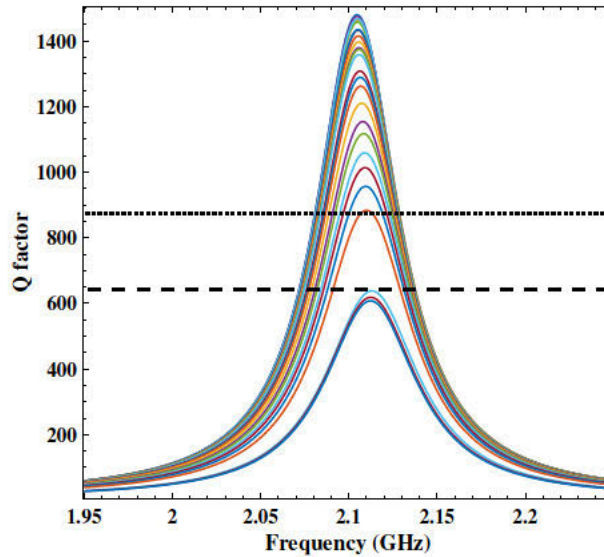


Figure 7.7: Power measurements algorithm-fitted Q-factor of  $\eta = 50\%$  LSAW resonator with HPH tone located at series frequency.

Finally, we can conclude that the proposed application is validated with measurements of the input impedance of a set of on-wafer LSAW resonators with different duty factors. Using this method, we have evaluated how much power the resonators can deal without losing their performance. Among the main features, the proposed method allows to precise small-signal measurements (S-parameters) when the device is heated by a HP CW signal at a given frequency. The main advantage of using this set-up is the flexibility to perform measurements at any frequency of interest with no limitations to obtain the reflection coefficient since the HP signal can either be located at series, shunt or maximum stress resonant frequency. This can be useful to better understanding physical mechanism, such as electro-migration effects [100, 101].

Moreover, we have observed that until a certain amount of power there is a reversible resonator frequency shift and Q-factor degradation but there is also a power level at which the resonator is destroyed. Stress induced migration and heat dissipation may prone the electrodes to be affected severely, being degradation of the metallization one of the possible failure modes.

## 7.2 Tone-injection modulated signals

As stated previously, acoustic technology-based filters offers a superior performance in terms of signal rejection, insertion losses and degree of miniaturization. However, its intrinsic nonlinear behavior can compromise the overall system's linearity and thus quality performance [103].

Current scenarios with spectral efficient multicarrier waveforms and technologies, such as carrier aggregation and MIMO, together with the coexistence of concurrent multi-band or multiple Radio Access Technology communications, open up new challenges in the field of nonlinear characterization and mitigation. Third-order manifestations of the nonlinear effects, such as IMD3, might also have an impact on the system's performance, reducing the receiver's sensitivity. This reawakens the interests on the full understanding and modeling of such nonlinear effects [23] and even more important, on seeking methods to mitigate the IMD3 phenomenon occurring in complex filtering architectures [104].

All-digital cancellation techniques have been previously used to mitigate potential receiver desensitization due to intermodulation products generated by the transmitter leakage [105]. We have already applied the concept of the tone injection technique to cancel out the passive IMD3 generated in a BAW resonator [106] and the cancellation technique was validated using single-tone fundamental sources.

In this section the idea is to go a step further toward to a practical implementation, by proving that this technique can be also applied to modulated signals. Note that since the cancellation technique requires predominant second-order nonlinear effects in the DUT, this technique is not suitable when second-order nonlinearities are low, such as in symmetric SAW resonators [89].

Consequently, a technique for the reduction of IMD3 occurring in BAW filters and multiplexers is presented. The method consists of using the intrinsic IMD2 generated by BAW filters and multiplexers themselves by injecting an externally controlled amplitude and phase modulated signal at low frequency which mixes-up with one of the two modulated fundamental signals and thus, suppressing the resulting IMD3. The key factor of this proposal is that the technique exploits the fact that the generation of intrinsic second-order nonlinearities are higher than the generation of IMD3 in BAW devices [24]. This means that a generated low frequency and low power canceling signal may produce an IMD2 signal that cancels out the IMD3 generated by the two high-power transmitting signals.

The validity of the proposed technique has been tested in a laboratory environment as a proof-of-concept. The applicability of this technique lays in the fact that the required canceling signal that must be generated, is a low power and low frequency signal that can be digitally generated in the low frequency stages of the transceiver in a similar way as the baseband predistorted signals are generated when linearizing high-power amplifiers [107]. Apart from the laboratory set-up no component is required aside from the generation of the low-power low-frequency signal at the same time than the data to be transmitted.

### 7.2.1 IMD3 cancellation expressions

Derivation of equations for the IMD and H2 applied to an ideal film bulk acoustic resonator (FBAR) were done in the past in [108] and [22]. Obtaining closed-form expressions for the nonlinearities in a SMR-type BAW resonator is not an easy task because, in addition to the piezoelectric material, there are several materials composing the resonator and some of them can generate nonlinearities [22]. Since identifying which are the most relevant or dominant terms falls out of the main scope here, only  $\varphi_5^2$  and  $c_3^E$  nonlinear term will be considered for the H2 and IMD3 generation thus, the other nonlinear terms will be disregarded. Note that, from a practical point of view, the cancellation process is independent of the specific terms that may cause second- and third-order nonlinearities. In this subsection, a simplified theoretical demonstration of the cancellation is presented just to illustrate an example of the cancellation mechanism.

Let us assume that a device is fed with two high power transmitted signals with fundamental frequencies  $f_{Tx1}$  and  $f_{Tx2}$ , and phasor voltages  $V_{in,Tx1}$  and  $V_{in,Tx2}$ . If, we intend to cancel out the IMD3 that falls at  $2f_{Tx1} - f_{Tx2}$ , the injected signal will have the frequency  $f_{IT} = f_{Tx2} - f_{Tx1}$ , and phasor voltage  $V_{in,IT}$ . Following the same reasoning as in [81], it is possible to obtain an expression for the IMD2 and the IMD3 considering only the most relevant second- and third-order derivative constants explained before. Assuming these hypotheses, IMD3 of the two fundamental signals can be caused by direct generation of third-order nonlinear constants ( $c_3^E$  in this example) or remix effects due to second-order nonlinear constants ( $\phi_5$ ) [81]. Therefore, we can obtain the following voltage nonlinear expressions for the IMD2 and IMD3 that falls at the same frequency  $2f_{Tx1} - f_{Tx2}$ ,

$$\begin{aligned} V_{out,IMD2} &= K(\omega)\varphi_5 V_{in,Tx1} V_{in,IT}^* \\ V_{out,IMD3} &= (J(\omega)\varphi_5^2 + H(\omega)c_3^E) V_{in,Tx1}^2 V_{in,Tx2}^* \end{aligned} \quad (7.1)$$

where,  $K(\omega)$ ,  $J(\omega)$ , and  $H(\omega)$  represent the frequency dependent response of the device at given frequencies and where \* denotes complex conjugate. Considering that the two equations must be equalized and isolating  $V_{in,IT}$  from them we get:

$$V_{in,IT} = \left( \frac{J(\omega)}{K(\omega)}\varphi_5 + \frac{H(\omega)c_3^E}{K(\omega)\varphi_5} \right)^* V_{in,Tx1}^* V_{in,Tx2} \quad (7.2)$$

If only direct generation is considered, equation (7.2) can be simplified just neglecting the first term inside the parenthesis. Instead, if we consider IMD3 generation due to remix effects, only the first term inside the parenthesis is considered. More nonlinear constants and different materials could be considered in the equations just adding more terms. Note that in practical situations no generality is lost since finally the phase and amplitude of the injected tone maybe experimentally adjusted.

### 7.2.2 Measurement system

Figure 7.9 outlines the proposed cancellation system, having at the left-top the two HP signals ( $f_{Tx1}$  and  $f_{Tx2}$ ) feeding the DUT and at the right-bottom the injected signal at frequency  $f_{IT}$  (used to generate the proper IMD2). Specifically, the injected signal, denoted as  $f_{IT}$ , was an injected baseband modulated signal having the same modulation than  $f_{Tx2}$ . The cancellation technique allows us to cancel the generated by the DUT IMD3 nonlinearities at both sides of the fundamental signals,  $2f_{Tx1} - f_{Tx2}$  and/or  $2f_{Tx2} - f_{Tx1}$ . Previous to the cancellation procedure, it is verified that the setup IMD3 levels without the DUT are below the noise floor of the measurement setup. Further details about the measurement system were described in [106].

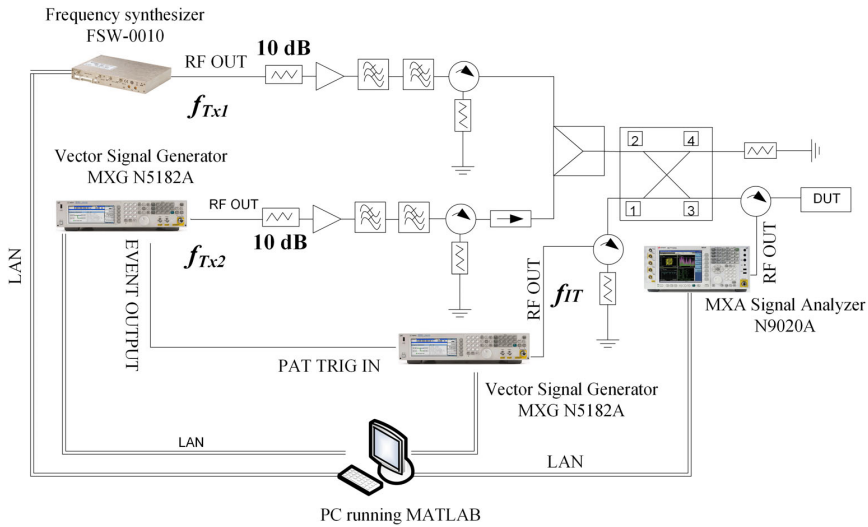


**Figure 7.9:** Tone-injection experimental cancellation setup block diagram.

## Signal generation

Regarding the signals generation, a personal computer oversees the instrument control along with the code used for the generation of the modulated signals. In this experiment,  $f_{Tx1}$  signal is just a single-tone generated using a Phase Matrix FSW-0010 frequency synthesizer (FS), and  $f_{Tx2}$  and  $f_{IT}$  are both modulated signals generated using two Agilent N5182A MXG vector signal generators (VSG), being both VSG's and the FS synchronized through an Agilent N9020A MXG SA. Moreover, since both signals must be modulated, first step is to initialize both VSGs setting their powers and frequencies and disabling the arbitrary waveform generation (ARB) capabilities.

Later, the digital to analog converter range of the VSG is set in such a way that a waveform file must be in the volatile memory of the dual ARB player. Following that, the sample clock rate for the dual ARB format is set and both the automatic leveling control is used to maintain the signal generator's output power level, as well as the ARB function is turned on. Moreover, a Matlab script generates a pair of in-phase (I) and quadrature (Q) vectors having the VSGs configured in such a way that they expect the input files of said pair of vectors, reading them, and generating the desired modulated signals.

Furthermore, as we are using two VSGs as baseband generators, system synchronization is needed. Moreover, a trigger is used to control the data transmission and deciding when the signal generator transmits the modulated signal. The trigger type of the master VSG corresponding to the  $f_{Tx2}$  signal is set to continuous and free run, and the trigger type of the slave VSG corresponding to the  $f_{IT}$  signal is set to trigger and run. Moreover, the trigger source of the  $f_{IT}$  signal is set to ex-



ternal, considering that plays the waveform after receiving master trigger. System synchronization occurs after the master signal generator sends an event pulse and propagates it to the slave by using the EVENT output signal to trigger the slave. Prior to this, the slave is configured to wait for this event pulse through the PAT TRIG connector. System delay is reduced to a minimum in both VSGs by setting the I/Q delay properly to compensate for any latency between the EVENT output signal and the RF output. Apart from that, a proper synchronization between the VSGs carriers, the FS, and the SA using the REF IN and the 10 MHZ OUT connectors is done.

### 7.2.3 Experimental results

The proposed technique has been experimentally verified by performing IMD3 measurements in a single BAW resonator subject to several modulated signals under a nonlinear scenario. The tested resonator is a commercial SMR BAW resonator based on a piezoelectric AlN layer, sandwiched between two electrodes and lying on an acoustic reflector. Its corresponding series resonance frequency is 2.438 GHz and its shunt resonance frequency is 2.502 GHz.

Several nonlinear measurements were done to validate the application of the proposed technique to the cancellation of modulated signals. Specifically, two different case scenarios were established: an amplitude modulated (AM) signal and a random noise modulated signal. These modulations are taken as an example of signals that take-up a wide spectrum while allowing to have a power spectral density superior to that of the noise level.

To speed up the cancellation process, and before activating the modulation of the carriers, some previous steps are done, as a sort of pre-calibration. First, the generated IMD3 (signal to be canceled) is measured feeding the DUT with only the two HP tones. Second, if we intend to cancel out the IMD3 at  $2f_{Tx1} - f_{Tx2}$ , the required injected tone  $f_{IT}$  is set on and the signal at  $f_{Tx2}$  is set off, producing an IMD2 (combination of  $f_{Tx1}$  and  $f_{IT}$ ) falling at the same frequency than the targeted IMD3. The magnitude of the injected tone is adjusted to provide the same level of IMD2 than the IMD3 measured in the first step. Once this is done, all the modulated carriers are set on and the cancellation process starts by adjusting the phase of the injected signal and making minor magnitude corrections.

#### AM measurements

In this example the fundamental tones  $f_{Tx1}$  and  $f_{Tx2}$  were located at 2.45 and 2.47 GHz with input powers of 22.6 and 21.0 dBm, respectively. The injected tone was placed at the same frequency of the separation between the fundamental tones  $f_{IT} = 20$  MHz and the required power of the injected tone was set to 17.2 dBm in the precalibration process. Then, the AM modulations are activated.

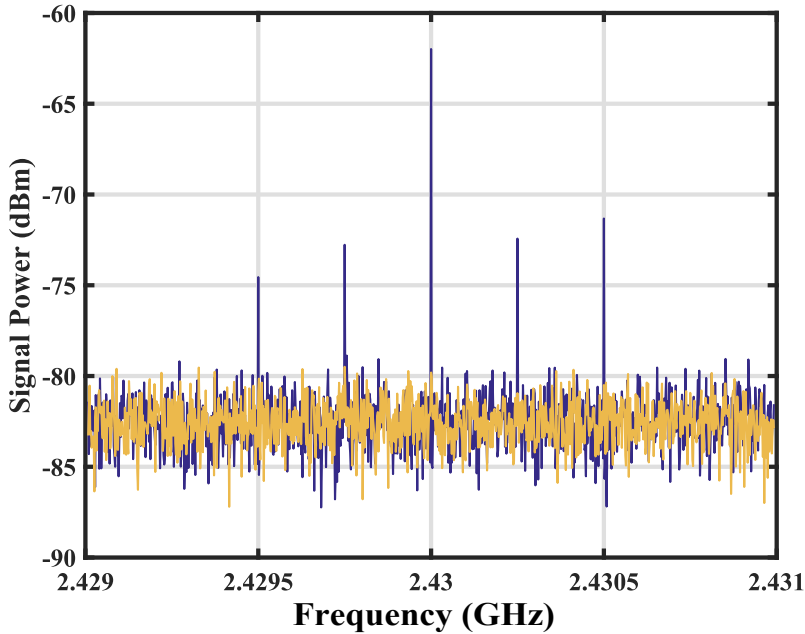


**Figure 7.10:** IMD3 cancellation example of a two-tone AM modulated signal with a 1 MHz bandwidth and modulation index of 0.3. The blue trace represents the response without cancellation and the yellow trace the canceled response.

Figure 7.10 depicts the measured IMD3 at  $2f_{Tx1} - f_{Tx2}$ , using a two-tone AM modulation for  $f_{Tx2}$ . The blue trace shows the IMD3 response before activating the cancellation algorithm. The injected tone at  $f_{IT}$  is then modulated with the same baseband signal, and fine tuning its magnitude value and adjusting its phase, the IMD3 is canceled out (in yellow) with the own IMD2 generated by the resonator. Figure 7.10 shows almost 20 dB cancellation at the carrier frequency of an AM signal having 1 MHz of spectral bandwidth. The actual cancellation level can be higher since the canceled level is below the noise floor of the SA.

### Random noise measurements

In this second example, the central frequency of the signals  $f_{Tx1}$  and  $f_{Tx2}$  were located at 2.45 and 2.55 GHz, respectively, and the injected signal at  $f_{IT} = 100$  MHz. In this case,  $f_{Tx1}$  is generated as a single-tone and  $f_{Tx2}$  and  $f_{IT}$  are carriers modulated with the same random noise in order to fully occupy the signal bandwidth. Two different bandwidths have been tested, 100 kHz and 1 MHz, leaving the power of the injected canceling signal constant. Figure 7.11 depicts the measured third-order random noise IMD3 response at  $2f_{Tx1} - f_{Tx2}$ . Following the same reasoning as explained previously, the cancellation is shown in the whole bandwidth.

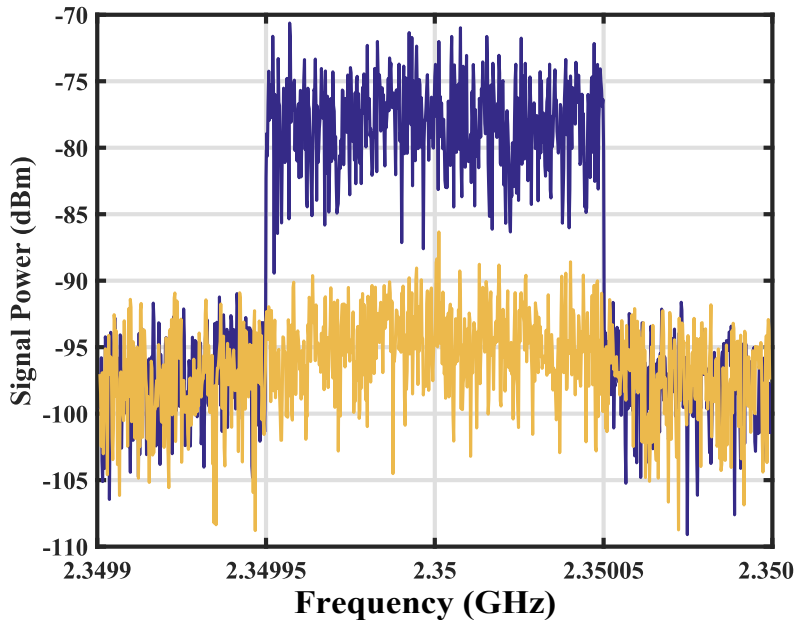


**Figure 7.11:** IMD3 cancellation example of a random noise modulated signal with a 100 kHz bandwidth. The blue trace represents the response without cancellation and the yellow trace the canceled response.

It is important to notice that the signal power level in this scenario was smaller in comparison with the AM modulation case, since the same available power must be distributed in a greater bandwidth given the nature of the noise-modulated signal. Consequently, signal power levels on Fig. 7.11 and Fig. 7.12 are different in comparison with Fig. 7.10. Moreover, Fig. 7.11 shows cancellation figures between 15 and 20 dB in the entire bandwidth for the 100 kHz case, and, at least, 10 dB for the 1 MHz case in Fig. 7.12.

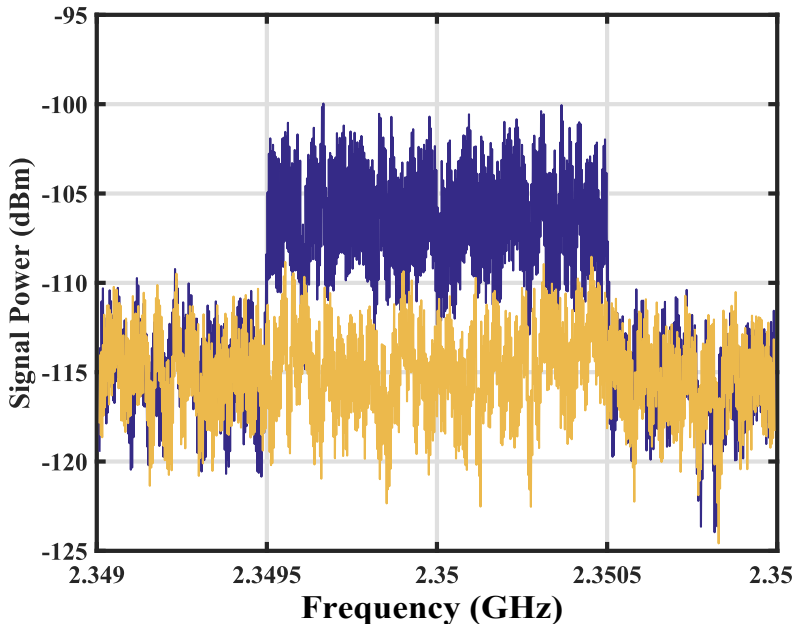


**Figure 7.12:** IMD3 cancellation example of a random noise modulated signal with 1 MHz bandwidth. The blue trace represents the response without cancellation and the yellow trace the canceled response.

Finally, we have experimentally demonstrated a suitable method for an active cancellation of the harmful IMD3 occurring in complex wireless scenarios where electro-acoustic devices are used on the filtering stages. Validation of such concept requires of a careful development of a cancellation setup where a given modulated signal is used to feed the DUT at the operating frequency band and at the same time with a lower frequency version of the modulated signal, whose amplitude and phase can be controlled in real-time. This concept can indeed be applied in more complex scenarios where several modulated signals coexist, and several electro-acoustic devices are leading to several nonlinear manifestations. For example, in frequency selective devices like a quadplexer where the transmitter and receiver share the antenna, IMD3 generation can cause interfering signals at a given receiver band, affecting its sensitivity.

The conceptual advantage of the application of this technique to real transceivers is that the low frequency canceling signals could be digitally generated into the same transceiver if the IMD3 to be canceled is coming from two HP transmitting signals, whose properties are well known by the own transceiver. This technique in combination with real time adaptive algorithms, which act on the parameters that characterize the all-digital canceling signal, could even cancel the variation of the IMD3 signal due to the external environment. Changes of the input impedance of the duplexer antenna could modify the generated IMD3 to be canceled falling in the receiver frequency band, requiring therefore adaptive algorithms to cancel out this spurious signal.



## Chapter 8

# Conclusions and future research lines

### 8.1 Conclusions

The main goal of this thesis is, the accurate linear and nonlinear characterization of SAW devices and their corresponding modeling. The models used for the SAW devices are based on equivalent distributed circuits of Mason crossed-field model. After the SAW linear parameters are known, the models have been tested on several resonators showing a good accuracy between measurements and simulations. Moreover, the models have been also evaluated among different technologies such as LT-SAW and TC-SAW devices allowing to predict the behavior of devices with different in-plane geometries. Finally, to validate the models more complex structures of ladder-type and CRF filters have been also analyzed.

The main conclusions of this thesis can be summarized in the following points:

- The modeling and simulation of nonlinearities have been one of the most important milestones of the thesis. For usefulness and reduction of the computational time in the characterization process, the presented equivalent circuit models have been used in combination with mathematical techniques based on equivalent sources to synthesize compact circuit network models accounting for the nonlinear mechanism occurring in SAW devices.
- A new developed method called IOES method is presented to analyze nonlinearities in SAW devices and, at the same time, reducing the computational time. The proposed application of the IOES method has demonstrated to be extremely useful for the analysis of large distributed nonlinear circuits, as it is the case of SAW resonators and more complex structures such as filters.

- Following these developed models, we have used the measurements to compare them with simulations and demonstrate the validity of the proposed method. Specifically, the method has been proven to be an effective tool to predict the in-band IMD3 and H3 nonlinear response of SAW resonators and filters. Besides, using this method we have identified the nonlinear parameters involved in the nonlinear generation.
- The IOES method has been applied to analyze the measured IMD3 of several one-port resonators concluding that only one shape-independent parameter, the third order term of the elastic constant  $c_{3,MR}^E$ , can explain all the measured in-band IMD3 around resonance for both the LT-SAW and TC-SAW resonators. This physical parameter is independent of device geometry and its value -which varies depending on the used stack- was obtained by fitting simulations with measurements.
- It has been confirmed that the same parameter is a good candidate to simulate the overall main in-band IMD3 response of other SAW devices such as ladder-type and CRF-based filters. With regard to the filters, the IOES method has also shown to be an effective method to predict its nonlinear behavior and it has been confirmed that using only two shape-independent nonlinear parameters  $c_{3,MR}^E$  and  $c_{3,NMR}$  with equal value is possible to properly fit the measured in-band IMD3 of both the TC-SAW ladder filters and the CRF test structures.
- Several measurement systems have been developed to characterize the SAW devices under different conditions. In a first instance, measurement methods to quantify the harmonics and intermodulation response over a frequency spectrum have been proposed. Moreover, the influence of the measurement setup has been included in the IOES method for a proper characterization. Characterization of SAW devices is performed as the nonlinear response of SAW resonators with respect to the frequency. A thorough analysis of the IMD3, H3 and H2 response of different SAW resonators has been performed. In addition, apart from the standard large signal measurement system to measure harmonics and intermodulation products, a feed-forward cancellation method is proposed for the analysis and characterization of the out-of-band IMD3 response.
- [REDACTED]

- [REDACTED]
- [REDACTED]
  - Based on the same concept of feed-forward cancellation loop, another approach is presented to monitor and characterize the SAW resonator behavior at HP levels that can damage the device. The proposed application is validated with measurements of the input impedance of a set of on-wafer SAW resonators with different duty factors. Among the main features, the proposed method allows to precise S-parameters measurements when the device is heated by a HP CW signals at any frequency of interest, with no limitations to obtain the reflection coefficient. Besides, it provides useful information for a better understanding of the possible failure mechanism.
  - It was experimentally demonstrated a suitable method for an active cancellation of an IMD3 modulated signal occurring in complex wireless scenarios where electro-acoustic devices are used on the filtering stages. The method consist of using the intrinsic IMD2 generated by BAW filters themselves by injecting an externally controlled amplitude an phase modulated signal at low frequency which mixes-up with one of the modulated fundamental signals and thus, suppressing the resulting IMD3.



## 8.2 Future research lines

In terms of the future research lines, many topics presented in this thesis are of interest for further research. Linearity requirements and nonlinear distortion in the mobile front-end system are, and will be, one of the driving forces of electro-acoustic devices research.

Manufacturing acoustic devices entails a complex process in which linear and nonlinear requirements must be taken into consideration. As mobile communication technology evolved, acoustic filters and duplexers had to meet a large number of specifications parameters related to the linearity. Harmonic emissions and intermodulation effects are the most critical nonlinear effects in which considerable efforts are required to meet the requirements. Power requirements are also taking the focus of attention since according to latest ETSI technical specification, acoustic devices for newly future standards such as for 5G and 6th Generation (6G) are expected to meet even power class 3 specifications.

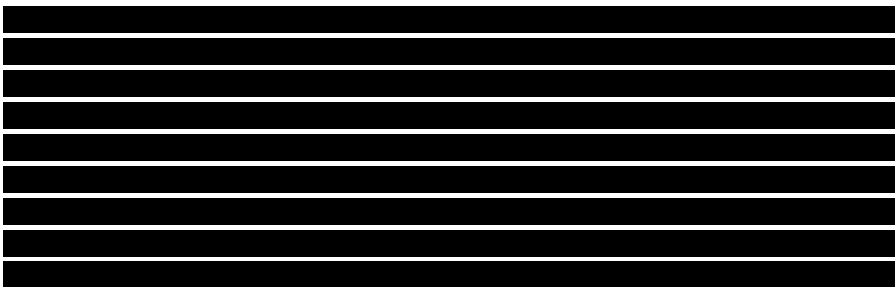
Developing a single tool capable of simulate at the same time, the linear and nonlinear response provides a huge improvement in terms of the optimization and design of the product development process. Note that many further processes are necessary prior the design and manufacturing of an acoustic device and are beyond the scope of this thesis.

Moreover, the characterization process provides a deep knowledge of the nonlinear device response, which allows to anticipate the possible nonlinear problems in a more realistic scenario and to include the founded constraints into the design methodology to obtain feasible solutions.

Among others, the main areas for future work can be summarized into the following points:

1. *Linear model*

The equivalent circuit models proposed in this thesis are based on the one dimensional piezoelectric constitutive equations. It has been demonstrated that is an efficient 1D physical model which considers a set of assumptions but still achieving good agreement between simulations and measurements of SAW resonators and filters.



[REDACTED]

2. *H2*

[REDACTED]

3. *H3*

For a proper modeling of the H3, the model was extended to account for non-uniform electric field distribution across the electrodes. [REDACTED]

[REDACTED]

4. *IMD3 out of band*

[REDACTED]

[REDACTED]

[REDACTED]

[REDACTED]

### 5. *Improve IOES tool*

The IOES method has been implemented in Matlab as a proprietary software tool. The main target of this tool is to model and characterize the linear and nonlinear response of SAW devices. Moreover, its key advantage is that unifies, under a controlled environment, both the simulation of the linear and nonlinear response and the characterization process by including the measurements set-up.

Nevertheless, there is still a long way to improve the code, for example:

- [REDACTED]
- [REDACTED]
- [REDACTED]
- [REDACTED]
- [REDACTED]

[REDACTED]

### 6. *Lumped models*

[REDACTED]

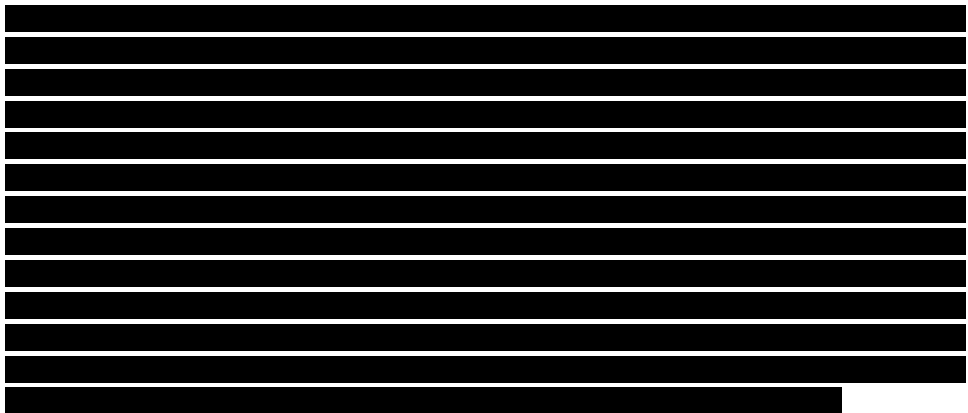
# Appendices

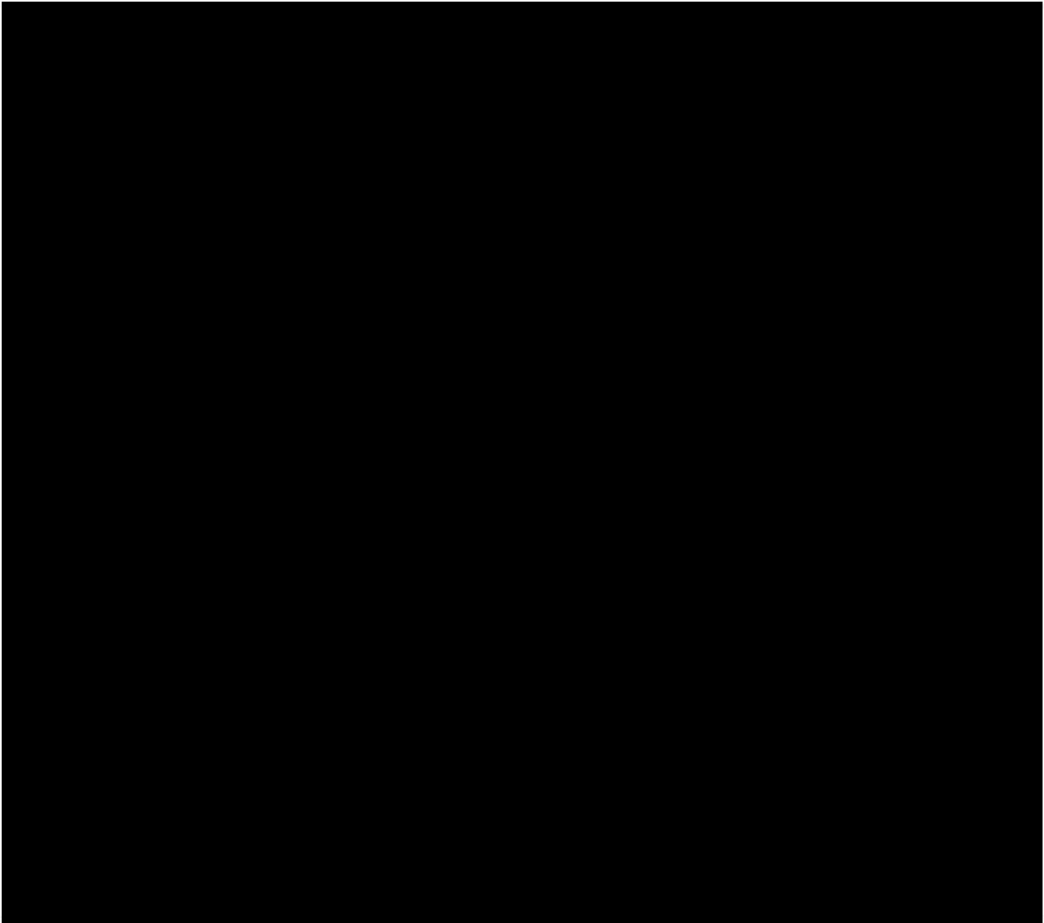


# Appendix A

## Admittance matrix formulation

### A.0.1 Admittance matrix concatenation process in Matlab





## Appendix B

# Frequency domain nonlinear equations

The nonlinear equations presented previously in Chapter 2 can also be represented in the frequency domain. Frequency-domain equations in the steady state are mathematical expressions that provide closed-form expressions of a given H or IMD for weak nonlinearities. In our case, we use the frequency domain equations in the IOES Matlab tool, to solve the nonlinear equations of Chapter 4.

Considering the previous equation (2.46) in the frequency domain, we can obtain closed-form expressions for the harmonic distortion of the second order and third order spurious signals are respectively

$$V_{out,NL}(2\omega_1) = \frac{1}{2}a_2 |A_1|^2 e^{j2\phi_1} = \frac{1}{2}a_2A_1^2, \quad (\text{B.1})$$

$$V_{out,NL}(2\omega_2) = \frac{1}{2}a_2 |A_2|^2 e^{j2\phi_2} = \frac{1}{2}a_2A_2^2, \quad (\text{B.2})$$

$$V_{out,NL}(3\omega_1) = \frac{1}{4}a_3 |A_1|^3 e^{j3\phi_1} = \frac{1}{4}a_3A_1^3, \quad (\text{B.3})$$

$$V_{out,NL}(3\omega_2) = \frac{1}{4}a_3 |A_2|^3 e^{j3\phi_2} = \frac{1}{4}a_3A_2^3. \quad (\text{B.4})$$

Similarly, the corresponding equations defined in the frequency domain for the



IMD products of second and third order respectively will take the form

$$V_{out,NL}(\omega_2 - \omega_1) = a_2 |A_1| |A_2| e^{j(\phi_2 - \phi_1)} = a_2 A_1^* A_2, \quad (\text{B.5})$$

$$V_{out,NL}(\omega_2 + \omega_1) = a_2 |A_1| |A_2| e^{j(\phi_1 + \phi_2)} = a_2 A_1 A_2, \quad (\text{B.6})$$

$$V_{out,NL}(2\omega_1 - \omega_2) = \frac{3}{4} a_3 |A_1|^2 |A_2| e^{j(2\phi_1 - \phi_2)} = \frac{3}{4} a_3 A_1^2 v_2^* \quad (\text{B.7})$$

$$V_{out,NL}(2\omega_2 - \omega_1) = \frac{3}{4} a_3 |A_1| |A_2|^2 e^{j(2\phi_2 - \phi_1)} = \frac{3}{4} a_3 A_1^* A_2^2. \quad (\text{B.8})$$

## Appendix C

# Standing wave patterns at targeted frequency for remix purposes (metallized region)

To illustrate the required steps to evaluate the remix effects, let us assume we want to calculate the H3 generated by remix effects. Then, we will need to find the standing wave pattern at the frequency H2, which cannot be done as it was done before for the fundamental signals since the nonlinear sources at H2 are distributed along the section.

Once the circuit is evaluated for H2, we know the input and output voltages  $V_{1,2\omega_1}$ ,  $V_{3,2\omega_1}$  and  $V_{2,2\omega_1}$ ,  $V_{4,2\omega_1}$  (left-side and right-side voltages of the 4-port network respectively) and its corresponding currents are calculated using the 4 –  $ABCD$  matrix of the metallized region at the frequency H2:

$$I_1 = Y_{11} \cdot V_1 + Y_{12} \cdot V_2 + Y_{13} \cdot V_3 + Y_{14} \cdot V_4 - I_{e1} \quad (\text{C.1})$$

$$I_3 = Y_{31} \cdot V_1 + Y_{32} \cdot V_2 + Y_{33} \cdot V_3 + Y_{34} \cdot V_4 - I_{e3} \quad (\text{C.2})$$

where  $I_{e1}$  and  $I_{e3}$  are the input equivalent sources at H2 that were previously calculated. Now we can apply equation 4.31 to find the next vector  $V_2$ ,  $I_2$ ,  $V_4$ ,  $I_4$  at each unit-cell, and repeat this procedure along the section. Finally, we obtain  $S(z)$  and  $E(z)$  as

$$S(z) = -\frac{z_p}{A_L c^E} (I_1(z) - I_2(z)) \quad (\text{C.3})$$

$$E(z) = \frac{1}{d} (V_3(z)) \tag{C.4}$$

A similar procedure is followed to find the IMD3 due to remix effects. The main difference is that the remix effect of the IMD3  $2f_1 - f_2$  for example might come from the mix of H2 at  $2f_1$  with  $f_2$  and from the mix of the IMD2  $f_2 - f_1$  with  $f_1$ . Therefore, the magnitude distributions at  $2f_1$  and at  $f_2 - f_1$  must be calculated.

# Appendix D

## Simulation parameters

### D.1 L-SAW resonators

#### D.1.1 Uniform electric field

**Table D.1:** L-SAW linear response simulation parameters of Set 1 resonators considering uniform electric field.

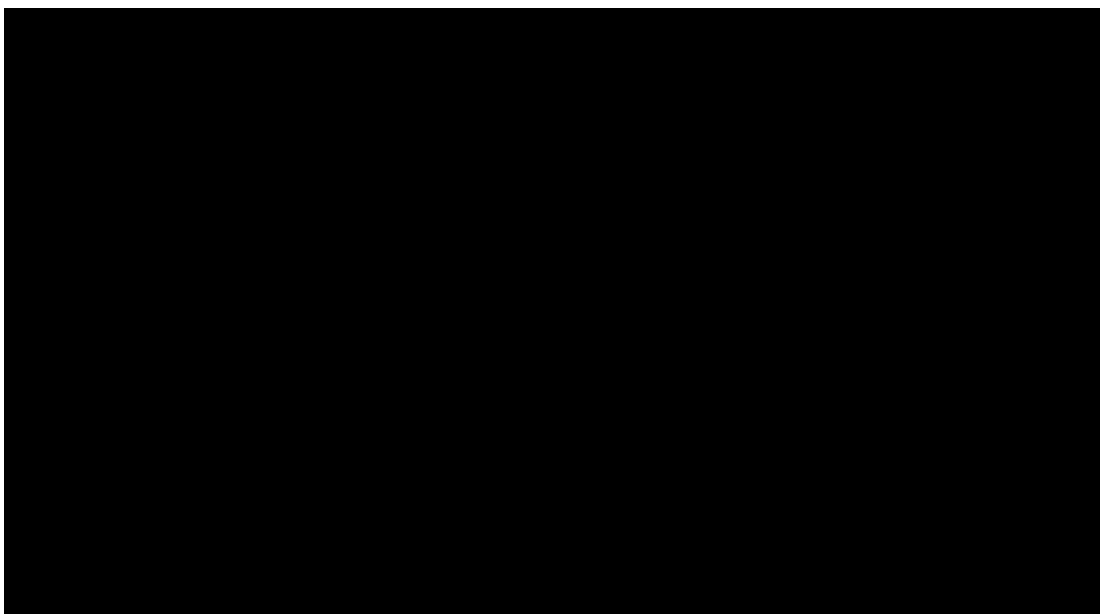


**Table D.2:** L-SAW linear response simulation parameters of Set 2 resonators considering uniform electric field.

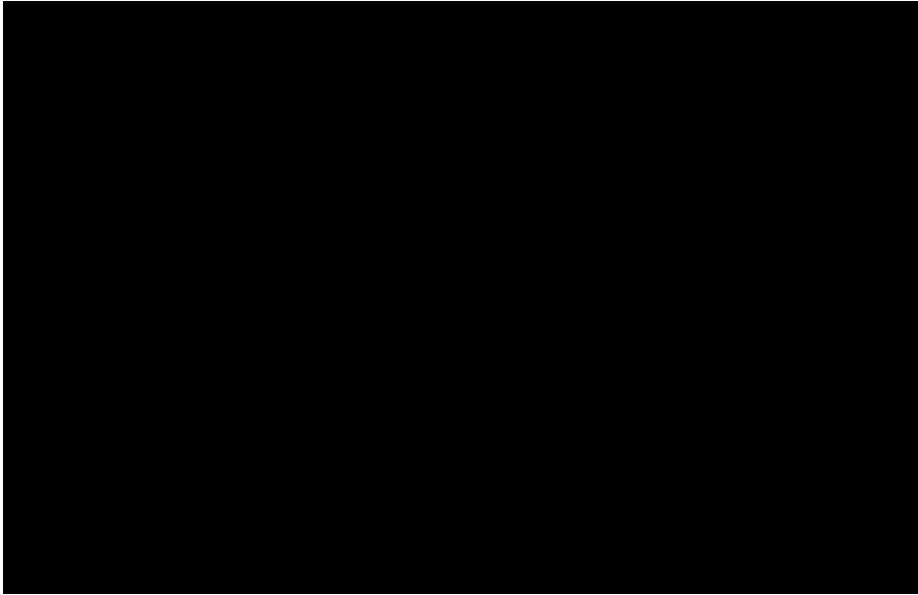
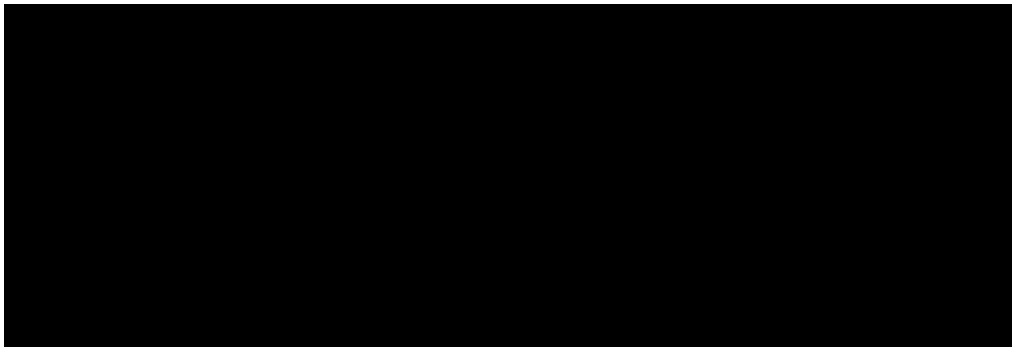


**Table D.3:** L-SAW nonlinear response simulation parameters of Set 1 and Set 2 resonators considering uniform electric field.



### D.1.2 Edge-E electric field

**Table D.4:** L-SAW linear response simulation parameters of Set 1 resonators considering edge-e electric field.

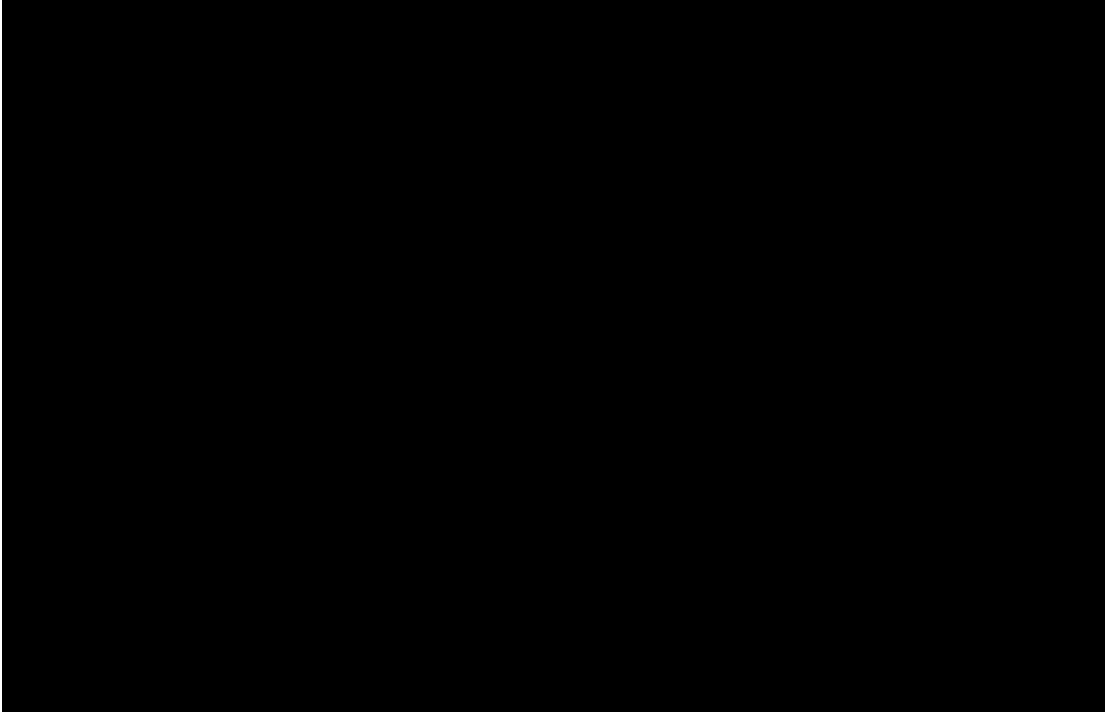


**Table D.5:** L-SAW linear response simulation parameters of Set 2 resonators considering edge-e electric field.

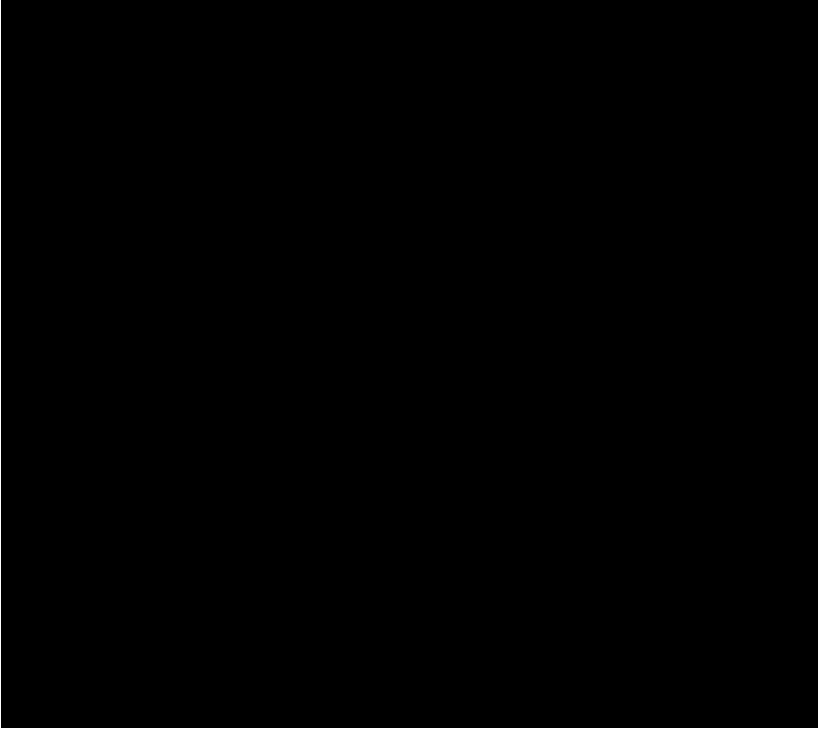
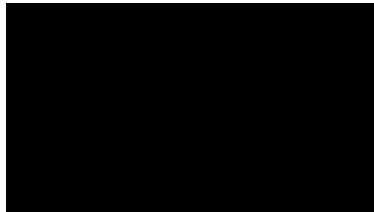


**Table D.6:** L-SAW nonlinear response simulation parameters of Set 1 and Set 2 resonators considering edge-e electric field.



### D.1.3 IMD3 out-of-band

**Table D.7:** L-SAW linear response simulation parameters of Set 1 and Set 2 resonators considering uniform electric field.

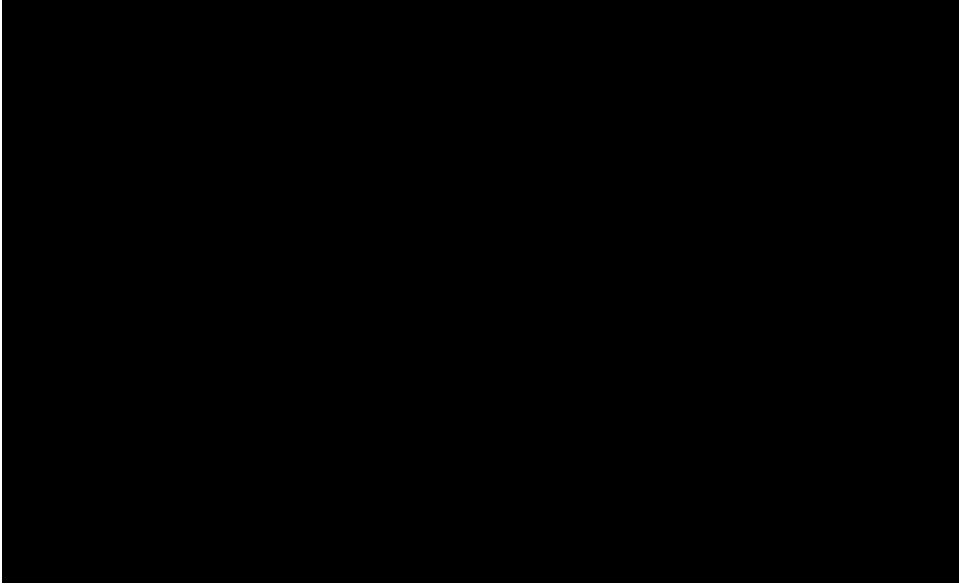
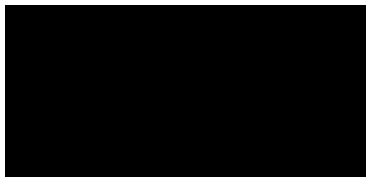


**Table D.8:** L-SAW nonlinear response simulation parameters of Set 1 and Set 2 resonators considering uniform electric field.





### D.1.4 H2 response

**Table D.9:** L-SAW H2 linear response simulation parameters of Set 1 resonators considering uniform electric field.

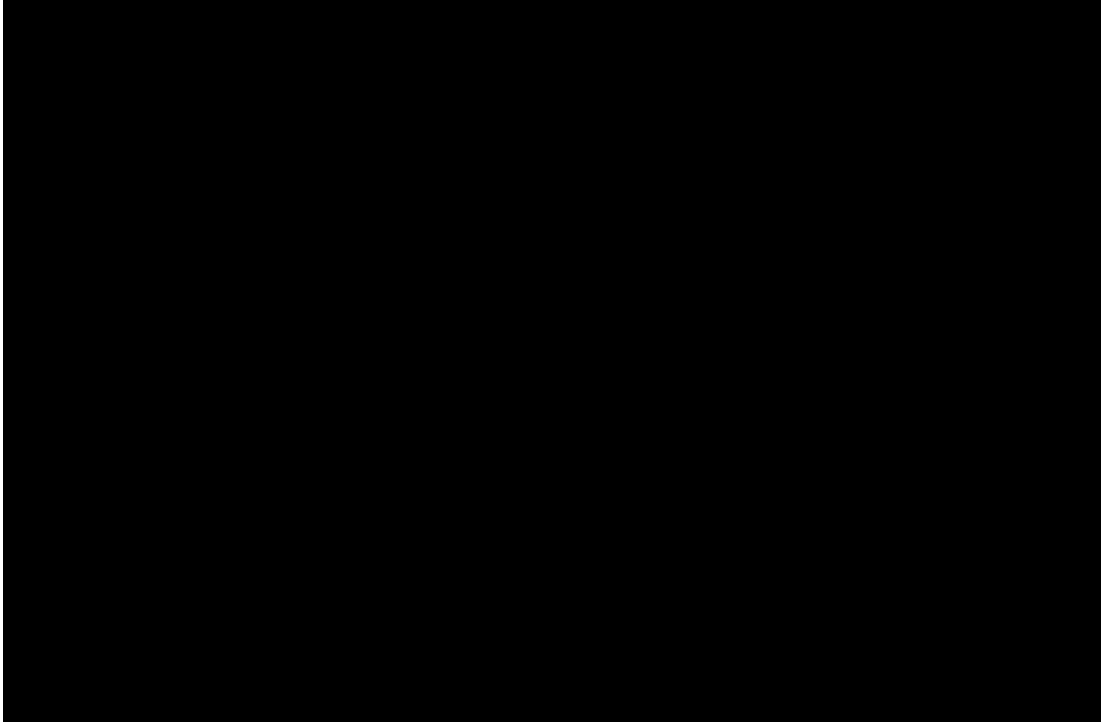
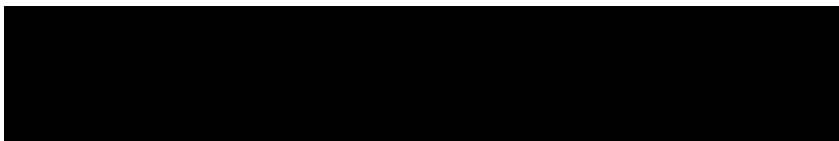


**Table D.10:** L-SAW H2 nonlinear response simulation parameters of Set 1 resonators considering uniform electric field.



## D.2 TC-SAW

### D.2.1 Uniform electric field

**Table D.11:** TC-SAW linear response simulation parameters of Set 3 resonators considering uniform electric field.

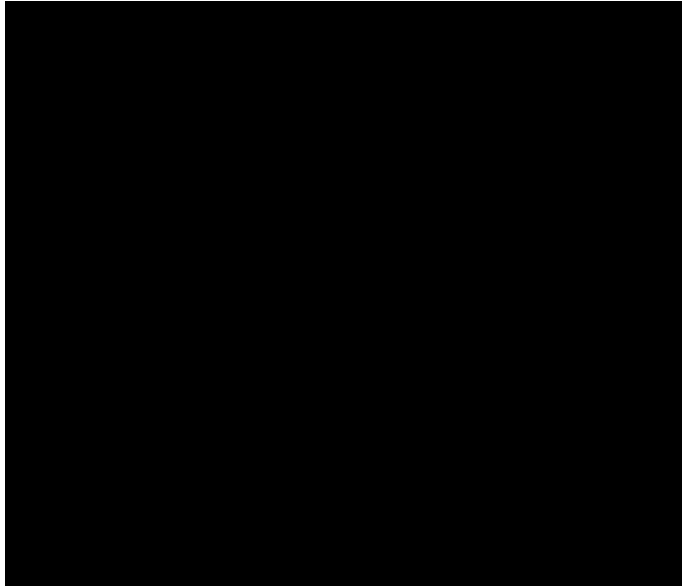


**Table D.12:** TC-SAW linear response simulation parameters of Set 4 resonators considering uniform electric field.

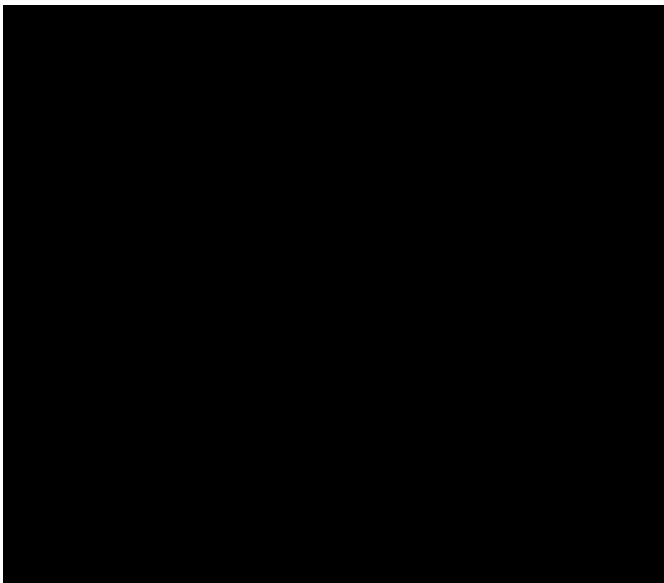
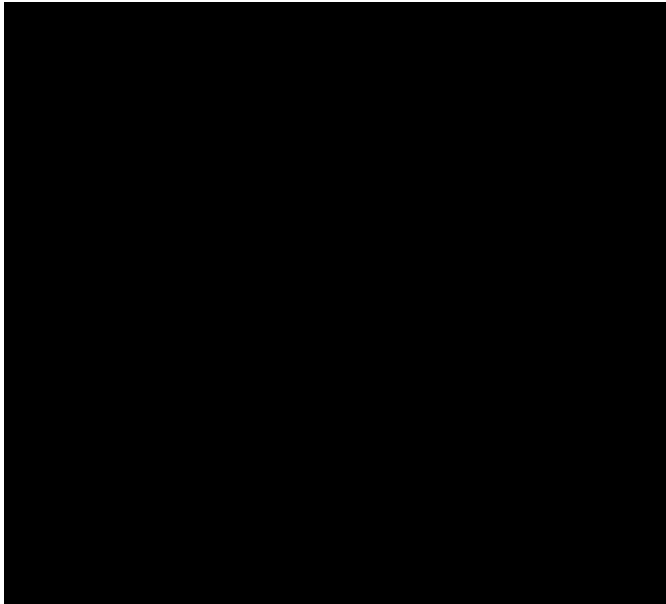


**Table D.13:** TC-SAW linear response simulation parameters of Set 5 resonators considering uniform electric field.



## D.2.2 Edge-E electric field

**Table D.14:** TC-SAW linear response simulation parameters of Set 3 resonators considering edge-e electric field.

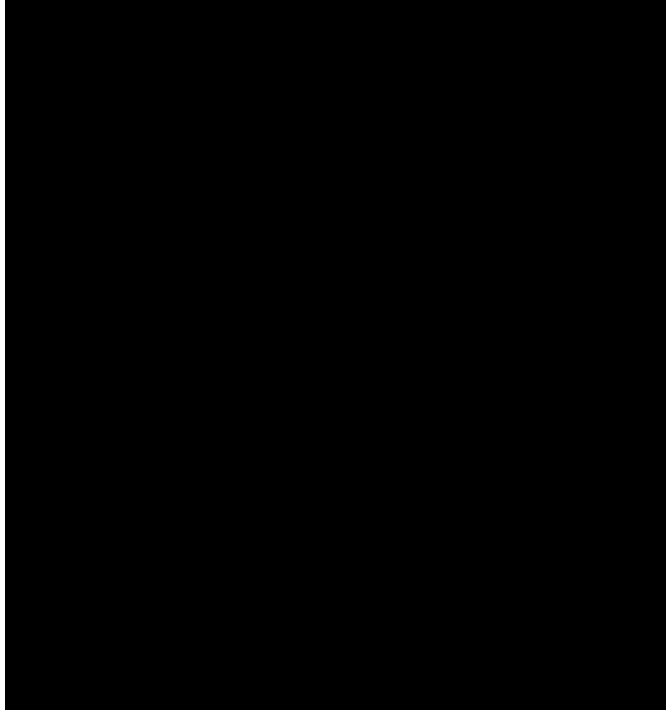


**Table D.15:** TC-SAW linear response simulation parameters of Set 4 resonators considering edge-e electric field.

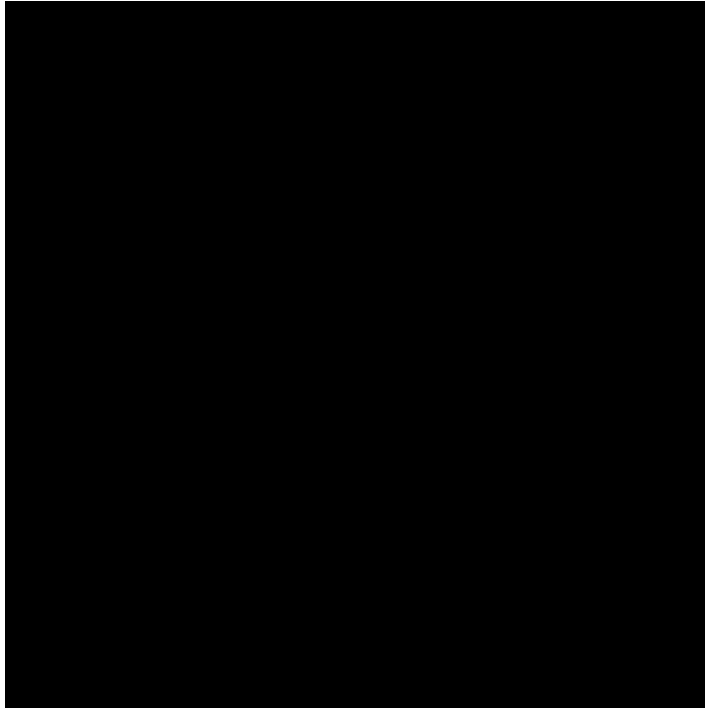
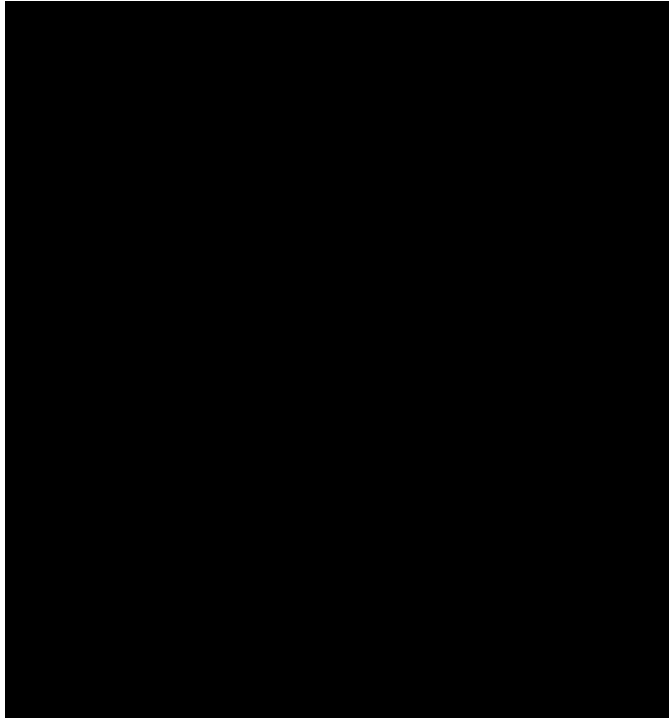


**Table D.16:** TC-SAW linear response simulation parameters of Set 5 resonators considering edge-e electric field.





# Appendix E

## List of author's contributions

This Ph.D. thesis has contributed to develop the tasks “T1. Modelado y diseño de resonadores” and “T3. Electrical characterization of resonators and sensors”, of the TEC2017-84817-C2-2-R project, TEC2017-88343-C4-2-R project : “Sensores gravimétricos de gases basados en resonadores electro-acústicos de película delgada de AlN piezoeléctrico”, project supported by the Spanish Government. With the support, in part, by the Universities and Research Secretary of the Generalitat de Catalunya, and in part by the European Social Fund under Grant 2019FI\_B\_00136 and Grant 2017 SGR 813.

Besides, this thesis has been realized in collaboration with the US company Qorvo Inc. that provided all the samples and has supervised this work.

### E.1 Research Contributions

The different novelties of this Ph.D. dissertation have been published in several research contributions. The total number of publications are 4 journal papers, 9 conference papers and 1 patent.

#### Journal Papers

- M. González-Rodríguez, C. Collado, J. Mateu, J.M. González-Arbesú and S. Huebner, “Distributed Nonlinear Model and Fast Analysis for In-Band IMD3 Prediction of Surface Acoustic Wave Resonators”, in *IEEE Transactions on Ultrasonics, Ferroelectrics and Frequency Control (T-UFFC)*, vol. 69, no. 6, pp. 2190-2205, June 2022.
- [83] C. Collado, M. González-Rodríguez, J. Mateu, R. Perea-Robles and R. Aigner, “The Input-Output Equivalent Sources Method for Fast Simulations of Distributed Nonlinearities in Bulk Acoustic Wave Resonators and Filters”,



in *IEEE Transactions on Ultrasonics, Ferroelectrics and Frequency Control (T-UFFC)*, vol. 68, no. 5, pp. 1907-1918, May 2021.

- [109] M. González-Rodríguez, C. Collado, J.M. González-Arbesú, J. Mateu, G. Montoro and PL. Gilabert, “Tone injection-based cancellation technique for nonlinear distortion reduction of modulated signals in BAW resonators”, in *IEEE Microwave and Optical Technology Letters (MOTL)*, vol. 63, no. 3, pp. 781-786, September 2020.
- [94] C. Collado, M. González-Rodríguez, J.M. González-Arbesú, J. Mateu, J. Verdú, A. Hueltes, “Feed-forward Technique to Measure S-Parameters Under CW High Power Signals”, in *IEEE Transactions on Microwave Theory and Techniques (T-MTT)*, vol. 66, no. 10, pp. 4627-4633, October 2018.

### Conference Papers

- [110] M. González-Rodríguez, C. Collado, J. Mateu, J.M. González-Arbesú, S. Huebner and R. Aigner, “Simulation of in-band third order nonlinearities in SAW resonators and filters”, in *2022 IEEE International Ultrasonics Symposium (IUS)*, Venice (Italy), 2022.
- M. González-Rodríguez, C. Collado, J. Mateu, J.M. González-Arbesú, S. Huebner, R. Aigner “Application of the Input-Output Equivalent Sources Method for the Simulation of Nonlinearities in TC-SAW Resonators and Filters”, in *IEEE MTT-S International Conference on Microwave Acoustics and Mechanics (IC-MAM)*, Munich (Germany), July 2022. **Invited lecturer on Non-linearities Session.**
- [110] M. González-Rodríguez, C. Collado, J. Mateu, J.M. González-Arbesú, S. Huebner and R. Aigner, “Method to measure reflection coefficient under CW High-Power signals in SAW resonators”, in *2021 IEEE International Ultrasonics Symposium (IUS)*, Xian (China), 2021.
- [77] M. González-Rodríguez, C. Collado, J. Mateu, J.M. González-Arbesú, S. Huebner and R. Aigner, “Fast Simulation Method of Distributed Nonlinearities in Surface Acoustic Wave Resonators”, in *2020 IEEE International Ultrasonics Symposium (IUS)*, Las Vegas (United States of America), 2020. **Student Paper Finalist Group 4 Microacoustics SAW, FBAR, MEMS.**
- [111] M. González-Rodríguez, C. Collado, J. Mateu, J.M. González-Arbesú and R. Aigner, “Analytical modeling method of thermal spreading resistance in BAW filters”, in *2019 IEEE International Ultrasonics Symposium (IUS)*, Glasgow (United Kingdom), 2019.
- [112] D. García-Pastor, J. Mateu, C. Collado, R. Perea-Robles, M. González-Rodríguez and J.M. González-Arbesú, “Comprehensive Nonlinear Characterization and Modelling of a BAW Duplexer”, in *2019 IEEE/MTT-S International Microwave Symposium - IMS*, Boston (USA), 2019, pp. 857-860.

- [106] M. González-Rodríguez, C. Collado, J.M. González-Arbesú, J. Mateu, “New Technique to Cancel IMD3 in Electroacoustic Filters”, in *2018 IEEE International Ultrasonics Symposium (IUS)*, Kobe (Japan), 2018, pp. 1-4.
- [113] J. Mateu, C. Collado, A. Hueltes, R. Perea-Robles, D. García-Pastor, M. González-Rodríguez and J.M. González-Arbesú, “Outline Process from the synthesis towards the nonlinear modeling of Bulk Acoustic Wave Filters”, in *2018 IEEE/MTT-S International Microwave Symposium - IMS*, Philadelphia (USA), 2018, pp.413-416.
- [114] D. García-Pastor, M. González-Rodríguez, A. Hueltes, C. Collado, J. Mateu, S. Kreuzer and R. Aigner, “Nonlinear Effects of Electrode and Bragg Reflector Materials in BAW Resonators”, in *2017 IEEE International Ultrasonics Symposium (IUS)*, Washington (USA), 2017, pp. 1-4.

### Patents

- C. Collado, J. Mateu, J.M. González-Arbesú, A. Hueltes, M. González-Rodríguez, D. García-Pastor and R. Perea-Robles, “Método y sistema de medida de parámetros eléctricos de dispositivos de radiofrecuencia bajo condiciones de alta potencia”, ES 2684570 A1, 2017-03-31.

## E.2 Academic Contributions

This Ph.D. thesis has contributed to the academic environment with the realization of 2 bachelor's degree final thesis.

### Bachelor's Degree Final Thesis

- A. Rodríguez Zornoza, “Diseño de un software integrado para el control de una cámara de vacío criogénica”, *Advisors: José María González-Arbesú (UPC), Marta González-Rodríguez (UPC)*, presented in September 2018.
- A. Romero Hazas, “Diseño y caracterización de un sonar de seguimiento basado en Arduino”, *Advisors: José María González-Arbesú (UPC), Marta González-Rodríguez (UPC)*, presented in September 2019.

### Additional info Other contributions

- Support as technical expert with topics related to antenna patents in Commercial Court no. 1 of Barcelona in the Mobile World Congress 2019. Dates: 25 and 26 February 2019

- **IEEE International Ultrasonics Symposium (IUS) 2020 Student Paper Finalist Group 4 Microacoustics SAW, FBAR, MEMS**
- Stay at company Spectron Microsystems SRL Padova, Italy 2 months April-June 2021. Research, electrical and acoustic modeling of on-chip micro-scale devices for radio frequency filtering applications.

# Bibliography

- [1] S. Elisabeth, “Intensifying technology competition in the acoustic wave filter market,” *Microwave Journal*, October 2020.
- [2] C. C. W. Ruppel, “Acoustic wave filter technology—a review,” *IEEE Transactions on Ultrasonics, Ferroelectrics, and Frequency Control*, vol. 64, no. 9, pp. 1390–1400, sep 2017.
- [3] A. Hagelauer, G. Fattinger, C. C. W. Ruppel, M. Ueda, K. ya Hashimoto, and A. Tag, “Microwave acoustic wave devices: Recent advances on architectures, modeling, materials, and packaging,” *IEEE Transactions on Microwave Theory and Techniques*, vol. 66, no. 10, pp. 4548–4562, oct 2018.
- [4] L. Miller, *5G for dummies*. Qorvo Special Edition, 2017.
- [5] R. Aigner, “MEMS in RF-filter applications: thin film bulk-acoustic-wave technology,” in *The 13th International Conference on Solid-State Sensors, Actuators and Microsystems, 2005. Digest of Technical Papers. TRANSDUCERS '05*. IEEE.
- [6] J. D. Lisle, “Portable wireless products drive filter miniaturization,” *Microwaves and RF*, June 2015.
- [7] T. Takai, H. Iwamoto, Y. Takamine, T. Wada, M. Hiramoto, M. Koshino, and N. Nakajima, “Investigations on design technologies for SAW quadplexer with narrow duplex gap,” in *2016 IEEE MTT-S International Microwave Symposium (IMS)*. IEEE, may 2016.
- [8] Q. X. et al., “Investigation of incredible high performance surface acoustic wave properties with a structure of  $\text{idt}/0 \text{ yx-litao}_3/\text{tio}_2/\text{aln}/\text{silicon}$ ,” *Symposium on Piezoelectricity, Acoustic Waves, and Device Applications (SPAWDA)*, October 2017.
- [9] H. Odagawa and K. Yamanouchi, “SAW device beyond 5 GHz,” *International Journal of High Speed Electronics and Systems*, vol. 10, no. 04, pp. 1111–1142, dec 2000.
- [10] J. R. Wilkerson, P. G. Lam, K. G. Gard, and M. B. Steer, “Distributed passive intermodulation distortion on transmission lines,” *IEEE Transactions on Microwave Theory and Techniques*, vol. 59, no. 5, pp. 1190–1205, may 2011.

- [11] C. Collado, J. Mateu, and J. O'Callaghan, "Analysis and simulation of the effects of distributed nonlinearities in microwave superconducting devices," *IEEE Transactions on Applied Superconductivity*, vol. 15, no. 1, pp. 26–39, mar 2005.
- [12] J. Mateu, J. C. Booth, C. Collado, and J. M. O'Callaghan, "Intermodulation distortion in coupled-resonator filters with nonuniformly distributed nonlinear properties—use in HTS IMD compensation," *IEEE Transactions on Microwave Theory and Techniques*, vol. 55, no. 4, pp. 616–624, apr 2007.
- [13] J. Rosenbaum, *Bulk Acoustic Wave Theory and Devices*. ARTECH HOUSE INC, 1988. [Online]. Available: [https://www.ebook.de/de/product/4296357/joel\\_rosenbaum\\_bulk\\_acoustic\\_wave\\_theory\\_and\\_devices.html](https://www.ebook.de/de/product/4296357/joel_rosenbaum_bulk_acoustic_wave_theory_and_devices.html)
- [14] G. Kino, *Acoustic waves : devices, imaging, and analog signal processing*. Englewood Cliffs, N.J: Prentice-Hall, 1987.
- [15] W. P. Mason, *Electromechanical transducers and wave filters*. D. Van Nostrand Co., 1948.
- [16] W. Mason, *Piezoelectric crystals and their application to ultrasonics*. D. Van Nostrand Co., 1950.
- [17] E. D. Daniel Royer, *Elastic Waves in Solids I*. Springer Berlin Heidelberg, 1999.
- [18] B. A. Auld, *Acoustic Fields and Waves in Solids, Volume I*. John Wiley & Sons, 1973.
- [19] R. J. Atkin, *An introduction to the theory of elasticity*. Mineola, N.Y: Dover Publications, 2005.
- [20] A. Einstein, "Die grundlage der allgemeinen relativit tstheorie," *Annalen der Physik*, vol. 354, no. 7, pp. 769–822, 1916.
- [21] M. Ueda, M. Iwaki, T. Nishihara, Y. Satoh, and K. y. Hashimoto, "A circuit model for nonlinear simulation of radio-frequency filters using bulk acoustic wave resonators," *IEEE Transactions on Ultrasonics, Ferroelectrics and Frequency Control*, vol. 55, no. 4, pp. 849–856, apr 2008.
- [22] C. Collado, E. Rocas, J. Mateu, A. Padilla, and J. O. Callaghan, "Nonlinear distributed model for bulk acoustic wave resonators," *IEEE Transactions on Microwave Theory and Techniques*, vol. 57, no. 12, pp. 3019–3029, dec 2009.
- [23] D. S. Shim and D. A. Feld, "A general nonlinear mason model of arbitrary nonlinearities in a piezoelectric film," in *2010 IEEE International Ultrasonics Symposium*. IEEE, oct 2010.
- [24] E. Rocas, C. Collado, J. Mateu, N. Orloff, J. Booth, and R. Aigner, "Electrothermo-mechanical model for bulk acoustic wave resonators," *IEEE Transactions on Ultrasonics, Ferroelectrics and Frequency Control*, vol. 60, no. 11, pp. 2389–2403, nov 2013.

- [25] C.Liu and M.Damgaard, "Ip2 and ip3 nonlinearity specifications for 3g/wcdma receivers," *High Frequency Electronics*, 2009.
- [26] T. Ranta, J. Ella, and H. Pohjonen, "ECWT: Antenna switch linearity requirements for GSM/WCDMA mobile phone front-ends," in *The European Conference on Wireless Technology, 2005*. IEEE.
- [27] L. Xiao, "Nonlinearity analysis and predistortion of 4g wireless communication systems," Ph.D. dissertation, Portland State University, 2013.
- [28] L. Chen, "A novel nonlinear mason model and nonlineardistortion characterization for surface acousticwave duplexers," Ph.D. dissertation, University of Central Florida, 2013.
- [29] N. B. C. Jose Carlos Pedro, *Intermodulation Distortion in Microwave and Wireless Circuits*, A. House, Ed., 2003.
- [30] S. A. Maas, *Nonlinear Microwave and RF Circuits*. ARTECH HOUSE INC, Jan. 2003. [Online]. Available: [https://www.ebook.de/de/product/3396478/stephen\\_a\\_maas\\_nonlinear\\_microwave\\_and\\_rf\\_circuits.html](https://www.ebook.de/de/product/3396478/stephen_a_maas_nonlinear_microwave_and_rf_circuits.html)
- [31] C. Campbell, *Surface Acoustic Wave Devices and Their Signal Processing Applications*. Elsevier Science Techn., Dec. 2012. [Online]. Available: [https://www.ebook.de/de/product/21133169/colin\\_campbell\\_surface\\_acoustic\\_wave\\_devices\\_and\\_their\\_signal\\_processing\\_applications.html](https://www.ebook.de/de/product/21133169/colin_campbell_surface_acoustic_wave_devices_and_their_signal_processing_applications.html)
- [32] Ruppel, Ruile, Scholl, Wagner, and Manner, "Review of models for low-loss filter design and applications," in *Proceedings of IEEE Ultrasonics Symposium ULTSYM-94*. IEEE, 1994.
- [33] J. R. Pierce, "Coupling of modes of propagation," *Journal of Applied Physics*, vol. 25, no. 2, pp. 179–183, feb 1954.
- [34] Y. Suzuki, H. Shimizu, M. Takeuchi, K. Nakamura, and A. Yamada, "Some studies on SAW resonators and multiple-mode filters," in *1976 Ultrasonics Symposium*. IEEE, 1976.
- [35] H. A. Haus, "Modes in SAW grating resonators," *Journal of Applied Physics*, vol. 48, no. 12, pp. 4955–4961, dec 1977.
- [36] H. Haus, "Bulk scattering loss of SAW grating cascades," *IEEE Transactions on Sonics and Ultrasonics*, vol. 24, no. 4, pp. 259–267, jul 1977.
- [37] P. Wright, "A new generalized modeling of SAW transducers and gratings," in *Proceedings of the 43rd Annual Symposium on Frequency Control*. IEEE, August 2002.
- [38] V. Plessky and J. Koskela, "Coupling-of-Modes Analysis of SAW Devices," *International Journal of High Speed Electronics and Systems*, vol. 10, no. 04, pp. 867–947, dec 2000.

- [39] J. Koskela, V. Plessky, and M. Salomaa, "COM parameter extraction from computer experiments with harmonic admittance of a periodic array of electrodes," in *1997 IEEE Ultrasonics Symposium Proceedings. An International Symposium (Cat. No.97CH36118)*. IEEE.
- [40] K.-Y. Hashimoto, J. Koskela, and M. Salomaa, "Fast determination of coupling-of-modes parameters based on strip admittance approach," in *1999 IEEE Ultrasonics Symposium. Proceedings. International Symposium (Cat. No.99CH37027)*. IEEE, 1999.
- [41] G. Tobolka, "Mixed matrix representation of SAW transducers," *IEEE Transactions on Sonics and Ultrasonics*, vol. 26, no. 6, pp. 426–427, nov 1979.
- [42] M. Mayer, S. Ammann, M. Pernpeintner, J. Johnson, T. Ebner, and K. Wagner, "Multi-mode p-matrix models for the description of interacting modes in TCSAW and LSAW devices," in *2018 IEEE International Ultrasonics Symposium (IUS)*. IEEE, oct 2018.
- [43] V. Chauhan, M. Mayer, W. Ruile, T. Ebner, I. Bleyl, K. Wagner, R. Weigel, and A. Hagelauer, "A p-matrix model for third order electric and acoustic nonlinearities in TC-SAW devices," in *2018 IEEE International Ultrasonics Symposium (IUS)*. IEEE, oct 2018.
- [44] E. D. Daniel Royer, *Elastic Waves in Solids II*. Springer-Verlag GmbH, 1999.
- [45] B. Fleischmann and H. Skeie, "Higher harmonic surface transverse wave filters," in *Proceedings., IEEE Ultrasonics Symposium*. IEEE.
- [46] K. Wagner and O. Manner, "A fast green's function method for calculating bulk wave frequency responses from SAW frequency responses," in *IEEE Symposium on Ultrasonics*. IEEE.
- [47] P. Ventura, J. Hode, J. Desbois, and H. Solal, "Combined FEM and green's function analysis of periodic SAW structure, application to the calculation of reflection and scattering parameters," *IEEE Transactions on Ultrasonics, Ferroelectrics and Frequency Control*, vol. 48, no. 5, pp. 1259–1274, sep 2001.
- [48] M. Buchner, W. Ruile, A. Dietz, and R. Dill, "FEM analysis of the reflection coefficient of SAWs in an infinite periodic array," in *IEEE 1991 Ultrasonics Symposium*. IEEE.
- [49] K. Hashimoto and H. Yamaguchi, "General-purpose simulator for leaky surface acoustic wave devices based on coupling-of-modes theory," in *1996 IEEE Ultrasonics Symposium. Proceedings*. IEEE.
- [50] V. Plessky and T. Thorvaldsson, "Periodic green's functions analysis of SAW and leaky SAW propagation in a periodic system of electrodes on a piezoelectric crystal," *IEEE Transactions on Ultrasonics, Ferroelectrics and Frequency Control*, vol. 42, no. 2, pp. 280–293, mar 1995.

- [51] “IRE standards on piezoelectric crystals-the piezoelectric vibrator: Definitions and methods of measurement, 1957,” *Proceedings of the IRE*, vol. 45, no. 3, pp. 353–358, mar 1957.
- [52] J. Larson, P. Bradley, S. Wartenberg, and R. Ruby, “Modified butterworth-van dyke circuit for FBAR resonators and automated measurement system,” in *2000 IEEE Ultrasonics Symposium. Proceedings. An International Symposium (Cat. No.00CH37121)*. IEEE, 2000.
- [53] W. Smith, H. Gerard, J. Collins, T. Reeder, and H. Shaw, “Analysis of interdigital surface wave transducers by use of an equivalent circuit model,” *IEEE Transactions on Microwave Theory and Techniques*, vol. 17, no. 11, pp. 856–864, nov 1969.
- [54] T. Kojima and K. Shibayama, “An analysis of an equivalent circuit model for an interdigital surface-acoustic-wave transducer,” *Japanese Journal of Applied Physics*, vol. 27, no. S1, p. 163, jan 1988.
- [55] G. A. W.C. Wilson, “A comparison of surface acoustic wave modeling methods,” *Nanotech Conference and Exposition*, 2009.
- [56] L. Chen, M. Solal, J. Briot, S. Hester, D. Malocha, and P. Wahid, “A nonlinear mason model for 3rd order harmonic and intermodulation simulations of SAW duplexers,” in *2012 IEEE International Ultrasonics Symposium*. IEEE, oct 2012.
- [57] Y.-K. Yong and X. Pang, “Nonlinear frequency response of second harmonic generation in SAW IDT resonators,” in *2017 IEEE International Ultrasonics Symposium (IUS)*. IEEE, sep 2017.
- [58] L. Chen, J. Briot, P. Girard, C. Ledesma, M. Solal, K. Cheema, D. Malocha, and P. Wahid, “Third order nonlinear distortion of SAW duplexers in UMTS system,” in *2010 IEEE International Ultrasonics Symposium*. IEEE, oct 2010.
- [59] S. Inoue, M. Hara, M. Iwaki, J. Tsutsumi, H. Nakamura, M. Ueda, Y. Satoh, and S. Mitobe, “A nonlinear elastic model for predicting triple beat in SAW duplexers,” in *2011 IEEE International Ultrasonics Symposium*. IEEE, oct 2011.
- [60] R. Nakagawa, T. Suzuki, H. Shimizu, H. Kyoya, and K. ya Hashimoto, “Study on generation mechanisms of third-order nonlinearity in SAW devices,” in *2015 IEEE International Ultrasonics Symposium (IUS)*. IEEE, oct 2015.
- [61] R. Nakagawa, T. Suzuki, H. Shimizu, H. Kyoya, K. Nako, and K. ya Hashimoto, “Discussion about generation mechanisms of third-order nonlinear signals in surface acoustic wave resonators based on simulation,” *Japanese Journal of Applied Physics*, vol. 55, no. 7S1, p. 07KD02, jun 2016.
- [62] R. Nakagawa, T. Suzuki, H. Shimizu, H. Kyoya, and N. Katsuhiko, “A new simulation method for nonlinear characteristics of saw devices,” in *2013 European Microwave Integrated Circuit Conference*, 2013, pp. 292–295.



- [63] M. Mayer, W. Ruile, J. Johnson, I. Bleyl, K. Wagner, A. Mayer, and E. Mayer, "Rigorous COM and p-matrix approaches to the simulation of third-order intermodulation distortion and triple beat in SAW filters," in *2013 IEEE International Ultrasonics Symposium (IUS)*. IEEE, jul 2013.
- [64] M. Mayer, W. Ruile, J. Johnson, J. Kiwitt, R. S. Jose, E. Schmidhammer, I. Bleyl, K. Wagner, A. Mayer, and E. Mayer, "Application of a rigorous nonlinear p-matrix method to the simulation of third order intermodulation in test devices and duplexers," in *2014 IEEE International Ultrasonics Symposium*. IEEE, sep 2014.
- [65] M. Solal, L. Chen, J. Gratier, and S. Hester, "A nonlinear p matrix model to simulate intermodulation products in SAW devices," in *2012 IEEE International Ultrasonics Symposium*. IEEE, oct 2012.
- [66] R. Nakagawa and K. ya Hashimoto, "Influence of electrode width of interdigital transducer on third-order nonlinearity of surface acoustic wave devices on 42°YX-LiTaO3 substrate," *Japanese Journal of Applied Physics*, vol. 57, no. 7S1, p. 07LD18, jun 2018.
- [67] S. Inoue, S. Matsuda, J. Tsutsumi, M. Ueda, Y. Satoh, and S. Mitobe, "Visualization of nonlinear SAW displacements in resonators induced by nonlinear elasticity," in *2012 IEEE International Ultrasonics Symposium*. IEEE, oct 2012.
- [68] R. Nakagawa, T. Suzuki, H. Shimizu, H. Kyoya, and K. ya Hashimoto, "Influence of electrode structure on generation of third-order nonlinearity in surface acoustic wave devices," *Japanese Journal of Applied Physics*, vol. 54, no. 7S1, p. 07HD11, jun 2015.
- [69] X. Pang and Y.-K. Yong, "Characteristics of BAW modes harmonically generated (f-2f-3f) in LiNO3 SAW devices," in *2019 Joint Conference of the IEEE International Frequency Control Symposium and European Frequency and Time Forum (EFTF/IFC)*. IEEE, apr 2019.
- [70] M. Solal, K. Kokkonen, S. Inoue, J.-B. Briot, B. P. Abbott, and K. J. Gamble, "Observation of nonlinear harmonic generation of bulk modes in SAW devices," *IEEE Transactions on Ultrasonics, Ferroelectrics, and Frequency Control*, vol. 64, no. 9, pp. 1361–1367, sep 2017.
- [71] X. Pang and Y.-K. Yong, "Simulation of nonlinear resonance, amplitude-frequency, and harmonic generation effects in SAW and BAW devices," *IEEE Transactions on Ultrasonics, Ferroelectrics, and Frequency Control*, vol. 67, no. 2, pp. 422–430, feb 2020.
- [72] M. Ueda, M. Iwaki, T. Nishihara, Y. Satoh, and K. ya Hashimoto, "Investigation on nonlinear distortion of acoustic devices for radio-frequency applications and its suppression," in *2009 IEEE International Ultrasonics Symposium*. IEEE, sep 2009.

- [73] S. Inoue, S. Mitobe, M. Hara, M. Iwaki, J. Tsutsumi, H. Nakamura, M. Ueda, and Y. Satoh, "A precise nonlinear simulation for saw duplexers considering nonlinear elasticity," in *2011 41st European Microwave Conference*, 2011, pp. 599–602.
- [74] V. Chauhan, M. Mayer, E. Mayer, W. Ruile, T. Ebner, I. Bleyl, A. Mayer, K. Wagner, R. Weigel, and A. Hagelauer, "Role of metal electrodes in the generation of third-order nonlinearities in TC-SAW devices," in *2017 IEEE International Ultrasonics Symposium (IUS)*. IEEE, sep 2017.
- [75] K. ya Hashimoto, X. Li, J. Bao, L. Qiu, and T. Omori, "Perturbation analysis of nonlinearity in radio-frequency bulk acoustic wave resonators using the mass–spring model," *IEEE Transactions on Ultrasonics, Ferroelectrics, and Frequency Control*, vol. 67, no. 7, pp. 1479–1484, jul 2020.
- [76] D. A. Berlincourt, D. R. Curran, and H. Jaffe, "Piezoelectric and piezomagnetic materials and their function in transducers," in *Physical Acoustics*. Elsevier, 1964, pp. 169–270.
- [77] M. Gonzalez-Rodriguez, C. Collado, J. Mateu, J. Gonzalez-Arbesu, S. Huebner, and R. Aigner, "Fast simulation method of distributed nonlinearities in surface acoustic wave resonators," in *2020 IEEE International Ultrasonics Symposium (IUS)*. IEEE, sep 2020.
- [78] K. Hashimoto, M. Yamaguchi, G. Kovacs, K. Wagner, T. Ruile, and R. Weigel, "Effects of bulk wave radiation on IDT admittance on 42/spl deg/YX-LiTaO/sub 3/," *IEEE Transactions on Ultrasonics, Ferroelectrics and Frequency Control*, vol. 48, no. 5, pp. 1419–1425, sep 2001.
- [79] D. A. Feld and D. S. Shim, "Determination of the nonlinear physical constants in a piezoelectric AlN film," in *2010 IEEE International Ultrasonics Symposium*. IEEE, oct 2010.
- [80] R. Perea-Robles, D. Garcia-Pastor, J. Mateu, C. Collado, and R. Aigner, "Fast procedure for the nonlinear analysis of BAW resonators," in *2018 IEEE International Ultrasonics Symposium (IUS)*. IEEE, oct 2018.
- [81] C. Collado, J. Mateu, D. Garcia-Pastor, R. Perea-Robles, A. Hueltes, S. Kreuzer, and R. Aigner, "Nonlinear effects of SiO<sub>2</sub> layers in bulk acoustic wave resonators," *IEEE Transactions on Microwave Theory and Techniques*, vol. 66, no. 4, pp. 1773–1779, apr 2018.
- [82] D. Garcia-Pastor, C. Collado, J. Mateu, and R. Aigner, "Third-harmonic and intermodulation distortion in bulk acoustic-wave resonators," *IEEE Transactions on Microwave Theory and Techniques*, pp. 1–8, 2019.
- [83] C. Collado, M. Gonzalez-Rodriguez, J. Mateu, R. Perea-Robles, and R. Aigner, "The input–output equivalent sources method for fast simulations of distributed nonlinearities in bulk acoustic wave resonators and filters," *IEEE Transactions on Ultrasonics, Ferroelectrics, and Frequency Control*, vol. 68, no. 5, pp. 1907–1918, may 2021.

- [84] D. M. Pozar, *Microwave Engineering*. John Wiley & Sons Inc, 2011. [Online]. Available: [https://www.ebook.de/de/product/14948033/david\\_m\\_pozar\\_microwave\\_engineering.html](https://www.ebook.de/de/product/14948033/david_m_pozar_microwave_engineering.html)
- [85] R. Nakagawa, H. Kyoya, H. Shimizu, T. Kihara, and K. ya Hashimoto, "Study on generation mechanisms of second-order nonlinear signals in surface acoustic wave devices and their suppression," *Japanese Journal of Applied Physics*, vol. 54, no. 7S1, p. 07HD12, jun 2015.
- [86] M. Ueda, M. Iwaki, T. Nishihara, Y. Satoh, and K. ya Hashimoto, "Nonlinear distortion of acoustic devices for radio-frequency front-end circuit and its suppression," *Japanese Journal of Applied Physics*, vol. 49, no. 7, p. 07HD12, jul 2010.
- [87] K. T. Advanced Design System, *Santa Rosa, CA*, Jan 2016.
- [88] M. Gonzalez-Rodriguez, C. Collado, J. Mateu, J. M. Gonzalez-Arbesu, and S. Huebner, "Distributed nonlinear model and fast analysis for in-band IMD3 prediction of surface acoustic wave resonators," *IEEE Transactions on Ultrasonics, Ferroelectrics, and Frequency Control*, vol. 69, no. 6, pp. 2190–2205, jun 2022.
- [89] R. Nakagawa, H. Kyoya, H. Shimizu, and T. Kihara, "Effective suppression method for 2nd nonlinear signals of SAW devices," in *2014 IEEE International Ultrasonics Symposium*. IEEE, sep 2014.
- [90] C. A. Balanis, *Antenna Theory*. Wiley John + Sons, Apr. 2016. [Online]. Available: [https://www.ebook.de/de/product/24340252/constantine\\_a\\_balanis\\_antenna\\_theory.html](https://www.ebook.de/de/product/24340252/constantine_a_balanis_antenna_theory.html)
- [91] J. R. Wilkerson, K. G. Gard, and M. B. Steer, "Automated broadband high-dynamic-range nonlinear distortion measurement system," *IEEE Transactions on Microwave Theory and Techniques*, vol. 58, no. 5, pp. 1273–1282, may 2010.
- [92] J. M. Wetherington and M. B. Steer, "Robust analog canceller for high-dynamic-range radio frequency measurement," *IEEE Transactions on Microwave Theory and Techniques*, vol. 60, no. 6, pp. 1709–1719, jun 2012.
- [93] G. Lasser, R. Langwieser, and C. F. MecklenbrÄuker, "Automatic leaking carrier canceller adjustment techniques," *EURASIP Journal on Embedded Systems*, vol. 2013, no. 1, may 2013.
- [94] C. Collado, M. Gonzalez-Rodriguez, J. M. Gonzalez-Arbesu, J. Mateu, J. Verdu, and A. Hueltes, "Feed-forward technique to measure the reflection coefficient under CW high-power signals," *IEEE Transactions on Microwave Theory and Techniques*, vol. 66, no. 10, pp. 4627–4633, oct 2018.
- [95] K. ya Hashimoto, "Advances in RF SAW devices: What are demanded?" in *2016 European Frequency and Time Forum (EFTF)*. IEEE, apr 2016.

- [96] J. Costa, S. McHugh, N. Rice, P. J. Turner, B. A. Willemsen, N. O. Fenzi, R. B. Hammond, J. D. Ha, C. H. Lee, and T. Sato, "Design and characterization of SAW filters for high power performance," in *2017 IEEE International Ultrasonics Symposium (IUS)*. IEEE, sep 2017.
- [97] R. Ruby, S. Gilbert, S. K. Lee, J. Nilchi, and S. W. Kim, "Novel temperature-compensated, silicon SAW design for filter integration," *IEEE Microwave and Wireless Components Letters*, vol. 31, no. 6, pp. 674–677, jun 2021.
- [98] R. Takayama, H. Nakanishi, and K. Hashimoto, "Impact of composition and structure of al alloy electrodes to power durability of SAW devices," in *2014 IEEE International Ultrasonics Symposium*. IEEE, sep 2014.
- [99] T. Omori, S. Ohara, C.-J. Ahn, and K. ya Hashimoto, "Study of power durability measurement of RF SAW devices for IEC standardization," in *2015 IEEE International Ultrasonics Symposium (IUS)*. IEEE, oct 2015.
- [100] H. Schmidt, S. Menzel, M. Weihnacht, and R. Kunze, "Investigation of SAW-induced acoustomigration effects in cu- and al-based metallizations," in *2001 IEEE Ultrasonics Symposium. Proceedings. An International Symposium (Cat. No.01CH37263)*. IEEE.
- [101] W. Ruile, G. Raml, A. Springer, and R. Weigel, "A novel test device to characterize SAW acoustomigration," in *2000 IEEE Ultrasonics Symposium. Proceedings. An International Symposium (Cat. No.00CH37121)*. IEEE.
- [102] G. Raml, W. Ruile, A. Springer, and R. Weigel, "Characterization of acoustomigration with on-wafer measurement system," in *2001 IEEE Ultrasonics Symposium. Proceedings. An International Symposium (Cat. No.01CH37263)*. IEEE.
- [103] K. ya Hashimoto, *Rf Bulk Acoustic Wave Filters for Communications*. Artech House, 2009.
- [104] E. Rocas, J. Mateu, C. Collado, A. Hueltes, J. Verdu, C. Billard, J. David, and A. Reinhardt, "Nonlinear Performance of BAW Filters Including BST Capacitors," *Radioengineering*, vol. 14, no. 1, pp. 369–374, Apr. 2014.
- [105] H.-T. Dabag, H. Gheidi, P. Gudem, and P. M. Asbeck, "All-digital cancellation technique to mitigate self-jamming in uplink carrier aggregation in cellular handsets," in *2013 IEEE MTT-S International Microwave Symposium Digest (MTT)*. IEEE, jun 2013.
- [106] M. Gonzalez-Rodriguez, C. Collado, J. Gonzalez-Arbesu, and J. Mateu, "New technique to cancel IMD3 in electroacoustic filters," in *2018 IEEE International Ultrasonics Symposium (IUS)*. IEEE, oct 2018.
- [107] K.-K. Cheng and C.-S. Leung, "A novel generalized low-frequency signal-injection method for multistage amplifier linearization," *IEEE Transactions on Microwave Theory and Techniques*, vol. 51, no. 2, pp. 553–559, feb 2003.

- 
- [108] E. Rocas, C. Collado, A. Padilla, J. Mateu, and J. M. O'Callaghan, "Nonlinear distributed model for IMD prediction in BAW resonators," in *2008 IEEE Ultrasonics Symposium*. IEEE, nov 2008.
- [109] M. González-Rodríguez, C. Collado, J. M. González-Arbesú, J. Mateu, G. Montoro, and P. L. Gilabert, "Tone injection-based cancellation technique for nonlinear distortion reduction of modulated signals in BAW resonators," *Microwave and Optical Technology Letters*, vol. 63, no. 3, pp. 781–786, sep 2020.
- [110] M. Gonzalez-Rodriguez, C. Collado, J. Mateu, J. Gonzalez-Arbesu, S. Huebner, and R. Aigner, "Method to measure reflection coefficient under CW high-power signals in SAW resonators," in *2021 IEEE International Ultrasonics Symposium (IUS)*. IEEE, sep 2021.
- [111] M. Gonzalez-Rodriguez, J. Mateu, C. Collado, J. Gonzalez-Arbesu, and R. Aigner, "Analytical modeling method of thermal spreading resistance in BAW filters," in *2019 IEEE International Ultrasonics Symposium (IUS)*. IEEE, oct 2019.
- [112] D. Garcia-Pastor, J. Mateu, C. Collado, R. Perea-Robles, M. Gonzalez-Rodriguez, and J. M. Gonzalez-Arbesu, "Comprehensive nonlinear characterization and modeling of a BAW duplexer," in *2019 IEEE MTT-S International Microwave Symposium (IMS)*. IEEE, jun 2019.
- [113] J. Mateu, C. Collado, A. Hueltes, R. Perea-Robles, D. Garcia-Pastor, M. Gonzalez-Rodriguez, and J. M. Gonzalez-Arbesu, "Outline process from the synthesis towards the nonlinear modeling of bulk acoustic wave filters," in *2018 IEEE/MTT-S International Microwave Symposium - IMS*. IEEE, jun 2018.
- [114] D. Garcia-Pastor, M. Gonzalez-Rodriguez, A. Hueltes, C. Collado, J. Mateu, J. M. Gonzalez-Arbesu, S. Kreuzer, and R. Aigner, "Nonlinear effects of electrode and bragg reflector materials in BAW resonators," in *2017 IEEE International Ultrasonics Symposium (IUS)*. IEEE, sep 2017.